DEVELOPMENT OF Ti-MCM-41 SUPPORTED Bi-METALLIC CATALYST FOR HYDRODEOXYGENATION OF LIGNIN DERIVED BIO OIL MODEL COMPOUNDS

MURTALA MAIDAMMA AMBURSA

INSTITUTE OF GRADUATE STUDIES
UNIVERSITY OF MALAYA
KUALA LUMPUR

2018

DEVELOPMENT OF Ti-MCM-41 SUPPORTED Bi-METALLIC CATALYST FOR HYDRODEOXYGENATION OF LIGNIN DERIVED BIO OIL MODEL COMPOUNDS

MURTALA MAIDAMMA AMBURSA

THESIS SUBMITTED IN FULFILMENT OF THE REQUIREMENTS FOR THE DEGREE OF DOCTOR OF PHILOSOPHY

INSTITUTE OF GRADUATE STUDIES
UNIVERSITY OF MALAYA
KUALA LUMPUR

2018

UNIVERSITY OF MALAYA

ORIGINAL LITERARY WORK DECLARATION

Name of Candidate: MURTALA MAIDAMMA AMBURSA

Matric No: HHC130025

Name of Degree: DOCTOR OF PHILOSOPHY

Title of Project Paper/Research Report/Dissertation/Thesis ("this Work"):

DEVELOPMENT OF Ti-MCM-41 SUPPORTED Bi-METALLIC CATALYST FOR HYDRODEOXYGENATION OF LIGNIN DERIVED BIO OIL MODEL COMPOUNDS

Field of Study: CHEMISTRY (CATALYSIS)

I do solemnly and sincerely declare that:

(1) I am the sole author/writer of this Work;
(2) This Work is original;
(3) Any use of any work in which copyright exists was done by way of fair dealing and for permitted purposes and any excerpt or extract from, or reference to or reproduction of any copyright work has been disclosed expressly and sufficiently and the title of the Work and its authorship have been acknowledged in this Work;
(4) I do not have any actual knowledge nor do I ought reasonably to know that the making of this work constitutes an infringement of any copyright work;
(5) I hereby assign all and every right in the copyright to this Work to the University of Malaya ("UM"), who henceforth shall be owner of the copyright in this Work and that any reproduction or use in any form or by any means whatsoever is prohibited without the written consent of UM having been first had and obtained;
(6) I am fully aware that if in the course of making this Work I have infringed any copyright whether intentionally or otherwise, I may be subject to legal action or any other action as may be determined by UM.

Candidate's Signature Date:

Subscribed and solemnly declared before,

Witness's Signature Date:

Name: Dr Lee Hwei Voon

Designation: Senior Lecturer

DEVELOPMENT OF Ti-MCM-41 SUPPORTED Bi-METALLIC CATALYST FOR HYDRODEOXYGENATION OF LIGNIN DERIVED BIO OIL MODEL COMPOUNDS

ABSTRACT

The effective and efficient catalyst for hydrodeoxygenation of lignin derived bio oil has been the major challenge. To provide remedy to that, this research work aimed to developed effective modified supported Ni-Cu catalysts for hydrodeoxygenation of lignin derived bio oil via its model compounds (Guaiacol and Dibenzofuran). The catalysts development began with experimental studies begins with preliminary studies using metal oxides (CeO_2, ZrO_2 and TiO_2) supported Cu-Ni catalysts at 250^oC, 5MPa and 4 hours which screen out TiO_2 species as a better support and hence provide basis for the synthesis of Ti-MCM-41 from MCM-41 by Ti incorporation through hydrothermal method followed by characterizations. The Cu-Ni/Ti-MCM-41 catalysts was also synthesized and optimized via Ni loading from 5 to 12.5%, characterized followed by hydrodeoxygenation of Guaiacol and dibenzofuran at 260^oC, 10MPa and 6 hours after optimization of reaction parameters which revealed 7.5% Ni loading as the optimum catalysts. The influence of Ti loading on structure and activity was studies at which revealed 20wt.% Ti loading as the optimum. Then narrow optimization further revealed support Ti-MCM-41 with 18wt.% as the optimum Ti loading which was impregnated with Cu-Ni catalysts and compared with MCM-41 and TiO_2 supported Cu-Ni catalysts for hydrodeoxygenation of guaiacol and dibenzofuran. The results showed that, Cu-Ni/Ti-MCM-41 catalysts, displayed higher activity than Cu-Ni/TiO_2 and Cu-Ni/MCM-41 catalysts respectively. The reusability studies showed that, Cu-Ni/Ti-MCM-41 catalysts is stable for up to 4 cycles.

Key words: Cu-Ni/Ti-MCM-41, Hydrodeoxygenations, Guaiacol, Dibenzofuran

PEMBANGUNAN MANGKIN Ti-MCM-41 BERPENYOKONG KEPADA Bi-METALIK UNTUK HIDRODIOKSIGENESI UNTUK LIGNIN BERASASKAN KEPADA MINYAK BIO SEBATIAN MODEL

ABSTRAK

Mangkin heterogen yang berkesan dan cekap untuk hidrodeoksigenasi lignin telah menjadi satu cabaran utama dalam penghasilan biofuel. Oleh demikian,, kerja penyelidikan ini bertujuan untuk membangunkan mangkin heterogen yang disokong dengan Ni-Cu untuk hidrodeoksigenasi lignin dengan menggunakan sebatian model (Guaiacol dan Dibenzofuran). Sintesis mangkin bermula dari kajian percubaan dengan menggunakan logam aktif (Cu-Ni) yang disokong oleh oksida logam (CeO_2, ZrO_2 dan TiO_2) melalui wet impreganation. Selapas itu, TiO_2 spesies dipilih sebagai sokongan yang paling baik untuk menyediakan Ti-MCM-41 melalui kaedah hidrotermal. Selain itu, Cu-Ni/Ti-MCM-41 telah disintesis dan kepekatan logam aktif (Ni) dari 5 hingga 12.5% telah dikaji, dicirikan dan diikuti dengan hidrodeoksigenasi Guaiacol dan dibenzofuran pada 260 oC, 10MPa dan 6 jam. Keputusan kajian menunjukkan 7.5% Ni memberikan tindak balas yang paling aktif. Seterusnya, Ti dengan pelbagai % menunjukan 20 wt. % Ti adalah terbaik dalam Cu-Ni/Ti-MCM41. Keputusan menunjukkan pemangkin Cu-Ni / Ti-MCM-41 bagi aktiviti yang lebih tinggi daripada pemangkin Cu-Ni / TiO_2 dan Cu-Ni/MCM-41. Kajian reusability menunjukkan bahawa pemangkin Cu-Ni / Ti-MCM-41 stabil hingga 4 kitaran.

Kata kunci: Cu-Ni/Ti-MCM-41, Hidrodeoksigenasi, Lignin, Guaiacol, Dibenzofuran

ACKNOWLEDGEMENTS

At the onset, all praises and total submission are due to almighty God most gracious most merciful who has spared my life to this extent and additionally, grant me more success throughout my academic programme.

I wish to deeply acknowledge and express my sincere appreciation to my late supervisor; Prof. Dr Sharifah bee Abdul Hamid for her excellence guidance, advices, contributions both academically and financially as well as encouragements within the period of three years, which led to success of this work. I pray for Allah to forgive all her short coming and made Jannatul Firdaus her final abode.

I would like to express my deepest gratitude and appreciation as well to my current supervisors; Associate Prof. Dr Juan Joon Ching and Dr Lee Hwei Voon for their supports and valuable advices and contributions which led to success of this work.

I would like to appreciates the sponsorship and financial supports acquired from Tertiary Education Trust Fund (TETFUND) through Kebbi state university of science and technology, Aliero and research grant from Ministry of Higher Education (Grant No. HIR – F000032), Grand challenge (GC Grant No. GC001A-14AET) to meet the success of this work.

My special thank goes to Dr Yakubu Yahaya, Dr Aminu Rabi'U Koko, Dr Muhammad Gwani, Dr Tammar Hussain Ali, Dr Jimmy Nelson and my entire colleagues from Kebbi State University of Science and Technology Aliero Kebbi State Nigeria.

Last but most important, I wish to express my profound gratitude and appreciation to my parents for their tremendous effort, assistance and constant prayer throughout my study period and I also pray for Allah to forgive and rewards them abundantly

Table of Contents

LIST OF FIGURES

LIST OF TABLES

LIST OF SYMBOLS AND ABBREVIATIONS

HDO	:	Hydrodeoxygenation
DBF	:	Dibenzofuran
MCM-41	:	MOBIL COMPOSITION OF MATTER NO 41
GUA	:	Guaiacol
Ti-MCM-41	:	Titanium doped mesoporous MCM-41
Zr,	:	Zirconium
Ce,	:	Cerium
Ti,	:	Titanium
V	:	Vanadium
Cr	:	Chromium
^{o}C	:	Degree Celsius
MPa	:	Mega pascal
T	:	Time
M-MS	:	Metal doped mesoporous silica
mg	:	Milligram
GC-MS	:	Gas chromatography-mass spectrometry
GC-FID	:	Gas chromatography
K_2CO_3	:	Potassium carbonate
$Ca(OH)_2$	:	Calcium hydroxide
Na(OH)	:	Sodium hydroxide
H_2O	:	Water
CO_2	:	Carbon dioxide
OH	:	Hydroxyl
OCH_3	:	Methoxy

Al_2O_3,	:	Alumina
SiO_2	:	Silica
ZrO_2	:	Zirconia
TiO_2	:	Titania
CeO_2	:	Ceria
C	:	Carbon
CNT	:	Carbon nanotube
TMS	:	Transition metal sulphide
H	:	Hydrogen
O	:	Oxygen
H_2S	:	Hydrogen sulphide
SO_2	:	Silica
wt%	:	Weight percent
DH	:	Dehydration
HYD	:	Hydrogenation
DME	:	Demethylation
nm	:	Nanometre
THDBF	:	Tetrahydrodibenzofuran
HHDBF	:	Hexahydro dibenzofuran
CHCHOH	:	Cyclohexyl cyclohexanol
CHCHE	:	Cyclohexyl cyclohexene
BCH	:	Bicyclohexane
PCHOH	:	Phenyl cyclohexanol
CHCHO	:	Cyclohexyl cyclohexanone
Iso-BCH	:	Cyclopentyl methyl cyclohexane
CHPOH	:	Cyclohexyl phenol

CHB	:	Cyclohexyl benzene
(NaOH)	:	Sodium hydroxide
CTAB	:	Cetyl trimethyl ammonium bromide
TEOS	:	Tetra ethyl ortho silicate
$Ti(OiPr)_4$	:	Titanium iso-propoxides
RPM	:	Revolution per minute
DI	:	Deionized water
XRD	:	X-Ray diffractions
FTIR	:	Fourier Transform-Infrared Spectroscopy
RAMAN	:	Raman spectroscopy
DR-UV Vis	:	UV-VIS Diffuse Reflectance Spectroscopy
TGA	:	Thermal gravimetric analysis
TPO	:	Temperature–Programmed oxidation
XPS	:	X-Ray Photoelectron Spectroscopy
BET	:	Brunauer-Emmett-Telle
BJH	:	Barrett-Joyner-Halenda
TEM	:	Transmission Electron Microscope
EDX	:	Energy Dispersive X-Ray spectroscopy
ICP-MS	:	Inductively Coupled Plasma-Mass Spectrometry
H_2-TPR	:	Hydrogen Temperature–Programmed Reduction
FESEM	:	Field Emission Scanning Electron Microscopy
NH_3-TPD	:	Ammonia Temperature–Programmed Desorption

LIST OF APPENDICES

CHAPTER 1: INDRODUCTION

1.1 Research backgrounds

The world population growing continuously which lead to increase of the world energy demand as well as energy consumption. Despite tremendous current and future energy demand, the major world energy source (fossil fuels) encountering significant negative setback. Firstly, fossil fuels are non-renewable and therefore forward toward extension due to continuous depleting of its proven reserve. Secondly, it emits greenhouse gas (carbon dioxides) upon combustion which poses detrimental effect (global warming) in the environment (Nigam and Singh 2011). Consequently, scientists were compelled to search for promising alternative energy sources for production of chemical and fuels for the sustainable ecosystem and economic growth (Runnebaum et al., 2012. In this regard, the efficient valorisation of low cost biomass to high-value products (biofuels or biochemical) are currently received significant research attention. Biomass render various unique characteristics, such as highly abundance, superior renewability, and remarkable sustainability, thus its effective valorisation could provide potential alternative to overcome the negative impacts of the fossil fuels usage (Bykova et al., 2012b). Another advantage of using biomass as energy resource is that, the existing municipal solid waste can be reduce and converts it into useful product (such as bio oil) (Xiu and Shahbazi, 2012). In recent years there are growing interest for lignin conversion and it subsequent upgrading to transportation fuels. The aroused interest was due to large amount of lignin residue from pulp and paper industry. The lignin component of lignocellulose appeared to be a promising renewable feedstock for the production of a variety of fuels and chemicals. The advantage of lignin derived bio-oil (Lignin derived oil) is that, it can be upgraded to higher quality transportation fuels (Runnebaum et al., 2012). Fast-pyrolysis is one of the widely-used processes for converting lignin into bio-oil (Runnebaum et al., 2012, Lee et al., 2015). However, the potential properties of Lignin-derived bio-oil

(Lignin derived oil) has been limited due to presence of various oxygenated functional groups, leading to undesirable physicochemical properties, such as low heating value, low thermal and chemical stability, high density, high viscosity, polarity (Fatih Demirbas, 2009, Rutkowski, 2012). The oxygenated compounds composed in bio oil are including ketone, aldehydes, hydroxyl, methoxy, acid, ester etc (Berenguer et al., 2016). Consequently, lignin-derived oil become incompatible for either direct utilization or in combination with a petroleum fraction. This scenario stimulating the researchers to search for better upgrading processes to improve commercial aspects of lignin-derived bio-fuels (Runnebaum et al., 2012, Nimmanwudipong et al., 2011a).

In order to enhance the quality of lignin-derived oil, several process such as steam reforming, zeolite cracking, and hydrodeoxygenation (HDO) processes have been considered for upgrading of lignin-derived oil (Tyrone Ghampson et al., 2012). As refer to literature study, the biomass upgrading process by using hydrodeoxygenation (HDO) pathway with catalytic systems can efficiently remove the chemically bonded oxygen from lignin-derived oil (González-Borja and Resasco, 2011, Lee et al., 2015). The new applications of catalysts system in hydrodeoxygenation of lignin derived oil is associated with many challenges due to the complex nature of its oxygenated aromatic compounds, such as guaiacol, anisole, methyl anisole, furan, benzofuran, dibenzofuran, phenols, and catechol (Runnebaum et al., 2012). Therefore, in order to obtained insight chemistry and reactivity of catalyst in terms of activity, selectivity and stability, catalytic study for HDO of lignin-based model compounds is one of the best options and has received tremendous research interest in the recent times (Lee et al., 2015). Guaiacol is the most suitable lignin-based model compound to investigate the upgrading process of Lignin derived-oil because of its considerable similarity with other lignin-derived model compounds, such as phenol, catechol, anisole, and methyl anisole as a result from its three different C-O linkages (C_{AR}-OCH_3, C_{AR}-OH and $C_{AR}O$-CH_3) (Zhang et al., 2013b, Sun et al., 2013). In

addition, study on HDO of dibenzofuran model compound could serve as representation to other heterocyclic aromatics components of Lignin derived oil (Ambursa et al., 2016b). The existence of dibenzofuran in lignin-derived oil has been observed and demonstrated its sources from phenol coupling reactions.

Researchers have been reported that heterogeneous catalysts with metal functions are suitable for hydrogenation of aromatic ring and acidic catalyst support for best deoxygenation process, thus combination of this catalyst design will meet the requirement for HDO reactions (Zhang et al., 2013b, Zhang et al., 2013c) . The active hydrogenation functionalities of conventional CoMoS and NiMoS supported on Al_2O_3 catalysts have been examined but, its affiliated challenge such as, over dependent of active sites on sulfiding agents, products contamination and quick deactivation of alumina support making its unsuitable for this processes (Badawi et al., 2013). Consequently, noble metals, such as Pt, Pd, Ru, Pt-Pd, and Ru-Co-based catalysts have been previously studied (de Souza et al., 2015, Gao et al., 2015, Gutierrez et al., 2009b, Hong et al., 2014b, Lee et al., 2012, Lee et al., 2015, Leiva et al., 2015, Lin et al., 2011, Wang et al., 2011). However, the high cost and scarcity of these noble metals limit their applicability in the industrial scale (Zhang et al., 2013b). As searching for effective alternatives, various non-noble transition metals, such as Co, Ni, Fe, Cu-Ni, and Ni-Fe-based catalysts have been studied, and it was found that Ni-Cu catalysts exhibit better catalytic activity in hydrodeoxygenation reaction (Zhang et al., 2013b, Zhang et al., 2013c, Tran et al., 2016b, Olcese et al., 2012b). The Cu-Ni-based catalyst was found to maintain Ni stability during HDO process. (Bui et al., 2011a).

On the other hand, the relevance of SiO_2 supports have been hindered by weak acidity and that of Al_2O_3 by high acidity and boehmite nature during HDO process**.** The potential of ZrO_2, CeO_2, and TiO_2 have limited by coking and deactivation at high temperature during HDO process as well as smaller surface area Schumacher et al., 2003. Thus, the

need for catalytic materials with large surface area and high acidity properties has drawn attention towards the choice of mesoporous silicate structures, which exhibit larger surface areas of up to 1500 m^2/g, high mechanical strength and high thermal stability particularly mesoporous MCM-41 (Bing et al., 2012, Khalil, 2007, Parlett et al., 2011). In addition, mesoporous materials have suitable pore dimensions which facilitate the diffusion of the substrates to the active site of catalyst and provide suitable confinement for contacting during reaction (Argyle and Bartholomew, 2015). A considerable drawback is that mesoporous silica materials show mild acidic nature, which can be improved by the incorporation of transition metals, such as Zr, Ce, Ti, V, Cr-based active metals, etc. (Bianchi et al., 2001, Bore et al., 2005, Eliche-Quesada et al., 2003, Jiménez-López et al., 2001, Bendahou et al., 2008, Moreno-Tost et al., 2002, Do et al., 2005, Guidotti et al., 2003, Weckhuysen et al., 2000). Particularly, the incorporation of Ti active metals into the mesoporous silica improve the acidity properties with large amounts of Lewis and Bronsted acid sites, which could play a key role in HDO reactions (Szegedi et al., 2010, Corma, 1997, Bianchi et al., 2001, Eliche-Quesada et al., 2003, Hirai et al., 1999, Wu et al., 2002, Rajakovic et al., 2003, Corma et al., 2004).

1.2 Problem statement

The challenges of low chemical and thermal stability, low heating value, high viscosity, and high density of lignin derived oil as a consequence of existed oxygenated compounds such as ketone, aldehyde, ether, ester, acid, and hydroxyl group could be illuminated through hydrodeoxygenation process with the assistance of efficient catalytic system. In search of effective and efficient catalytic system for upgrading of lignin derived oil into high quality biofuel, many type of heterogeneous catalysts have been studied via catalytic HDO of model compounds. However, there are low activity, and selectivity to saturated hydrocarbons remain a big challenge. Therefore, research focusing toward modification of catalysts properties through the application of supported metals

doped mesoporous silica for HDO reactions, which could improve the catalytic performance (activity, selectivity and stability). Furthermore, severe reaction condition for HDO process with extreme to high temperature (300-450ºC) and high pressure (above17MPa) is another challenge for the bio oil upgrading process. Therefore, a target to control the reaction temperature of HDO reaction to mild condition with the aids of reactive catalyst is another aims to lead to more effective and economical HDO of lignin derived oil.

1.3 Justification of the study

The low cost and effective HDO catalysts (high catalytic activity, product selectivity and catalyst stability) for upgrading of lignin derive oil to high quality hydrocarbon-based biofuel are of current research interest. These criteria will no doubt in enhancing the economic feasibly of the biomass upgrading process, which render a price of biofuel comparable to petroleum-based fuel. Therefore, the use of transition metal doped mesoporous silica supported bimetallic Cu-Ni catalysts for hydrodeoxygenation of guaiacol and dibenzofuran under mild reaction conditions could be geared towards achieving that.

1.4 Aim and Objectives of the research

The aim of the present research is to develop an efficient heterogeneous catalyst for the catalytic hydrodeoxygenation (HDO) of lignin-based model compounds (guaiacol and dibenzofuran) into high quality hydrocarbon molecules under mild reaction conditions. The main research objectives designed to achieve the aim are as follows: -

1. To synthesize and characterize acidic metal-doped mesoporous silica (M-MS) as HDO catalyst support.
2. To synthesize and characterize acidic metal-doped mesoporous silica supported Copper-Nickel bimetallic promoted catalysts (Cu-Ni/M-MS catalysts).

3. To determine catalytic activity of prepared acidic M-MS supported Cu-Ni catalysts via hydrodeoxygenation of lignin-derived bio oil model compounds (guaiacol and dibenzofuran).

1.5 Scope of the research

The scope of the research is to develop an efficient hydrodeoxygenation (HDO) catalyst, which namely mesoporous silica supported bimetallic based catalysts. The catalysts composed of Cu-Ni catalysts supported on metal doped-MCM-41 support. The catalytic performance for the prepared catalysts was further investigated via hydrodeoxygenation of Lignin derived oil model compounds (Guaiacol and dibenzofuran) under batch reactor. Generally, the mesoporous catalyst support was chosen for the HDO reaction is mesoporous Ti-MCM-41. It is estimated that, incorporation of titanium species within the matrix of mesoporous MCM-41 will generate acidic active sites. The presence of acidic sites from mesoporous catalysts support could influence the activity of Cu-Ni bimetallic active metal for HDO reactions. The developed catalyst could be able to catalysed the HDO reaction under milder reaction (260^{o}C, 10MPa and 6 hours of reaction time and 100mg of catalysts)

1.6 Outline of the thesis

CHAPTER 1

This chapter highlight the detail background of current research towards the prospect, challenges and catalytic method for upgrading of biomass-derived bio oil into high quality product via catalytic hydrodeoxygenation system. In addition, the chapter reported the problem statement of current study, justification of the research, aim and objective of the research, scope of the research as well as the thesis structures.

CHAPTER 2

In this chapter, the review of relevant literature on thermo-chemical conversion of lignocellulose biomass into bio oil, various bio oil upgrading techniques to high quality product, study on bio oil model compounds for hydrodeoxygenation process, reaction mechanism of HDO by using model compounds were presented. The chapter also includes relevant literature on HDO catalysts with different metallic system and, potential catalyst support for efficient HDO reaction.

CHAPTER 3

Chapter 3 presented the methodology of the whole research study, which included types of reagent use for reaction and analysis, catalysts synthesis procedures, and HDO reaction. The chapter also includes catalysts characterization techniques with details of characterization method used. It also encompasses description of HDO batch reactor (High pressure batch reactor) as well as catalysts activation/pre-treatment unit. The detail of catalytic performance test using batch reactor and products analysis using GC-MS and GC-FID were also describes in this chapter.

CHAPTER 4

In this chapter, results and discussion for catalysts characterization and catalytic performance tests were presented. Within the results sections, each figure and table is preceded with appropriate caption and detail explanation. The results were presented into six (6) section. Section one (1) reported the results of preliminary study using different metal oxides supported Cu-Ni catalysts, and section two (2) display results for optimization of Ni loading over metal oxide supported catalysts. Section three (3) presents the results for synthesis of mesoporous Ti-MCM-41 and MCM-41 supports, then section four (4) indicate the results for optimization of Ni loading toward hydrodeoxygenation activity of Cu-Ni/Ti-MCM-41 catalysts. The section five (5) of this chapter was discussed

with results for optimization of titanium content Cu-Ni/Ti-MCM-41catalysts toward the hydrodeoxygenation activity, and section six (6) shows the results of comparative studies between metal oxides and mesoporous supported catalysts for hydrodeoxygenation of guaiacol and dibenzofuran (DBF), the results of stability study and proposed catalytic reaction pathway for Guaiacol and dibenzofuran conversion toward saturated hydrocarbon over Cu-Ni/Ti-MCM-41 catalysts was discussed herein.

CHAPTER 5

In this chapter, the summary of research finding and recommendation for future work was presented.

CHAPTER 2: LITERATURE REVIEW

2.1 Chemical Components of Lignocellulose Biomass

The lignocellulose biomass is a renewable and inedible organic materials that potentially apply as a source of fuel or energy. The biomass includes forestry residues (hardwood, softwood and grasses), agricultural waste (straw, husks and stalks) and municipal wastes are found in large distribution around the world (Lange, 2007, Cherubini and Strømman, 2011). Malaysia is one of the world largest producer of palm oil, having current palm trees plantation area of about 4 million hectares with biomass production capacity of > 200 million tons that out of theses population, oil only account for 10% of the whole biomass. The remaining 90% of this biomass is consist of empty fruit bunches, fronds and trunk (Mekhilef et al., 2011), which chemically composed of cellulose, hemicellulose and lignin (Figure 2.1) . Generally, all types of biomass are build up from plant cell surrounded by protective layer called cellular cell wall. The cell wall is made up complex structures of fibrous material which consist of three basic components; cellulose, hemicellulose and lignin that co-exist in different proportion depending on the biomass types; Grasses, Softwood, Hardwoods and other agricultural waste as given in Table 2.1. (Wang et al., 2015a, Lange, 2007, Sjöström, 1993, Akhtar and Amin, 2011).

Among these three components, cellulose occupy larger amount in range of 35-50%. Cellulose polymer is hydrophilic in nature with chemical structures consisting homopolymer of D-glucose linked by β-(1,4) glycosidic bond. The large number of glucose monomers between 300-15000 units are linked in an organized structure with the help of hydrogen bonding between the adjacent hydrogen and aside oxygen from the other chain, in order to form orderly crystalline structures (Xu et al., 2014, Saha, 2004) as indicated in the Figure 2.1 above. (Wang et al., 2015a, Lange, 2007, Sjöström, 1993, Akhtar and Amin, 2011).

The content of Hemicellulose from lignocellulose biomass is range from 25-30%. Hemicellulose is known as heterogeneous polymer of pentose sugars (e.g. xylose, arabinose), and hexose sugars (e.g. mannose, glucose, galactose) linked to one another to form xylan, arabinoxylan, glucuronoxylan, glucomannan and xyloglucan monomer unit depending on the biomass sources. Unlike cellulose, hemicellulose possesses lower degree of polymerization between 70-200 basic structural monomer unit (Joffres et al., 2013b).

The lignin component in lignocellulose biomass is a three-dimensional polyaromatic biopolymers with large structural branching, which resulted to high degree of amorphousity. Methoxylated phenylpropane unit are linked to one another to form various group such as coumaryl alcohol and sinapyl alcohol. It provides useful protection from water and bacteria or viruses to the trees due to its hydrophobic characteristic. The usual proportion of lignin in lignocellulose is ranging between 18-30%. However, in terms of energy density, lignin occupies more than 40% due to higher structural stability as compared to cellulosic compounds (Wang et al., 2015a, Lange, 2007, Sjöström, 1993, Akhtar and Amin, 2011).

Table 2.1: Chemical components of of lignocellulose biomass (Akhtar & Amin, 2011)

Biomass	(%) lignin	(%) cellulose	(%) hemicellulose
Hardwood	15.5- 24.1	40-53.3	18.4 - 35.9
Softwood	20.0- 27.9	42.0 - 50.0	11- 27.0
Agricultural waste	6.0 - 25.0	29.2 – 47.0	12 - 35
Grasses	10.0 -30.0	25 – 40%	25.0 – 50.0

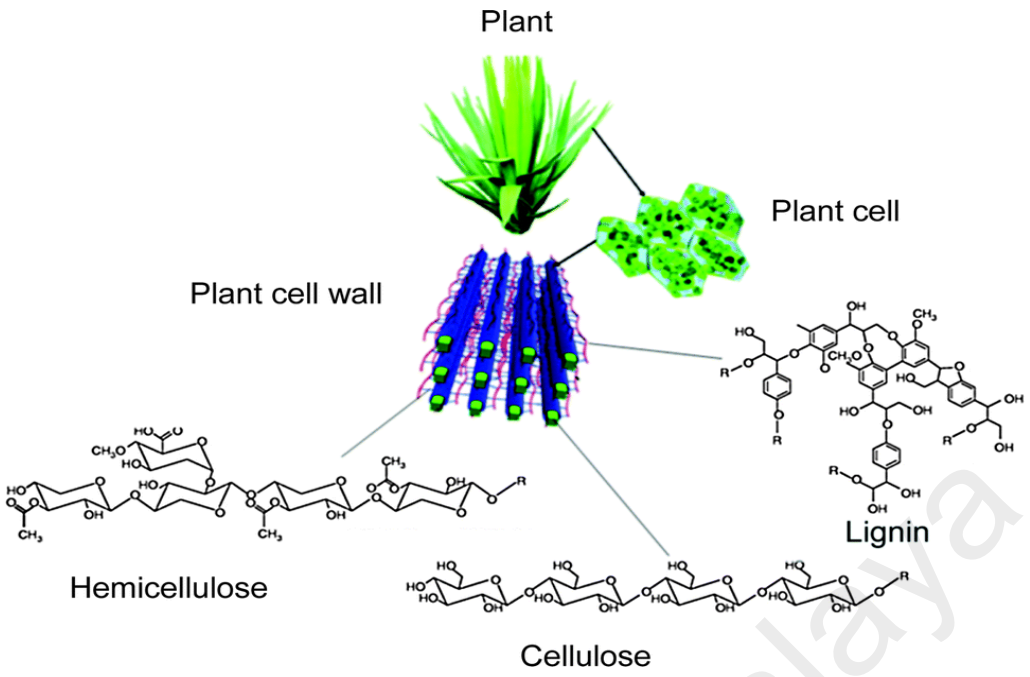

Figure 2.1: Structural component of lignocellulose biomass

2.2 Structural composition of lignin

Chemically, lignin consist of hydrophobic structures with highly branched and three-dimensional amorphous network of aromatic compounds (Saidi et al., 2014). The chemical structures of lignin are highly dependent on the natural sources and processes used in extraction or separation of lignin from other components (cellulose and hemicellulose). For all the sources of biomass, it consists of hydroxyl-phenyl propane as the basic structural unit since it forms the skeletal structures in all the three lignin monomers as shown in Figure 2.2. These monomers include; p-coumaryl alcohol (P-hydroxyphenyl), coniferyl alcohol (Guaiacyl) and sinapyl alcohol (Syringyl), which are distributed differently in various type of biomass (Saidi et al., 2014, Joffres et al., 2013a). The woody lignin contains mainly of p-coumaryl alcohol and coniferyl alcohol monomers, however, herbaceous lignin consists of all types of monomers (Joffres et al., 2013b, Jongerius et al., 2013a, Xu et al., 2014).

The most common linkages available in lignin are ether linkages with little disparities from softwood to hardwood. The β-O-4 linkages occupy 50% in soft wood and 60% in hardwood, α-O-4 and 4-O-5 ether bond only account for 8 and 5% of the total bonds in both type of woods, where the remaining interactions are included 5-5 biphenyl linkages (18%), β-5 phenylcoumaran (11%), and β-β (2%). Many functional groups such as phenolic hydroxyl, methoxyl, benzyl alcohol, aliphatic hydroxyl, and carbonyl account for reactivity of lignin fragments (Xu et al., 2014, Wang et al., 2015a, Jongerius et al., 2013a, Joffres et al., 2013b, Joffres et al., 2013a).

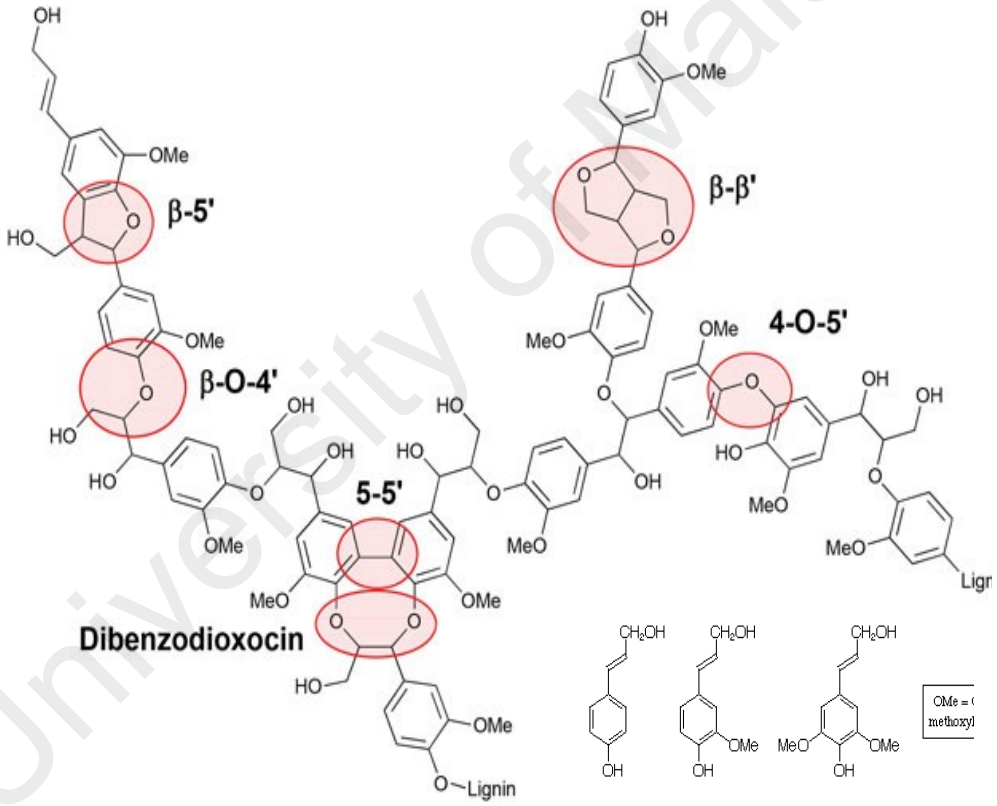

Figure 2.2: Chemical structures of lignin polymer

In contrast to that, cross-linking frequencies has also been reported with less than 1 in 19 monomer units. Further investigation also revealed the existence of isolated lignin in the form of lamella-like sheet without any cross linking ((Banoub and Delmas, 2003, Banoub et al., 2015)).

2.3 Lignin Conversion processes

Lignin is one of the major bio-component that abundantly found in lignocellulose biomass (Joffres et al., 2013a). More than 55 million tons of lignin are separated from cellulose and hemicellulose through Kraft process in pulp and paper industries across the world. Generally, lignin will undergo combustion to generate heat as low grade energy source (Zhou, 2014, Joffres et al., 2013a). The excessive world energy requirement and series of emanating environmental regulation on other energy sources have raise the research interest to produce bio-based chemical platforms (such as aromatic and phenol) and liquid biofuels-derived from lignin. Research on biochemical platform have been far going and showed that, the obtained phenolic compounds from lignin sources possess high potential toward production of value added chemicals (Benoit Joffres et al., 2013).

Recently, there are numerous interest in lignin conversion into high grade product such as transportation fuels. The potential of lignin-derived liquid product shows comparable characteristic to that of petroleum-based transportation fuel. The conversion of lignin to biofuel is further regarded as an effort to avoid under-utilization of this fragment comparing to cellulose and hemicellulose, which their conversion to fuels and chemical have been far going (Runnebaum et al., 2012). It appeared that lignin conversion to biofuels will quantitatively and qualitatively add more value as compare to the conversion of cellulose and hemicellulose components to biofuels (Ben et al., 2013, Bui et al., 2011b). Besides that, adopting lignin as precursor to transportation fuels could yield high octane fuels than cellulose and hemicellulose precursors. The potential of lignin toward suitable transportation fuels could be affiliated to extra stability of aromatic structures, which resulted to formation of more cyclic compounds than aliphatic types. The conversion of lignin to targeted hydrocarbons molecules, involved cleavage of inter unit linkages (C_9–O–C_9 and C_9–C_9 bonds). The bond dissociation energy of C-O-C bond (218–314 kJ mol^{-1}) is lower than C-C bond (~384 kJ mol^{-1}) in lignin fragment (Wang et

al., 2015a), which could result to more C-O-C cleavage than C-C bond cleavage under a particular reaction conditions to hydrocarbon range making up the transportation fuel. (Azadi et al., 2013, Runnebaum et al., 2012, Nimmanwudipong et al., 2011a).

Currently, several thermochemical and biochemical approaches are available for lignin conversion to fuels. The thermochemical methods used for lignin conversion to liquid fuels includes combustion, gasification and hydrolysis, liquefaction and pyrolysis processes (Selvaraj et al., 2015). The obtained liquid products from thermochemical process (such as liquefaction and pyrolysis) of lignin are known as lignin derived bio oil or lignin derived oil. These processes are given below with respect to lignin conversion to liquid fuels.

2.3.1 Combustion

Combustion involved direct thermal decomposition of lignin in the presence of oxygen. The generated heat and power can be used directly for heating purpose, cooking etc. (Demirbas, 2009). The major advantage of combustion allowed utilization of biomass waste to generate heat energy. However, the major challenge associated with combustion includes; low efficiency, greenhouse gas emission and ash handling, and immediate consumption of heat (Joffres et al., 2013a).

2.3.2 Gasification and Hydrolysis

In this process, Lignin is directly converted to gaseous fuels. The gaseous products can further be converted into liquid products (saturated hydrocarbons) through Fischer-Tropch process or directly burn to release energy for other processes especially for turbine rotation for electricity generation. The heating value of generated gas ranges from low (~5MJ/m^3) to medium (~10-20MJ/m^3) depending on the gasification methods. The usual operating temperature ranges is between 900 – 1400^oC and the composition of the generated gas (such as CO_2, CO, H_2, CH_4) rely directly on the nature and dryness of the

lignin feeds, operating temperature and amount of oxygen used (Demirbas, 2009). The major limitation of gasification process is that, lignin is in completely converted to gaseous products even with the presence of alkali catalysts (Demirbas, 2009, Badin and Kirschner, 1998). The tar residue left behind lead to technical issues for turbine and boiler during combustion processes.

2.3.3 Liquefaction

Liquefaction processes involved lignin conversion to liquid fuels at high pressure. In this processes, highly moisturized lignin precursor is converted to fuel at lower temperature (~400^{o}C), long residence time (0.2 – 1.0hr) and higher-pressure (5 -20MPa) using water or organic liquids as solvent in the presence of alkali or metal catalysts (Joffres et al., 2013a). The prefer used of water as solvent, low oxygen content of liquid products and higher heating value are the main advantages of liquefaction method. However, this method is affiliated to low oil yield and uneconomical process due to expensive of higher-pressure lead severe energy consumption (Vuori, 1988). The two most frequently use liquefactions methods as it applied to lignin conversion are hydrothermal and solvolysis methods. Hydrothermal conversion is a process, which convert lignin to biofuels using sub-critical and super-critical water. When another solvent is used instead of water, the process is called solvolysis (Connors et al., 1980), which are discussed below:

2.3.3.1 Hydrothermal conversion

Hydrothermal conversion of lignin is carried out under subcritical or supercritical condition at a temperature between 280^{o}C – 400^{o}C, 20- 25MPa reaction pressure, water to lignin ratio between 2 -50 with reaction time of 2 - 180 minutes. The major advantage of this process is that process can reach critical conditions (22MPa, 374^{o}C) due to polarity neutralization, which enhance lignin solubility, fast, homogenous and efficient reaction.

As many investigated, hydrothermal conversion of lignin resulted to the formation of liquids phase, gaseous phase and sometimes solid phase (chars) (Toor et al., 2011, Pińkowska et al., 2012). The liquid contains organic and water phase with the yield of organic phase up to 20% and predominantly, consist of phenols, catechol, Guaiacol and other formed of methoxy phenols, which emanated from the hydrolysis of ether-bonds (Sasaki and Goto, 2008). It also observed that, further hydrolysis of these products leads to formation of benzene. Other studies proposed that, water-soluble compounds are formed at the beginning of the reaction, which further convert to water-insoluble products due to polymerization reaction occurring at long residence time (Barbier et al., 2012, Bobleter, 1994). To avoid unfavourable side reaction such as polymerization, cross-linking reaction and coke formation, various catalysts such as K_2CO_3, $Ca(OH)_2$, and Na(OH) together with water-other solvent mixture such as water-ethanol, phenol, formic acid have been considered to enhance of products solubility and reduced products polymerization. However, coke formation and low oil yield remained a major challenge (Oasmaa and Johansson, 1993, Ramsurn and Gupta, 2012).

2.3.3.2 Solvolysis

In a hydrothermal conversion processes, when water is replaced by other solvents such as alcohol, acids or a mixture of two solvents is referred to as solvolysis (Joffres et al., 2013a). To improved hydrogenation and oil yield of pyrolysis process, the use of hydrogen donor-solvent have been explored. So far, Tetralin solvent has displayed remarkable and interesting properties than any other solvent and therefore, seem to be the most outstanding solvent for solvolysis process (Connors et al., 1980, Vuori, 1988, Jegers and Klein, 1985). As reported, tetralin possessed hydrogenation/dehydrogenation properties and strong ability for radical stabilization; hence limiting re-condensation of the initial lignin products into larger molecules and therefore, low char formation (Connors et al., 1980). In the solvolysis process, many organic solvents such as ethanol,

glycerol, m-cresol and a mixture of ethanol and formic/ acetic acid/ iso-propanol have been used and proved to be efficient for lignin conversion to aliphatic hydrocarbons and phenols (Vuori, 1988, Vuori, 1986).

2.3.4 Pyrolysis process

Pyrolysis is generic terms applied to thermal decomposition of biomass to obtained bio oil in the absence of oxygen (Babu, 2008). The same technique is also applied to convert lignin to liquid fuels depending on the pyrolysis condition. Pyrolysis process involved heating of lignin under inert environment at low pressure without catalysts, but when the processes are carried out in the presence of catalysts is referred to as catalytic pyrolysis or catalytic cracking (Mullen and Boateng, 2010, Meier et al., 1992). In analogous, fast pyrolysis of lignocellulose biomass occurring at 600 – 1000 ºC, 0.5 – 10s, but for lignin pyrolysis proceed at relatively lower temperature between 400ºC - 750ºC to decompose macromolecules into char, liquids, and gases (Bridgwater and Peacocke, 2000, Kaminsky and Schwesinger, 1980). The lignin derived liquid from pyrolysis will produce majority of amount at 40-60wt%, gases 8-20wt% and char between 30-40wt% (Li et al., 2012, Amen-Chen et al., 2001). The composition of lignin derived liquid consists of H_2O, unsaturated molecules as well as stable aromatic oxygenated molecules such as phenolic compounds. Although, more than 40wt% liquid content was produced above 400ºc, but over-degradation resulted in low oil yields and unfavourable tar formation (Jegers and Klein, 1985). To improve oil yield, catalytic pyrolysis and hydro-pyrolysis (with H_2 without solvent) were conducted, the reported outcome showed that higher oil yield up to 74wt% was obtained with more selectivity toward aromatic compounds such as Benzene, toluene and xylene (Joffres et al., 2013a, Dorrestijn et al., 2000, Jegers and Klein, 1985). The pyrolysis of lignin involved several reaction pathways as given in the below (Figure 2.3) (Joffres et al., 2013a).

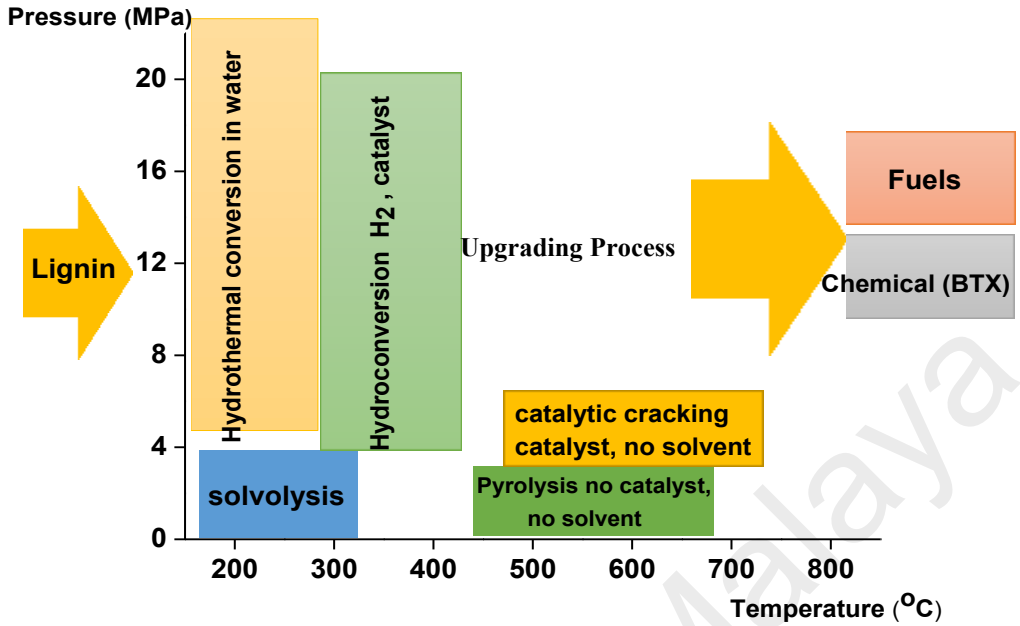

Figure 2.3 : Various thermochemical conversion routes of lignin

2.3.5 Hydro-conversion processes of lignin.

Hydro-Conversion involved the use of hydrogen with or without any solvents in the presence of catalysts (Meier et al., 1992). Various hydro-processing types such as hydrodeoxygenation and hydrocracking are considered in this category (Joffres et al., 2013b). Hydro-conversion processes (e.g. Hydrodeoxygenation or hydrocracking processes) involved carbon to carbon cleavage or carbon to heteroatom (oxygen atom in this case) cleavage with the help of catalysts. The usage of hydrogen is functioning to eliminate oxygen in the form of water, and also hydrogenate unsaturated compounds to highly stable hydrocarbon graded molecules (Joffres et al., 2013a, Saidi et al., 2014). Despite the major challenges in selective transformation of lignin fragment due to structural heterogeneity and difficulty in hydrolysing its cross-linked structures as well as degradation of intermediates reactivity. Catalytic hydrodeoxygenation followed by cracking reactions tend to give way forward towards lignin conversion to hydrocarbon fuel (Yan et al., 2008). The quality of generated fuel by lignin hydrodeoxygenation

process is largely dependent on the efficiency and performance of the applied catalysts. An ideal hydrodeoxygenation catalyst for fuel generation should possess the following properties: (i) high activity for hydrogenolysis of C_9–O–C_9, C_{sp2}-OCH_3, C_{sp2}-OH and $C_{AR}O$-Csp^3H_3 bonds (inter unit linkages, demethoxylation, dihydroxylation or demethylation properties), (ii) high resistivity against formation of coke, and ease of regeneration and ease of catalysts separation from the solid residue (Azadi et al., 2013, De Wild et al., 2009).

2.4 Composition of Lignin derived oil

Bio-oils, is also called bio-crude oils, pyrolysis oils, pyrolysis liquids which is dark brown and free following liquids with characteristic of an acid smoky odour (Demirbas, 2009). When it sources directly from lignin, it may refer as lignin derived oil or lignin derived bio oil (Majid Saidi, 2014). The chemical composition of lignin derived oil is dependent on the lignin sources (since basic structural content differed) as well as pyrolysis types and process condition. Lignin derived oils are multi-component mixtures of various molecules derived from depolymerisation of lignin polymer or pyrolysis process. Depending on its sources, for example, lignin from soft wood produced more guaiacol and derivatives compounds plus other components. However, lignin from hard wood yield more of both guaiacol and syringyl derivatives compounds as the major oil components (Saidi et al., 2014). According to literature, lignin derived oil have been reported to contained the following mixture of compounds; guaiacol (typically 39-46.92%), syringyl (16%), and phenol derivatives (4.34-45%), acetic acid (0.86%), propanoic acid (0.22%), 2-Methoxy-phenol (46.92%), 4-Methyl-phenol (1.44%), 4-Methyl-2-methoxy-phenol (4.60%), 1,2-Benzenediol (15.81%), 3-Methyl-1,2-benzenediol (3.91%) 4-Methyl-1,2-benzenediol (8.74%), 4,5-Dimethyl-1,3-benzenediol (1.23%), Butylated hydroxytoluene (5.05%), benzofurans, dibenzofurans, anisole and,

cyclohexanone have been reported in various proportions (Karagöz et al., 2005, Saidi et al., 2014, Telysheva et al., 2007).

2.5 Properties of lignin derived oil

Due to higher oxygen contents in lignin derived oil (35-40%) with the presence of various functional groups, which resulted to poor properties and limitation at long-run in this oil (Zakzeski et al., 2010, Saidi et al., 2014). These poor properties includes: low thermal and chemical stability, low calorific value, high viscosities, some level of acidity and water contents, which limit suitability of lignin derived oil towards direct fuel applications (Saidi et al., 2014). Also high oxygen content resulted to high polarity, hence denied its miscibility with petroleum oil and therefore, preventing the advantage of blending (Liguori and Barth, 2011). The high thermal and chemical instability are due to high reactivity of oxygen bearing functional groups, of the respective lignin derived oil which undergo different types of reactions such as polymerization reactions during storage and heating processes and hence making it difficult to handle. On the other hand, the low calorific value of this oil come from two major sources; low energy density of the oxygen linkage of these functional group, which automatically release small amount of energy upon combustions by exothermic reactions. Secondly, the water contents of the oil which comes from moisture content and product dehydration during pyrolysis and storage, lower calorific value (heating value) or flame temperatures by absorption of heat energy during combustions of this oil (Gutierrez et al., 2009b, González-Borja and Resasco, 2011). Additionally, water and acids contents caused corrosions of pipes and vessels as well as bio-refinery fractionation equipment's. On the other hand, the carbon content (54 -58%) and hydrogen (5.5 – 7.0%) of lignin derived oil are comparatively lower to corresponding value of 85 % (carbon content) and 11% (hydrogen content) for conventional petroleum, respectively (González-Borja and Resasco, 2011, Şenol et al., 2007b, Bykova et al., 2012c, Bridgwater, 2012). In order to overcome these challenges

and improve the quality of lignin derived oil to meet up fuels standards and comparable to conventional fuels, efficient upgrading process is necessary.

2.6 Upgrading of lignin derived oil.

Due to poor quality of lignin derived oil, suitable upgrading process is required before being transform and utilized as appropriate transportation fuel. Having known that, the nuisance in lignin-derived oil is attributed by the presence of oxygenated compounds with different functional groups such alcohols, ketones, aldehydes, ether, acids, e.t.c. The upgrading processes of lignin derived oil mainly focus in elimination of oxygenated compounds. In this context, various techniques have been considered in upgrading lignin derived oil. The considered methods included physical upgrading, catalytic upgrading and chemical upgrading process. Physical upgrading consists of emulsification, filtrations and solvents extractions pathways. On the other hand, chemical upgrading methods involves aqueous phase reforming, gasification, mild cracking and esterification pathways. While catalytic upgrading includes; steam reforming, zeolite-catalysed cracking and hydrodeoxygenation reactions (Saidi et al., 2014, Bridgwater, 2012). Generally, steam reforming lead to formation of hydrogen at the end of the process, Zeolite cracking is similar to fluid catalytic cracking of petroleum in which oxygen is removes without involvement of hydrogen. However, major challenged with zeolite cracking are elimination of oxygen in form of CO_2, which shorten the hydrocarbon chain, excessive coke formation resulted of catalyst deactivation, and CO_2 is detrimental to our environment (Bridgwater, 2012, Yang et al., 2009, Girgis and Gates, 1991, Yan et al., 2008). On the other hand, catalytic hydrodeoxygenation (HDO) has been considered more promising due to its extra advantages of **(i)** oxygen is remove in the form of water (which is environmental friendly unlike CO_2 in the case of zeolites), **(ii)** the process increased H to C ration and reduces O to C ration thereby enhancing bio oil containing compounds stability and more energy density hence, high heating value in the final upgraded fuels,

(iii) yield more saturated hydrocarbons compared to Zeolites cracking (more aromatic and unsaturated hydrocarbons) (Yan et al., 2008, Yan et al., 2010). In hydrodeoxygenation reaction, effective catalysts is very crucial for the success of upgrading process, and the lignin-based model compounds are usually selected for catalytic HDO performance test in order to understand its reactions pattern and mechanisms. The choice of model compounds is necessary due to structural complexity of multi components molecules in lignin derived bio oil (Ambursa et al., 2016b, Yan et al., 2010, Lee et al., 2015). (Ambursa et al., 2016b, Yan et al., 2010, Lee et al., 2015). During hydrodeoxygenations reactions, other reactions such as decarbonylations, hydrogenations, cracking and hydrocracking were also observed to occurred (Xiangling Lia et al., 2018) but, our attention will focuses on hydrodeoxygenation and hydrogenation reactions since they directly lead to realizations of transportation fuels.

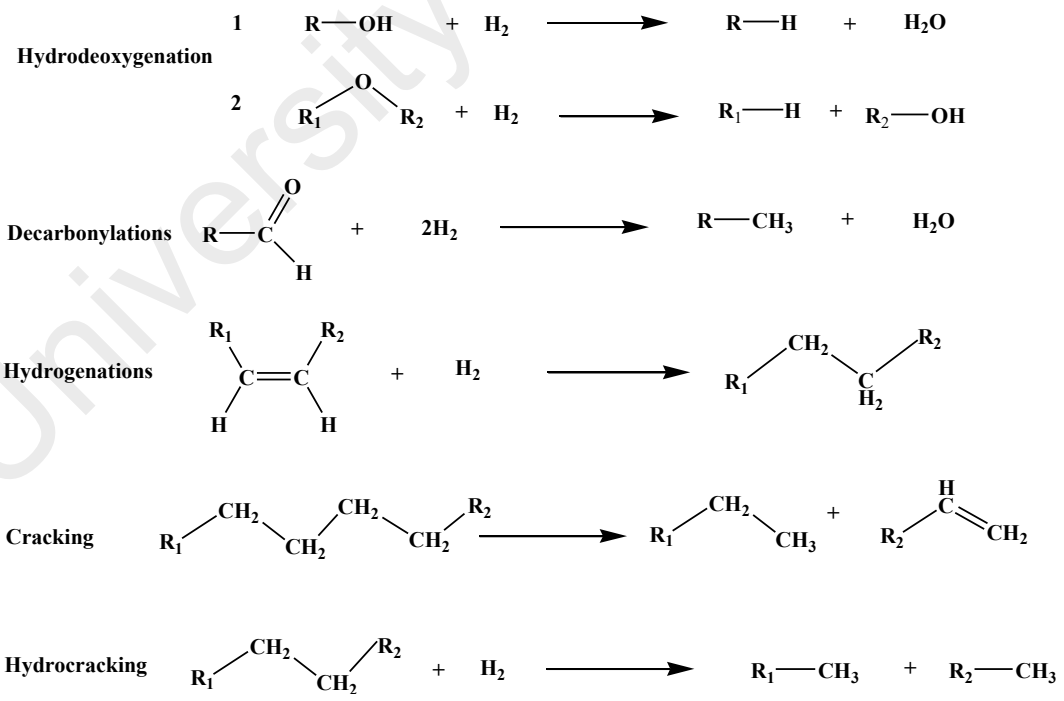

Figure 2.4: various reactions taking place during hydrodeoxygenation reactions

2.7 Lignin derived oil model compounds

Generally, initial step of design and develop HDO catalysts for lignin derived oil upgrading process was using lignin derived model compounds. Lignin model compounds are those collective compounds obtained from liquefaction or pyrolysis of lignin materials. These compounds include, benzofuran, dibenzofuran, guaiacol, phenol, anisole, cresol and their derivatives as indicated in Figure 2.4 (Saidi et al., 2014). Besides phenolic and furanic species, other compounds in the form of aldehyde, ketone, acids and ester were observed in lignin derived oil. Most of the later compounds could be produced from either decomposition of oxygenated products coupling of small intermediates during pyrolysis or liquefaction processes. The chemical or structures for some of these model compounds are presented in the Figure 2.4 below: -

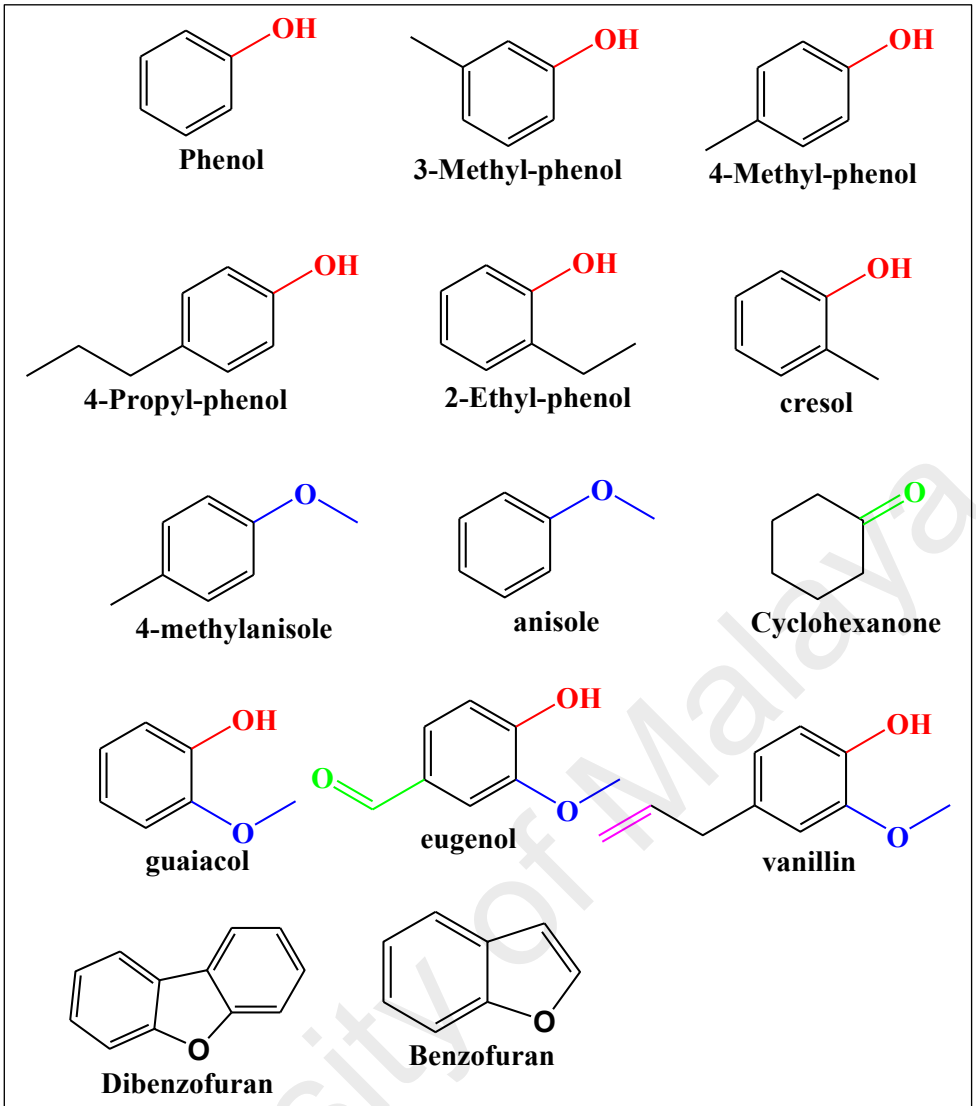

Figure 2.5 : Lignin derived Bio oil model compounds as adopted from (Saidi et al., 2014)

The proportion of these occurring compounds varied in lignin derived oil. However, guaiacol with the IUPAC name as 2-methoxyphenol having both –OH and –OCH_3 groups as well as aromatic ring has been reported to occur with highest amount. According to (Roberts et al., 2011), guaiacol is the most occurring phenolic form of bio-oil model compounds. It possessed three types of C-O linkages: C_{sp}^2-OCH_3, C_{sp}^2-OH and Csp^3- OAr (figure 2.5) with the corresponding bond dissociation energy of 409 – 421, 466, and 262 – 276 $kJmol^{-1}$ respectively. The value of bond dissociation energy indicates that, cleavage of Csp^2–OMe and Csp^2–OH require more potential than Csp^3–OAr as represented in the structures below (Song et al., 2015).

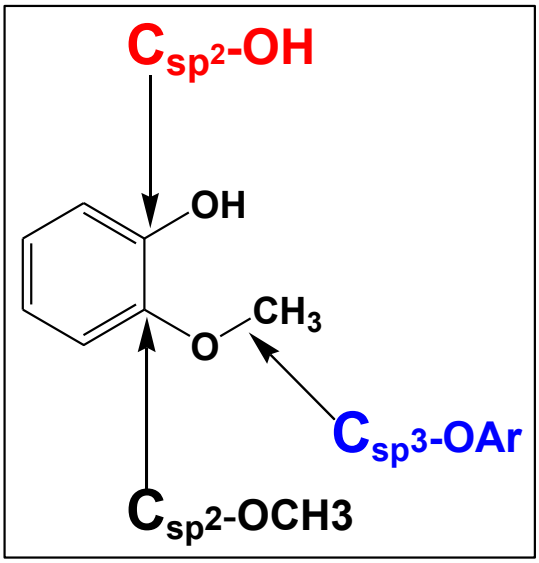

Figure 2.6: Representation of Guaiacol structures

The use of Guaiacol molecules as lignin derive oil model compound for catalytic hydrodeoxygenation performance test is geared toward better understanding of structure-activity relationship, hence taking developed catalysts activity close to reality for hydrodeoxygenation of Lignin derived bio oil (Lee et al., 2015, Ambursa et al., 2016b). Another advantage of using Guaiacol molecule as lignin derived oil model compounds is that, it possesses peculiar similarities to other occurring model compounds (such as catechol, anisole, methyl anisole, phenol, etc.) due to presence of three available functional group such as hydroxyl group, methoxy group and aryl group, which are commonly found in lignin derived oil (Ambursa et al., 2016b, Ambursa et al., 2017). Table 2.2 below summarized the comparison properties of crude bio oil and guaiacol model compound. It was evidence that, many similarities exist between crude bio oil and guaiacol model compound, which confirming suitability of guaiacol molecules to be used as model compounds to test effectiveness of developed catalysts for hydrodeoxygenation of lignin derived oil to hydrocarbon-grade fuels molecules.

Table 2.2: compared products compositions between real bio oil and its model compounds

S/No	Properties	Real bio oil	Model compd.
		Fast pyrolysis	Guaiacol
1	Carbon (wt. %)	32-49	68
2	Hydrogen (wt. %)	6.9-8.6	6
3	Nitrogen (wt. %)	0-0.4	0
4	Oxygen (wt. %)	44-60	36
5	Sulphur (wt. %)	0.01-0.05	0
6	Chlorine (ppm)	3-75	0
7	Ash (ppm)	100-200	0
8	pH	2.0-3.7	0
9	Density (kg/L)	1.11-1.30	1.11
10	Water (wt. %)	15-30	0

The Dibenzofuran is a bicyclic hydrocarbon compound with two aromatic benzene rings connected by furan. The used of dibenzofuran molecule as lignin derived oil model compound is based on the consideration that: (i) it's being observed to occur in the lignin derive oil, (ii) it served as representative to other occurring furan and furanic derivatives such as benzofuran Figure 2.6. The utilization of dibenzofuran to investigate catalytic activity of developed catalysts for hydrodeoxygenation of lignin derived oil will surely revealed its performance and selectivity towards hydrogenation and deoxygenation behaviour during HDO processes. This will give a clear picture and understanding about the dominant functional catalytic sites. In general, the role of HDO support and supported catalysts could be visibly observed. The structures of dibenzofuran have been display according (Wang et al., 2015b) below.

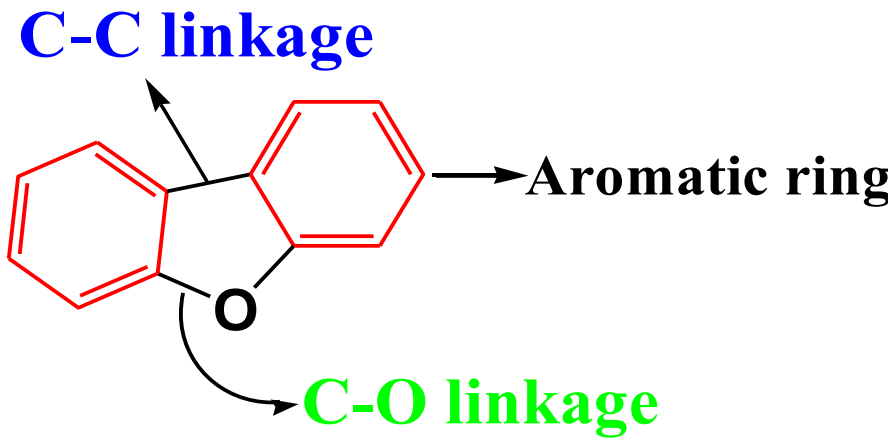

Figure 2.7 : Representation of Structures of dibenzofuran

2.8 Hydrodeoxygenation (HDO) Catalysts Literature (requirements and applied catalysts)

The role of catalysts in hydrodeoxygenation reactions is highly tremendous. It's even viewed that, the future and prospect of hydrodeoxygenations processes relied heavily on the efficiency and effectiveness of the applied catalysts (Saidi et al., 2014, Li et al., 2016). Based on structure-activity relations from previously reported works on hydrodeoxygenation lignin derived bio oil particularly with prototypes compounds that, Bi-functional catalysts system has been more recognised as required catalysts system for hydrodeoxygenation of lignin derived bio oil. Since it was observed experimentally to influence high performance in hydrodeoxygenation of lignin derived bio oil (Ambursa et al., 2017, Lup et al., 2017). This bi-functional catalysts system consist of active metal (such as Pt, Ru, Ni, Fe, Co, Ir, Re, Pd), catalysts support (Such as transition metal oxides, silica materials e.t.c.) and in most cases with promoter to active metals (Such as Mo, Cu, etc.) or catalysts support (such as metal oxides or silica materials as well) are employed (Lup et al., 2017, Saidi et al., 2014). The required bi-functional catalysts system should as well allow synergistic role between the active metal and supports during hydrodeoxygenation reactions. The role of metal is primarily to promote hydrogenation

of aromatic ring or unsaturated compounds during hydrodeoxygenations reactions (Ambursa et al., 2017, Lup et al., 2017). Besides that, the active metallic material could influence deoxygenation process by direct hydrogenolysis (Li et al., 2016) as given in the next paragraph. The duty of catalysts supports in hydrodeoxygenation reactions is very crucial. Beside dispersing and stabilizing the active metal species, catalysts supports is highly expected to provides functional sites for activation of C-O bonds during hydrodeoxygenations reactions (Ambursa et al., 2017, Ambursa et al., 2016b). Therefore, acidic supports with Lewis acidity or Bronsted acidity or the presence of both Lewis and Bronsted acidity are prefer for hydrodeoxygenation reactions (Selvaraj et al., 2014, Tran et al., 2016a). Acidic supports have also been notice to influence the state and stability of the active phase through metal-supports interactions during activation process (Zanuttini et al., 2015, He and Wang, 2012) the more detail literature survey for hydrodeoxygenation supports have given in the later paragraph. In hydrodeoxygenation reactions the catalysts promoter is usually employed to enhance activity, selectivity or stability of the active metals. It has observed experimentally that, the synergy between promoters and active metals displayed great influence on the catalytic activity, selectivity or stability and hence bimetallic catalysts is more active than mono metallic catalysts for hydrodeoxygenation of lignin derived bio oil (Gutierrez et al., 2017, Selvaraj et al., 2014, Mortensen et al., 2016).

The efficiency and effectiveness of hydrodeoxygenation depends on the performance of the applied catalysts. In this regard, various catalysts such as CoMoS, NiMoS, phosphides, nitrides and carbides, noble metal and non-noble metals catalysts have been explored for HDO of bio oil and its model compounds. On the other hand, various acidic and non-acidic supports such as zeolites, Al_2O_3, SiO_2, SBA-15, ZrO_2, TiO_2, CeO_2, C, and carbon nanotubes (CNTS) have been explores for HDO of bio oil and its model compounds.

2.8.1 Metal sulphides (TMS)

Metal sulphides are the initial applied catalysts for HDO of bio-oil and its model compounds. These catalysts were conventionally apply for hydrodesulphurization and hydrodenitrogenation process in petroleum refinery (Honkela et al., 2010, Ruddy et al., 2014). $CoMoS/Al_2O_3$ and $NiMoS/Al_2O_3$ catalysts are actively studied by researcher for HDO reactions. The composition of these catalysts consists of Co and Ni as catalysts promoter, Mo as the active catalysts while Al_2O_3 as acidic support (Romero et al., 2010, Krár et al., 2011, Toba et al., 2011). Previous studies have shown that, the catalytic activity of these catalysts mainly depend on the sulphides region of the catalysts since the loss of sulphur generate vacancies serving as the active site during HDO reactions (Tropsoe et al., 1996). According to them, generated vacancies located at the edges of WS_2 and MoS_2 exhibit Lewis acid properties with ability to absorb heteroatoms and resulted to C-O cleavage in hydrodeoxygenation reactions (Badawi et al., 2013). Beside the Lewis acids properties, the catalysts possess Bronsted Acids properties, which come from molecular hydrogen (H_2), alcohols, thiols, or water activation into SH^- and H^+ over the catalysts surface. The SH^- promote deoxygenation while H^+ per take multiple bond saturations to saturated C-C bonds (Badawi et al., 2013, Ruddy et al., 2014, Romero et al., 2010, Popov et al., 2010). The promoters (e.g. Ni and Co) enhance the catalytic activity of the process by controlling the bond strength between molybdenum and sulphur during hydrogenation and deoxygenation processes (Popov et al., 2010, Romero et al., 2010, He and Wang, 2012). For example, hydrodeoxygenation of 2-ethylphenol over $CoMoS/Al_2O_3$ and $CoMoS/Al_2O_3$ have been investigated by (Romero et al., 2010). They proposed mechanisms according to Figure 2.7, in which the sulphur component loss in the form of H_2S during the presence of H_2, which emanate vacancies to serve as the main active sites of the catalysts. The produced H_2S undergo heterolytic bond breaking, which lead to the formation of S–H and Mo–H. The adsorption of 2-

ethylphenol on the created active sites influence hydrogenation of its benzene ring to form 2-ethylcyclohexanol. Then, 2-ethylcyclohexanol undergo dehydration on the acidic sites of support followed by subsequent hydrogenation pathway to yield ethyl cyclohexane figure 2.7.

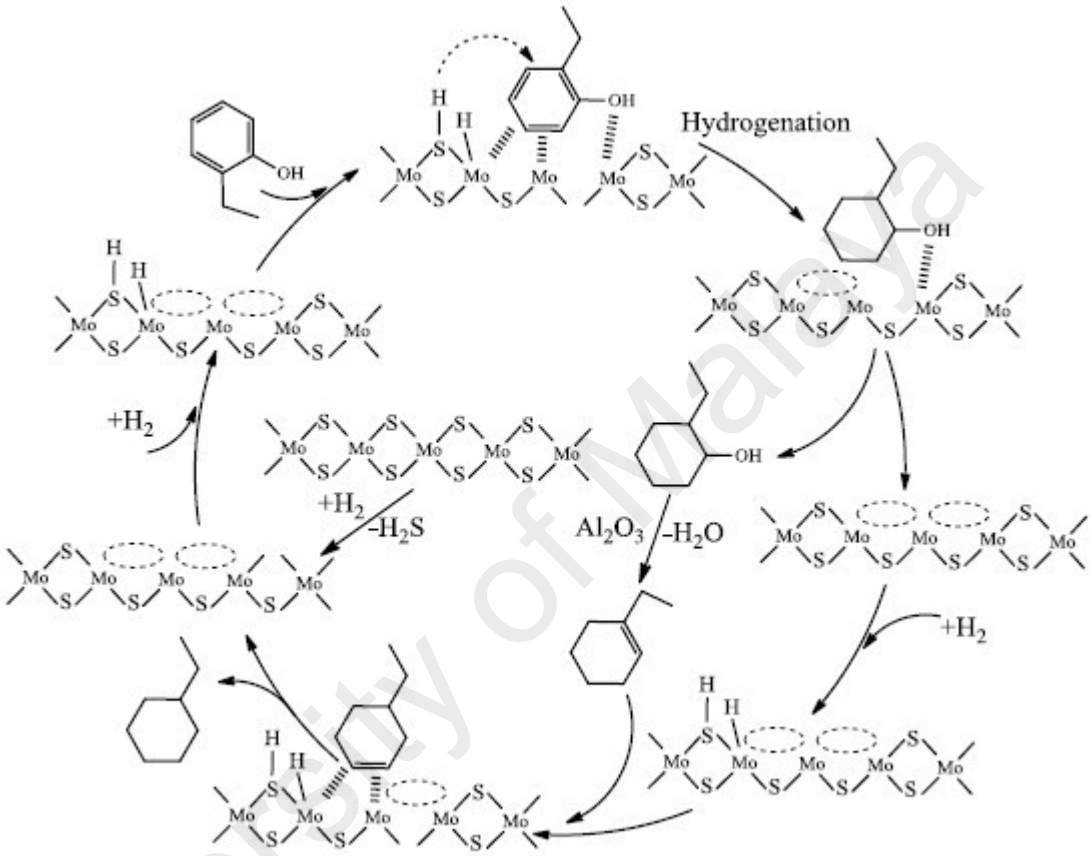

Figure 2.8: Mechanism of 2-ethylphenol HDO over MoS_2-based catalyst

2.8.2 Affiliated challenges of supported sulfided catalysts

Although sulphides catalysts exhibited high catalytic activity in HDO reactions, however, there are many challenges associated with these catalysts: (i), the active sites require sulfiding agent to keep it catalytically active in HDO process, (ii) the loss of sulphur during this processes and addition of sulfiding agent (H_2S) contaminates the products, (iii) unconverted sulphur in the products get oxidised to sulphur oxides (SO_2) and pollutes the environments (Furimsky, 2000, Viljava et al., 2000). Other researchers

also reported the formation of sulphur containing intermediates as unwanted by-products during the reactions (Gutierrez et al., 2009a, Şenol et al., 2007a). The earlier chosen supports for CoMoS and NiMoS was Al_2O_3, which was also associated with deactivation challenges in HDO reactions and it will be discussed later in this review.

The affiliated challenges with the supported catalysts have resulted to serious search for the next generation of HDO catalysts. In order to obtained the effective catalyst, two approaches have been adopted: (i) focus on the modification or replacement of the active phases (CoMoS and NiMoS) with other non-active metals, (ii) modification or substitution of Al_2O_3 support by maintaining the same active phase. On the firsts approach, literature survey has shown that, many catalysts of mono and bi functional types have been explored through the model compounds applications. The type of catalysts explored in this process includes Noble metals, Metals phosphides, metal sulphides, metals nitrides, metals carbides and non-noble transition metals.

2.8.3 Noble metals

Generally, fast catalyst deactivation is due to instability of supported sulphided catalysts in HDO reaction, hence, it is necessitated to search for non-sulphided-based catalysts to enhance the HDO process. Supported noble metal based-catalysts have been gain interest as potential catalyst for HDO process (Gutierrez et al., 2009a, Lin et al., 2011). The supported noble metal catalysts appeared to be more advantageous than sulphided catalyst since they do not require sulphuding agent for it activity to be maintained, and hence no products contamination is expected (Ruddy *et al.*, 2014; Honkela *et al.*, 2010). Additionally, they become more attractive as consequence of their high ability to activate H_2 under mild conditions (Ruddy et al., 2014, Honkela et al., 2010). The problem associated with the support (stability of Al_2O_3) is to overcome by substituting Al_2O_3 with other acidic and non-acidic supports for noble metals catalysts (Honkela et al., 2010, He and Wang, 2012). Many studies have reported HDO

of bio oil and its model compounds using noble metal catalysts, which includes Pt (Gutierrez et al., 2009a, Wang et al., 2014a, Wang et al., 2015b); Ru (Lee et al., 2012, Wang et al., 2014a, Zhang et al., 2014, Zhou, 2014); Pd (Hong et al., 2014a, Wang et al., 2014a, Zhao et al., 2011, Gutierrez et al., 2009a); and Rh (Gutierrez et al., 2009a, Zhao et al., 2011, Lee et al., 2012) as active component of the catalysts. The outcome of their finding revealed that, they are more catalytically active than previously applied sulphides catalysts. For instance, (Wildschut et al., 2009) compared Ru/C and $CoMo/Al_2O_3$ and also $NiMo/Al_2O_3$ catalysts for hydrodeoxygenation of bio oil in a batch reactor at mild (250^oC and 100 bar) and high (350^oC and 200 bar) reaction conditions. They reported that the Ru/C catalyst gave high performance in terms of both yield and degree of deoxygenations. Other recent studies of HDO of bio oil model compounds over noble metals supported catalysts have been given in table 2.3 below.

The observed reaction mechanisms over noble metal catalysed HDO reactions is that, the adsorption and dissociation of H_2 into corresponding radicals (H* species) by homolytics bond cleavage which takes place on metal sites. Through the influence of support and metal support interaction enable transfer and hydrogenation of reactants during HDO reactions. In the case of C-O bond cleavage, the support and metal-supports interface cooperatively adsorb the reactants via oxygen functionality and provide platform in which dissociated H* species spill over from the metal surface to the C-O activating sides which would lead to C-O cleavage and deoxygenation on the support surface through dehydrations. Most of the recent studies have shown that, both hydrogenation sites from metal and acidic sites from supports play corporative role in HDO reactions. In additions, they showed energetically favoured pathway toward obtaining saturated hydrocarbons in which reactions proceed with partial or complete hydrogenations of aryl ring, followed by dehydration and subsequent hydrogenations (Lee et al., 2012, Lin et al., 2011, Mendes et al., 2001).

Table 2.3: Display obtained results for hydrodeoxygenation of bio oil model compounds over noble metal supported catalysts

Catalyst	Support	Reactor	T(°C)	P(bar)	T(h)	Model compounds	Conversion	Major Products	References
ReS2	γ- Al_2O_3	Batch		50	4.4	Guaiacol	82	Cyclohexene, Cyclohexane	(Sepúlveda et al., 2012)
Pd	C	Batch	300	138	4.0	Guaiacol	99.0	Cyclohexane	(Elliott et al., 2009)
Ru	C	Batch	250	138	4.0	Guaiacol	100.0	Cyclohexane	(Elliott et al., 2009)
Pt–Rh	ZrO2	Batch	300	80	3	Guaiacol	79	Phenol, Benzene,	(Telysheva et al., 2007)
Rh	ZrO2	Batch	300	80	3	Guaiacol	68	Benzene,	(Telysheva et al., 2007)
Pd	C, HZSM-5	Batch	200	50	2	Guaiacol	80	Cycloalkanes	(Zhao and Lercher, 2012)
Pd/WOx	Al_2O_3	Batch	300	70	2.5	Guaiacol	100.0	Cyclohexane	(Hong et al., 2014c)
Rh	C	Batch	250	40	1.0	Guaiacol	95.0	2–methoxy-cyclohexanol	(Lee et al., 2012)
Pt	MFI	Batch	250	40	3.0	Dibenzofuran	100.0	1,1–bicyclohexyl, (cyclopentylmethyl)-Cyclohexane	(Lee et al., 2015)
Pt	Al_2O_3/SiO_2	Continuous	280	30	3.0	Dibenzofuran	95.0	1,1–bicyclohexyl	(Wang et al., 2015b)
Pd	SBA–15	Continuous	280	30	3.0	Dibenzofuran	70.0	1,1–bicyclohexyl, Hexahydro dibenzofuran	(Wang et al., 2014a)

2.8.4 Associated challenges with noble metals supported catalysts

The catalytic performance of noble metal supported catalysts for hydrodeoxygenation of bio oil and its model compounds have been shown to be higher than Sulphides catalysts. However, the challenges of expensiveness and less availability make it so difficult for commercial (large-scale) applications. Additionally, noble metals are less resistant to coking and sintering which resulted to their rapid deactivations during HDO reactions. (Ruddy et al., 2014, He and Wang, 2012, Honkela et al., 2010).

2.8.5 Non-noble transition metal catalysts

In continuation to search of new catalysts due to associated challenges with the use of supported noble metal catalysts, non-noble transition metals have been considered in the form of mono and bi-functional metals catalysts. Many of mono-metallic catalysts such as Ni (Bykova et al., 2014, Sankaranarayanan et al., 2015, Yang et al., 2014), Fe *(Olcese et al., 2012a),* Cu (Bykova et al., 2014), and Co (Olcese et al., 2012a, Sankaranarayanan et al., 2015). The cheap and availability of these non-noble metals give them superior advantage than noble metals. Like noble metals, these metals have the potential of dissociating hydrogen into two corresponding hydrogen radicals (H* + H*), the more detail of this activation can be observed in the reaction mechanisms proposed by (Olcese et al., 2012a, Popov et al., 2010). (Olcese et al., 2012a) studied work of Guaiacol HDO over Fe/SiO_2 catalyst at reaction condition of 350-450^oC and atmospheric pressure in a fixed-bed reactor and the proposed mechanisms shown in Figure 9, where the acidic site of support adsorbed the substrate via it oxygen atom. Then the available metal site activates the H_2 and the activated H_2 (H* + H*) are then spilled over onto the adsorbed oxygen atoms over the support surface. Then, finally result to C-O bond cleavage over the support surface through dehydrations. The orientation of molecules, and it stearic hindrance among other factors determined its adsorption sites. This type of mechanism (Figure 2.8) was in agreement with that proposed by (Popov et al., 2010).

Although the HDO performance of non-noble is obtained but still comparatively low as noble metal catalysed reaction. Also, the performance of metal phosphides such as Ni_2P, Co_2P, Fe_2P, WP Ni_2P, MoP and NiMoP were explored by (Zhao et al., 2011, Li et al., 2011, Yang et al., 2014, Whiffen and Smith, 2010), Mo_2C, W_2C and MoO_3, were investigated by (Santillan-Jimenez et al., 2015, Whiffen and Smith, 2010), metal nitrides (MoN, Mo_2N), were also explored by (Santillan-Jimenez et al., 2015, Ghampson et al., 2012a) for hydrodeoxygenation reactions. However, the major drawback observed with phosphides catalysts was high amount of carbonaceous deposits on the catalysts surface and hence, relative rapid deactivation of these catalysts. The major motivating factor for the use of nitrides in HDO reactions is the high electronegativity of nitrogen atom (resulted to electronegativity differences between metal and nitrogen) which provide many advantages such as possession of both acidic and basic sites, resistance to oxidation, simplicity of preparation and less cost. Its activity as well is related to vacancies created due to lost of nitrogen from the lattice (Ghampson et al., 2012a). It should be mention that, in HDO catalysts, design for these active metals with suitable choice of support is necessary since HDO performance is dependent on bi-functional role from catalysts(Olcese et al., 2012a, Song et al., 2015, Yang et al., 2014).

The study for non-noble metals-based catalysts in HDO reactions were still associated with other challenges. Further improvement on stability and performance of mono-metallic catalysts such as Ni, Co, Fe, and Cu, and bimetallic catalysts such as Ni-Cu, Ni-Fe, Ni-La, Ni-Co, and Ni-W (Yang et al., 2011, Bykova et al., 2012a, Wang, 2005, Echeandia et al., 2010) are continuously investigated.

The Guaiacol reaction mechanism as proposed by Olcese et al., 2012a, Popov et al., 2010

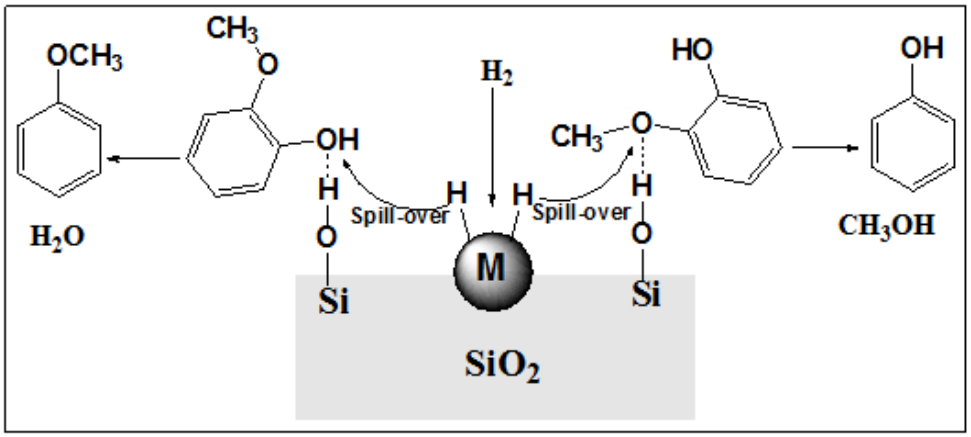

Figure 2.9: Mechanism of guaiacol HDO over non-noble metal catalysts

(Sankaranarayanan et al., 2015) investigated the effect of metal support interaction for anisole HDO over Ni and Co supported on Al-SBA15. (Song et al., 2015) also investigate the synergetic effects of Ni with Zeolites for HDO of phenolic compounds. Both studies reported that, synergic effect of metal hydrogenation capability and support acidity enhances the catalytic activity of bio oil and its model compounds. However, for these mono metallic catalysts, strong metal support interaction was found to negatively affect their performance in HDO reactions due to less ability of reduction from high oxidation state to zero oxidation state as required in HDO reactions. Example, Like Co^{2+} to Co^{0} in the case of Co/Al-SBA (Sankaranarayanan et al., 2015).

The comparative studies of catalytic activity between mono-metallic Ni based and bimetallic Cu-Ni based catalysts for hydrodeoxygenation of lignin derived bio oil model compounds revealed that, the synergy between Cu and Ni in Cu-Ni bimetallic catalysts greatly enhance its selectivity to saturated hydrocarbons over mono-metallic Ni based catalysts (Bykova et al., 2014). For example, Ni/SiO_2 and $Cu\text{-}Ni/SiO_2$ were compared for hydrodeoxygenation of Guaiacol at 320°C, 17MPa and 1h reactions time and they reported that, bimetallic $Cu\text{-}Ni/SiO_2$ displayed high cyclohexane selectivity of ~64% than Ni/SiO_2 with lower cyclohexane selectivity of ~3% (Bykova et al., 2012a). Yakove et al., (2009) investigated anisole HDO over Ni-Cu and Ni supported on Al_3O_2 at 300°C and 10

bars. He reported that both catalysts are active for HDO but bimetallic Ni-Cu catalysts are even more active than Ni catalysts. Due to Cu-Ni synergy between the two (Cu and Ni metals), more favourable catalytic attributes were achieved which influence hydrogen adsorption with moderate strength and making it easier to activate and desorb highly active hydrogen species from Cu-Ni bimetallic surface. Therefore, more number of activated hydrogen could promote reduction of aromatic ring and hydrodeoxygenation of methoxy or hydroxyl groups from guaiacol molecules either through direct hydrogenolysis or dehydrations leading to formations of more saturated hydrocarbons over Cu-Ni bimetallic surface than mono metallic nickel-based catalysts. Additionally, synergetic effect of Cu on Ni on Cu-Ni bimetallic catalysts facilitates reduction of Ni-O to Ni metal and the presence of Cu metal have been reported to prevents formation of nickel spinel than was observed in the mono metallic catalysts of nickel species.

From the fundamental point of view, the choice of Cu species as promoter to Ni metal for hydrodeoxygenation of lignin derived bio oil is due to its potential to electronically interact with d-orbital of Ni metal and result to its partial filling, hence change in catalytic activity and stability of nickel based catalysts in hydrodeoxygenation of lignin derived bio oil (Guo et al., 2015a, Izadi et al., 2014) According to electron band theory, the group 1B metal such as Cu has free d-electron and that of group VIII such as Ni has free d-orbital delocalised in the conduction band. Therefore, the interaction between the two might result to filling of the d-zone of nickel species leading to relatively low adsorption strength compared to mono-metallic Ni species (Guo et al., 2015a, Khromova et al., 2014). In line with modern catalytic theory that, catalysts species with moderate adsorption strength possess higher catalytic activity and possess more prefer attributes for catalysis hence wide consideration for Cu-Ni bimetallic catalysts for hydrodeoxygenation of lignin derived bio oil (Ambursa et al., 2016b, Ambursa et al., 2017, Hamid et al., 2017, Bykova et al., 2013).

Table 2.4 : Overview of results obtained for HDO of bio-oil model compounds over supported non-noble metal catalysts

S/No	Catalyst	Support	Reactor	T(°C)	P(bar)	T(h)	Lignin model compounds	Major Products	Reference
1	Co & Ni	Al-MCM-41	Continuous	400	10		Guaiacol	Benzene, Phenol	(Tran, 2016)
2	Fe	SiO_2	Continuous	400	10	2.5	Guaiacol	Benzene, Toluene	(Olcese et al., 2012a)
3	Ni	SiO_2	Batch	320	170	1.0	Guaiacol	Cyclohexane	(Bykova et al., 2012a)
4	Ni	SiO_2-ZrO_2	Batch	300	50	8.0	Guaiacol	Cyclohexane	(Zhang et al., 2013d)
5	Ni	HZSM-5	Batch	200	30	2.0	Guaiacol	Phenol	(Song et al., 2015)
6	Ni_2P	SiO_2	Packed bed	300	1	0.33	Guaiacol	Benzene	(Nimmanwudipong et al., 2011b)
7	MoP	SiO_2	Packed bed	300	1	0.33	Guaiacol	Benzene	(Nimmanwudipong et al., 2011b)
8	Co_2P	SiO_2	Packed bed	300	1	0.33	Guaiacol	Benzene	(Nimmanwudipong et al., 2011b)
9	Fe_2P	SiO_2	Packed bed	300	1	0.33	Guaiacol	Benzene	(Nimmanwudipong et al., 2011b)
10	WP	SiO_2	Packed bed	300	1	0.33	Guaiacol	Benzene	(Nimmanwudipong et al., 2011b)
11	Mo_2N	γ-Al_2O_3	Batch	300	50	6	Guaiacol	Phenol	(Furimsky et al., 1986)
12	Mo_2N	C	Batch	300	50	6	Guaiacol	Phenol	(Ghampson et al., 2012b)
13	W_2C	CNF	Batch	300–375	55	4	Guaiacol	Phenol	(Jongerius et al., 2013b)
14	Mo_2C	CNF	Batch	300–375	55	4	Guaiacol	Phenol	(Jongerius et al., 2013b)
15	CoMo	C	Batch	280	70	4	Guaiacol	Benzene, Cyclohexane	(Ferrari et al., 2002)
16	Ni	SiO_2	Batch	320	170	1	Guaiacol	Cyclohexane, Cyclohexanone	(Bykova et al., 2011)

17	Ni	SiO_2–ZrO_2	Batch	300–340	50	5	Guaiacol	Cyclohexane, Methyl-cyclohexane	(Zhang et al., 2013a)
18	Ni–Cu	SiO_2	Batch	320	170	1	Guaiacol	Cyclohexane, Cyclohexanone	(Bykova et al., 2011)
19	Ni–Cu	ZrO_2–SiO_2	Batch	320	170	1	Guaiacol	Cyclohexane, Cyclohexanone	(Bykova et al., 2011)
20	Ni–Cu	CeO_2–ZrO_2	Batch	320	170	1	Guaiacol	Cyclohexane, Cyclohexanone	(Bykova et al., 2011)
21	Ni–Cu	ZrO_2–SiO_2–La_2O_3	Batch	320	170	1	Guaiacol	Cyclohexane, Cyclohexanone	(Bykova et al., 2011)
22	Ni-Cu	SiO_2-ZrO_2-La_2O_3	Batch	320	170	1.0	Guaiacol	Cyclohexane	(Bykova et al., 2012a)
23	Ni-Cu	CNT	Batch	573	5MPa	4h	Guaiacol	cyclohexanol	(Dongil et al., 2016a)
24	Ni-Cu	Al_2O_3	Fixed-Bed	380	30.05MPa	24h	O-Cresol	saturated hydrocarbon	(Dickinson and Savage, 2014)
25	Reney NiCu	Al_2O_3	Fixed-Bed	380	30.05MPa	24h	O-Cresol	saturated hydrocarbon	(Dickinson and Savage, 2014)
26	CuNi-Mo	SiO_2-ZrO_2	Batch	320	17MPa	1h	Guaiacol	Cyclohexane	(Bykova et al., 2014)
27	Cu-Ni-	SiO_2-ZrO_2	Batch	320	17MPa	1h	Guaiacol	Cyclohexane	(Bykova et al., 2014)
28	Cu-Ni	SiO_2-ZrO_2	Batch	320	17MPa	1h	Guaiacol	Cyclohexane	(Bykova et al., 2014)
29	Cu-Ni-	Ti-MCM-41	Batch	260	10 MPa	6h	Guaiacol	Batch	(Ambursa et al., 2017)
30	Cu-Ni	Ti-MCM-41	Batch	260	10 MPa	6h	Guaiacol	Batch	(Hamid et al., 2017)

2.9 Review of HDO Supports

Supports (carrier) is another main key player in HDO reactions, besides dispersing and stabilizing the promoter and active phase, it also provides active site (Bronsted and Lewis acids) for HDO reactions. For HDO reaction as well, some supports interact with active phase thereby forming new active phase on the surface or at the active-support interface (Stakheev and Kustov, 1999).

2.9.1 Alumina (Al_2O_3)

Initially, Al_2O_3 is considered as a better choice catalysts support for HDO reactions due to its high concentration of Lewis acids sites, strength and high surface area which give excellent performance in hydrodesulphurization (HDS) and hydrodenitrogenation (HDN) reactions (Li et al., 2011). However, the performance of alumina in HDO reactions has been hindered by many factors. As mentions earlier, Al_2O_3 is much more prompt to deactivation in HDO reaction due to presence of water and coking resulting from its interactions with oxygen containing compounds (reactants and intermediate species), particularly with aromatics and di- or more oxygen containing molecules (Popov et al., 2010). In the case of water, Al_2O_3 support deactivates quickly due to its presence in bio-oil. Since H_2O are produce as by-products in HDO process and these undergo competitive adsorption, which resulted in strong adsorption on the Al_2O_3 active sites; preventing reaction taking place and hence become deactivated (Laurent and Delmon, 1994). Also, the water vapour produces during hydrodeoxygenation reactions cause recrystallization of Al_2O_3 to boehmites and partial oxidation of nickel sulphides to nickel oxides which in the former case cause deactivation of support and in the later case decrease catalytic activity of the catalysts (Honkela et al., 2010, Bu et al., 2012)

The mentioned affiliated challenges with the Al_2O_3 support in hydrodeoxygenation reactions necessitated the search for alternative catalysts supports as a second approach

toward realizations of robust HDO catalysts. In this direction, various supports such as metal oxides: CeO_2,(Bykova et al., 2012a) TiO_2, (Bui et al., 2011a), SiO_2 (Centeno et al., 1995), ZrO2 (Bui et al., 2011a, Ardiyanti et al., 2011, Yakovlev et al., 2009), carbons (Centeno et al., 1995), SBA-15, Ti-SBA-15 SBA-15, Al-SBA-15 (Gbadamasi et al., 2016, Duan et al., 2012), MgO (Yang et al., 2009) and MCM-41 (Chiranjeevi et al., 2008) etc. are being explored as an alternative to the Al_2O_3.

2.9.2 Silica supports

SiO_2 have been investigated as catalysts supports for HDO reactions. The inner characteristics and smaller interactions of silica with supported active phase have been the main earlier attracting features affiliated with silica support (Olcese et al., 2012a, Jasik et al., 2005). Additionally, compared to Al_2O_3-based catalysts, SiO_2-based catalysts show superior advantages of high selectivity, weak interactions with oxy-compounds. During HDO reactions, the SiO_2 selectively interacts with oxy-compounds via H-bonding and less affinity for aromatics compounds, thus making carbon stable for HDO reactions (Popov et al., 2010, Zhao et al., 2011) . But in the case of Al_2O_3, strong adsorbed species were observed which resulted to carbon formations and hence deactivations occurred (Popov et al., 2010). However, SiO_2 is lack of acidity (inertness), which is necessary for stabilization of active metal and provisions of second active sites remained resulted of low activity of $CoMo/SiO_2$ compared to sulfided $CoMo/\gamma\text{-}Al_2O_3$ (Gajardo et al., 1982, Centeno et al., 1995).

2.9.3 Metal Oxides

Metal oxides such as ZrO_2 and TiO_2 with unique properties of amphoteric character remained attractable in HDO reactions. TiO_2 have also being explained to enable good dispersion MoS_2 due to small crystallites, high sulfidability, reducibility as well as favourable morphology and high activity in HDS reactions (Breysse et al., 1991, Bui et

al., 2011a). On the other hand, ZeO_2 has been reported to have resistivity to coking due to its acidic and basic characters. It also shows goods textural properties. Moreover, ZeO_2 strongly enhance adsorption and redux attributes of the catalysts. (Ardiyanti et al., 2011, Bui et al., 2011a, Zhang et al., 2013d). The HDO of guaiacol was investigated by (Yakovlev et al., 2009)and (Schimming et al., 2015) over CeO_2–ZrO_2 and CeO_2 as the only catalysts without supported metals. At the end of their studies they reported that, CeO_2–ZrO_2 and CeO_2 possess greater ability to activate H_2 as well as ability to generate oxygen vacancies similar to sulphide catalysts. The general explanation is that, metal oxides such as TiO_2, ZrO_2 and CeO_2 possess suitable acidity to activate C-O bond during Hydrodeoxygenation reactions and their reported acidity ordered as $TiO_2 > ZrO_2 > CeO_2$ (He and Wang, 2012). However, despite the numerous advantages of metal oxides in hydrodeoxygenation reactions, their catalytic performance has been crippled by smaller surface area and lack of porosity.

2.9.4 Mesoporous silica

The small surface area and lack of porosity of metal oxide have addressed through the application of mesoporous silica in HDO reactions (He & Wang, 2012). Mesoporous silica such as MCM-41, SBA-15 possess larger surface area and high hydrothermal stability (Corma, 1997), which give more accessible actives sites for HDO reaction. These active sites could be resulted from its acidity and dispersed of active metal over its surface. The possession of moderate pore sizes (mesopores) enhance the rate of molecular diffusion of the large molecules of reactant and products, particularly dibenzofuran (He and Wang, 2012) and benzaldehyde (Procházková et al., 2007) through the mesopores (Duan et al., 2012).

SBA-15, Ti-SBA-15 and Al-SBA-15 supports were explored by (Selvaraj et al., 2014, Gbadamasi et al., 2016, Duan et al., 2012) for HDO reactions. They reported a good

performance of these support for HDO reactions. However, the textural properties of MCM-41 are usually higher than SBA-15. The surface area of MCM-41 up to nearly 1,500m^2g^{-1} have been reported in open literatures while that of SBA-15 is usually less than 1000 m^2g^{-1} (Gbadamasi et al., 2016). Several literature studies indicated that MCM-41 showed good performance for HDO reactions. For Example, (Chiranjeevi et al., 2008)s investigated MCM-41 supported molybdenum catalysts with various catalyst loading from 2-14 wt% for HDO of furan in a fixed bed reactor at 400ºC, and atmospheric pressure. The activity of this catalyst was compared with amorphous SiO_2 and Al_2O_3 supported molybdenum catalysts under the same reaction conditions. The results shown that MCM-41 supported catalysts rendered higher performance than SiO_2 and -Al_2O_3 supported catalysts.

However, MCM-41 possess weak acidic properties which is detrimental to stabilization and good dispersion of the active metal species. In additions to that, affiliated weak acidity does not provide enough acidic strength and Lewis acid active sites for C-O bond cleavage and also Bronsted acids sites necessary for dehydration pathway during HDO reactions.

2.10 Guaiacol Hydrodeoxygenation and Reaction mechanisms

2.10.1 Guaiacol HDO over Sulphide Catalysts

The hydrodeoxygenation of guaiacol over sulphide $CoMo/Al_2O_3$ and $NiMo/Al_2O_3$ catalysts (i.e. conventional hydrodesulphurisation catalysts) proceeds through 1, 2 and 3 reactions pathways (Bui et al., 2009, Bui et al., 2011c, Bui et al., 2011a, Hong et al., 2014c, Lin et al., 2011, Romero et al., 2010). Beside discussion on the expected products and intermediates for HDO of guaiacol, sulphur containing intermediates also reported in Figure 6. Researcher had been studied the hydrodeoxygenation of guaiacol using batch reactor at 300ºC and 8MPa over sulfided $CoMo/Al_2O_3$ catalyst and according to their

report, extra sulphated compounds formed such as dimethyl sulphide, methanethiol, methylthiolcyclohexane and cyclohexanethiol and in the liquid and gaseous phases respectively. They were affiliated with the formations of these unwanted products intermediates. Products contamination were also additional challenges which is mainly caused by the sulphurding agent or leached sulphur from the catalysts (Gutierrez et al., 2009a).

2.10.2 Guaiacol HDO over noble metal Catalysts

In the case of noble metals (Pd, Pt, Ru and Rh) supported catalysts, guaiacol HDO proceeds via route 4 of Figure 6 ((Hong et al., 2014a, Lee et al., 2012, Lin et al., 2011, Zhang et al., 2014, Gutierrez et al., 2009a). The noble metals supported on acidic supports displayed higher catalytic performance than sulphide $CoMo/Al_2O_3$ and $NiMo/Al_2O_3$ catalysts in guaiacol HDO (Zhao et al., 2011). Besides, high hydrogenating ability of these catalysts lead to new reactions pathway; routes 4, which is different from those observed with sulfided catalysts (Massoth et al., 2006). They reported that, the observed pathway is less energy demanding than 1, 2, and 3 pathways since it starts with hydrogenating of benzene over metal sites followed by easy C-O bond activation on acidic support through demethylation, dihydroxylation, demethoxylation or dehydration to yield saturated compounds. Hence, adopting bifunctional catalysts system (such as Ru/ZSM-5, Pt/H-Beta, Pt/Al_2O_3 etc.) is highly important, because dehydration and hydrogenation occurred on metal and acids sites (Zhang et al., 2014, Zhao et al., 2011). In addition to the role of support and metal, the final products from guaiacol HDO over noble metals and acidic supports depends on the reaction pressure and temperature. If the reactions temperature is sufficient, the usual product are cyclohexane but coking on catalysts surface is usually high, which caused instant deactivations (Zhao et al., 2011).

2.10.3 Mechanisms of Guaiacol HDO over non-noble metal catalysts

With regards to hydrodeoxygenation of guaiacol over non-noble metals catalysts such as mono-metallic supported catalysts (Ni/SiO_2 or $SiO_2–ZrO_2$, $SiO_2–ZrO_2–La_2O_3$, etc). proceeds through either 1, 2, or 3 pathways (figure 6) (Zhang et al., 2013d, Bykova et al., 2012a, Bykova et al., 2014). For instance, (Bykova et al., 2012a) had reported hydrodeoxygenation of guaiacol over $CeO_2–ZrO_2$, $SiO_2–ZrO_2–La_2O_3$, SiO_2 and Al_2O_3 supported Ni and NiCu catalysts in batch reactor at 320ºC and hydrogen pressure of 17MPa. With the exception of NiCu/ $CeO_2–ZrO_2$ which followed route 4, all the prepared supported catalysts followed either the 1, 2, or 3 reactions pathway. It was observed that, there are large number of different products formed and the major products includes; benzene, cyclohexanol, cyclohexene, and cyclohexane and in addition, small number of bicyclic compounds likes cyclohexyl-cyclohexanol, cyclohexyl-benzene, cyclohexyl-phenol and bicyclohexyl were also produced.

It has been reported that, the pathways through which hydrodeoxygenation of guaiacol proceed are determine by the experimental conditions and nature of the applied catalysts (Zhao et al., 2011). The guaiacol HDO were shown to proceed through (6) possible pathways as indicated below (figure 2.9) as adopted from (He and Wang, 2012).

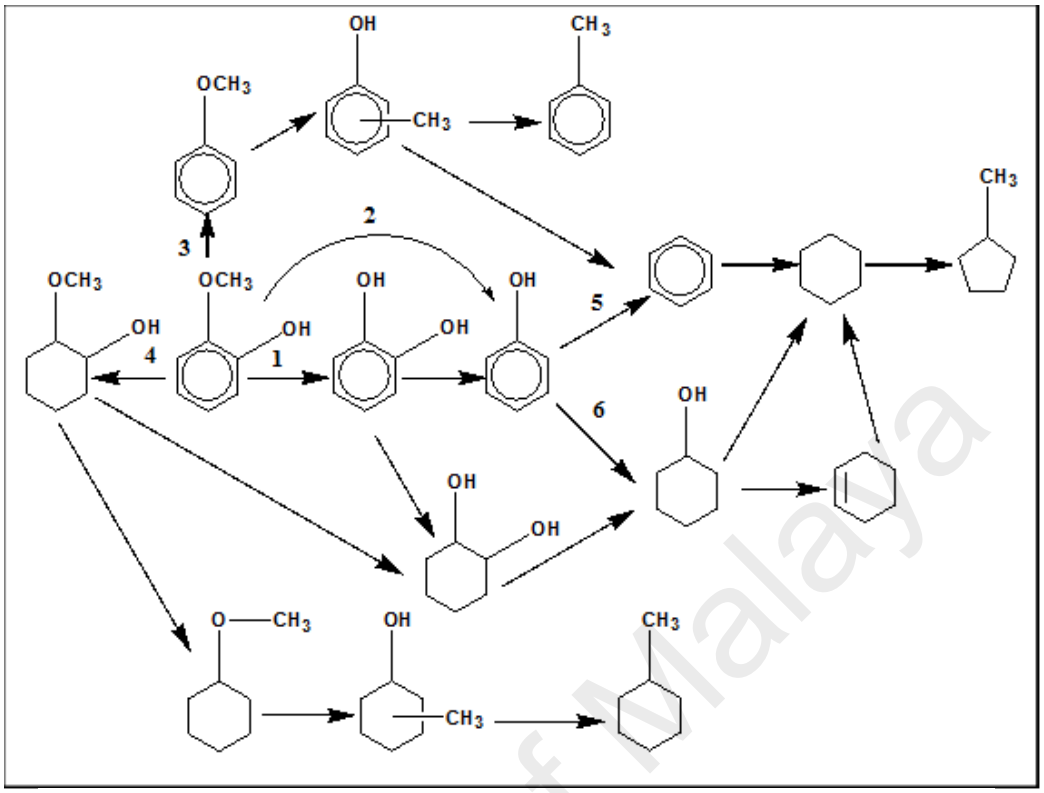

Figure 2.10 : reaction pathways for Guaiacol HDO

As refer to Figure 2.9, 1st (First) designated pathway involved formations of catechol (Benzene-1, 2-diol) via demethylation (DME) of Guaiacol (2-methoxyphenol), which subsequently undergo dihydroxylation (DH) and hydrogenation to form stable phenol (hydroxy-benzene) or undergo direct demethoxylation to produce phenol in the 2nd (second) reactions pathways. The 3rd (Third) pathway lead to production of anisole (methoxy-benzene), which subsequently undergo methyl transfer to produce cresol. In the 4th (Fourth) pathways, with hydrogenation (HYD) of benzene ring 2-methoxy-cyclohexanol is generated which undergo either DH or DME to produce methoxy-cyclohexane or cyclohexane-1, 2-diol. The 5th (fifth) pathway involved dihydroxylation DH of phenol to benzene followed by hydrogenation HYD to cyclohexane (He and Wang, 2012).

2.11 Hydrodeoxygenation of Dibenzofuran and Reaction mechanisms

Dibenzofuran (DBF) is a bicyclic compound with enclosed furans structure connecting 2 cyclic aromatic rings through C–O and C–C bonds linkage. It is regarded a bio-oil model compound having β–5 connection with 0.67 nm molecular size. (Huelsman and Savage, 2012, Xiang and Zhong, 2008, Wang et al., 2015b). In hydrodeoxygenation of dibenzofuran, the types of products obtained depends on the hydrogenating and deoxygenation sites of the catalysts as well as the reaction conditions (Temperature, Pressure and Time) (Wang et al., 2015b, Wang et al., 2013, Wang et al., 2014a, Lee et al., 2015). For instance, (Wang et al., 2015b) investigated the influence of supports on the hydrodeoxygenations of dibenzofuran over SiO_2, Al_2O_3/SiO_2, and ZrO_2/SiO_2 supported Pt catalysts. The types of HDO reactions pathway were observed to proceed through hydrogenation of aromatic ring with bicyclohexyl as the major product over Al_2O_3/SiO_2, and ZrO_2/SiO_2 supported Pt catalysts. Also, some trace amount of cyclohexane was obtained over Pt/ Al_2O_3/ SiO_2, and that, it is better performance was affiliated to the high acidity of the catalyst. The various reaction pathways reported that Dibenzofuran could be converted to bicyclic hydrocarbons as given in dibenzofuran reaction mechanisms (Figure 2.10).

According to reaction schemes (Figure 2.10) as adopted from (Wang et al., 2015b, Gbadamasi et al., 2016) , there are 7 possible reaction pathways. In the first (1) pathway, the dibenzofuran directly converted to tetrehydrodibenzofuran (THDBF) by partial hydro genation of benzene ring. But in the second (2) reactions pathway hexahydrodibenzofuran (HHDBF) was obtained directly from dibenzofuran complete hydrogenation of mono aromatic ring. In the third reaction pathway, hexahydrodibenzofuran (HHDBF) was totally hydrogenated to form decahydrodibenzofuran which undergo hydrogenolysis and dehydration to yield cyclohexyl-cyclohexanol (CHCHOH) cyclohexyl-cyclohexene (CHCHE). Then further hydrogenated to produce bicyclohexane (BCH) or isomerized

into methylpentylcyclohexane (Iso-BCH). However, in the fourth (4) pathway hexahydro dibenzofuran proceed through hydrogenolysis into phenyl-cyclohexanol (PCHOH) before hydrogenation to cyclohexyl-cyclohexanol (CHCHOH) and onward conversion to bicyclic saturated hydrocarbons (BCH or iso-BCH). In the fifth reaction pathway, hexahydrodibenzofuran (HHDBF) undergo hydrogenolysis into cyclohexyl-phenol (CHPOH) that, proceed to cyclohexyl-benzene (CHB) by C-OH hydrogenolysis followed by total hydrogenation into bicyclohexane or isomerized form of that. On the hand, cyclohexyl-phenol (CHPOH) got total hydrogenated into cyclohexyl-cyclohexanone (CHCHO) or cyclohexyl-cyclohexanol (CHCHOH) and subsequently convert to saturated hydrocarbons

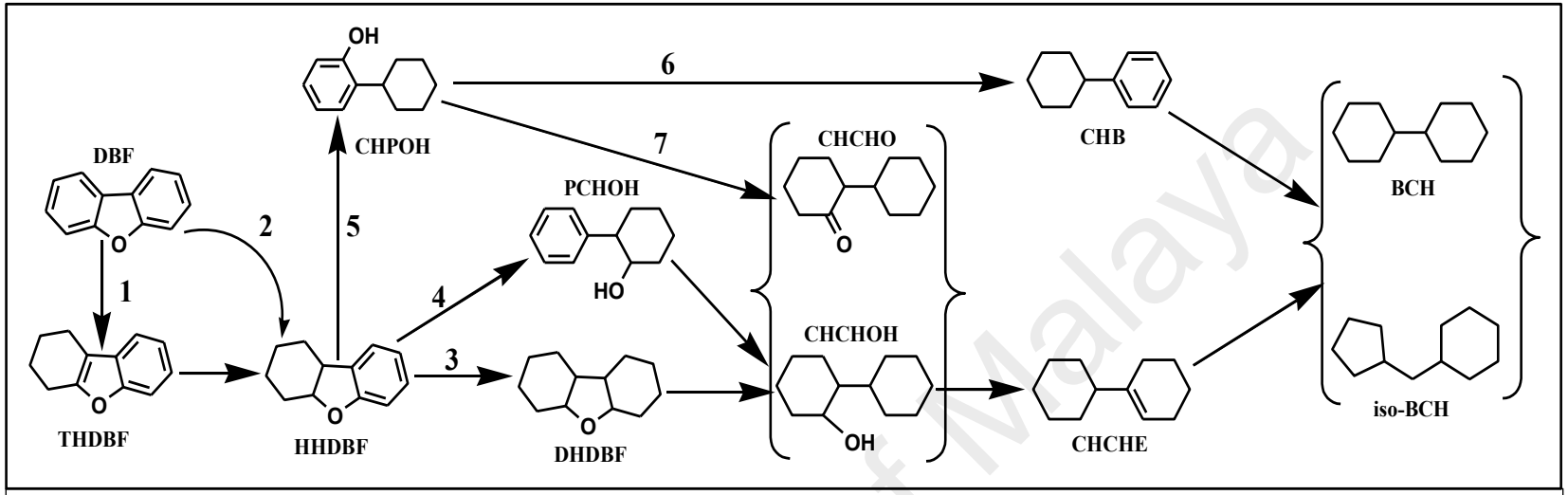

Figure 2.11 : Reactions pathways for hydrodeoxygenation of dibenzofuran over non-noble metal catalysts

CHAPTER 3: EXPERIMENTAL

Table 3.1: All chemicals and Reagents were used as received from various suppliers, as listed below:

Serial No.	Chemicals and Reagents	Purity (%)	Suppliers
1	Nickel (II) nitrate hexahydrate; $Ni(NO_3)_2 \cdot 6H_2O$	≥ 97	Friendemann Schmidt Chemical
2	Copper nitrates hexahydrates; $Cu(NO_3)_2 \cdot 3H_2O$	≥99.5	Friendemann Schmidt Chemical
3	Titanium dioxides (TiO_2)	≥99	Sigma Aldrich
4	Zirconium dioxides ZrO_2	≥ 99	Sigma Aldrich
5	Cerium oxides CeO_2	≥ 99.9	Sigma Aldrich
6	n–Heptane	≥ 99	Merck
7	Tetra ethyl ortho silicate (TEOS)	≥ 98	Sigma Aldrich
8	Titanium iso-propoxides (Ti(OiPr)4)	≥ 99.99	Sigma Aldrich
9	Dibenzofuran (DBF)	≥ 97	Merck
10	Guaiacol (2–methoxy-phenol)	≥ 98	Sigma Aldrich
11	Cetyl trimethyl ammonium bromide (CTAB)	≥ 99	Sigma Aldrich
12	Sodium hydroxides; (NaOH)	≥ 98	Sigma Aldrich
13	Absolute ethanol	≥ 99.9	Merck Millipore

3.1 Synthesis methodologies for supports and supported catalysts

3.1.1 Synthesis of Cu-Ni supported on metal oxides

All supported catalysts used in this study were prepared by a wet impregnation method following the procedure reported in **(Khromova et al., 2014).** In a typical procedure, the required quantity of nickel nitrate hexahydrate [$Ni(NO_3)_2 \cdot 6H_2O$] and copper nitrate trihydrate [$Cu(NO_3)_2 \cdot 3H_2O$] were dissolved in deionized water. The equivalent amount of TiO_2 (support) was dispersed in deionized water and then added to nickel-copper solution. The mixture was sonicated for 30 minutes and then aged at 70ºC to a highly viscous substance, which was further dried in an oven at 90ºC for 12 h and grounded to obtain powder material. The powdered sample was calcined in compress air with flow rate of 10 mL/min at 500ºC with the ramping rate of 5ºC/min for 4 h. After cooling to room temperature, the catalyst was collected and kept for further reduction in hydrogen

with flow rate of 5°/min at 500°C. The same procedure was repeated for ZrO_2 and CeO_2 supported Cu-Ni catalysts. The reported procedure was also given in Figure 3.1.

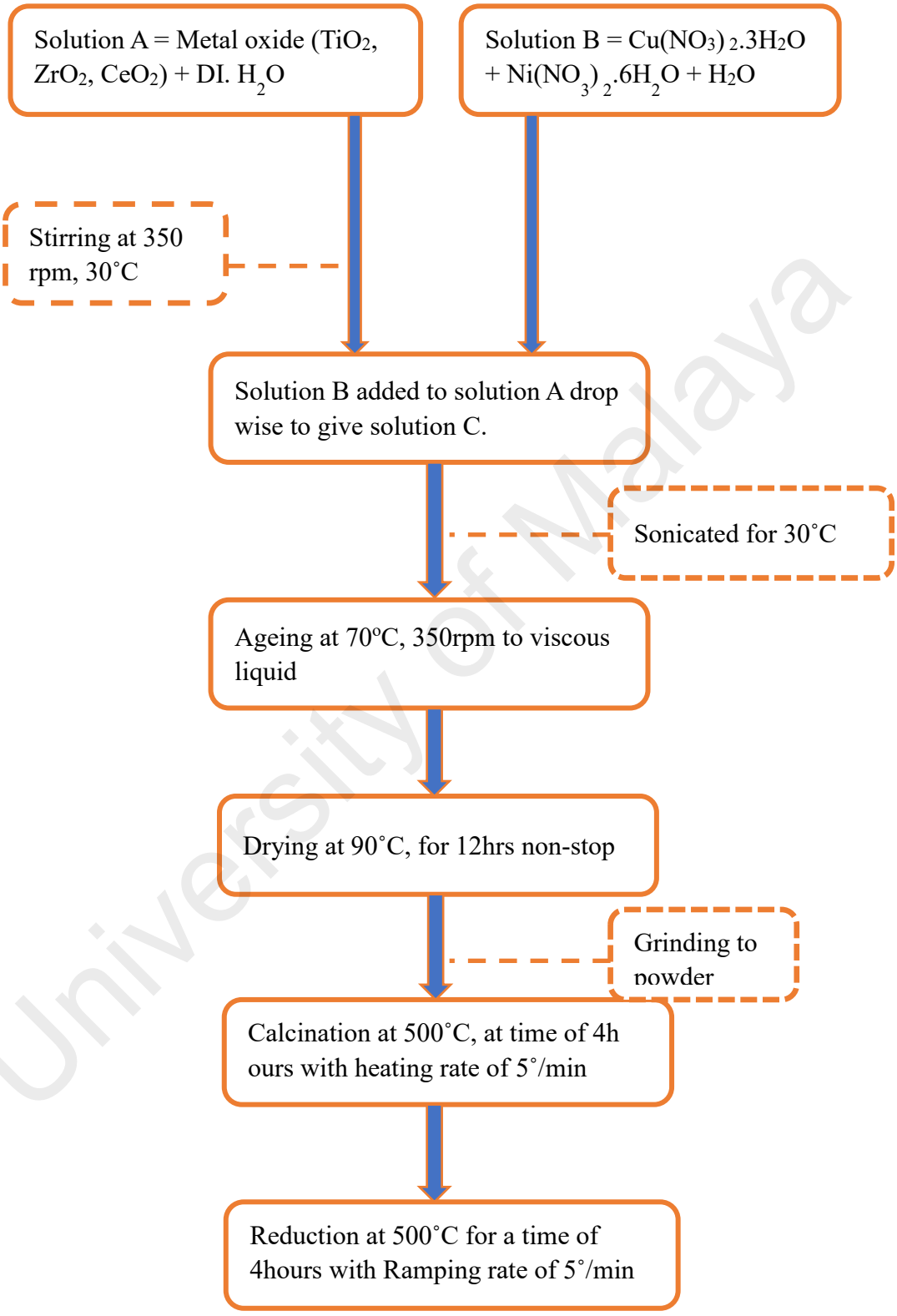

Figure 3.1: **Flow chart for the synthesis of Cu-Ni/MO_2 (MO_2 = TiO_2, ZrO_2 and CeO_2)**

3.1.2 Synthesis of MCM-41

The MCM-41 support was synthesized using hydrothermal synthesis methods via modification of the procedure reported by (Boukoussa et al., 2015). According to our modified procedure at standard conditions, required amount of CTAB was dissolved in 50 mL of deionized water in a 250-mL beaker, stirred at 250 rpm for 30 minutes. In the 2nd beaker, required amount of NaOH, in predetermine volume of water or water/ethanol were mixed and stirred at 250 rpm for 30 minutes at 80 °C. Afterwards, 4g of TEOS was added to the above solution with continuous stirring at 80ºC for 1 day. The resulting pH was then adjusted and aged for another two days followed by filtering and drying at 90ºC for 12 hours. Finally, the sample was calcined at 550ºC for 10 hours as given in the Figure 3.2.

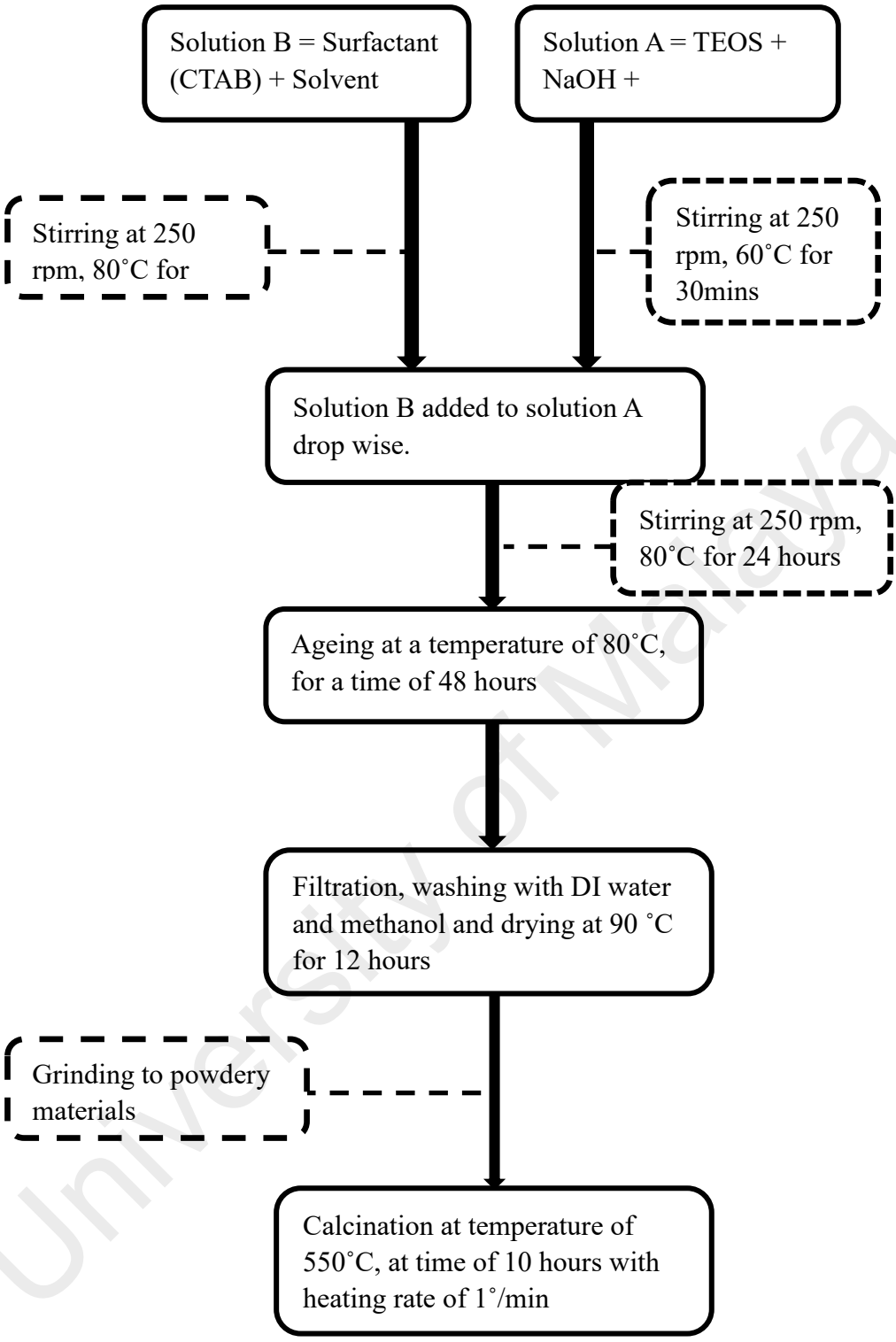

Figure 3.2: Flow chart for the synthesis of MCM-41

3.1.3 Synthesis of Ti-MCM-41

The Ti-MCM-41 support was synthesized using hydrothermal synthesis methods following the MCM-14 procedure with slight modification. According to our modified

procedure as given below, required amount of CTAB was dissolved in 50 mL of deionized water in a 250-mL beaker, stirred at 250 rpm for 30 minutes. In the 2nd beaker, required amount of NaOH, in predetermine volume of water or water/ethanol were mixed and stirred at 250 rpm for 30 minutes at 80 °C. Afterwards, 4g of TEOS was added to the above solution with continuous stirring for another 1 hour. Subsequently, required amount of $Ti(OiPr)_4$ was added with continuous stirring and aged at 80ºC for 1 day. The resulting pH was then adjusted and aged for another two days followed by filtering and drying at 90ºC for 12 hours. Finally, the sample was calcined at 550ºC for 10 hours Figure 3.3. The same procedure was repeated to optimized titanium content.

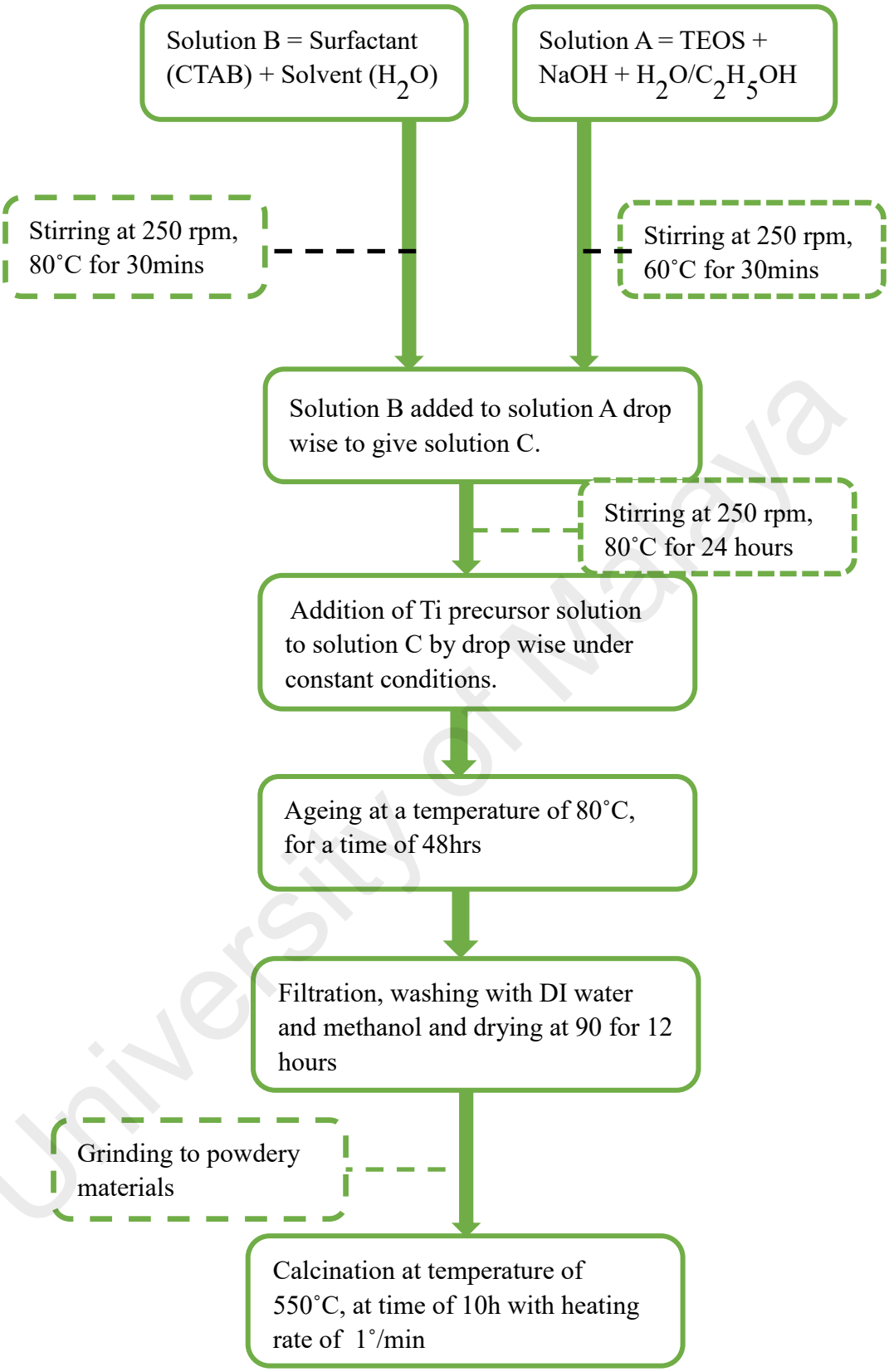

Figure 3.3: Flow chart for the synthesis of Ti-MCM-41

3.1.4 Synthesis of Cu-Ni supported on Ti-MCM-41

A co-impregnation method (Zhang et al., 2013b) was used to prepare Cu-Ni/Ti-MCM-41 with Ni loading of 5% and Cu loading of 2.5% as presented below . In this procedure, the required quantities of $Ni(NO_3)_2 \cdot 6H_2O$ and $Cu(NO_3)_2 \cdot 3H_2O$ were dissolved in 40 mL of deionized water in a 250-mL beaker. In a separate beaker, the Ti-MCM-41 support was dispersed in 100 mL of deionized water and sonicated for 30 minutes to ensure efficient dispersion of the support. The support solution was impregnated with the metal precursor solution, stirred at 250 rpm and aged at 70°C for 6 hours to obtain a viscous liquid. The obtained sample was oven-dried at 90°C for 18 hours and subsequently calcined in air at 600°C for 4 hours and further reduced at 600°C for 4 hours with ramping rates of 3°/min Figure 3.4**.** The same procedure was repeated to synthesized Cu-Ni/MCM-41 with various Ni loading of 7.5%, 10% and 12.5%.

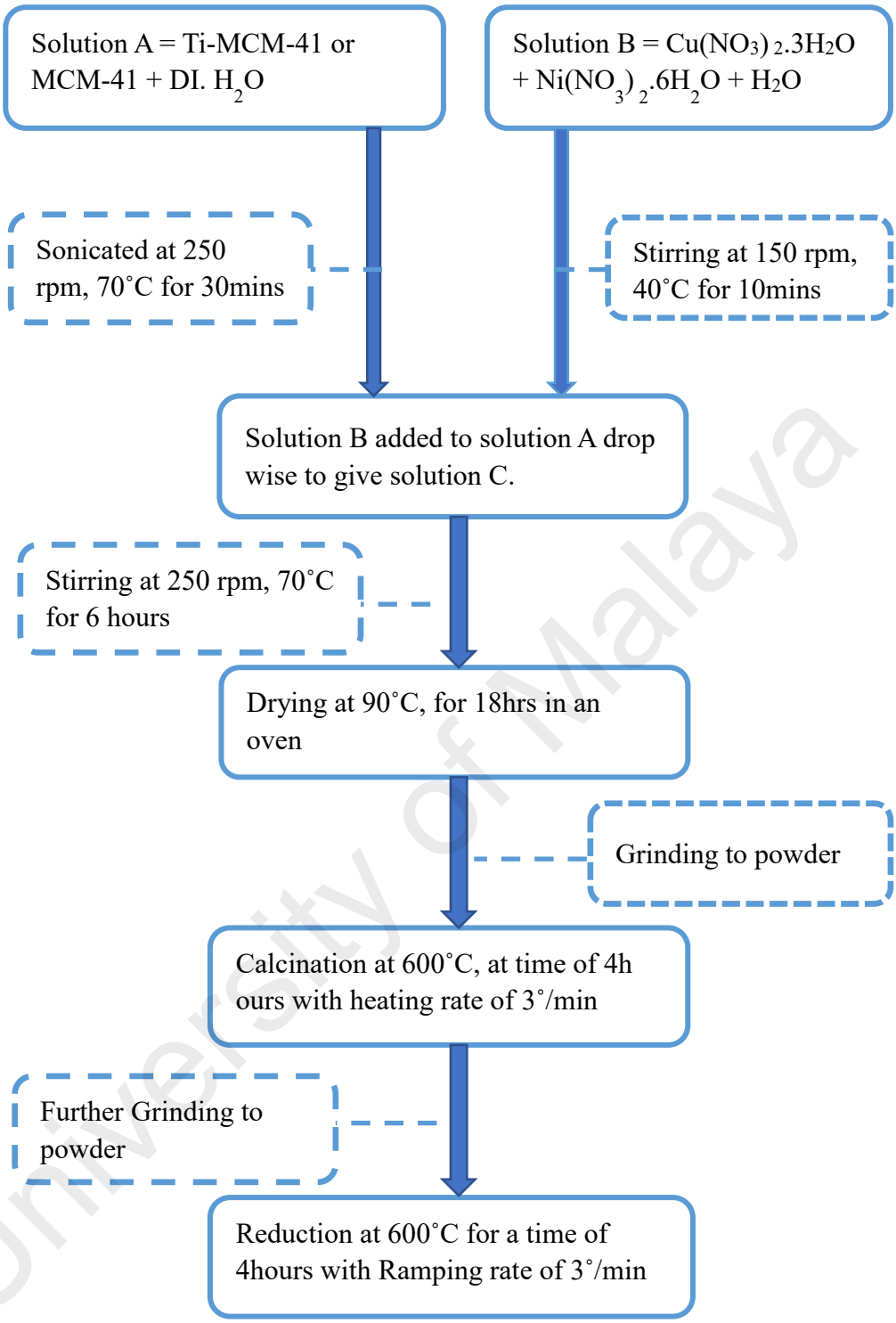

Figure 3.4: Flow chart for the synthesis of Cu-Ni/Ti-MCM-41

3.2 Characterization of support and supported catalysts

3.2.1 Introductions

In order to obtained information about structural and electronic attribute of the prepared catalysts materials, some physical, chemical and spectroscopic analysis are required. Information related to structural and electronic properties of the catalysts materials may give some fundamental knowledge about catalytic active sites and it surrounding environment which to some extent described the relationship between its physico-chemical properties and catalytic activity. The types of characterization techniques used in this research are given in the table below. Then, the brief explanation of the theory and principle of each technique is also given in Figure 3.5 below:

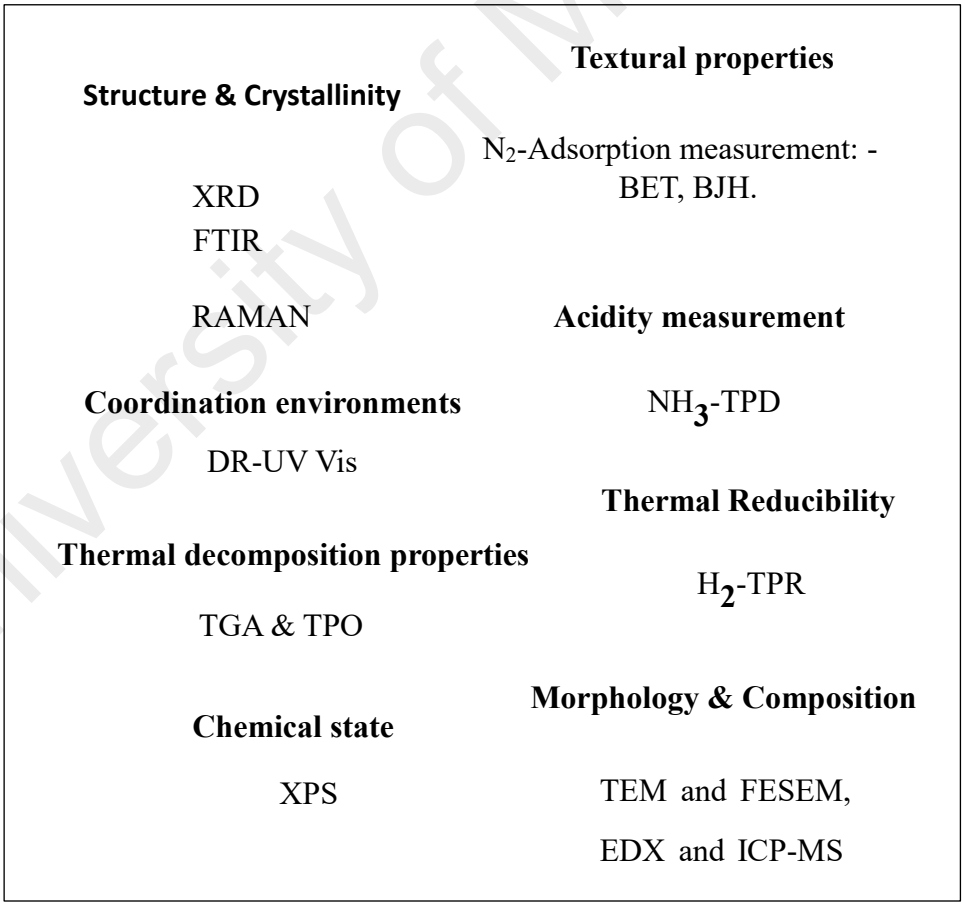

Figure 3.5: Support and supported catalyst's characterization techniques.

3.2.2 The X – Ray diffraction (XRD) analysis

The XRD analysis of the synthesized supports was conducted on small angle x-ray scattering (SAXS) diffractometer (Bruker with CuKα (λ = 1.54 Å) between the range of 0.0-5.0°. The XRD patterns of supported catalysts were obtained on X-ray diffractometer (Bruker D8 advance) equipped with Cu Kα (λ = 0.1542 nm) radiation run at 40 kV and 40 mA in the range of 2θ = 2 to 80° with the step size of 0.02° and step time of 1s.

3.2.3 N_2 adsorption Measurement

The BET surface area and BJH pore size and pore volume determination were conducted as followed; The N_2 adsorption–desorption measurements on the samples were carried out using Micrometrics TriStar II surface area and porosity analyser at a boiling point of liquid nitrogen (-196 °C) according to ASTM D3663–03 standard test method. Prior to analysis, the samples were outgassed to remove physically adsorbed gases and vapours on the sample surface. This was done by heating 300 mg of the sample at 300°C for 5 h in the analyser sample cells. The outgassed, sample in the samples cell was made airtight, re-weighed and connected to the analysis section of the analyser, and cooled in liquid nitrogen. The surface area of the samples was calculated by multiple point BET method and the BJH method was applied to the adsorption branch of the isotherms to obtained the pore size distribution and pore volume of the samples.

3.2.4 The Fourier Transform-Infrared Spectroscopy (FT-IR)

The FT-IR spectroscopic analysis, were performed on Bruker VERTEX 70 FT-IR Spectrometer using KBr pellet technique. Before doing the pellet, the samples were evacuated and spectral measurement were conducted in the transmission mode under atmospheric condition and room temperature. The spectral region was explored from 400 to 4000cm^{-1}.

3.2.5 UV-VIS Diffuse Reflectance Spectroscopy (UV-Vis-DRS)

The UV-visible DRS analysis of the samples was performed using a Shimadzu (2600) UV-visible spectrometer in the range of 200-800 nm with reference standards and CCD detector.

3.2.6 Temperature–Programmed Reduction (H_2–TPR) analysis

H_2-TPR of the samples were carried out on a Thermo-Finnigan TPDRO 1100 series equipped with thermal conductivity detector (TCD). For each analysis, 50mg of the sample was placed in a quartz tube reactor and pre-treated with nitrogen N_2 at 120°C for 1 hour to remove surface moisture of the catalysts. After sample pre-treatment, H_2-TPR analysis, was conducted by heating the samples from 30 to 650ºC at a heating rate of 10ºC/min with 5% H_2 in N_2 at a flow rate of 20 mL/min with a terminal holding time of 60 min.

3.2.7 Thermal gravimetric analysis (TGA)

Thermal gravimetric analysis (TGA) of the samples was conducted using a thermogravimetric analyser (Perkin Elmer TGA 7). Each of the sample was heated form 30-1000ºC with heating rate of 5ºC/min in the atmosphere of argon following at the rate of 10 mL/min.

3.2.8 Ammonia Temperature–Programmed Desorption (NH_3–TPD) analysis

NH_3-TPD analysis of the catalysts supports were conducted on a Thermo-Finnigan TPDRO 1100 instrument with Ser.Nr.20022896 equipped with thermal conductivity detector (TCD). For each experiment, 0.0516 mg of the catalyst was first outgassed in the TPDRO cell at 120ºC for 1 h in the following atmosphere of He gas, followed by cooling the system to 50ºC. At this temperature, the catalysts samples were subjected to 10% NH_3/He passing at 20 ml/min for 1 h. The weakly physiosorbed NH_3 was remove by purging the system with 100% helium for I hour. Then, thermal desorption of NH_3 was

carried out between the temperature of 100-900ºC at 10ºC/min in a He atmosphere flowing at 20 mL/min with a final holding time of 30 min.

3.2.9 Raman spectroscopic analysis

Raman spectra of the supported catalysts were recorded on Renishaw via confocal Raman microscope coupled with a charge coupled device (CCD) using 514 nm Ar laser and a power of 20 MW. In typical procedure, the sample was inserted inside the spectrometer, pressed into a self-supporting wafer then shined with a monochromatic light (laser) and the resulting scattered photons were measured by the CCD detector. The obtained data was immediately saved and further process using computer device.

3.2.10 Field Emission Scanning Electron Microscopy (FESEM) analysis

FESEM microscopic images were collected from FEI Quanta 200 electron microscope operated at 3 and 5 kV. Prior to analysis they were prepared as described above. The metal oxides supported samples were analysed without gold coating while silica samples were gold coated. Each of these samples was mounted on a sample holder and loaded inside the FESEM compartment. Air was evacuated by creating vacuum in the FESEM compartment prior to scanning. The Resulting images were taken at various KVa and magnification.

3.2.11 Energy Dispersive X-ray spectroscopy (EDX)

The elemental determination using EDX, were carried out immediately after FESEM analysis. The samples were re-focused and analysed using EDX and hence virtual images were displayed and collected.

3.2.12 Transmission Electron Microscopes (TEM)

The TEM measurements were conducted on a JEOL 2010F device with operating voltage of 200 kV.

3.2.13 X-Ray Photoelectron Spectroscopy (XPS)

The XPS of the synthesized support were investigated using an ULVAC-PHI Quantera II with a 32-channel Spherical Capacitor Energy Analyzer operating at a vacuum pressure of 1 x 10-6 Pa. using Al Kα radiation of 1486.8eV and energy width of 680 eV was used.

3.2.14 Inductively Coupled Plasma-Mass Spectrometry (ICP-MS)

The amount of Ni and Cu on supported MCM-41 based catalysts was obtained from ICP-MS (MODEL). This was carried out by dissolving the catalysts in concentrated HNO_3 followed by filtration and preparation of standard solution from which the metal content was obtained.

3.3 Catalysts activation

3.3.1 Catalysts Pre-treatment Unit Set up

The reduction was carried out using catalysts pre-treatment chamber. The pre-treatment chamber (Cambridge Reactor Design) Figure 3.6, comprised of two independent pre-treatment block that can operates separately with maximum operating temperature of 700^{o}C. each of these blocks is designed to accommodate six (6) parallel reactors which enable the chamber to run 12 reactors at the same time. For better automatic operations and control, each of these block is directly connected to temperature and pressure controller, cooling system that is based on compressed air. Besides these, they are also connected with hydrogen, compressed air and inert, gas line for air evacuation and subsequent reductions. The gas flow through the reactors are control by switching valves and the regulators connected to pre-treatment chamber.

Figure 3.6 : Pre-treatment chamber for catalysts reduction

3.3.2 Procedure for Catalysts Activation

Reduction of CuO-NiO/Ti-MCM-41, 100mg of each of the catalysts samples was measured and transferred inside the quartz glass reactor, the empty catalysts bulb was connected to the upper part of each reactor. The closely tight reactors were taken into the pre-treatment unit Figure 13, they were purged 3 times with nitrogen, then following the hydrogen gas for activation process by setting the hydrogen pressure of 2 bar and regulated it follow to 40ml/min. The temperature controller was set to 550^{o}C at a steady rate of 5^{o}C/min for all the connected reactors and maintained at 550^{o}C for 5 hours. Finally, the reactors were cooled down to 30^{o}C under the atmosphere hydrogen. At room temperature, the reduced catalysts from each reactor was transferred into the catalysts bulb by inverting the closed reactor upside down. Then the catalysts bulb was Sealed with a torch in the encapsulation unit Figure 14, which result to separation of the catalysts bulb with an empty reactor. The catalysts bulb was weighed with and without loaded catalysts

to obtained the weight of the reduced catalysts available for the reaction. The reduced catalysts were safely kept in a desiccator before the conduct of the reactions.

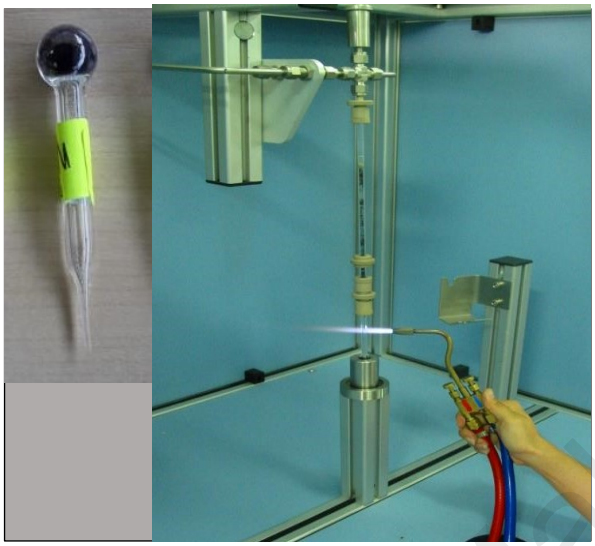

Figure 3.7 : Catalysts Bulb sealing in the encapsulation

3.4 Hydrodeoxygenations reactions

3.4.1 Reactor set-up

The high-pressure stainless-steel batch reactors were used to investigate catalytic activity (catalysts performance test) for HDO reactions. There are 12 assemble independent batch reactors (Cambridge Reactor Design) in the concerned workstation Figure 3.8. Each of these reactors has a total volume capacity of 100 ml with maximum operating temperature of 300ºC, and operating pressure of 300 bar. As indicated in the work station Each of these reactors, is connected with a thermocouple, a mechanical stirrer (with maximum rotation of 1,500 rpm), pressure sensor, inlet and outlet gas line. These reactors are automatically control by control panel connected to computerised system for command and visualizations during the operation of the reactors. Before the commencement of the reactions, the catalysts bulbs are directly tightened on the catalysts holder (Polyether ether ketone; PEEK) located at the left Conner of mechanical stirrer. As the reaction commence, the mechanical stirrer breaks the catalyst bulb, and the catalyst content is release into the reaction mixture. At the end of the reactions, the reactors are

cooled down by an effective cooling device (Julabo, FC 600 model) connected to the entire workstations which utilized deionized water as a cooling fluid. The usual range of operating temperature of this cooling device (Julabo) was from of –20ºC to +80ºC, and pumping rates of 20 l/min.

Apart from the direct hydrogen gas line coming to the reactors, a hydrogen-dosing unit which receives hydrogen supply from the main cylinder is also connected to each reactor. The main function of the dosing, is to stabilized and compensate (due to pressure drop) reactions pressure in the reactor and hydrogen supply from the dosing unit reach to each reactor via a check valve. In case of drop of hydrogen pressure during the reaction; possibly due to hydrogen consumption in the progressing reactions, the dosing automatically open via the check valve to compensate the loss of hydrogen pressure in the reactor by re-pressurizations.

Figure 3.8 : A workstation with 12 independent stainless-steel batch reactors

3.4.2 Catalyst performance test.

The catalytic performance of the prepared catalysts for hydrodeoxygenation of Guaiacol and Dibenzofuran were carried out in 100ml stainless steel batch reactor described above. For hydrodeoxygenation reaction of each model compound, the glass

catalyst's bulb containing reduced catalyst was tightened on a catalysts holder just before the commencement of the reaction. Both the catalyst holder and stirrer were enclosed in a mounted reactor containing 4wt.% model compounds and 96 wt.% heptane (as inert solvent). After pre-processing and leak check, the reactor was pressurized with desired pressure and temperature then, run for a period of time set at the beginning of the reactions. After the reaction and post processing, the obtained products were analysed qualitatively using GC-MS (Agilent GC-MS6890N) equipped with HP-5MS capillary column (30m X 0.250mm X 0.25µm) and for product quantification GC-FID (Agilent GC-6890N) attached with HP-5 (30m X 0.53mm) column was used. In all cases product analysis were followed immediately using GC-MS (Agilent GC-MS6890N) for qualitative analysis and GC-FID (Agilent GC-6890N) for Product quantification. Figure 3.9 show diagrammatic representation of reactor and reaction mixture during Hydrodeoxygenation reactions.

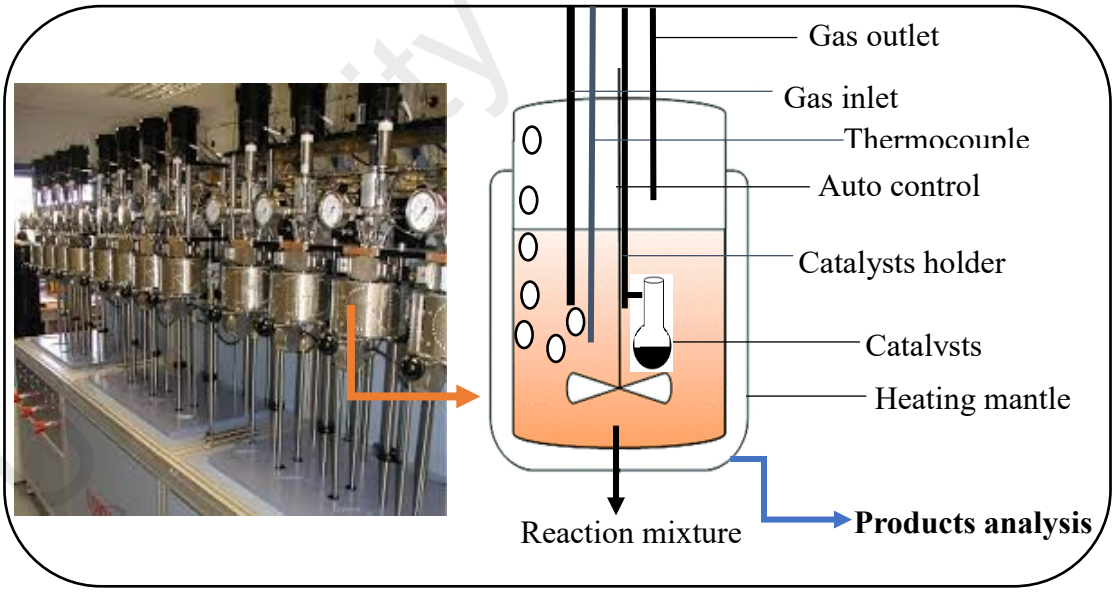

Figure 3.9 : Assemble of stainless steel batch reactors during HDO reactions

3.4.3 GC-MS and GC-FID analysis

Prior to GC-MS and GC-FID analysis, the catalyst was filtered from the reactions products using Agilent micro filter. Then products analysis were conducted using GC-MS (Agilent GC-MS6890N) equipped with HP-5MS (30m X 0.250mm X 0.25µm)

capillary column. Product quantification was carried out using GC-FID (Agilent GC-6890N) attached with HP-5 (30m X 0.53mm) column.

The DBF separation was carried out as follows; the initial oven temperature was held at 40^{o}C for a time of 5.0 min, then proceed to 161^{o}C with a steady rate of 15^{o}C/min and held at this condition for 10min. With similar rate of 15^{o}C/min the temperature was raised to 170 °C also maintained for 10.0 min.

The Guaiacol separation was carried out as follows: initial oven temperature was held at 40^{o}C for a time of 2.0 min, then proceed to 60^{o}C with a steady rate of 2^{o}C/min. Then the ramping was modified to 5^{o}C/min up to 100°C which was held for 2 min and finally with steady rate of 20^{o}C/min the temperature was increased to 200^{o}C and held for 2.0 min. After each GC run of DBF or Guaiacol, the obtained results were collected and used to determine the reactant's conversion and products selectivity via the following expression:

The conversion of DBF and the selectivity of bicyclohexane were calculated as follows (Lin et al., 2008, Reddy et al., 2012, Halilu et al., 2016)

$$\text{Conversion of DBF (\%)} = \frac{(\text{Moles of DBF})_{in} - (\text{moles of DBF})_{out}}{(\text{Moles of DBF})_{in}} \times 100 \quad \text{(Eq. 3.2)}$$

$$\text{Selectivity of BCH. (\%)} = \frac{\text{Number of moles of bicyclohexane produced}}{\text{Number of moles of DBF reacted}} \times 100 \quad \text{(Eq. 3.3)}$$

Then conversion of GUA and the selectivity of cyclohexane were calculated as follows

$$\text{Conversion of GUA. (\%)} = \frac{(\text{Moles of GUA})_{in} - (\text{moles of GAU})_{out}}{(\text{Moles of GUA})_{in}} \times 100 \quad \text{(Eq. 3.4)}$$

$$\text{Selectivity of CH. (\%)} = \frac{\text{Number of moles of cyclohexane produced}}{\text{Number of moles of GUA reacted}} \times 100 \quad \text{(Eq. 3.5)}$$

3.5 Reusability studies

The reusability study of the catalysts was carried out according to (Selvaraj et al., 2014, Mallesham et al., 2016) as followed; The catalysts was reused for four cycle, for each run,

the catalysts was filtered, washed with n-hexane to remove the residual deposit of reactants and products. The spent catalysts were then dry in an oven at 90ºC for 3hrs, activated under air at 450ºC for 4 hours followed by reducing them under hydrogen at at same conditions used for initial reductions.

CHAPTER 4: RESULT AND DISCUSSIONS

4.1 Introduction

In this chapter, the entire experimental results were presented and discussed herein. The results were presented into six (6) section. Section One (1) reported the results of preliminary study using metal oxides supported Cu-Ni catalysts while Section Two (2) display the experimental results for optimization of Ni loading over metal oxide supported catalysts. Section Three (3) presents the results for synthesis of mesoporous Ti-MCM-41 and MCM-41 supports, then Section Four (4) indicate the results for optimization of Ni loading toward hydrodeoxygenation activity of Cu-Ni/Ti-MCM-41 catalysts. Section Five (5) of this chapter was about the results for optimization of titanium content of Cu-Ni/Ti-MCM-41catalysts toward the hydrodeoxygenation activity, and Section Six (6) shows the results of comparative studies between metal oxides and mesoporous supported catalysts for hydrodeoxygenation of guaiacol and dibenzofuran (DBF). The results of stability study and proposed catalytic reaction pathway for Guaiacol and dibenzofuran conversion toward saturated hydrocarbon over Cu-Ni/Ti-MCM-41 catalysts.

4.2 Preliminary study using metal oxides supported Cu-Ni catalysts

Various types of non-noble metals-based catalysts have been explored for hydrodeoxygenation reactions. It was found that, silica supported Ni-Cu catalysts have been reported to be active in HDO reactions (Khromova et al., 2014). However, the high performance of this catalysts has been limited by weak acidity of silica support. Earlier studies on metal oxides (such as TiO_2, ZrO_2, and CeO_2) supported noble metal and molybdenum oxides catalysts had shown potential as hydrodeoxygenation catalyst supports (Mortensen et al., 2013, Badoga et al., 2014). Further limitation of these catalysts was limited by the expensiveness of noble metals. Moreover, the catalyst tends to promote coking and deactivation under high temperature during hydrodeoxygenation process. In

a contrary reaction, it has been reported that, mild reaction temperature control coking, catalysts deactivation and enhance catalysts stability (Schumacher et al., 2003). In view of these, three metal oxides (TiO_2, ZrO_2, and CeO_2) have been considered as catalysts supports for Cu-Ni catalysts in hydrodeoxygenation under mild reaction temperature. In this regard, Cu-Ni catalysts was supported on TiO_2, ZrO_2, and CeO_2 via impregnation method. Physico-chemical study of catalysts and catalytic study for hydrodeoxygenation of Dibenzofuran (DBF) and Guaiacol at 250ºC, 5MPa and 4 hours of reaction time were investigated. In this section, the experimental results for physico-chemical characterization and catalytic activity of the three different oxides were presented and discussed. Also, the results for optimisation of Ni loading of the most performing catalysts is also presented and discussed in this section.

4.2.1 Physico-chemical characterizations

4.2.1.1 Thermal gravimetric analysis (TGA)

Thermal gravimetric analysis (TGA) of the three samples were conducted, in order to understand the thermal decomposition behaviour of the synthesized materials during the calcination process, as shown in Figure 4.1 all the samples: (a) CuO-NiO/CeO_2, (b) CuO-NiO/ZrO_2 and (c) CuO-NiO/TiO_2 exhibited a similar decomposition trend with nearly 30% weight loss. There are three regions on each each curve: the weight loss from 49 to 108ºC, 54 to 154ºC and 45 to 103ºC for CeO_2, ZrO_2 and TiO_2 supported samples due to evaporation of moisture content and water crystallization associated with the salt precursor (Małecka et al., 2014). The second region of moderate weight loss observed in the range of 108-221, 155-252 and 104-211ºC for CeO_2, ZrO_2 and TiO_2 samples, were due to thermal decomposition of highly exposed surface nitrates. The last region observed at higher temperature i.e. ~345, 380 and 334ºC (major weight lost) for the respective samples, could be attributed to thermal decomposition of $Ni(NO_3)_2$ and $Cu(NO_3)_2$ to Cu-O and Ni-O (Małecka et al., 2014). Since the major weight loss was terminated at 450ºC,

all the samples were calcined at 500°C. It was obvious from Figure 1(a), (b) and (c) that all samples exhibit similar degradation patterns, indicating the existence of similar interaction between the catalyst precursors and supports, in line with the published results (Rahemi et al., 2014).

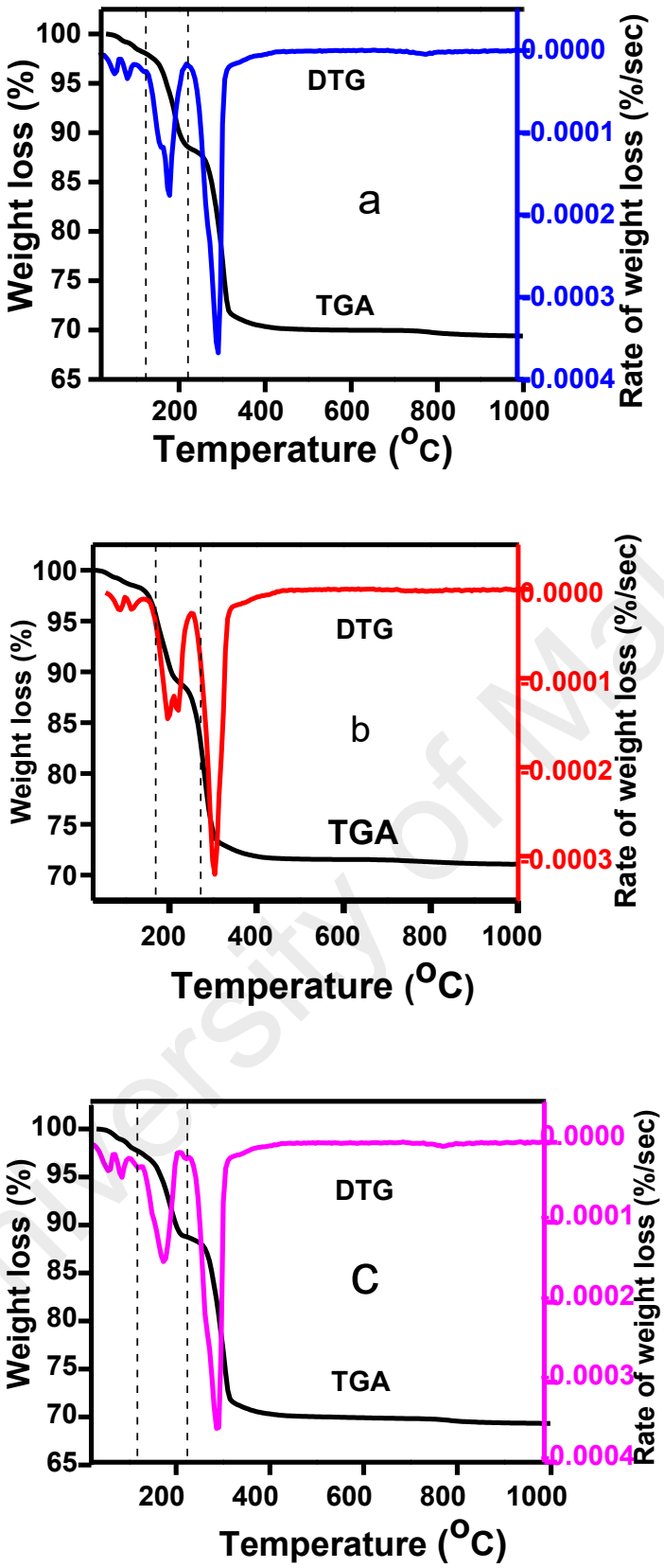

Figure 4.1: Thermogravimetric curves for the Cu-Ni precursor supported on (a) = CeO_2, (b) ZrO_2, and (c) TiO_2 before calcination.

4.2.1.2 Raman spectroscopy analysis

Raman spectra of CuO-NiO/CeO_2 (a), CuO-NiO/ZrO_2 (b), and CuO-NiO/TiO_2 (c) are presented in Figure 4.2. Generally, pure CeO_2 shows a major Raman peak at ~464 or 490 cm^{-1} due to F_{2g} band of cubic structured CeO_2 [31, 32]. However, in this study we observed a significant shifting of F_{2g} peak to 520 cm^{-1} for CuO-NiO/CeO_2 sample. This shifting indicates existence of strong interactions between Ni-Cu and CeO_2 support in Ni-Cu/CeO_2 catalyst, resulting in lattice strain of the CeO_2 and shifting of its F_{2g} band. On the other hand, the broadening of F_{2g} peak can be explained by phonon confinement resulted from the presence of smaller crystallite sizes of CeO_2 (Spanier et al., 2001, Pejova, 2013). Also, the Raman bands of Cu (I) oxide, Cu (II) oxide, and Ni (II) oxide are found to be ~200, 300 and 1100 cm^{-1}, respectively (Li et al., 2015, Luo et al., 2014b). However, the bands are shifted to 179, 331, and 1150 cm^{-1} for Cu (I) oxide, Cu (II) oxide, and Ni (II) oxide respectively in the synthesized catalysts which could be due to lattice straining effects. The observed broadening of Ni (II) oxide band could be also explained by small crystallites of Ni-O. In the case of ZrO_2 supported Cu-Ni catalyst, the observed 175 and 471 cm^{-1} bands can be assigned to monoclinic ZrO_2 (Zhu et al., 2013), while the bands related to Cu (II) oxide and nickel (II) oxides are slightly shifted to 331 and 1148 cm^{-1}, respectively. The appearance of Raman peak at ~141 cm^{-1} in the CuO-NiO/TiO_2 sample indicates the presence of anatase TiO_2 with a slight shifting backward from 147 cm^{-1} (Nguyen et al., 2014). As well, Raman bands corresponding to nickel (II) oxide and Cu (II) oxide for CuO-NiO/TiO_2 sample are shifted to 514 and 637 cm^{-1}, respectively, due to lattice strain effects.

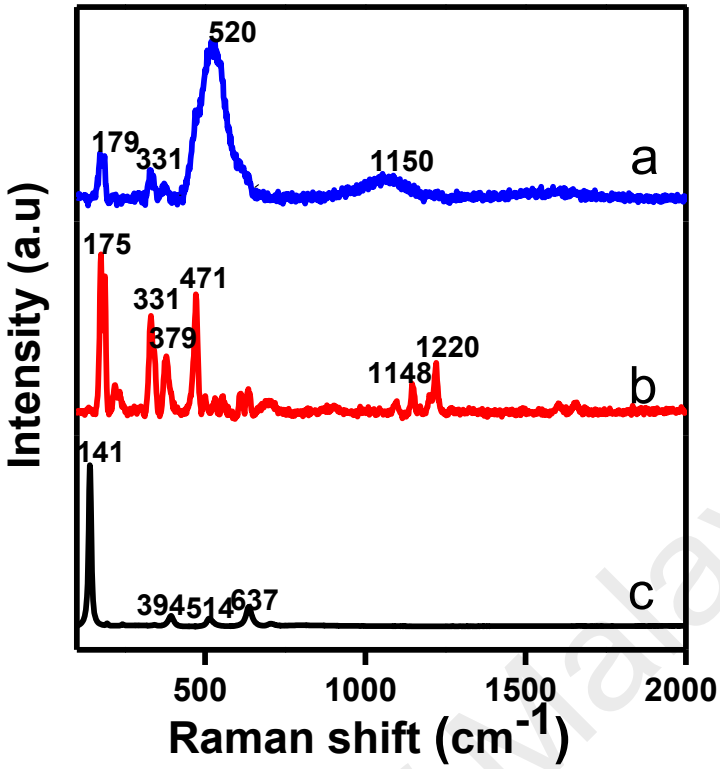

Figure 4.2 : The Raman spectra of CuO-NiO supported on (a) = CeO_2, (b) ZrO_2, and (c) TiO_2

4.2.1.3 Hydrogen temperature programmed reductions (H_2-TPR) analysis

The synthesized catalysts has been examined by H_2-TPR analysis (Figure 4.3**).** Three major peaks were found for CuO-NiO/CeO_2 catalyst (Sample CeO_2): The first peak was observed at 197.7°C could be assigned to the reduction of highly surface exposed Cu-O species to Cu metal, and the second peak observed at 297.2°C could be due to the reduction of remaining Cu^{2+} species to Cu^0. The observed larger peak at 400°C could be ascribed to the reduction of bulk CuO-NiO to bimetallic Cu-Ni. On the other hand, two major peaks are observed for ZrO_2 supported catalyst (sample b) at ~260 and 343°C, indicating the reduction of Cu^{2+} to Cu^0 and reduction of CuO-NiO to Cu-Ni bimetallic alloy, respectively. For TiO_2 supported Cu-Ni catalyst (sample c), a small peak was found at 252.8°C, indicating the reduction of Cu-O to Cu. As well, a large reduction peak was found at about 356.1°C, which could be assigned to the reduction of CuO-NiO to Cu-Ni

bimetallic alloy. Interestingly, a shoulder peak can be noticed at 286.1°C, indicating the reduction of remaining Cu-O to Cu metal.

The peak corresponding to the reduction of Ni-O to Ni was not found for all samples. The possible reason is that the reduction peak of Ni-O to Ni might be overlapped with CuO-NiO peak, resulting in the formation of a larger peak with higher hydrogen consumption (at 400, 343, and 356.1°C for CeO_2, ZrO_2 and TiO_2 supported catalysts, respectively) (Zhang et al., 2013b). One of the observed differences between CeO_2 supported catalyst and other two supported catalysts is that, the larger peak for CeO_2 supported catalyst ended sharply with no extension while those of TiO_2 and ZrO_2 supported catalysts possess little extension. The former was the indication of higher degree of overlapping of two peaks, while the extension for latter two catalysts show less degree of this overlap, which could be due to strong interaction between Ni-O and the supports (TiO_2 and ZrO_2). It is therefore possible that the reduction of both Cu^{2+} to Cu^o and Ni^{2+} to Ni^0 takes place in a single step, in good agreement with literatures (Pérez-Hernández et al., 2015, Reddy Kannapu et al., 2015, Khromova et al., 2014).

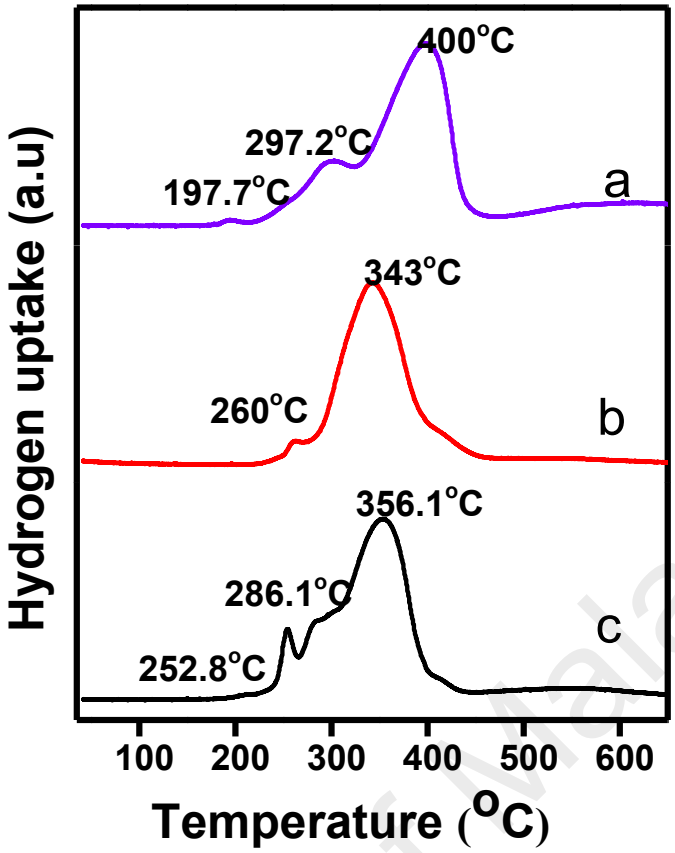

Figure 4.3 : The H_2-TPR profile of CuO-NiO supported on (a) = CeO_2, (b) ZrO_2, and (c) TiO_2

4.2.1.4 X-Ray diffraction analysis (XRD)

The XRD patterns of CuO-NiO supported on CeO_2, ZrO_2 and TiO_2 are shown in Figure 4.4. The matching of diffraction peaks with corresponding planes was obtained from powder diffraction file (PDF) of international centre for diffraction data using X'Pert High Score Plus software (version 3.0. 2011 released). The CuO-NiO/CeO_2 sample shows various diffraction peaks at 28.58 (111), 33.11 (200), 47.51 (220), and 56.39° (311), which confirm the presence of cubic CeO_2 phase (Ref code: 00-034-0394). The matching of ceria supported catalysts confirm the presence of cubic phase of Ni-O on the following diffraction peaks occurring at reflection indexed of 30 (111), 37 (200) and 63° (220) (Ref code: 96-101-0096). This confirmation strengthening our observation in Raman spectrum for CeO_2 supported catalysts (Figure 4.2). The XRD peaks corresponding to anatase TiO_2

were observed at 25.37 (101), 38.3 (112), 54.07 (105), and 63.5° (213) for CuO-NiO/TiO_2 sample (Ref code: 01-071-1166) (Neale and Frank, 2007, Masui et al., 2003, Li et al., 2014). Besides XRD peaks of anatase TiO_2, few other peaks indexed at 24 (101), 33 (104), 35 (110), 49.5 (107), 64 (300), and 75° (217) were also found in CuO-NiO/TiO_2 sample, which can be assigned to hexagonal phase of Ni/TiO_3 (Ref code: 96-900-7390).

The observed XRD peaks at 24.11, 28.25, and 31.58° with the diffraction planes of (101), (111), and (200), indicate the existence of monoclinic phase of ZrO_2 in CuO-NiO/ZrO_2 sample (Zhang et al., 2013b). In the case of active components, the XRD peaks of cubic phase Ni-O can be observed at 43.87 (111), 37.9 (200), and 63.7° (220) positions over ZrO_2 monoclinic phase for CuO-NiO/ZrO_2 sample (Ref code: 01-078-0423). In contrast, the XRD peaks related to Ni-O and Cu-O were not observed over TiO_2 supported catalysts (both Ni-O and Cu-O), ZrO_2 and CeO_2 supported catalysts (Cu-O). However, Raman results indicate the presence of these active components on the surface of ZrO_2, CeO_2 and TiO_2. The absence of these peaks over ZrO_2, CeO_2 and TiO_2 supported catalysts could be due to formation of smaller crystallite size, which is evidenced by FESEM analysis as shown in Figure 4.5.

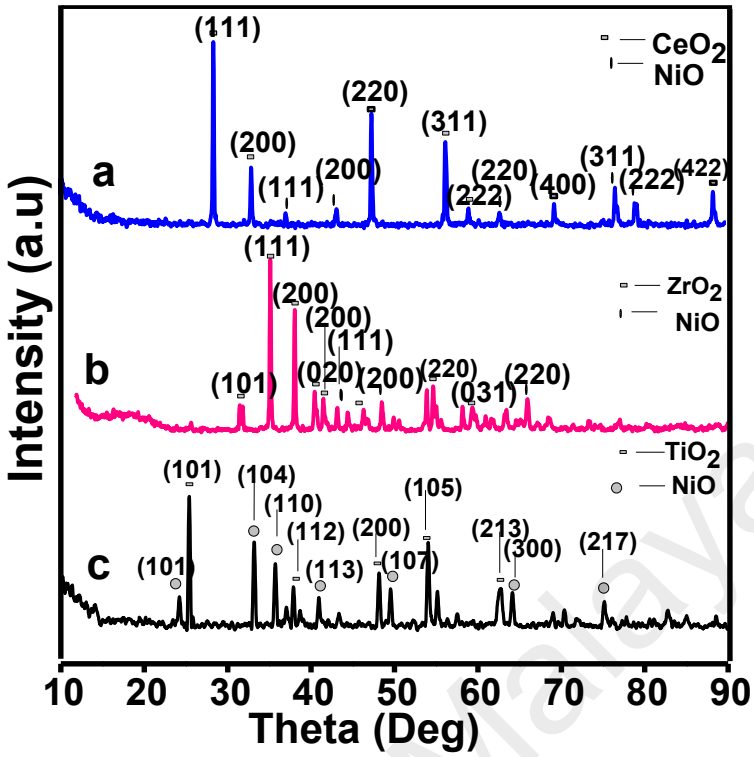

Figure 4.4 : The X-Ray diffraction (XRD) pattern of CuO-NiO supported on (a) = CeO_2, (b) ZrO_2, and (c) TiO_2

4.2.1.5 BET surface area analysis

The N_2 adsorption-desorption isotherms of CuO-NiO supported on CeO_2, ZrO_2 and TiO_2 is presented in Figure 4.5. All the three supported catalysts exhibited type III isotherms characteristics for microporous materials (ALOthman, 2012). Although, the isotherm for all the three catalysts manifest low surface area as given in Table 4.1 but relatively TiO_2 supported catalysts show larger surface area (10.77m^2/g) compared to CeO_2 (9.63m^2/g) and ZrO_2 (7.95m^2/g) supported catalysts. Also, CeO_2 supported catalysts is better than ZrO_2 supported catalysts as noted from these values. The small surface area of these catalysts is due to small surface area in the pure support couple with surface coverage by the supported active species.

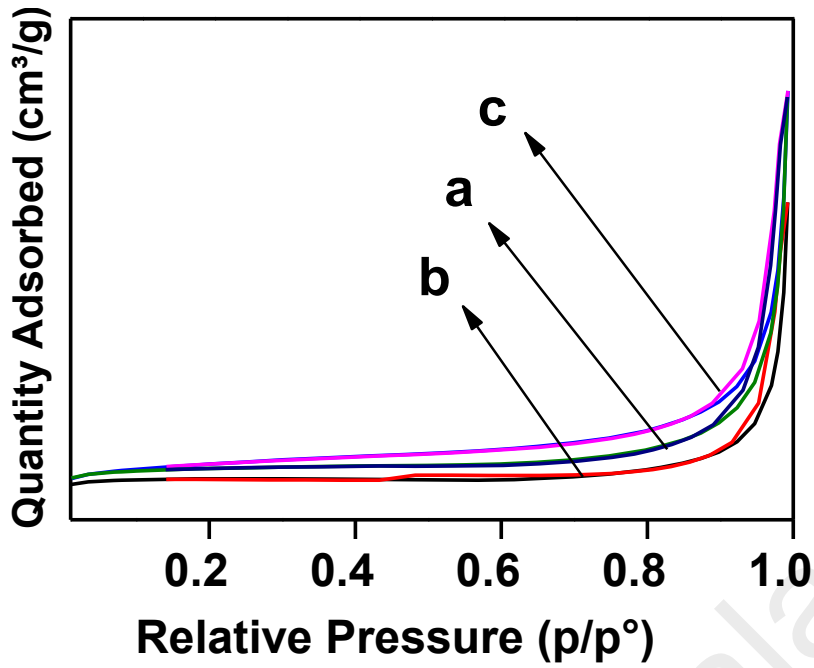

Figure 4.5 : The N_2 adsorption isotherms for CuO-NiO supported on (a) = CeO_2, (b) ZrO_2, and (c) TiO_2.

Table 4.1: - Acidity and structural properties of CuO-NiO supported on A (CeO_2), B (ZrO_2) and C (TiO_2).

Supported catalysts	BET Surface Area (m^2/g)	Acidity (µmol NH_3 g-1)	Crystallite sized (XRD) (nm)
A (Cu-Ni/CeO_2)	9.63	6230	28
B (Cu-Ni/ZrO_2)	7.95	5680	36
C (Cu-Ni/TiO_2)	10.77	7890	27

4.2.1.6 Ammonia temperature programmed desorption NH_3-TPD analysis

Figure 4.6 present NH_3-TPD profiles of CuO-NiO/CeO_2, CuO-NiO/ZrO_2 and CuO-NiO/TiO_2. CuO-NiO/CeO_2, sample shows the presence of weak acids sites at arounds 260°C and in addition to that also small amount of medium and strong acids sites between 400°C-550°C. The total acidity of CuO-NiO/CeO_2 sample amount to 6230µmol/g as given in Table 4.1. In the case of CuO-NiO/ZrO_2 sample, there exist two peaks between 330 and 450°C all corresponding to medium acids strength. The peaks have shifted to higher temperature than in CuO-NiO/CeO_2 but, the concentrations of acid sites (5680µmol/g)

decreases comparatively. On the contrary, CuO-NiO/TiO_2 show both increase of acids number and strength. According to Figure 4.6, there was a broad peak from 280-430ºC representing medium acidity strength with more concentration of acids sites (7890µmol/g) than both of CuO-NiO/CeO_2 (6230µmol/g) and CuO-NiO/ZrO_2 (5680µmol/g). This high amount of acidity appeared to play more favourable role in HDO of guaiacol as discussed in the later paragraphs.

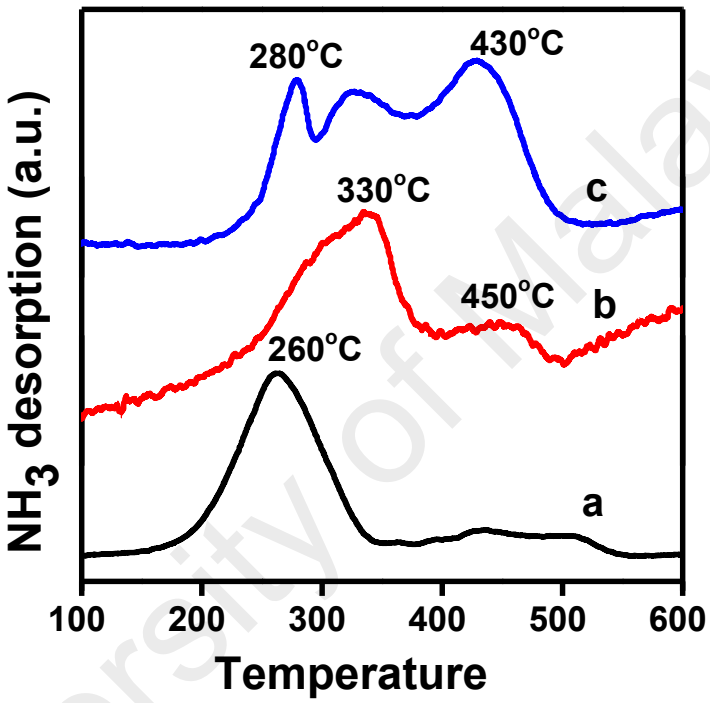

Figure 4.6 : NH_3-TPD profile for CuO-NiO supported on (a) = CeO_2, (b) ZrO_2, and (c) TiO_2.

4.2.1.7 Field emission scanning electron microscopes (FESEM) analysis

The FESEM micrograph (Figure 4.7) displays the surface morphology of Cu-Ni catalysts supported on **(**a**)** CeO_2, (b) ZrO_2, and (c) TiO_2. The FESEM image of sample A indicates a high dispersion of CuO-NiO particles on CeO_2 support. The high dispersion of small spherical particles of CuO-NiO could also influence the formation of small crystallite sizes, confirming the observations made from the XRD studies (Figure 4.4). In contrast, sample B shows agglomerated structure of supported CuO-NiO catalyst on ZrO_2

support, resulting in the formation of larger particles. This type of agglomerated structure is usual for Cu-Ni catalysts as reported elsewhere (Wang and Lua, 2015). As a result, the XRD peaks corresponding to CuO-NiO were found for the ZrO_2 supported catalyst (Figure 4.4). On the other hand, the heterogeneous dispersion of CuO-NiO particles can be observed on the surface of TiO_2 support.

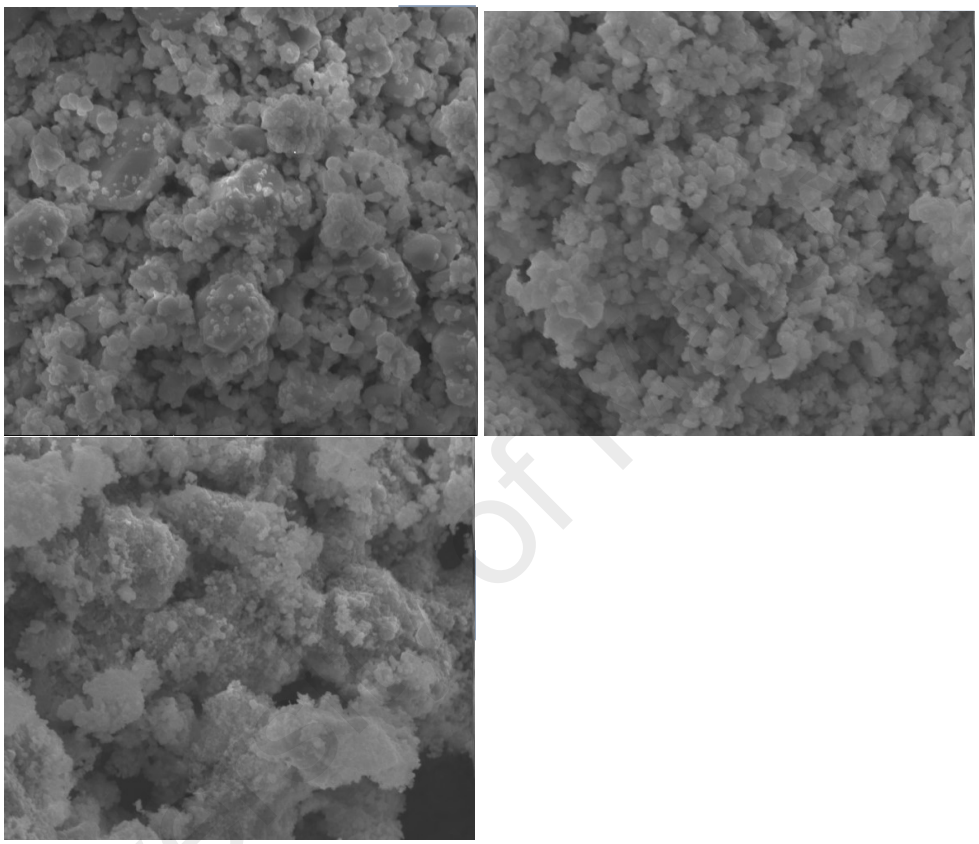

Figure 4.7 : FESEM morphology of CuO-NiO supported on (a) = CeO_2, (b) ZrO_2, and (c) TiO_2.

4.2.1.8 Energy dispersive X-Ray spectroscopy (EDX) analysis

In order to estimate the elemental composition of the catalysts, EDX analysis was conducted as shown in Figure 4.8**.** The composition of Ni and Cu was found to be nearly similar to the prepared ratio (15 and 5 moles (%) for Ni and Cu, respectively) for all the catalysts. The percentage of surface metal compositions for Ni and Cu are found to be ~14.82 and 6.20 mole% (Sample a), 14.85 and 4.33 mole% (Sample b), and 17.65 and

13.76 mole% (Sample c). The CeO_2 and ZrO_2 supported catalysts show slightly lower Ni and Cu composition than the prepared concentration, while TiO_2 supported catalyst has slightly higher Ni and Cu composition.

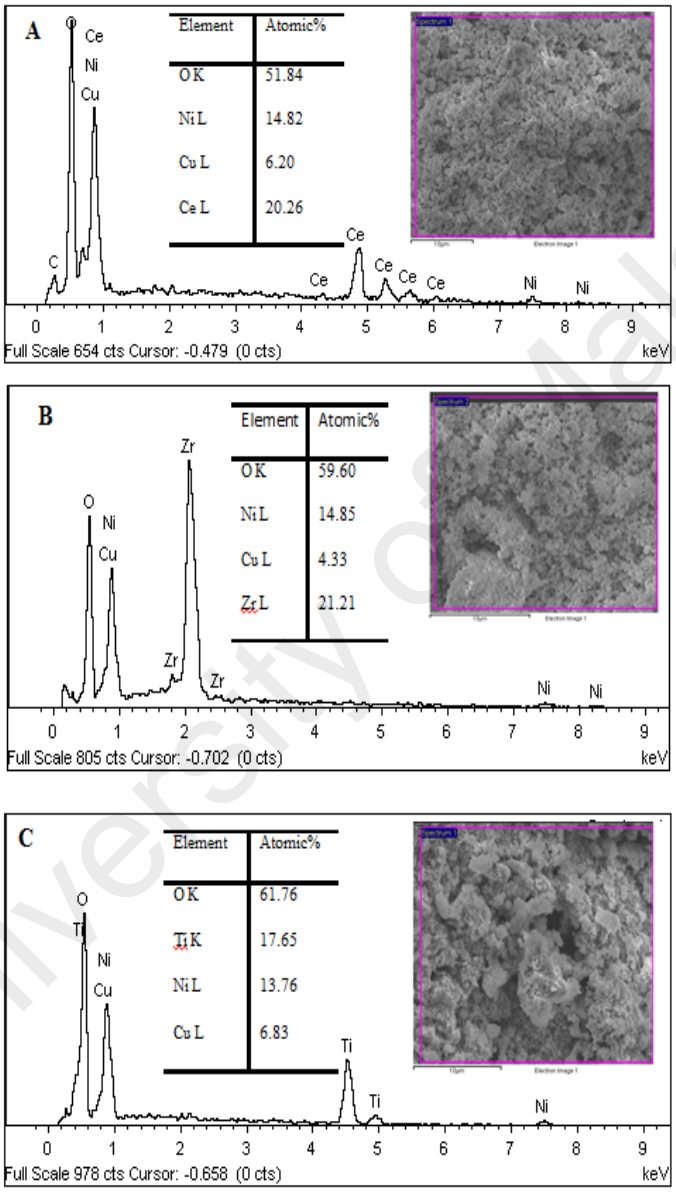

Figure 4.8 : The elemental composition of CuO-NiO supported on (a) = CeO_2, (b) ZrO_2, and (c) TiO_2 from EDX.

4.2.1.9 X-ray photoelectron spectroscopy (XPS) analysis

XPS analysis has been carried out, in order to investigate the chemical and electronic state of nickel and copper in bimetallic catalysts, Figure 4.9, indicates characteristic peaks of nickel species for all the reduced catalysts. According to (Jha et al., 2015) the first and the most intense peak (**$2P_{3/2}$**) at 852.6 eV could be assigned to reduced nickel species (**Ni^0**). The higher intensity of the peak signified reduction of most Ni-O (nickel oxide) to metallic state (Ni^0) during reduction process. Also according to **(Wei et al., 2014)** the other peak (**$2P_{1/2}$**) at higher binding energy (872.2eV) represent reduced nickel species too. The two peaks became separated due to spin-orbital splitting. Figure 4.9b display the presence of reduced metallic copper (**Cu^0**) with two different peaks (**$2P_{3/2}$** and **$2P_{1/2}$**) at 932.7eV and 952.47eV. The assigning of highest intensity peak (Cu $2P_{3/2}$) to Cu^0 are being confirmed by (Wolfbeisser et al., 2015, Wei et al., 2014, Jha et al., 2015, Zhang et al., 2015) and the other peak ($2P_{1/2}$) is in agreement with (Zhang et al., 2015).

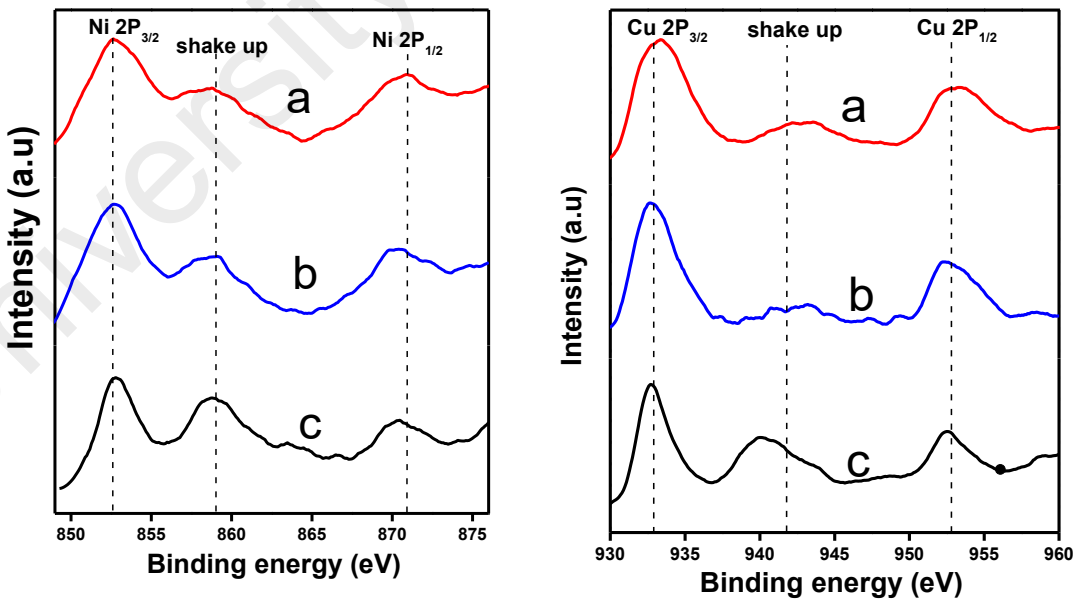

Figure 4.9 : The XPS spectra of (a) Ni $2P_{3/2}$ and $2P_{1/2}$, (b) Cu $2P_{3/2}$ and $2P_{1/2}$ of reduced Ni-Cu supported on (a) = CeO_2, (b) ZrO_2, & (c) TiO_2.

The existence of nickel and copper in metallic state confirms our presumption i.e. formation of Ni-Cu alloy in supported Ni-Cu catalysts, which could enhance the electronic influence toward catalytic active sites (Tao, 2012).

4.2.2 Hydrodeoxygenation activity of metal oxides supported Cu-Ni catalysts

4.2.2.1 DBF Conversions and bicyclohexane selectivity

The hydrodeoxygenation of DBF was investigated over Cu-Ni catalysts supported on CeO_2, ZrO_2, and TiO_2 at temperatures of 250^oC, 5MPa and 4 hours of reaction time (Figure 4.10). The obtained results indicated that the performance of Cu-Ni/TiO_2 catalysts rendered higher with DBF conversion of 46% than Cu-Ni/CeO_2 catalyst with relatively low conversion of 40% and Cu-Ni/ZrO_2 with lowest conversion of 32%, respectively. The low conversion of Cu-Ni/ZrO_2 catalyst could be due to agglomeration of supported bimetallic Cu-Ni catalysts on the ZrO_2 surface as evidenced from FESEM images (Figure 4.7). The agglomerated species could be resulted of limited expose of acidic sites on its surface, leading to loss of activity of certain sites during the HDO reaction. In addition to that, the agglomeration of active supported metal could reduce its surface area and couple with smaller surface area and low acidity of support as shown in Figure 4.5, which could reduce the overall catalytic activity of Cu-Ni/ZrO_2 catalyst. It is obvious that, the high catalytic efficiency of CeO_2 and TiO_2 supported Cu-Ni catalysts could be affiliated to high acidity and surface area of CeO_2 and TiO_2 as well as relatively better dispersion of Cu-Ni species over CeO_2 and TiO_2 surface as evidenced from FESEM images (Figure 4.7).

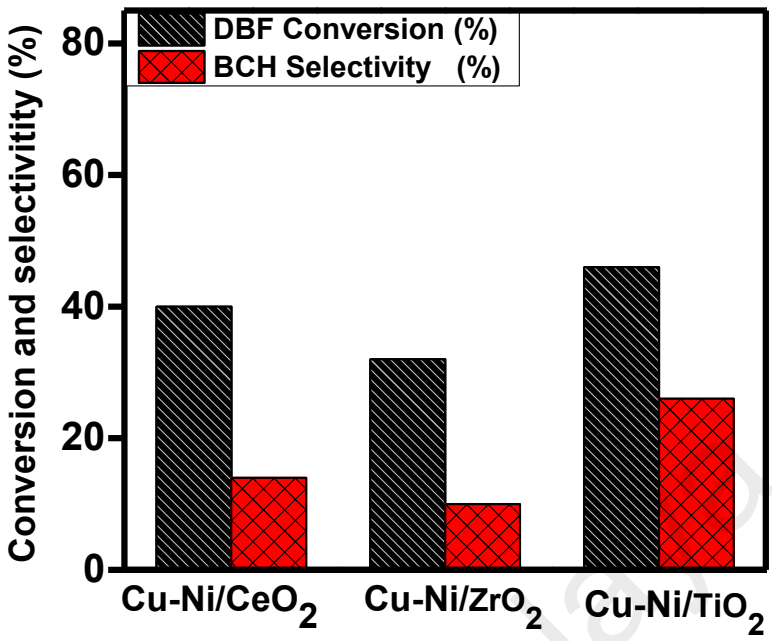

Figure 4.10 : DBF conversion and Bicyclohexane selectivity over Ni-Cu supported on CeO_2, ZrO_2 and TiO_2 at 250°C, 5MPa and 4 hours.

The presented results in Figure 4.10 also show bicyclohexane selectivity over three different supported catalyst. According to this, the selectivity of bicyclohexane also exhibited similar trends as DBF conversion. The observed bicyclohexane selectivity (26%) over Cu-Ni/TiO_2 is larger than Cu-Ni/CeO_2 (14%) and Cu-Ni/ZrO_2 with lowest selectivity of 10%. The high performance of Cu-Ni/TiO_2 in terms of selectivity to bicyclohexane could be influence by high surface area of TiO_2 (Table 4.1). The high surface area of catalyst able to influence better dispersion of supported Cu-Ni catalysts (as shown in FESEM images Figure 4.7) and due to relatively high amount of acids sites, there could be appearance of acids and redox sites in close proximity. Consequently, more hydrogenation of the converted products towards saturated hydrocarbons (bicyclohexane). But, in the case of Cu-Ni/ZrO_2 with lower selectivity of 10% could be due to relatively lower surface area (Table 4.1), the small number of acids sites of ZrO_2 appeared was covered by agglomerated supported metallic species over its surface and in addition to that, the agglomeration of supported metallic species resulted the decrease

number of free metals (active metallic species), hence caused low hydronations of the converted products toward saturated hydrocarbons and bicyclohexane in particular.

4.2.2.2 Guaiacol conversion and cyclohexane selectivity

The catalytic performance of Cu-Ni catalysts supported on CeO_2, ZrO_2 and TiO_2 have been carried out at 250^oC, 5MPa and 4 hours of reaction time. The experimental results from Figure 4.11 indicates the role of different supports on Guaiacol conversion and selectivity to saturated hydrocarbons at mild conditions. Considering Guaiacol conversions over the three supports, Cu-Ni/CeO_2 and Cu-Ni/TiO_2 show high conversion of 35 and 40% as compare to Cu-Ni/ZrO_2 with low conversion of 34%. This means that C-O cleavage take place over CeO_2 and TiO_2 support at faster reaction rates compared to ZrO_2 under this condition. The high performance of these two catalysts could be related to higher concentration of acids sites and surface area than ZrO_2 supported catalysts as indicated by BET and NH_3-TPD results (Table 4.1). The large number of acids sites of catalyst have been known to greatly influence hydrodeoxygenation activity (Lee et al., 2015). The relative high surface area of these species provides relatively better distributions of acidic sites and dispersion of supported metal sites as observe from FESEM results. On the other hand, ZrO_2 support suffered from agglomeration of its supported metals species which prevent accessibility of Guaiacol molecules to the available acids sites of catalyst. In summary, Guaiacol conversions over these catalysts under stated mild conditions increase in the order of Cu-Ni/TiO_2 (40%) > Cu-Ni/CeO_2 (35%) > Cu-Ni/ZrO_2 (34%).

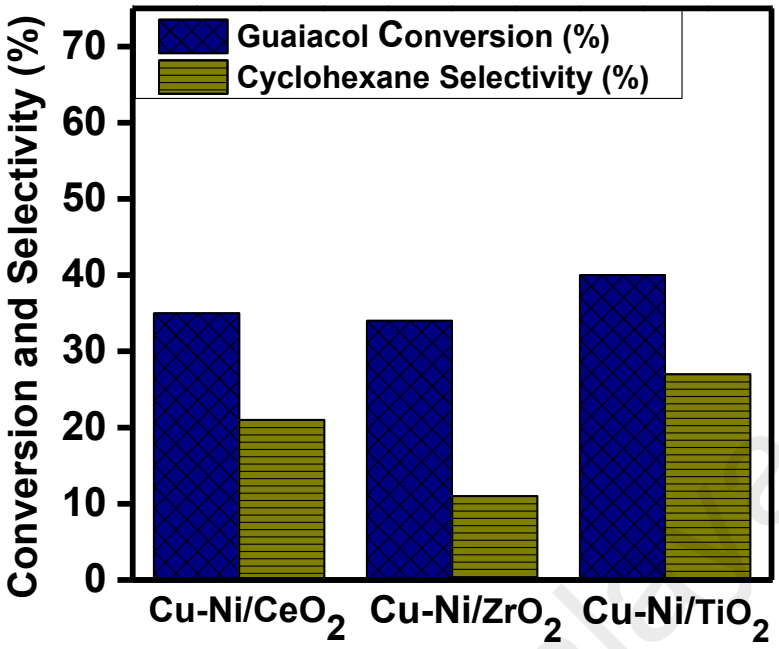

Figure 4.11: Guaiacol conversion and cyclohexane selectivity over Ni-Cu supported on CeO_2, ZrO_2 and TiO_2 at 250°C, 5MPa and 4 hours.

Cu-Ni/TiO_2 exhibit the highest selectivity to cyclohexane of 27% than Cu-Ni/CeO_2 having 21% followed by Cu-Ni/ZrO_2 with low performance of 11 %. In this regard, high surface area of Cu-Ni/TiO_2 play major roles towards deoxygenations and hydrogenations of Guaiacol molecules leading to generation of cyclohexane. It has been known that, redox sites from metallic species as active functional sites responsible for hydrogenation of aromatic and unsaturated structure in hydrodeoxygenation reactions. The relative high surface area of Cu-Ni/TiO_2 and Cu-Ni/CeO_2 enable better dispersion of supported bimetallic Cu-Ni catalysts as evidence from FESEM images (Figure 4.7), which leading to more accessible redox sites for Guaiacol molecules. In addition to that, good dispersion of redox sites could allowed close proximate between acids and redox sites leading to synergetic role and consequently, lead to high catalytic performance in hydrodeoxygenation reactions (Gbadamasi et al., 2016). On the contrary to that, agglomeration of the supported metals over Cu-Ni/ZrO_2 as evidence from FESEM results could be responsible for low selectivity of cyclohexane under this condition.

4.3 Effect of Ni loading on hydrodeoxygenation activity of Cu-Ni/TiO_2 catalysts.

It was observed in the previous section that, Cu-Ni/TiO_2 catalyst displayed high Guaiacol and dibenzofuran (DBF) conversion as well as selectivity to cyclohexane and bicyclohexane (BCH) as compared to Cu-Ni/CeO_2 and Cu-Ni/ZrO_2 catalysts. Despites Cu-Ni/TiO_2 catalyst showed high performance, however some agglomeration of supported metals species was observed due to high Ni loading, which could limit maximum performance under the employed experimental condition. To enhance better performance, optimization study of Ni loading was conducted. In this section, the experimental results for characterizations, and activity test for the various Ni loading (5 to 10%)was further presented and discussed in following section.

4.3.1 Physico-chemical characterizations Cu-xNi/TiO_2 (x = 5, 7.5 and 10%)

4.3.1.1 Raman spectroscopy analysis

Figure 4.12 displayed results for Raman spectroscopic studies for CuO-NiO/TiO_2 with various Ni loading from 5, 7.5 and 10%. As observed in this figure, the TiO_2 (anatase) phase has become obvious with the presence of highly intense peaks at 141 cm^{-1} (Nguyen et al., 2014). This bands stand for most identification band for TiO_2 and the band is highly pronounced due to presence of TiO_2 as a dominant face in CuO-NiO/TiO_2 catalysts. Other Raman bands at 514 and 637 cm^{-1} signified the presence of nickel (II) oxide (Ni-O) and Cu (II) oxide (Cu-O) in CuO-NiO/TiO_2 catalysts. According to this figure, there was no pronounce variation observed among the three different Ni loaded catalysts (from 5 to 10%) during Raman spectroscopic study stages.

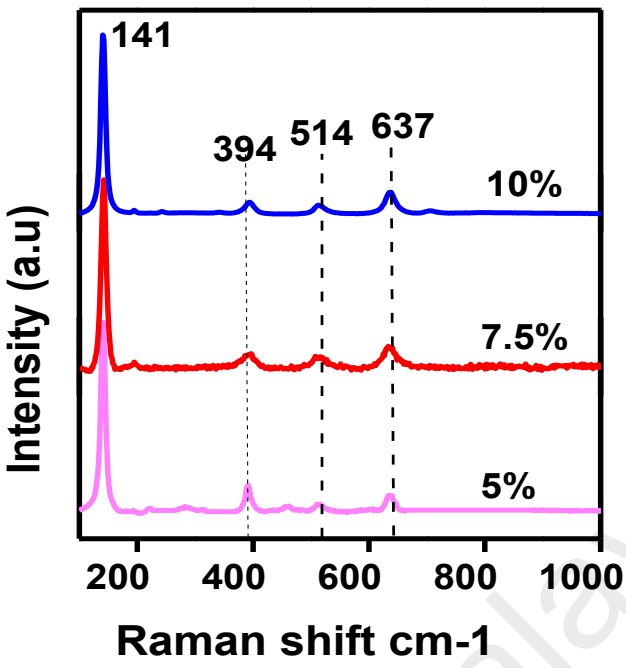

Figure 4.12 : Raman spectra of CuO-NiO supported on TiO_2 with various Ni loading.

4.3.1.2 X-ray diffraction (XRD) analysis

Figure 4.13 showed the powder XRD patterns of CuO-NiO supported on TiO_2 with different Ni loading from 5% to 10%. In order to confirm the presence of Ni metal phase, X'Pert High Score Plus software (version 3.0. 2011 released) with updated library of diffraction data known as powder diffraction file (PDF) from international centre for material's diffraction data was utilized in conjunction with some data from the literature. According to PDF matching, the XRD peaks confirming presence of Ni-O were observed to appeared at 2θ of 37, 48 and 63°. These peaks were confirmed to correspond to reflection planes indexed of (111), (200) and (220) belonging to cubic phase Ni-O (Ambursa et al., 2016b) code: 96-101-0096**).** Other XRD peaks confirmed the existence of Cu-O at 55 and 70° , which were found to correspond to reflection plane of (020) and (113) index, respectively (Ambursa et al., 2017). The presence of crystalline TiO_2 in anatase form were also confirmed by the occurrence of the most intense diffraction peaks at 2θ of 25 ° which was associated with the corresponding plane of (101) (Ref code: 01-

071-1166) (Neale and Frank, 2007, Masui et al., 2003, Li et al., 2014). The confirmation of phases due to Ni-O, Cu-O and TiO_2 in XRD study at all level of Ni loading, has further strengthens our observation during Raman spectroscopic study of these catalysts (Figure 4.12) and that, the confirmed oxides during Raman study were co-exist in crystalline form.

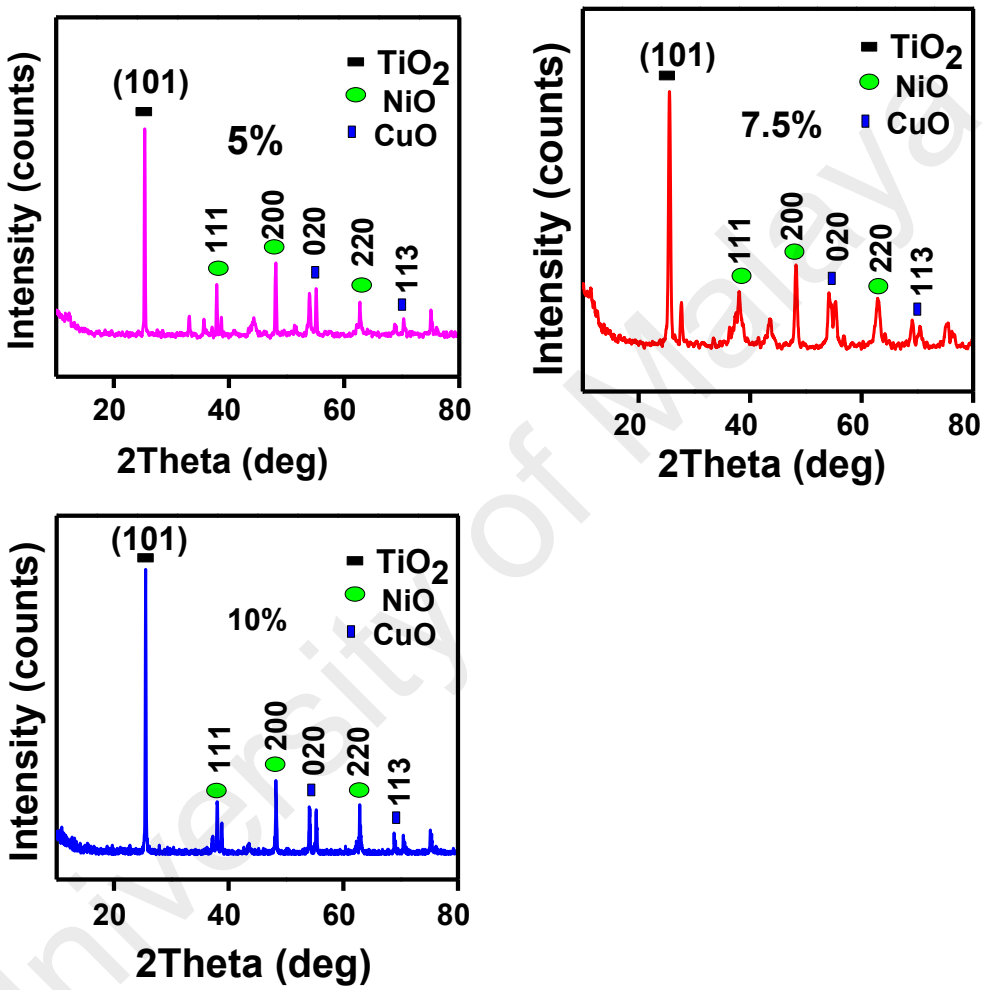

Figure 4.13 : XRD patterns of CuO-NiO supported on TiO_2 with various Ni loading.

4.3.1.3 Field emission scanning electron microscopes (FESEM) analysis

FESEM analysis was used to visualise the surface morphology and dispersion of supported CuO-NiO at different Ni loading from 5, 7.5, and 10% over TiO_2 support. Figure 4.14 (5, 7.5 and 10%) showed that the dispersion of white spherical particles

(supported catalysts; CuO-NiO) over the larger particles (support; TiO_2) appeared to be visible on all various Ni loaded catalysts (5%, 7.5% and 10% of Ni in CuO-NiO/TiO_2). However, the dispersion seems to be better over 5 and 7.5% of Ni loaded catalysts and begin to look agglomerated dispersed over 10% Ni loaded catalysts. This suggest that, as Ni loading increase from 7.5% upward the dispersion is becoming poor over TiO_2. The better dispersion of CuO-NiO over 5 and 7.5%Ni loaded catalysts could enhance the formation of small crystallite sizes which could played favourable role during HDO reaction. On the contrary to that, relatively moderate dispersion of CuO-NiO over 10% Ni loaded catalysts were obtained in which, good dispersion can be observed on its most part. However, due to higher loading of Ni, some agglomeration begins to occur over this catalyst. This type of agglomerated behaviour of Cu-Ni supported catalysts with increase of metal loading was also reported elsewhere (Wang and Lua, 2015).

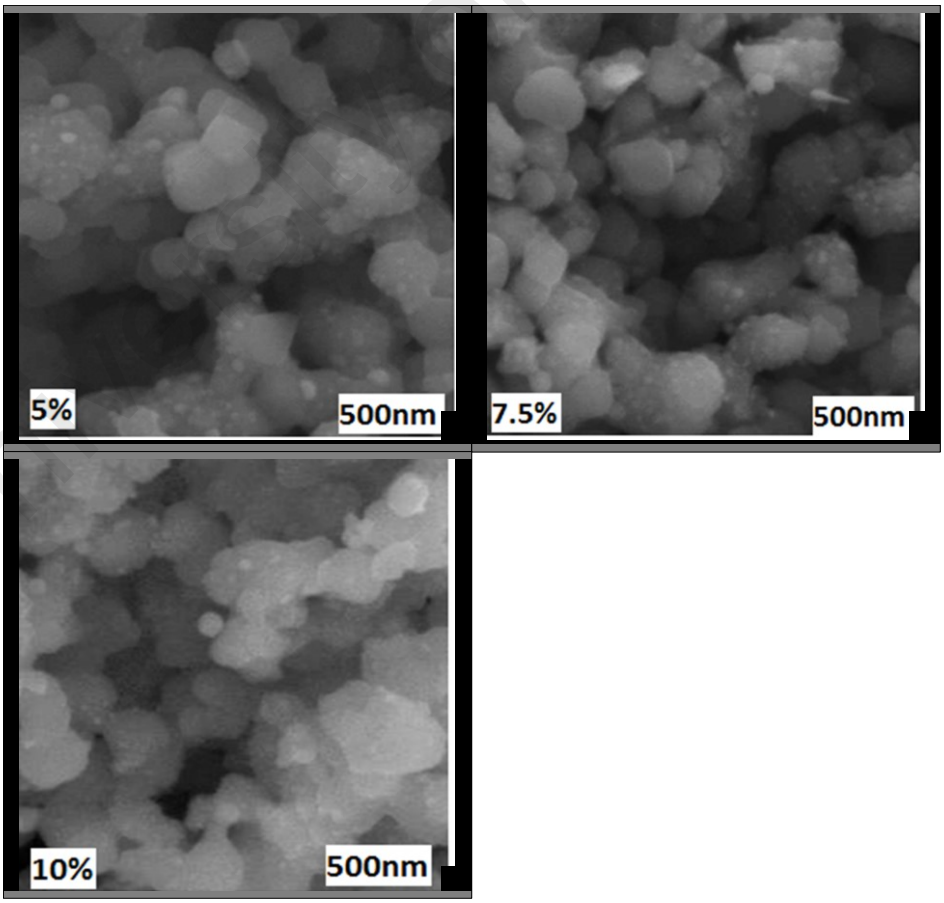

Figure 4.14: FESEM Images CuO-NiO supported on TiO_2 with various Ni loading.

4.3.1.4 Energy dispersive X-Ray spectroscopy (EDX)

The elemental composition of various Ni loaded catalysts (from 5, 7.5 and 10%) was carried out by using Energy Dispersive X-Ray spectroscopic (EDX). The results from Figure 4.15 show the experimental composition of Ni and Cu species over different percentage Ni loaded catalysts and its was nearly equal to the prepared concentration. The percentage of Ni and Cu were observed to be 5.64 and 2.65 wt.% for 5% Ni loading and 2.5% Cu loading which indicates that bimetallic content of the prepared catalysts was slightly above theoretically calculated compositions. However, the experimentally observed Ni and Cu concentration (7.04 and 2.76 wt.%) over 7.5 and 2.5% Ni and Cu loaded catalysts were found to differ with 0.46wt% less for Ni and 0.26wt.% above for Cu from theoretical calculation. But, slight contrary to that, 9.40 and 2.30wt% were obtained over 10 and 2.5wt% Ni and Cu loaded catalysts which show 0.6 and 0.2wt% decrease from theoretical concentration.

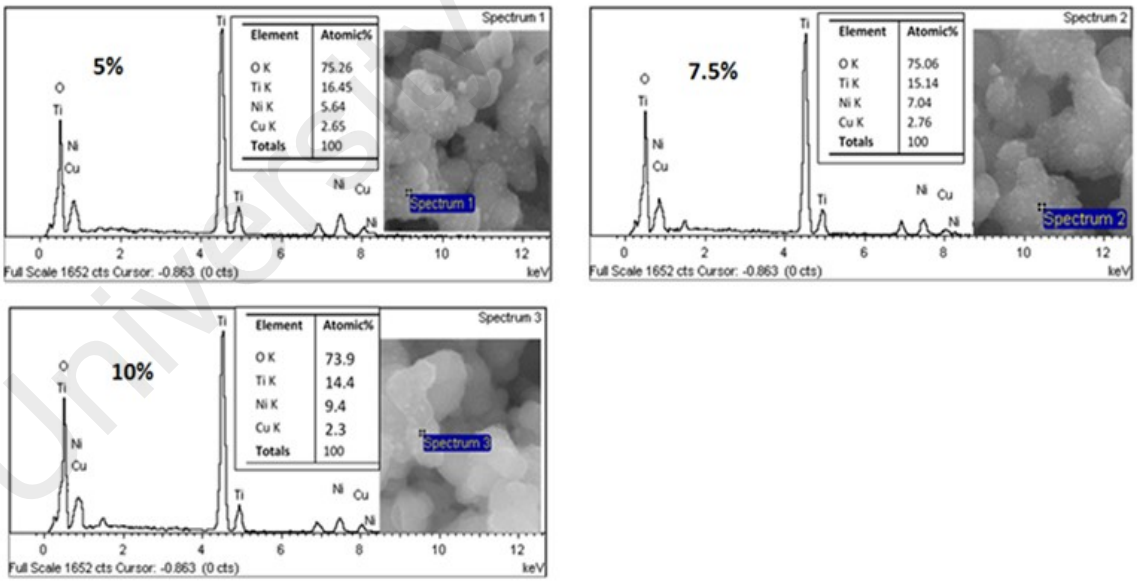

Figure 4.15 : EDX Images of CuO-NiO supported on TiO_2 with various loading.

4.3.1.5 The hydrogen temperature programmed reductions (H_2-TPR)

H_2-TPR analysis was conducted for various percentage (5, 7.5 and 10%) of Ni loaded catalysts. The obtained H_2-TPR profile from Figure 4.16 showed that there are two major

peaks for each prepared catalyst. The first peaks at 251, 251 and 254ºC for 5, 7.5 and 10% Ni loaded catalysts could be assigned to reduction of Cu-O (Cu^{2+}) to Cu (Cu^0) while the second larger peaks at 337, 361 and 364ºC could appeared as overlapping peaks which could be ascribed to reduction of CuO-NiO to Cu-Ni bimetallic alloy as well as un-associated NiO over these catalysts. The absence of reduction peak higher than 400ºC indicated that the NiO species were moderately interacted between NiO and TiO_2 support leading to shifting and overlapping of these peaks with bimetallic CuO-NiO species as similarly observed by (Zhang et al., 2013b). Although it interesting to mention that, the reduction temperature among these catalysts were nearly similar but some slight differences in reduction temperature could be observed as Ni loading increase from 5 to 10%. This suggest that, as Ni loading increases from 5 to 10%, slight degree of interaction between support and supported catalysts increases which is in-line with previously reported (Pérez-Hernández et al., 2015, Reddy Kannapu et al., 2015, Khromova et al., 2014).

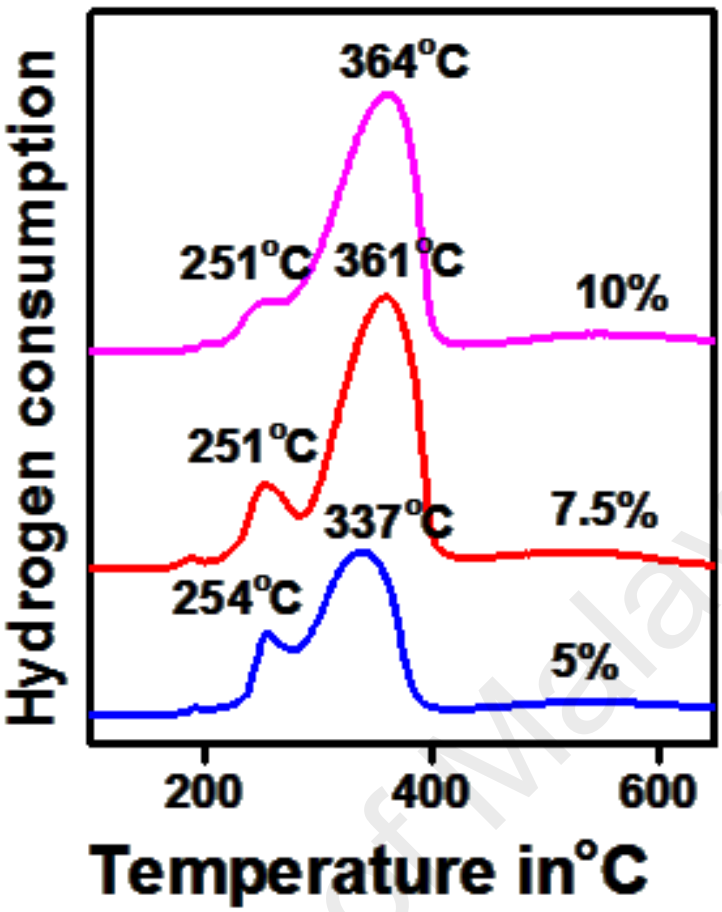

Figure 4.16 : H_2-TPR profile of CuO-NiO supported on TiO_2 with various Ni loading.

4.3.2 Hydrodeoxygenation activity Cu-xNi/TiO_2 (x = 5, 7.5 and 10wt.%)

4.3.2.1 DBF conversion and bicyclohexane selectivity

The result of dibenzofuran conversion and bicyclohexane selectivity over Cu-xNi/TiO_2 (x = 5, 7.5 and 10%) under reaction conditions of 250°C, 5MPa, and 4 hour of reaction time in batch reactor is shown in Figure 4.17. As the trend of Guaiacol conversion, the conversion of dibenzofuran was found to increase with increase of Ni loading from 5 to 10%. The observed conversion of 36%, 42% and 63% were obtained over 5, 7.5 and 10% Ni loaded supported catalysts, respectively. It was also found that, 10% Ni loaded supported catalysts display highest dibenzofuran conversion as compared to 5 and 7.5% Ni loaded catalysts. This is due to the presence of highest Ni content than

the other two supported catalysts. The high Ni loading could provide more number of redox sites that, in conjunction with available acids sites could enhance deoxygenation and hydrogenation potential of this catalysts and consequently more dibenzofuran l conversion during hydrodeoxygenation reaction.

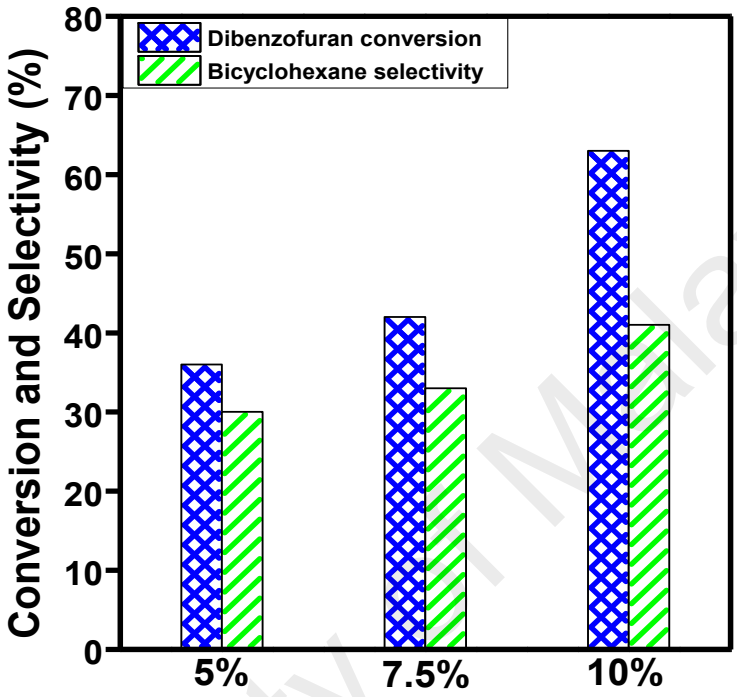

Figure 4.17 : Effect of Ni loading on dibenzofuran conversion and Cyclohexane selectivity at 250°C, 5MPa and 4 hours over Cu-Ni/TiO_2

Figure 4.18 showed the selectivity of bicyclohexane over 5, 7.5 and 10% Ni loaded supported catalysts under the experimental condition of 250°C, 5MPa, and 4 hour of reaction time in batch reactor. The total bicyclohexane selectivity of 30%, 33% and 41% were observed over 5, 7.5 and 10% Ni loaded catalysts. Therefore, 10% Ni loaded catalysts show maximum bicyclohexane selectivity which was similar to its performance for selectivity of cyclohexane as observed during hydrodeoxygenation of Guaiacol reactions. As shown in Hydrodeoxygenation of Guaiacol, it's obvious that 10% Ni loaded catalysts out perfumed all other catalysts and this could be affiliated to high

deoxygenation and hydrogenation potential due to more Ni loading, appreciable dispersion and reducibility of this catalysts and hence, it has been selected for comparative studies with mesoporous based catalysts.

4.3.2.2 Guaiacol conversion and cyclohexane selectivity

Figure 4.18 shows the Guaiacol conversion and cyclohexane selectivity over Cu-xNi/TiO_2 (x = 5, 7.5 and 10wt.%) catalysts that was conducted under reaction conditions of 260^oC, 10MPa, and 6 hours of reaction time by using high pressure batch reactor. It's obvious from the Figure 4.18 that, Guaiacol conversion was improved as the nickel loading increased from 5 to 10%. The observed Guaiacol conversion over 5% Ni loaded catalysts was 45%, which further increased to 53% over 7.5% Ni loaded catalysts. The conversion was improved to 61% over 10% of Ni loaded supported catalysts. Results indicated that 10% Ni loaded supported catalysts display high Guaiacol conversion than 5 and 7.5% Ni loaded supported catalysts. The high performance in this catalyst could be affiliated to high concentration of Ni species in the TiO_2 supported catalyst. Although the dispersion in 5 and 10% Ni loaded supported catalysts are limited, the concentration of Ni species in the partially good dispersed sides out-weight the other two catalysts, which lead to high HDO catalytic activity. Even the 5 and 7.5% supported catalysts show appreciable catalytic performance under this condition and the associated reason to that, could be affiliated to good crystalline structures and reducibility of this catalysts as shown by XRD and TPR results (Figure 4.13 and 4.16).

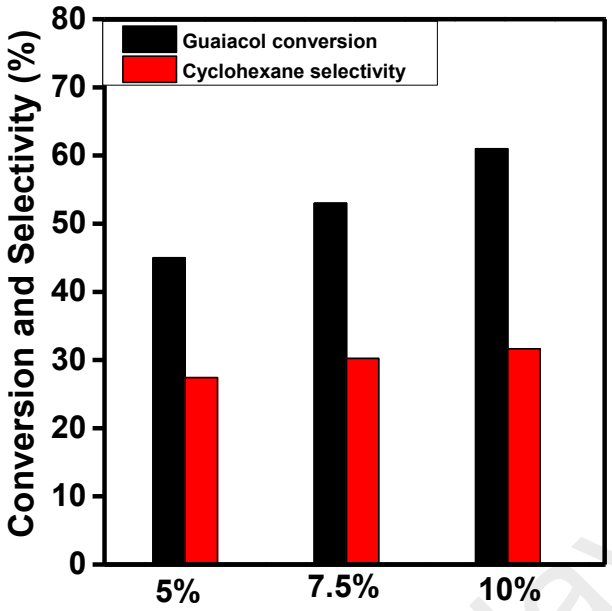

Figure 4.18 : Effect of Ni loading on Guaiacol conversion and Cyclohexane selectivity at 250°C, 5MPa & 4 hours over Cu-Ni/TiO_2

Figure 4.18 display selectivity of cyclohexane over Cu-xNi/TiO_2 (x = 5, 7.5 and 10%) catalysts that was conducted under reaction conditions of 250°C, 5MPa, and 4 hour of reaction time in the same batch reactor. According to the figure, the increase in cyclohexane selectivity as nickel loading increase from 5 to 10% was not significant as in the case of Guaiacol conversion. There was only 3% and 2% selectivity increase from 5 to 7.5% and 7.5 to 10% Ni loading, respectively. The performance selectivity over these catalysts were observed to be 27%, 30% and 32% over 5%, 7.5% and 10% Ni loaded supported catalysts. All the three supported catalysts show good selectivity to cyclohexane under this condition. It performance could be related to good dispersion and reducibility of Cu-Ni bimetallic species of these supported catalysts. Their associated active metal dispersion could lead to better contact of Guaiacol and its intermediate molecules with redox sites on the surface of these catalysts, resulted to high hydrogenation potential of the catalysts. Although, all the three catalysts showed good selectivity performance however, 10% supported catalysts showed better catalytic

activity than the other two and could be affiliated to its more Ni loading and hence considered as the optimum catalysts for comparative studies with mesoporous-based catalysts.

4.4 Titanium containing mesoporous MCM-41 (Ti-MCM-41) and mesoporous MCM-41 as hydrodeoxygenation supports.

4.4.1 Introductions

In the previous section, the optimum Ni loaded Cu-Ni/TiO_2 showed moderate conversion with low selectivity to saturated hydrocarbon. However, the catalyst supports playing an important role to enhance the conversion and product selectivity in hydrodeoxygenation reaction. It appears that, more conversion and hydrocarbon selectivity was limited by low surface area and lack of porosity of TiO_2 supports. It has been reported that, the support with high surface area and acidity enhance the conversions in hydrodeoxygenation reaction (Selvaraj et al., 2014). In addition, confinement or porosity of support influence selectivity to hydrocarbons molecule during hydrodeoxygenation reactions (Dongil et al., 2016b). Therefore, hydrodeoxygenation support with high surface area, acidity and porosity could be the key factors better hydrodeoxygenation reactions toward hydrocarbons enhanced molecules. Mesoporous silica such as MCM-41 have been reported to possess high surface area and porosity (Meléndez-Ortiz et al., 2013). It has been reported that, incorporation of transition metal within the matrix of mesoporous silica, enhance it stability and acidity (Selvaraj et al., 2014). To improve hydrodeoxygenation performance of Cu-Ni catalyst, the supports was modified by incorporating Ti species in the matrix of mesoporous silica (Ti-MCM-41). In this section, the characterization results of the synthesized regular mesoporous MCM-41 and Ti-MCM-41 were presented and discussed herein.

4.4.2 Physico-chemical characterization of MCM-41 and Ti-MCM-41

4.4.2.1 Low angle XRD analysis

The low angle XRD patterns of MCM-41 and Ti-MCM-41 supports are shown in Figure 4.19. It was found that both MCM-41 and Ti-MCM-41 supports show an intense and sharp diffraction peak appearing at (100) reflection plane. This peak typically represents reflection of ordered hexagonal mesoporous structures (major characteristic peak of MCM-41). It can be noted that this characteristic peak was shifted from 2.3° in MCM-41 to 2.6° for Ti-MCM-41, which revealing the occurrence of structural changes due to the incorporation of Ti species into the MCM-41 support. Two broad diffraction peaks can be noticed at 4 and 4.8° in MCM-41, which can be assigned to a long-range array of hexagonal cylindrical mesopores (Lin et al., 2008). However, these peaks were absent in Ti-MCM-41 support, which signifies relatively short range ordered mesopores in Ti-MCM-41 as compared to regular MCM-41. This may due to the heavy nature of larger titanium species with large atomic radius of Ti^{4+} = 0.72 Å (Sun et al., 2002) compared to the small silica species with small atomic radius of Si^{4+} = 0.41 Å (Park et al., 1999). As shown in Table 4.2, the MCM-41 slightly differ from Ti-MCM-41 in terms of wall thickness and cell parameter. In the regular MCM-41 the wall thickness and cell parameters values are observed to be 40.56 and 14.16 A° but, with incorporation of titanium species in Ti-MCM-41 and these values decreased to 36.50 and 9.5 A° which means that, the wall thickness shrink as Titanium atom substituted silicon atoms which also account for additional evidence to incorporation of titanium species within the silica matrix.

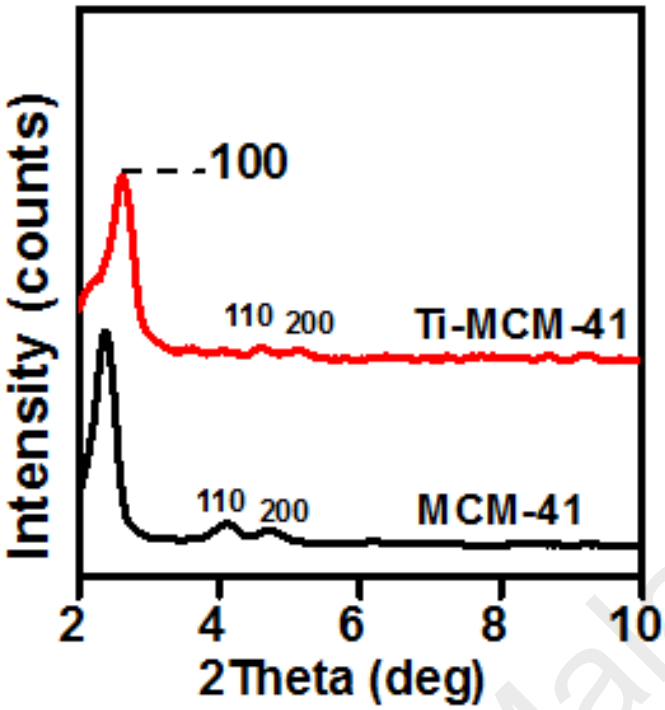

Figure 4.19 : Small angle XRD of MCM-41 and Ti-MCM-41.

Table 4.2 : Structural properties of MCM-41 and Ti-MCM-41

Supports	XRD Peaks (2θ)			d_{100}	a^o (A^o)	Ws (A^o)
	100	110	200			
MCM-41	2.30	4.18	5.14	35.13	40.56	14.16
Ti-MCM-41	2.67	4.64	5.85	31.61	36.50	9.5

d_{100} = d_{100} spacing; a^o = Cell Parameters, Ws = Wall thickness

4.4.2.2 FT-IR spectroscopy analysis

The FT-IR results of the MCM-41 and Ti-MCM-41 supports are presented in Figure 4.20. Both MCM-41 and Ti-MCM-41 samples show a major band at ~1090 and 1085 cm^{-1}, respectively. These peaks represent internal asymmetric stretching vibration and serve as identification peak for mesoporous MCM-41 (Popova et al., 2008, Anunziata et al., 2008a). The Ti-MCM-41 support shows the presence of Ti-O-Si at the band of 960 cm^{-1}, thus indicating that titanium exists in tetrahedral coordination within the mesoporous

structure of the MCM-41 (Popova et al., 2008, Anunziata et al., 2008a). The band noticed at ~464 and 460cm^{-1} for MCM-41 and Ti-MCM-41 samples were attributed to the bending vibration of the Si-O-Si linkage (Wang et al., 2014b). The observed peak at ~1638cm^{-1} can be ascribed to the presence of Si-OH group, which is main characteristic of MCM-41 (Izadi et al., 2014). It has been reported that the incorporation of titanium into the MCM-41 support results in the generation of both Lewis and Bronsted sites (Song et al., 2014). The Bronsted acidity was attributed to the partial coordination of the -OH group towards the Lewis centre (in titanium). Therefore, the presence of Si-OH groups is essential for achieving abundant acidic sites. The values correspond to observed atomic linkages of MCM-41 and Ti-MCM-41 are given in Table 4.3.

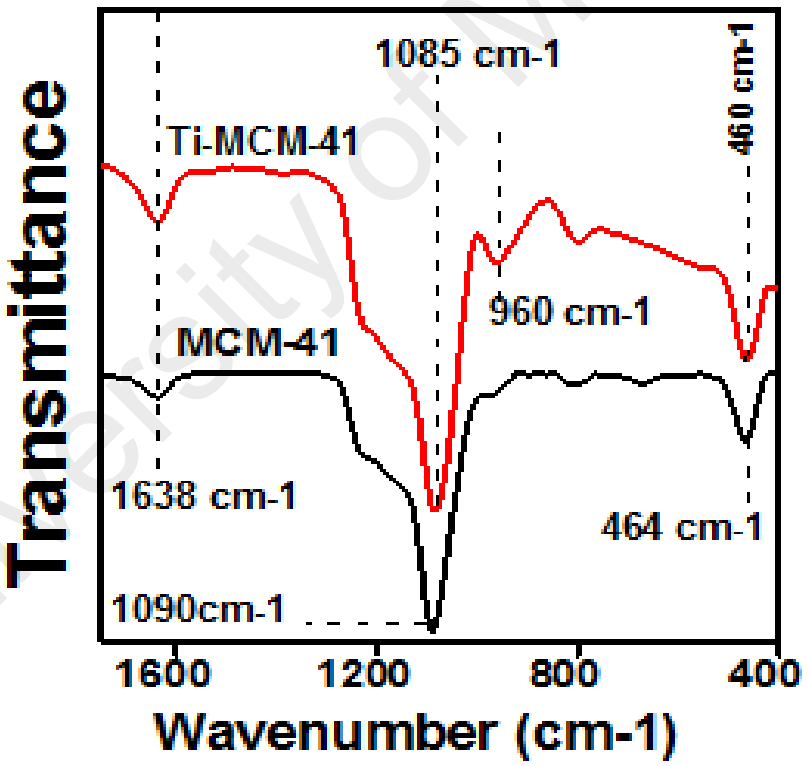

Figure 4.20 : FTIR spectra of MCM-41 and Ti-MCM-41.

Table 4.3: FTIR and UV visible spectroscopic data for MCM-41 and Ti-MCM-41

Supports	Si-O-Si Asymmetric stretching modes (CM^{-1})	Si-O-Ti Asymmetric stretching modes (CM^{-1})	Si-O-Si Bending vibrations (CM^{-1})	L-MCT absorptions (nm)
MCM-41	1090	ND	464	Negligible
Ti-MCM-41	1085	960	440	228

4.4.2.3 DR UV-visible spectroscopy analysis

The coordination environment of the incorporated titanium species was investigated by DRS UV-visible spectroscopy. Table 4.3 and Figure 4.21 presents UV-visible absorption spectra of Ti-MCM-41 and MCM-41. There was negligible absorption for MCM-41, indicating the absence of metal to ligand charge transfer within the hexagonal mesostructured. However, in the case of Ti-MCM-41, a highly intense peak was observed at around 227 nm. This band clearly describes a charge transfer from a 2p orbital in tetrahedrally linked oxygen (O^{2-}) to a 3d orbital in a tetrahedrally linked titanium species, which is the characteristic absorption for identification of tetrahedral coordination environment for Ti^{+4} (Lin et al., 2008). The red shift of the absorption wavelength towards the low energy region of the UV spectrum further confirmed that Ti species exist as flexible isolated sites rather than the rigid framework sites found in the meso-structured of MCM-41.

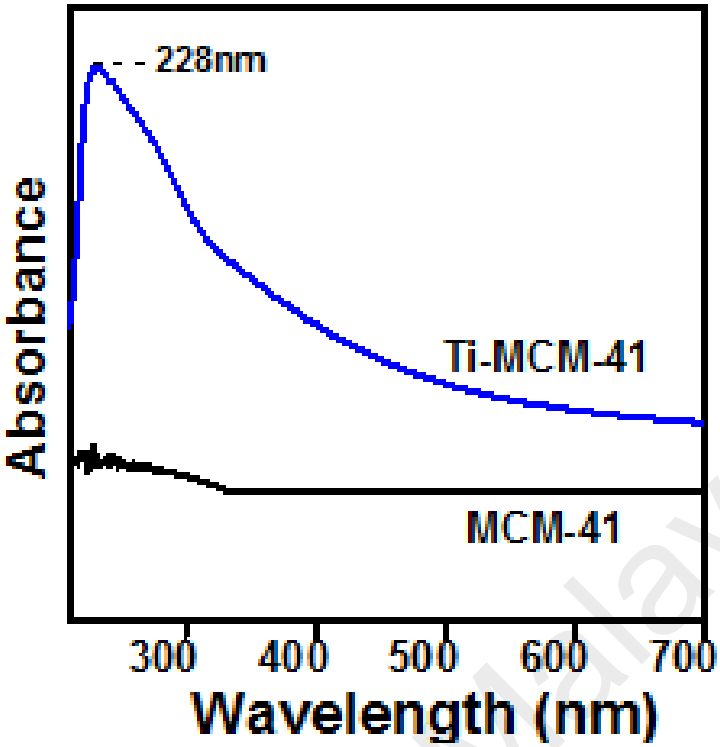

Figure 4.21 : UV. Visible spectra of MCM-41 and Ti-MCM-41.

4.4.2.4 BET surface area and porosity analysis

The N_2 adsorption-desorption isotherms and the pore size distribution profiles of MCM-41 and Ti-MCM-41 supports are shown in Figures 4.22 and 4.23. The obtained textural properties are depicted in Table 4.4. As shown in Figure 4.22, both supports show type IV adsorption isotherm with H_3 loop, indicating the mesoporous nature of the materials (Kim et al., 2015). The presence of pronounced and strong adsorption between 0.25-0.38 and 0.22-0.35 relative pressure for MCM-41 and Ti-MCM-41, respectively, is due to pore filling by capillary condensation (Appaturi et al., 2012). This indicates the presence of hexagonal cylindrical channels (major features of MCM-41) **(**Kim et al., 2015). Both MCM-41 and Ti-MCM-41 supports show a narrow pore size distribution. The results presented in Figure 4.23 and Table 4.4 show an average pore size of 2.64 nm with corresponding pore volume of 0.89 cm^3g^{-1} for MCM-41 and a greater pore size

distribution of 2.73 nm. However lower pore volume of 0.68 cm^3g^{-1} for Ti-MCM-41. The observed difference in pore diameter was due to the incorporation of titanium into the hexagonal structures of mesoporous silica. This incorporation could widen the mesopores in Ti-MCM-41 due to the larger ionic radius of Ti than Si and thus, greater bond length of Ti-O linkage than Si-O linkage. The surface area of MCM-41 was greater (~983 m^2g^{-1}) than Ti-MCM-41 (~724.91 m^2g^{-1}), which is due to the collapse of some structural parts of silicate material in MCM-41 upon incorporation with denser Ti species.

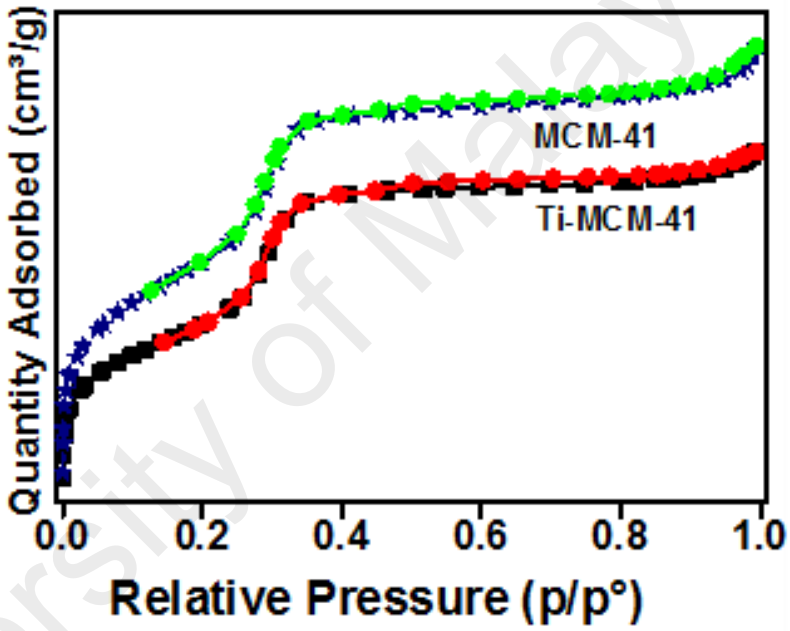

Figure 4.22 : N_2 adsorption isotherms for MCM-41 and Ti-MCM-41

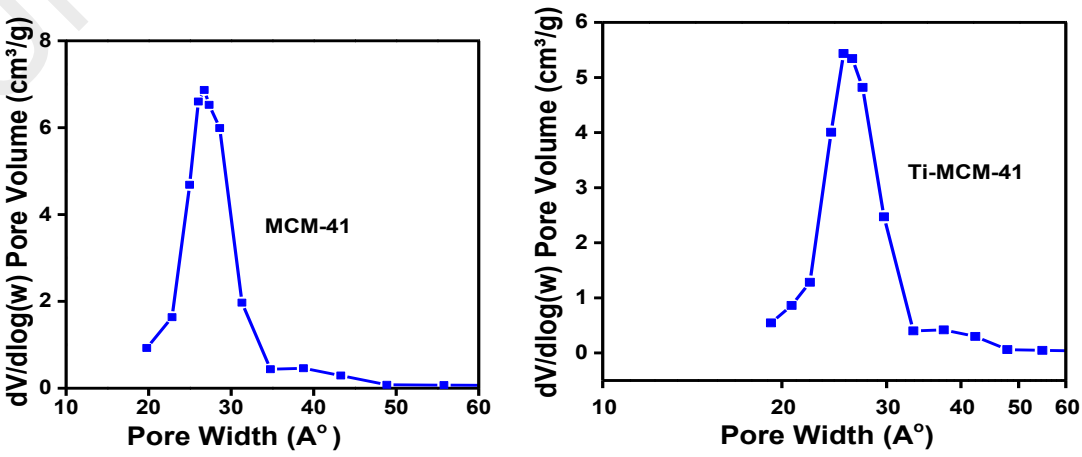

Figure 4.23 : Pore size for MCM-41 and Ti-MCM-41

Table 4.4 : **Textural and acidic properties of MCM-41 and Ti-MCM-41**

Supports	BET Surface area ($m^2 g^{-1}$)	Pore volume ($cm^3 g^{-1}$)	Pore size (nm)	NH_3-TPD Peaks (^oC)			Acids Conc. (µmol/g)
				Weak	Medium	Strong	
MCM-41	983.06	0.89	2.64	223	301	ND	119.00
Ti-MCM-41	724.91	0.68	2.73	ND	350	515	1928.76

ND: - Non-detected

4.4.2.5 Ammonia-temperature programmed desorption (NH_3-TPD) analysis

In order to elucidate the acidic strength of the supports, ammonia-temperature programmed desorption (NH_3-TPD) was performed (Mallesham et al., 2013, Sudarsanam et al., 2014). The results presented in Figure 4.24 show that, pure MCM-41 displays small peaks at around 223 and 301ºC compared to Ti-MCM-41. These peaks indicate the presence of weak acidic sites, originating from silicon centre (Gianotti et al., 2002b)**.** On the other hand, Ti-MCM-41 support exhibits broad peaks at around 350ºC indicating the presence of weak acidic sites on the hydroxyl group linked to the silanol group that is directly associated with the tetrahedral titanium centre via an oxygen bridge (Gianotti et al., 2002a). The high intensity peak observed at 515ºC indicates desorption of NH_3 molecules from tetrahedral titanium IV centre, which indicates the formation of strong acid sites originated from tetrahedrally coordinated titanium (IV) centre within the mesostructured MCM-41 framework. The data for amount of desorbed NH_3 indicates that, Ti-MCM-41 support (1928.76 µmol/g) has high concentration of acidic sites compared to pure MCM-41 support (119.00 µmol/g), revealing the favourable role of incorporated Ti species in improving the acidic properties of MCM-41 support toward deoxygenation potential (Table 4.4).

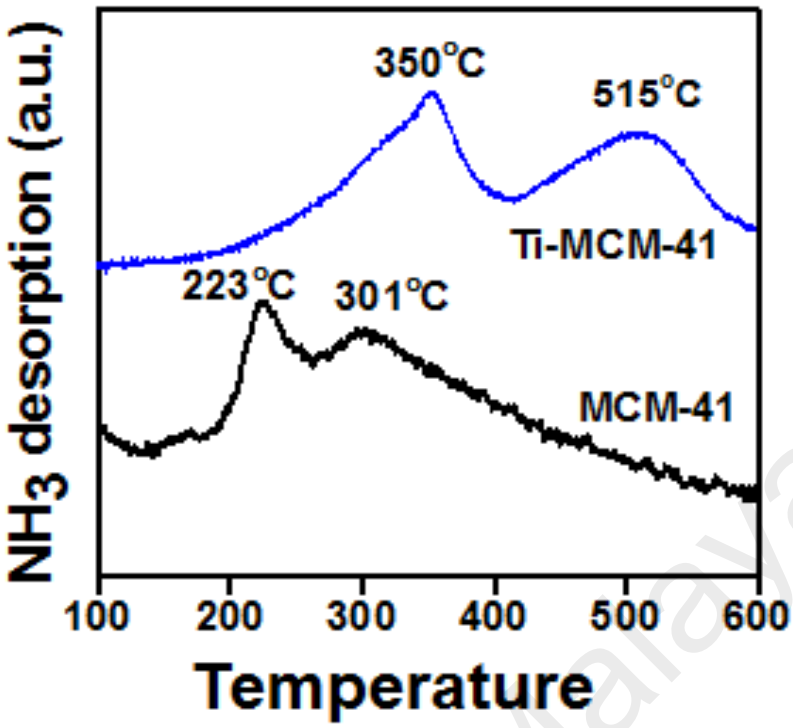

Figure 4.24 : NH_3-TPD profile of MCM-41 and Ti-MCM-41

4.4.2.6 Field emission scanning electron microscopes (FESEM) analysis

The FESEM Microgram of the two supports samples have been displayed in Figure 4.25. Both images show clearly short and long cylindrical tube likes particles. A rough like coated surface as a consequence of gold coating due to charging effect.

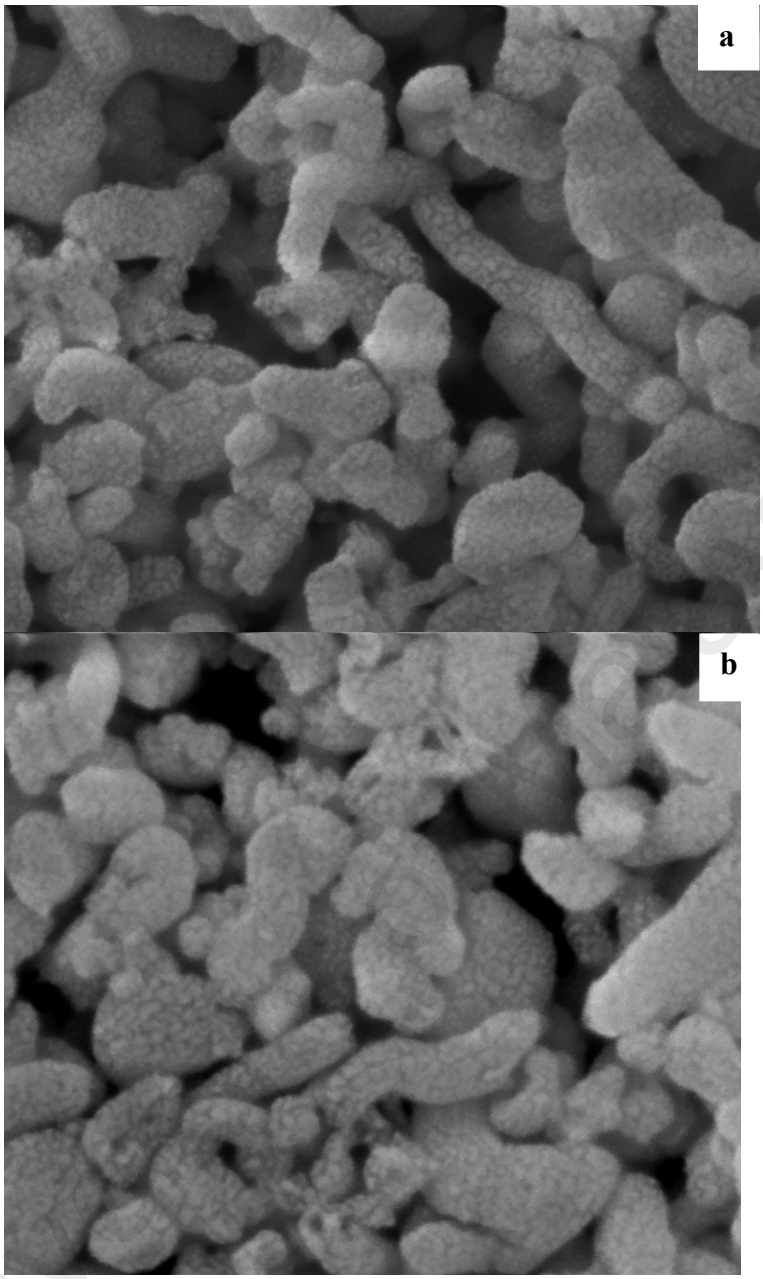

Figure 4.25 : FESEM images of a = MCM-41 and b = Ti-MCM-41 samples

4.5 Influence of Ni loading on hydrodeoxygenation activity of Cu-Ni/(15%)Ti-MCM-41.

4.5.1 Introduction

In the context of bifunctional requirement of catalyst in hydrodeoxygenation reactions in which acids and redox sites are required, the role of support is highly tremendous and

our previous studies showed that, support could positively influence the performance of supported catalysts. Pertaining to that, when new support is applied, certain catalytic properties of the supported catalysts such as dispersion of the active components, metal support interactions and reducibility of supported metallic species will be different. Therefore, it is important to study the optimal loading of supported catalysts required for high performance of the modified supported catalysts. In-line with this, support modification was investigated from bulk TiO_2 to mesoporous Ti-MCM-41 for Cu-Ni catalysts and Ni loading was further optimised for high performance of Cu-Ni/Ti-MCM-41 catalysts. This was conducted, by fixed the weight percent (wt.%) of Cu metal (2.5wt.%) and varies Ni loading from 5 to 12.5wt.% were supported on with Ti-MCM-41 (15wt.%% Titanium content), the physico-chemical properties of catalyst was studied. Prior to catalysts testing, experimental parameters such as temperature, pressure and reaction time were investigated for Guaiacol and DBF conversion. Then, the catalytic activity was further performed at the optimum reaction conditions. In this section, the results for physico-chemical characterization, optimization of reaction parameters and catalytic activity of the synthesized supported catalysts are presented and discussed.

4.5.2 Physico-chemical properties of the prepared catalysts

4.5.2.1 Temperature programmed oxidation (TPO) analysis

In order to determine the sample oxidation condition, the as-prepared catalysts precursors were subjected to TPO analysis. The plotted results shown in Figure 4.26 indicate that, above 500°C, the entire catalysts precursors could be converted to metal oxides in oxygen environments. According to this result, nitrate ligand from Cu and Ni nitrates has been illuminated by two steps decomposition patterns as indicated by manifestation of the two intense peaks for each loaded catalyst precursor. The first peak at moderate temperature below 300ºC could be related to oxidation of weakly interacted

nitrate or well exposed on the surface. While the other ones at higher temperatures could be attributed to bulk nitrate oxidations. The plotted peaks for these catalysts precursors also revealed that, the required calcination temperatures increase with increasing nickel loading from 5 to 12.5 wt.% which could be affiliated to overall increase of interaction between supports and catalysts precursors as metal loading increases (Wu et al., 2011). Due to strong interactions, there would be higher energy demands to detached and decompose nickel and copper nitrates to metal oxides over Ti-MCM-41 supports. The oxygen consumption from Table 4.5 show maximum oxygen uptake of 505 µmol/g by catalysts precursor with 10wt.% Ni loading.

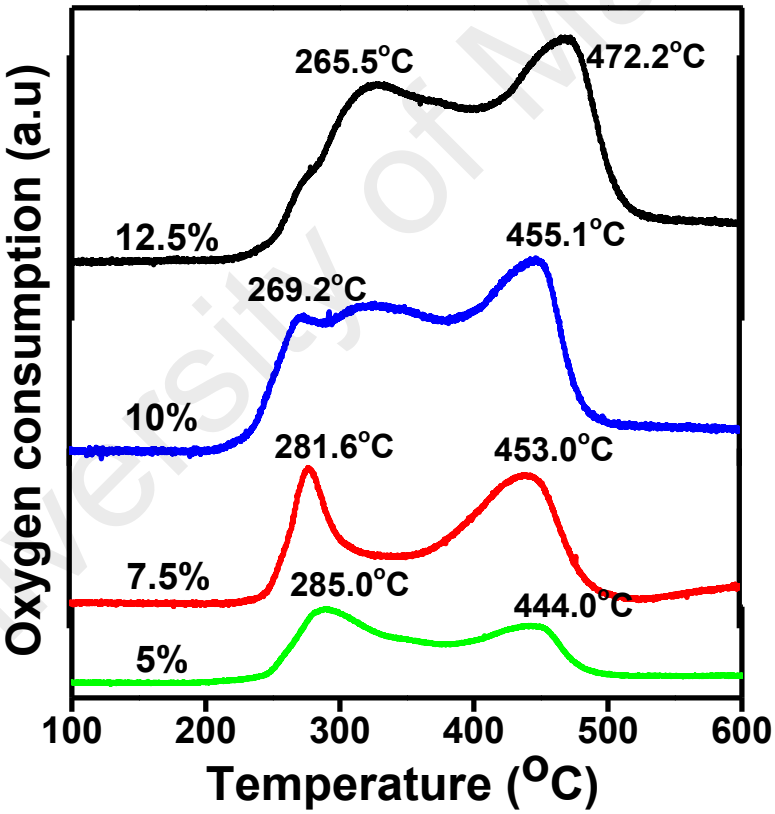

Figure 4.26 : TPO of Cu and Ni precursors with various loading supported on Ti-MCM-41

Table 4.5: **Oxygen consumption data for Cu and Ni nitrate supported on Ti-MCM-41 (15%) with Cu loading of 2.5%.**

Supported catalysts precursors	TPO Peaks (°C)		Oxygen consumptions (µmol/g)
	First (F)	Second (S)	
5 %Ni	285	444	115.45
7.5 %Ni	281.6	453	221.71
10 %Ni	269	466	505.10
12.5 %Ni	265	472	299.67

4.5.2.2 Raman spectroscopy analysis

Figure 4.27. shows the Raman spectra of CuO-NiO/Ti-MCM-41 with 5, 7.5, 10, and 12.5wt.% Ni loading. All recorded Raman spectra show two bands at around 615 cm^{-1} and 1080 cm^{-1}. The first peak centred at 615 cm^{-1} is assigned to vibrational mode of Cu-O. However, the band corresponding to Cu-O could not be clearly seen as separate peak due to overlapping with the broad asymmetric and symmetric stretching vibration of the Si–O–Si bond signals which should be observed between 499 cm^{-1} to 982 cm^{-1}. In addition, the peak attributed to Ni-O asymmetric stretching mode around 1080 cm^{-1} showed very weak Raman band. This could be related to the interactions between Ni-O species and Ti-MCM-41 support. The greater intensity of the 1080 cm^{-1} band in 12.5 wt.% Ni loaded catalyst disclose the presence of higher concentration of Ni-O species.

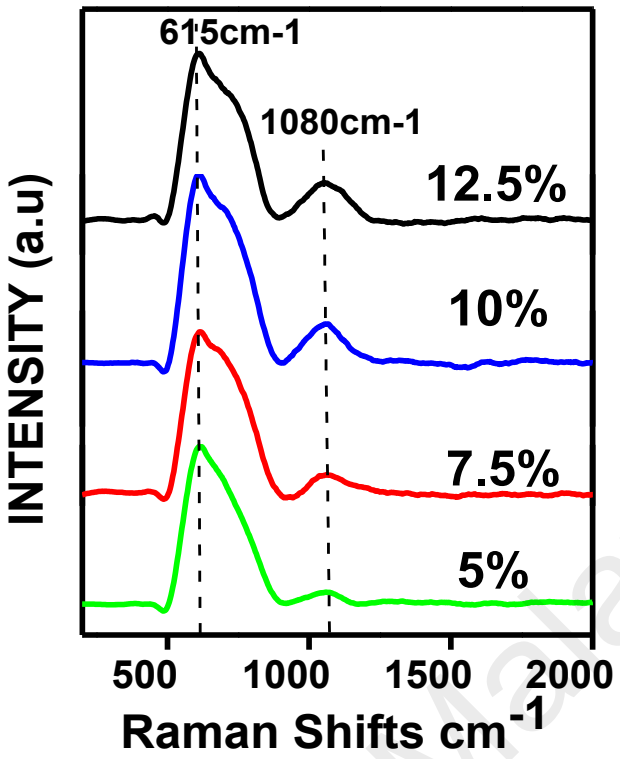

Figure 4.27: Raman of Cu-O and Ni-O supported on Ti-MCM-41with various Ni

4.5.2.3 X-Ray diffraction analysis (XRD)

The wide angle XRD patterns of CuO-NiO/Ti-MCM-41 with different Ni loadings are shown in Figure 4.28. All the three catalysts have a broad peak at around 23° which is assigned to the amorphous silica in Ti-MCM-41 support. The intensities of the amorphous peaks debased in 10wt.% Ni loading catalyst, which was caused by the increased amount of NiO species. The 5, 7.5, 10 and 12.5 wt.% Ni loaded catalysts demonstrated intense diffraction peak centred at 2θ values of 38°, 43° and 63° corresponding to (111), (200) and (220) reflections, respectively (Lensveld et al., 2001). Obviously, the intensity of the diffraction peak increased with the increase of Ni loading from 5 to 10 %, while slight decrease was observed for 12.5 % Ni loaded catalyst. This could be related to poor dispersion of metal species as there would be more agglomeration of these metals over the catalyst support surface. Therefore, the number of free Ni-O species available for

reflecting penetrated radiation have been reduced to minimum. The XRD spectra of 5 to 10 %, loaded Ni catalyst exhibited two weak diffraction peaks at 2θ values around 36° and 39° attributed to the CuO crystallites phase(Ambursa et al., 2016b), . However, with increasing Ni content to 12.5wt.%, the intensity of diffraction peak belonging to CuO was diminished. This observation is consistent with the H_2-TPR results (Figure 4.29). The structures of the catalysts were also presented in Table 4.6. It is evidence from that increased of Ni loading resulted the increased of crystallite size which is further support the fact of agglomeration of active species at high metal loading.

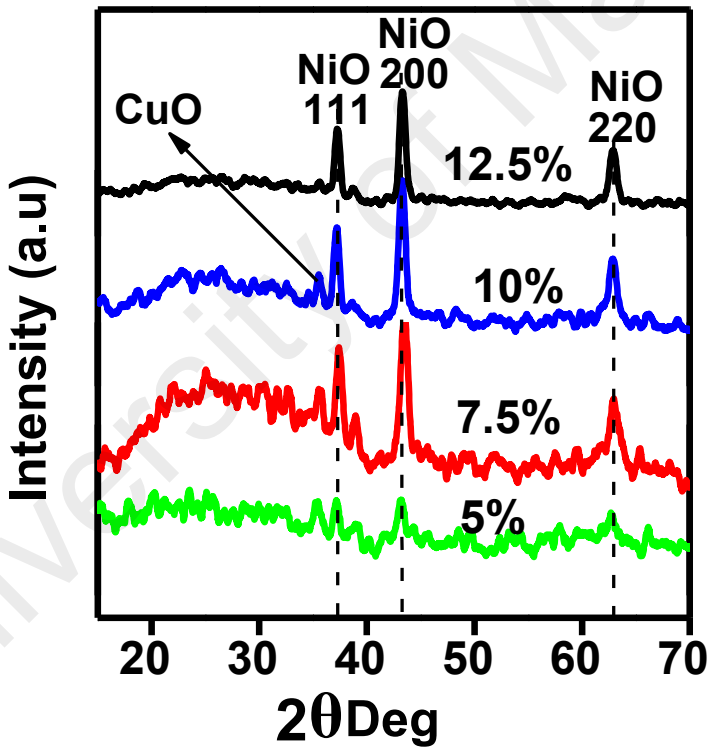

Figure 4.28 : XRD of CuO-NiO supported on Ti-MCM-41 with various Ni loading

Table 4.6: S**tructural properties of CuO-NiO/(15%)Ti-MCM-41 from XRD.**

CuO-NiO/Ti-MCM-41	CuO		NiO					
	111		111		200		220	
	2θ	C. size	2θ	C. size	2θ	C. size	2θ	C. size
5%Ni	35.42	8.42	37.44	17.8	43.45	13.6	62.98	9.9
7.5%Ni	35.16	9.11	37.19	26.61	43.40	18.1	62.88	10.6
10%Ni	35.32	9.55	37.26	28.72	43.30	25.1	62.92	14.2
12.5%Ni	ND	ND	37.34	32.45	43.41	27.2	62.98	14.8

C. size = crystallite size

4.5.2.4 Field Emission Scanning Electron Microscopy (FESEM) analysis

Figure 4.29 shows the FESEM images of CuO-NiO/Ti-MCM-41 catalysts. There are scattered and well homogenously dispersed of small white spots over 5 and 7.5% Ni loaded CuO-NiO/Ti-MCM-41 samples which confirm good dispersion of nickel oxide species at these Ni loading over Ti-MCM-41 supports. This better metal dispersion could be associated to low and moderate metal loading. As the Ni loading increases to 10 and 12.5%, the white spots become more densely populated and even some of the particles are agglomerated on the surface of the support leading to poor dispersion of nickel oxides species over the supports. On the other hand, the CuO species could not be observed which is due to small particle size of Cu and good metal dispersion with smaller Cu loading as compared to Ni concentration in the catalysts.

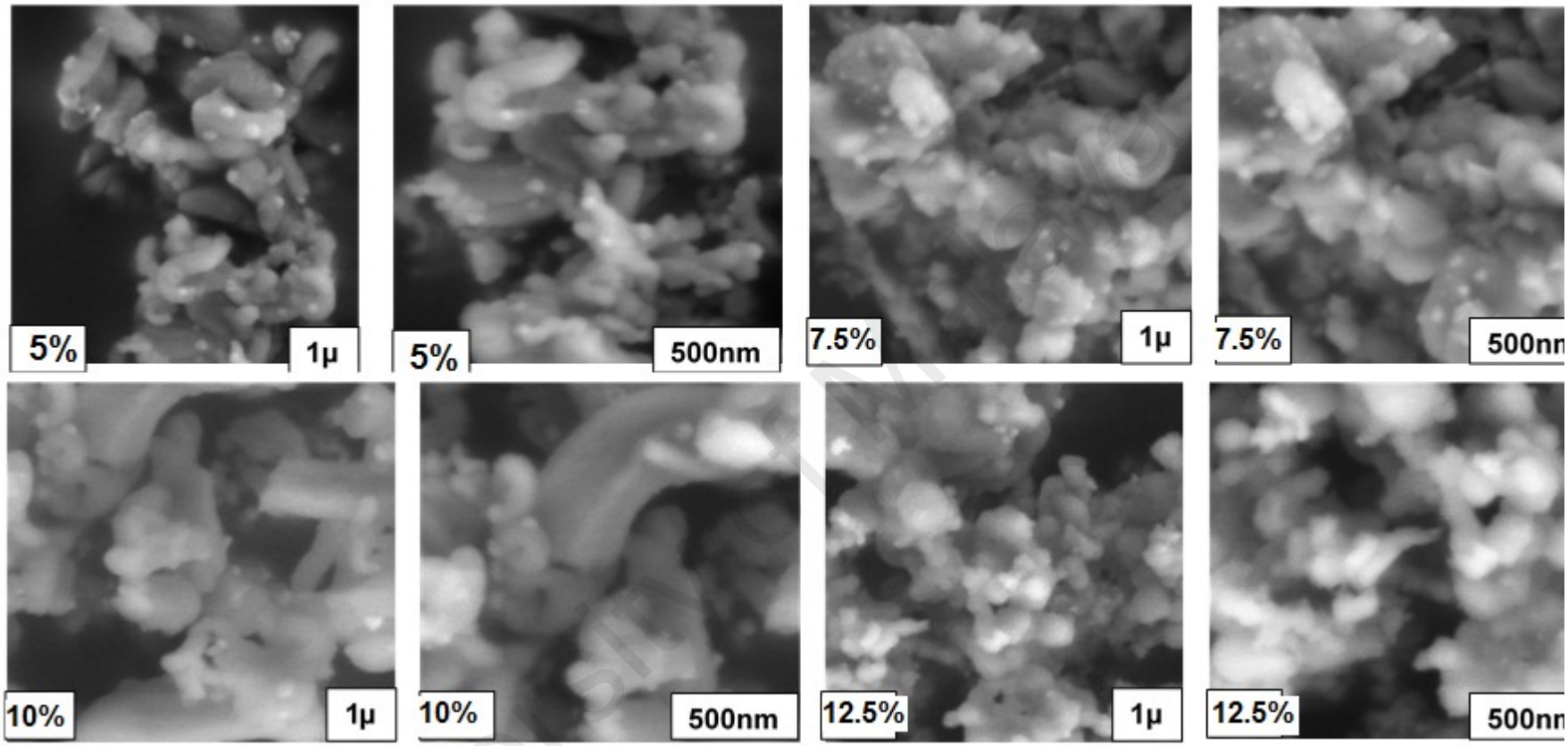

Figure 4.29 : FESEM Images for CuO-NiO supported on Ti-MCM-41 with different Ni loading.

4.5.2.5 Inductively couple plasma- mass spectrometry (ICP-MS) analysis

The ICP-MS analysis methods were adopted for quantification of metal contents (Ni and Cu loading) by considering its high detection limit and reliability. According to the obtained results from the conducted analysis (Table 4.7) show that, there was slightly decreased of Ni loading from the theoretically calculated values of 5., 7.5, 10. and 12.5wt.% to experimentally observed values of 4.93, 7.41, 9.44 and 12.00wt.% sequentially over these variously Ni loaded catalysts. The small decreased of Ni loading observed could be affiliated to little loses during the synthesis of these catalysts. With regards to Cu loading as well, the theoretically calculated amount differed from constant loading of 2.5wt.% to experimentally determined amount of 2.47, 2.40, 2.42 and 2.45wt.% respectively over these variously Ni loaded catalysts.

Table 4.7:: Weight percent of Ni and Cu loading in variously Ni loaded supported catalysts

Catalysts	Ni loading (wt.%)		Cu loading (wt.%)	
	Theo	Expr	Theo	Expr
5% Ni	5.00	4.93	2.5	2.47
7.5% Ni	7.50	7.41	2.5	2.40
10%Ni	10.00	9.44	2.5	2.42
12.5% Ni	12.50	12.00	2.5	2.45

Theo = Theoretical, Expr = Experimental

4.5.2.6 Temperature Programmed Reduction (H_2-TPR) Analysis

Figure 4.30 shows the H_2-TPR profiles for CuO-NiO/Ti-MCM-41. The reducibility of CuO-NiO species supported on Ti-MCM-41 containing different Ni loadings from 5 to 12.5wt.% were investigated by using H_2-TPR technique. The position of the reduction peaks for both copper and nickel oxides were shifted to higher temperatures with the increase of Ni loading from 5, 7.5, 10 to 12.5 wt.%. This indicate presence of stronger interactions of both copper and nickel oxides species with the Ti-MCM-41 as Ni loading increases. The observed peaks at 255, 277 and 285^{o}C for 5, 7.5 and 10 wt.% Ni loaded

samples, respectively, could be assigned to reduction of CuO to Cu, while the peaks noticed at 380, 320 and 399ºC for these samples could be ascribed to the reduction of CuO-NiO to Cu-Ni (Ambursa et al., 2016a). The associated peaks appearing at higher temperature could be assigned to reduction of NiO species having more interaction with Ti-MCM-41 support (Ambursa et al., 2016b). In the case of 12.5wt.% loading only two reductions peaks at 360.9ºC and 465ºC were observed which could be affiliated to reduction of CuO-NiO and NiO species to Cu-Ni and Ni metallic species. The absence of reduction peaks for CuO species are due to high Ni loading which out weight little concentration of CuO species available over the surface of these supports. Even, the available peak for CuO-NiO species overlapped with that of NiO species due to small amount of CuO species in the alloyed (Fang et al., 2017, Carraro et al., 2016). According to results of hydrogen uptake presented in Table 4.7 that, 7.5wt.% Ni loaded catalysts show maximum reducibility with 16379.24 µmol/g than other percentage of Ni loading.

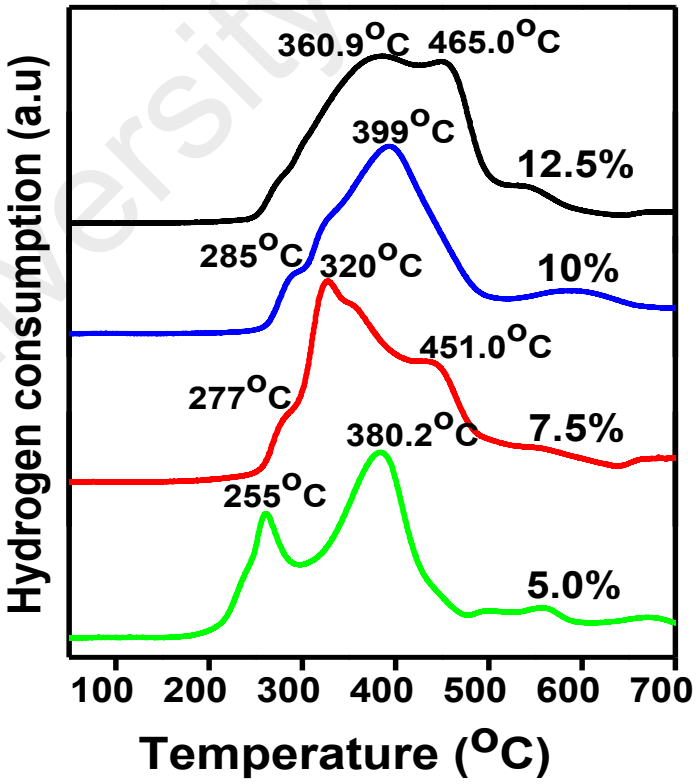

Figure 4.30 : TPR of CuO-NiO supported on Ti-MCM-41 with various Ni loading

Table 4.8: **Hydrogen consumption with corresponding temperature from TPR study**

CuO-NiO/Ti-MCM-41	H_2-TPR Peaks (^oC)			Hydrogen Consumptions (µmol/g)
	First (F)	Second (S)	Third (T)	
5%Ni	255	-	380.2	6774.00
7.5%Ni	277	320	451	16379.24
10%Ni	285	-	399	11793.03
12.5%Ni	360	-	465	5550.79

4.5.3 Effect of reaction parameters on guaiacol conversion and cyclohexane selectivity.

4.5.3.1 Reaction time

The characterization study showed that, 2.5%Cu-7.5%Ni/15%Ti-MCM-41 indicate better dispersion and reducibility and hence selected for parameters optimization studies. The effect of reaction time on Guaiacol conversion and cyclohexane selectivity over 2.5%Cu-7.5%Ni/15%Ti-MCM-41 was conducted at 250ºC, 5MPa 100mg of catalysts and 1-7 hours of reaction time. is presented in Figure 4.31. The results showed that, Guaiacol conversion increase from 6.47 to 44.55% when the reaction time elevated from 1 to 6 hours. However, as the reaction proceed to 7 hours of reaction time the conversion decreased to 43.99%. This result suggests that, 6 hours of reaction time represent equilibrium time for Guaiacol conversion under this condition. Also, the cyclohexane selectivity increases in a similar manner to guaiacol conversion as the reaction time increases. The cyclohexane selectivity showed drastic increase from 0.9% to 20.43% due to increase of reaction time from 1 to 6 hours. However, beyond this point the selectivity decreased to 18.85% after 1 hour of reaction time. It further suggests that, reaction time greatly influence Guaiacol conversion and cyclohexane selectivity.

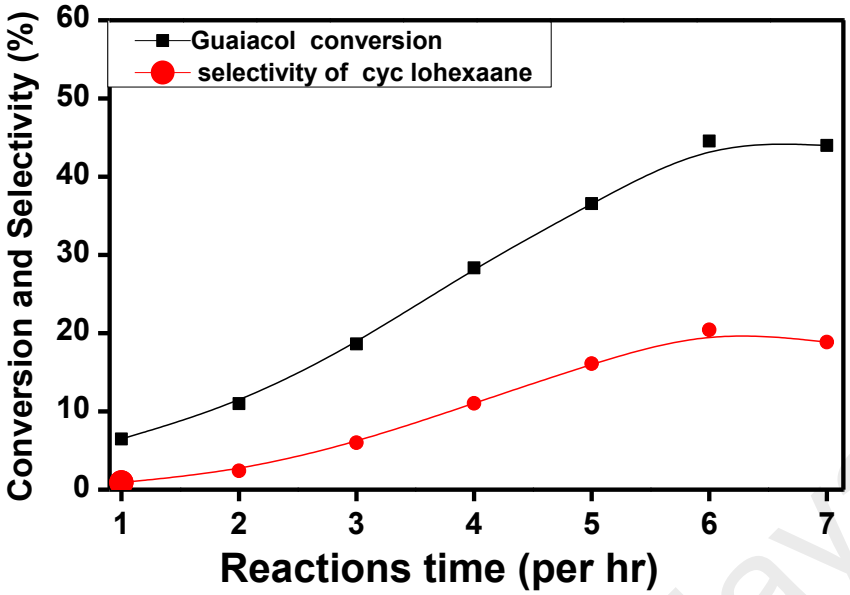

Figure 4.31 : Effect of reaction time on Guaiacol conversion and Cyclohexane selectivity over 2.5%Cu-7.5%Ni/15%Ti-MCM-41 (conditions: 250°C, 5MPa and 1-7 hour's reaction time)

4.5.3.2 Reaction temperature

The results presented in Figure 4.32 indicate that, reaction temperatures greatly influence guaiacol conversion and cyclohexane selectivity over 2.5%Cu-7.5%Ni/15%Ti-MCM-41 catalyst. As the temperature rises from 220 to 280°C the Guaiacol conversion increase from 16.83% to 57.98%. But, in the case of cyclohexane selectivity, increases occurred from 5.05% to 23.14% for temperature of 220°C to 260°C. meanwhile, when the temperature proceeds to 280°C the selectivity decreases to 19.34%. Therefore, the results suggest that 260°C is the optimum reaction temperature due to more selectivity of cyclohexane. Even though relatively, low conversion at this temperature when compared to 280°C but the consideration is more towards low temperature and cyclohexane selectivity. The decrease of cyclohexane selectivity could be affiliated to competitive reaction between hydrogenation and unfavourable polymerization reactions due to high reaction temperature (Zhang et al., 2013a)

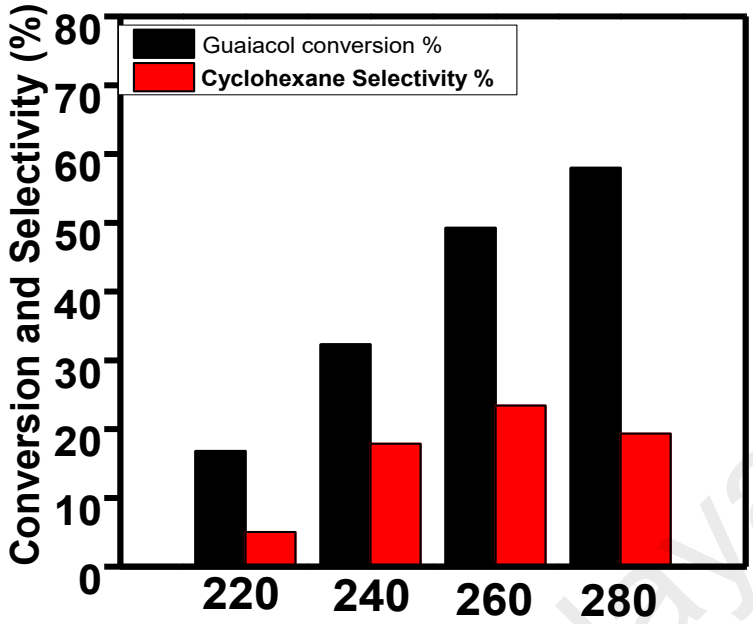

Figure 4.32 : Effect of temperature on Guaiacol conversion and cyclohexane selectivity over 2.5%Cu-7.5%Ni/15%Ti-MCM-41 (conditions: (220°C-280°C), 5MPa and 6 hours)

4.5.3.3 Reaction pressure

Consideration of relevance of hydrogen pressure on hydrodeoxygenation reaction, the effect of various pressure has been studied from 4 to 12MPa given in Figure 4.33. The result show that, Guaiacol conversion increases from 52.91% to 71.62% when the pressure increases from 4MPa to 10MPa. However, as the pressure increase to 12MPa the conversion of Guaiacol was dropped to 69.55%. Also, the trend in cyclohexane selectivity followed the same pattern with guaiacol conversion. It was noticed that, as the hydrogen pressure elevated from 4MPa to 10MPa the cyclohexane selectivity increased from 24.84% to 45.46%. Beyond 10MPa there was no further increment in cyclohexane selectivity (45.76%). Considering high Guaiacol conversion and cyclohexane selectivity, 10MPa have been taking as the optimum hydrogen pressure under this reaction conditions and hence chosen for further study.

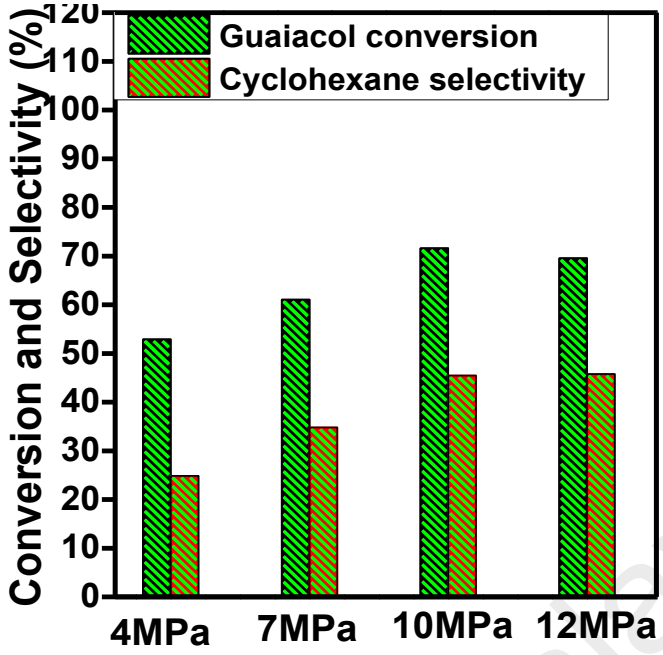

Figure 4.33 : Effect of pressure on Guaiacol conversion and cyclohexane selectivity over 2.5%Cu-7.5%Ni/15%Ti-MCM-41 (conditions: (4-12MPa), 260°C and 6 hours of reaction time)

4.5.4 Hydrodeoxygenation of Guaiacol over 2.5%Cu-x%Ni/(15%)Ti-MCM-41 (x = 5, 7.5, 10 and 12.5%).

4.5.4.1 Guaiacol conversion and cyclohexane selectivity

Figure 4.34, show hydrodeoxygenation of Guaiacol was studied over 2.5%Cu-X%Ni/15%Ti-MCM-41 catalysts with various metal loading from 5, 7.5, 10 and 12.5 % and it was conducted under optimised reaction conditions of 100mg, 260°C, 10MPa, and 6 hours reaction time (obtained from optimization study in Section 4.4.2). The result of this study showed that, Guaiacol conversion increase and decrease with nickel loading. It was observed that, as the nickel loading increased from 5 to 7.5wt.% the conversion increase from 61.96 to 73.91wt.%. However, as nickel loading continue to increase to 10 and 12.5wt.%, there was decrease in guaiacol conversion to 62.33% and 60.76%. The most performing catalysts was found to be 2.5%Cu-7.5%Ni/15%Ti-MCM-41 (7.5%

nickel loaded catalysts) and taking as the optimum supported catalysts under this condition. The high performance of 7.5 wt.% Nickel loaded catalysts was due to well dispersion of supported metallic species as well as high reducibility of this catalysts as can be observed from FESEM images and TPR-H_2 results. Also, additional evidence can be noticed from XRD analysis due to small crystallite size which resulted for better reducibility and high HDO activity of this catalysts. On the other hand, the low performance of 10 and 12.5wt.% Nickel loaded supported catalysts could be affiliated to agglomeration and low reducibility of supported metallic species due to poor dispersion as indicated by FESEM images and TPR-H_2 results.

As shown in Guaiacol conversion profile, cyclohexane selectivity was also observed to increase and decrease from 5% to 12.5wt.% Nickel loaded catalysts. The initial increased from 33.35% to 46.09% as nickel loading elevate from 5 to 7.5 wt.% in 2.5%Cu-X%Ni/15%Ti-MCM-41 could be associated to more increased of metal sites which enable more hydrogenation of unsaturated cyclic hydrocarbons compounds to cyclohexane. The more number of reducible metal species with better dispersion over 7.5 wt.% nickel loaded supported catalysts could contributes for more hydrogenation ability of this catalysts. On the contrary, further addition of Nickel loading beyond this point toward 10 and 12.5 wt.% could result to metallic particle growth and agglomeration which might result to low hydrogenation potential of 2.5%Cu-10%Ni/15%Ti-MCM-41 (10 wt.% Nickel loaded catalysts) and 2.5%Cu-12.5%Ni/15%Ti-MCM-41 (12.5% Nickel loaded supported catalysts) and hence, low selectivity to cyclohexane of 41.04% and 38.65% over 10 and 12.5 wt.% Nickel loaded supported catalysts.

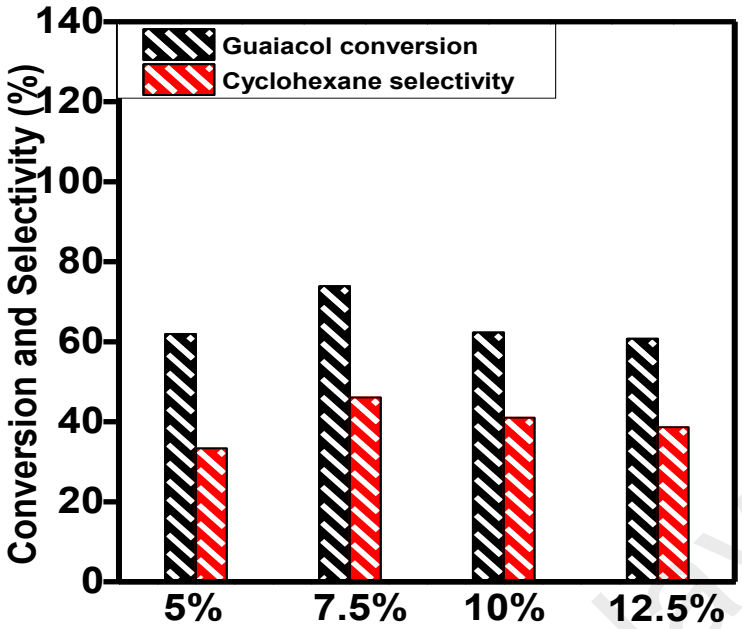

Figure 4.34 : Guaiacol conversion and Cyclohexane selectivity over 2.5%Cu-x%Ni/15%Ti-MCM-41 (conditions: 260°C, 10MPa and 6 hours)

4.5.5 Effect of reaction parameters on dibenzofuran conversion and bicyclohexane selectivity

4.5.5.1 Reaction time

In order to investigate the effect of reaction time on dibenzofuran (DBF) conversion and bicyclohexane selectivity, the reaction time was studied from 2 to 6 hours using 2.5%Cu-7.5%Ni/15%Ti-MCM-41. Figure 4.35 shows that, DBF conversion increases with increase of reaction time. DBF conversion proceed rapidly from 2 to 5 hours with DBF converted value of 17.02% to 42.41%. However, thereafter that, DBF conversion increased at lower rate with an increase from 42.41% to 47.30% when the time changes from 5 to 6 hours. This result suggests that, reaction time greatly affect DBF conversion over 2.5%Cu-7.5%Ni/15%Ti-MCM-41 catalysts. Also, it was observed that, bicyclohexane selectivity show increasing trend from 2 to 6 hours. It proceeds at faster rate during the initial stage from 2 to 3 hours but, beyond this point there was continuous

increase at moderate rate from 3 to 5 hours and slower toward 6 hours. The lowest and maximum selectivity observed from 2 to 6 hours were 5.31% and 30.44% respectively. The six (6) hours of reactions time was considered as the optimum due to high DBF conversion and bicyclohexane selectivity.

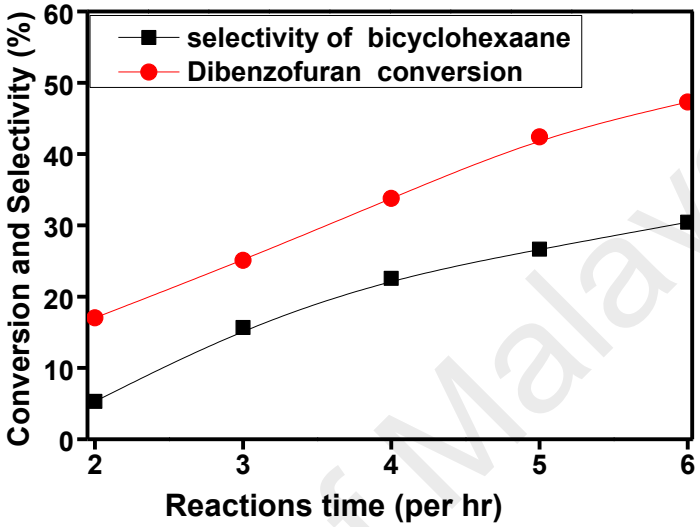

Figure 4.35 : Effect of reaction time on DBF conversion and bicyclohexane selectivity over 2.5%Cu-7.5%Ni/15%Ti-MCM-41 (conditions: 250°C, 6MPa and 2-6

4.5.5.2 Reaction temperature

The effect of reaction temperature on DBF conversion and bicyclohexane selectivity has also being studied from 200°C to 260°C over 2.5%Cu-7.5%Ni/15%Ti-MCM-41 (Figure 4.36). The DBF conversion show an increasing pattern from 27.49% to 41.40% as the temperature changes from 200 to 220°C and when temperature increased from 220°C to 240°C the conversion elevates to 52.19%. With further increase of temperature from 240°C to 260°C, high conversion of 60.59% was obtained. Possible explanation from these results was the increased reaction rate of DBF conversion as the temperature elevated from 200°C to 260°C. This phenomenon indicates no deactivation occurred over the catalyst under the range of reaction temperature. In the case of bicyclohexane selectivity, it was observed the increase from 17.65% to 24.79% and 35.45% when the temperature changes from 200°C to 220°C and 240°C, respectively. However, beyond

240ºC to 260ºC the BCH selectivity remained steady with no further increase of percentages at 35.24% under 260ºC. As consequence of high DBF conversion even though no increase of BCH selectivity was observed, 260ºC have been adopted for subsequent studies.

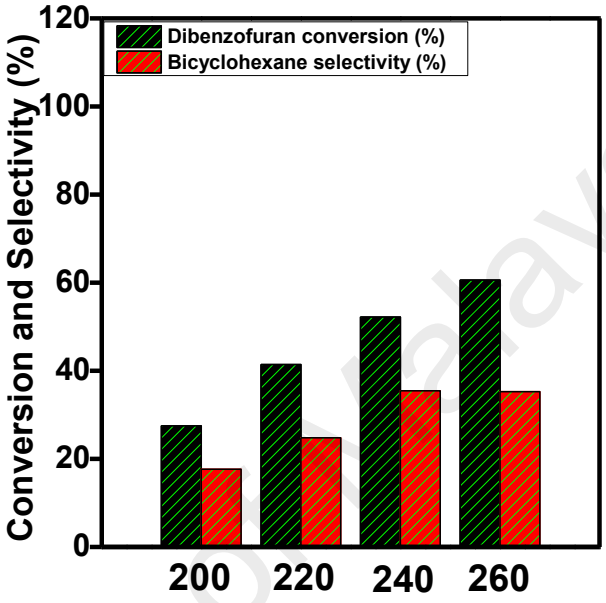

Figure 4.36 : Effect of temperature on DBF conversion and bicyclohexane selectivity over 2.5%Cu-7.5%Ni/ 15%Ti-MCM-41 (conditions: (200ºC – 260ºC), 6MPa and 6 hours).

4.5.5.3 Reaction Pressure

In order to observed dependent of DBF conversion and bicyclohexane selectivity on hydrogen pressure over 2.5%Cu-7.5%Ni/15%Ti-MCM-41, reaction at various hydrogen pressure from 4MPa to 12MPa (Figure 4.37) were studied. The DBF conversion increases from 55.91% to 78.62% as the pressure increase from 4MPa to 10MPa and further increase of hydrogen pressure to 12MPa lead to decrease in conversion to 77.55%. As the similar trend in DBF conversion, bicyclohexane selectivity was observed to increase from 34.84% to 47.46% when the pressure elevates from 4MPa to 10MPa. Beyond this point, the selectivity decreased to 47.46% as the hydrogen pressure reached 12MPa.

Consequently, 10MPa was adopted for continuous study due to high conversion and products selectivity.

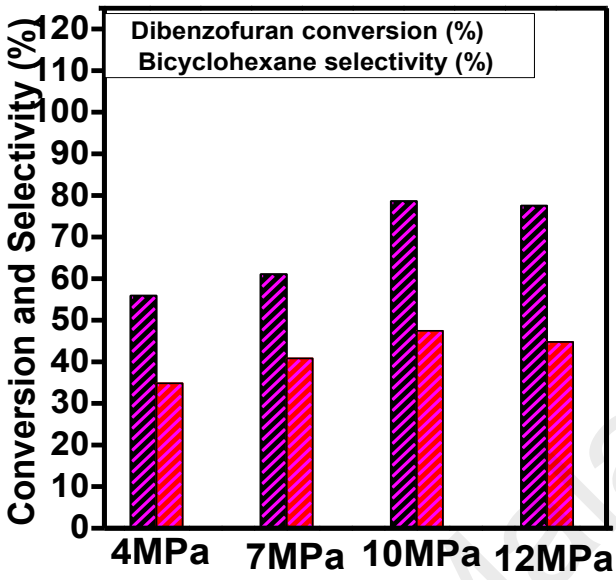

Figure 4.37 : Effect of pressure on DBF conversion and bicyclohexane selectivity over 2.5%Cu-7.5%Ni/(15%)Ti-MCM-41 (conditions: (4-12MPa), 260^{o}C and 6 hours)

4.5.6 Hydrodeoxygenation of dibenzofuran over 2.5%Cu-x%Ni/(15%)Ti-MCM-41 (x = 5, 7.5, 10 and 12.5wt.%) .

4.5.6.1 Guaiacol conversion and cyclohexane selectivity

Figure 4.38 shows catalytic performance of 2.5%Cu-X%Ni/15%Ti-MCM-41(x: 5, 7.5, 10, 12.5wt.%) on hydrodeoxygenation of dibenzofuran under optimized reaction conditions (100mg, 260^{o}C, 10MPa and 6 hours reaction time). The DBF conversion was observed to show increasing and decreasing pattern as nickel loading increase from 5% to 12.5%. The DBF conversion increased from 49.59% to 78.30% when Nickel loading changes from 5 to 7.5wt.%. However, beyond 7.5 wt.% Nickel loading, low DBF conversion of 59.52% and 55.78% was observed with 10 and 12.5 wt.% nickel loaded supported catalysts (2.5%Cu-10%Ni/15%Ti-MCM-41 and 2.5%Cu-12.5%Ni/15%Ti-MCM-41). In the case of bicyclohexane selectivity there was increasing and decreasing

trend as nickel loading elevate from 5 to 12.5 wt.% in nickel loaded supported catalysts (2.5%Cu-x%Ni/15%Ti-MCM-41**(**x: 5, 7.5, 10, 12.5%**)).** It was noticed that, selectivity of bicyclohexane changes from 36.07 to 49.57% as a consequent of additional nickel loading from 5% to 7.5 wt.%. Further increasing nickel loading to 10wt.% and 12.5 wt.% lead to bicyclohexane selectivity decrease to 42.94% and 38.42%. Its obvious that, 7.5wt.% nickel loaded supported catalysts displyed high HDO perfomance both in terms of DBF conversion and bicyclohexane selectivity. The high perfomance of these catalysts could related to its better dispersion of supported catalysts and degree of reducibility as shown by TPR and FESEM results (Figures 4.29 and 4.30). The available reduced and dispersed supported catalysts could enable easy contact between DBF molecule and supported metal over this catalyst and hence high catalytic activity and bicyclohexane selectivity.

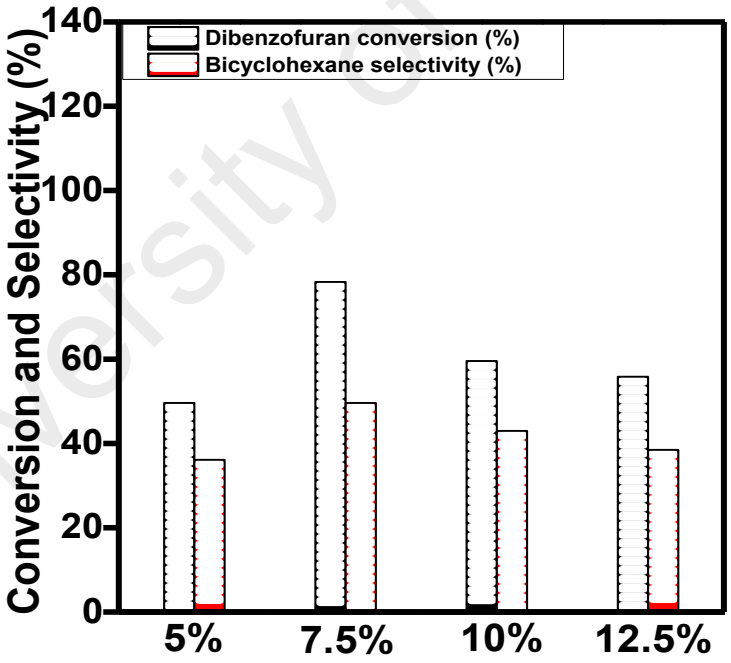

Figure 4.38 : DBF conversion and bicyclohexane selectivity over 2.5%Cu-x%Ni/15%Ti-MCM-41 (conditions: 260°C, 10MPa, 6 hours

4.6 Optimization of Ti content in Ti-MCM-41 for hydrodeoxygenation performance Cu-Ni/Ti-MCM-41 catalysts.

4.6.1 Introduction

It was observed that, the incorporated of Ti species in the matrix of mesoporous MCM-41support (Ti-MCM-41) generated medium and strong acids sites influence the hydrodeoxygenation of Guaiacol and dibenzofuran. To enhance the acidity of Ti-MCM-41 supports, the Ti content was optimized and tested for hydrodeoxygenation of Guaiacol and dibenzofuran. In this regard, the optimization was conducted in two stages; wide and narrow optimization. In the wide optimization stages, Ti incorporation was studied up to 30wt.%. In the case of narrow optimization, Ti incorporation was studied around the optimum loading. The physico-chemical properties of supports were further studied in detail. In this section, the entire results of both wide optimization (characterization of supports and supported catalysts as well as catalytic activity test for 10, 20 & 30 wt.% Ti loading) and narrow optimizations (characterizations of supports; 18, 22 & 25 wt.% Ti loading) were presented and discussed.

4.6.2 Physico-chemical characterization of Ti-MCM-41 supports (Ti loading 10-30wt.%)

4.6.2.1 X-Ray diffraction (XRD) analysis

Small angle XRD patterns of Ti-MCM-41 (different Ti loading at 10-30wt%) samples are shown in Figure 4.40. All the samples show a high intensity XRD peak indexed at (100) plane. This peak indicates the formation of ordered hexagonal cylindrical structures as a model for MCM-41 (Marler et al., 1996). With the increase of Ti loading particularly from 20 to 30 wt.%, there was a peak shifting towards lower angle side. This is due to the distortion of hexagonal structure of MCM-41, an evidence for the incorporation of

titanium species within the silica matrix (Eimer et al., 2008). Owing to higher ionic radius of titanium (Ti^{4+} = 0.72 Å) (Sun et al., 2002) than that of silicon (Si^{4+}= 0.41 Å) (Park et al., 1999) , the coordination of Ti species within the silica matrix (in Ti-MCM-41) could expand the unit cell resulting in the distortion of hexagonal structure in Ti-MCM-41.

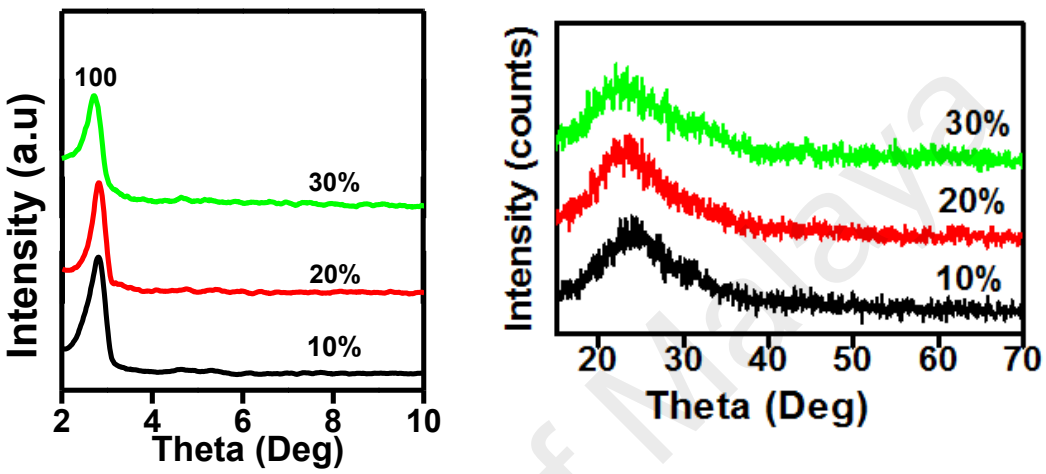

Figure 4.39: Low and high angle XRD patterns of y%Ti-MCM-41support (y = 10, 20 and 30 wt.%).

4.6.2.2 FTIR Spectroscopy analysis

Figure 4.41 shows the FT-IR spectra of various Ti loaded MCM-41 supports. All the samples exhibit a highly intense peak at ~1086 cm^{-1} along with two more broad peaks at ~802 and ~465 cm^{-1}, which indicate Si-O-Si asymmetric and symmetric stretching as well as bending vibration, (Anunziata et al., 2008b). Appearance of these FT-IR peaks reveals the formation of hexagonal silicate network of mesoporous MCM-41. The presence of a broad peak at around ~1640 cm^{-1} in all samples could be assigned to Si-OH vibration. This peak also signifies the existence of attached hydroxyl species in the silanol group. This explains the possibilities of generation of Bronsted acidic sites around the vicinity of incorporated Ti sites. The noticed band at ~960 cm^{-1} can be assigned to Ti-O-Si linkages, which indicates the incorporation of Ti species in the MCM-41 matrix (Anunziata et al., 2008b, Eimer et al., 2008). It was found that the intensity of ~960 cm^{-1}

peak increases as the concentration of Ti increases, suggesting more amount of Ti incorporation into the MCM-41 network.

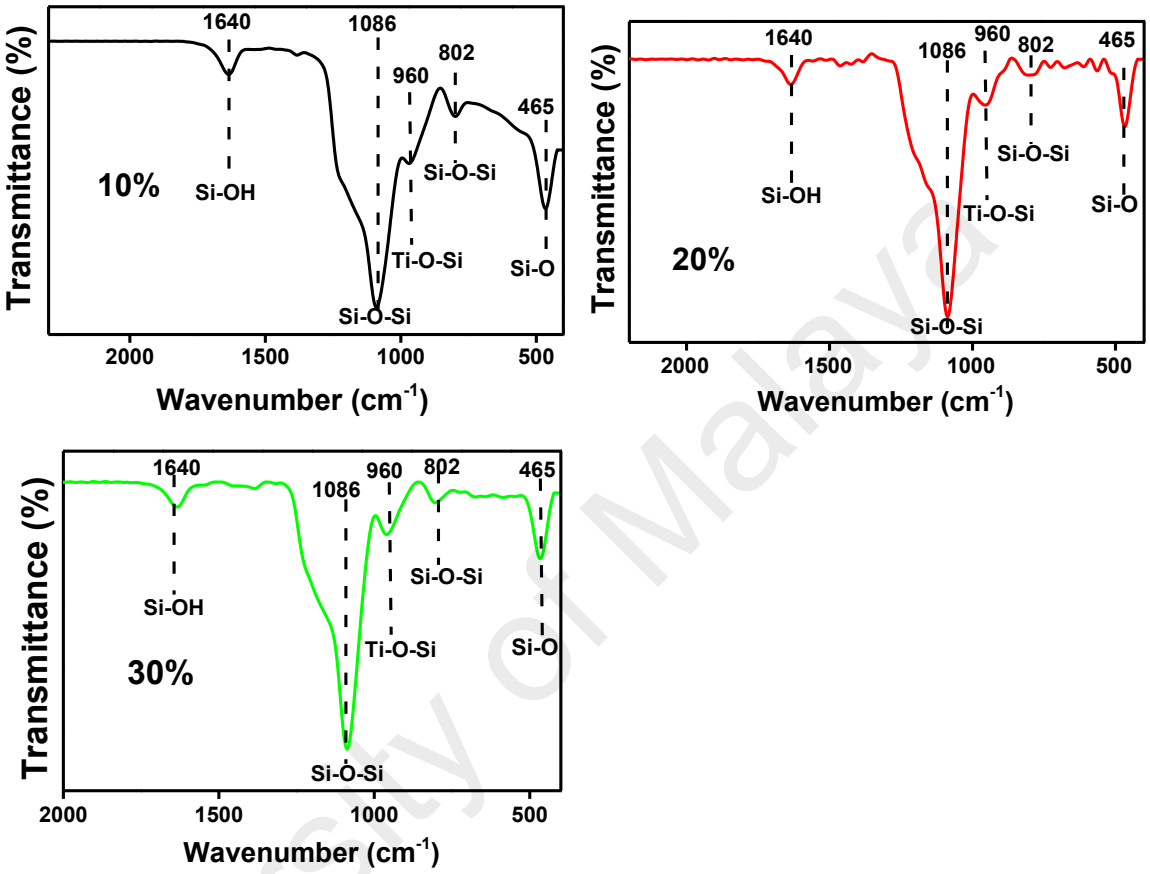

Figure 4.40: FT-IR spectra of y%Ti-MCM-41support (y = 10, 20 and 30wt.%)

4.6.2.3 UV-Visible DRS Spectroscopic analysis

The UV-visible DRS spectroscopy is a highly sensitive technique in terms of intensity and position of absorption band to different coordinated Ti species that may exist as tetra, penta and hexahedral coordinated species in the MCM-41 matrix. Figure 4.42 shows the UV-visible DRS spectra of Ti-MCM-41 supports with different Ti loadings. All the samples exhibit a high intensity band at ~228 nm, which is due to charge transfer transition from tetrahedral O^{-2} to central Ti^{+4}. Appearance of this band further reveals the formation of isolated tetrahedral coordinated titanium species within the MCM-41

network (Jin et al., 2007). This observation supports the FT-IR peak of Si-O-Ti at around 960 cm^{-1} (Figure 4.41). It can be noticed that, from Figure 4.42 the intensity of absorption band at 228 nm increases with the increase of Ti loading from 10 to 30wt.%. This observation reveals the existence of more number of tetrahedral coordinated Ti species in the MCM-41 structure at higher Ti loadings. It is interesting to note that 30wt.% Ti loaded MCM-41 sample shows a shoulder band centred at ~300 nm, indicating the existence of octahedral coordinated Ti species (Lin et al., 2008). The absence of anatase TiO_2 and octahedral titanium $[TiO_6]^{-6}$ in smaller Ti loading samples (10 and 20%) reveals good dispersion of Ti species than in higher Ti loading samples (30 wt.%).

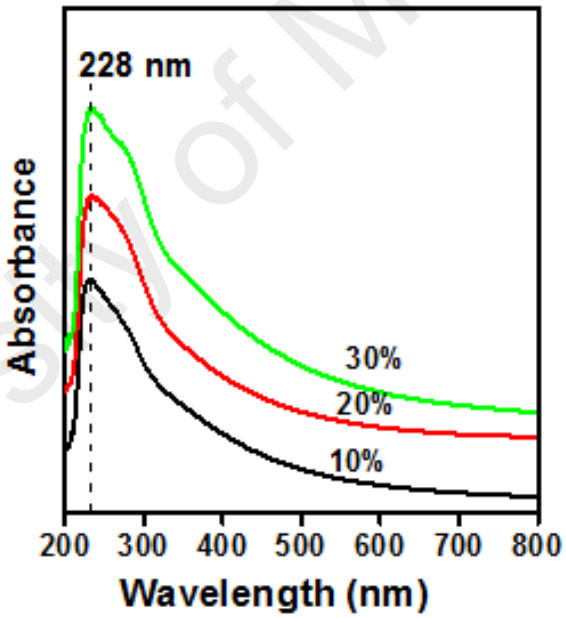

Figure 4.41:UV-visible DRS spectra of y%Ti-MCM-41 support (y = 10, 20 & 30 wt.%).

4.6.2.4 Surface area and porosity analysis

Figure 4.43 shows the N_2 adsorption-desorption isotherms of Ti-MCM-41 samples. According to IUPAC classification, all the samples show type IV with H_3 hysteresis loop, indicating mesoporous nature of the materials (Lin et al., 2008). The textural properties of Ti-MCM-41 samples are summarised in Table 4.9. The surface area of Ti-MCM-41

sample is decreased from ~833, 731, and 496m^2/g with the increase of Ti loading from 10, 20 and 30 wt.%, respectively. Similarly, the pore volume of Ti-MCM-41 sample is decreased from ~0.5, ~0.4, and ~0.3cm^3/g with the increase of Ti loading from 10, 20 and 30wt%, respectively. The decrease of surface area and pore volume at higher Ti loadings could be attributed to collapsed structure as evidenced by XRD studies (Figure 4.40) due to the heavy nature of incorporated titanium species (since titanium atom is larger and heavier than the silicon atom). On the contrary, the average pore size of Ti-MCM-41 increases from ~2.6, ~2.7, and ~3.0 nm with the increase of Ti loading from 10, 20, and 30 wt.%, respectively.

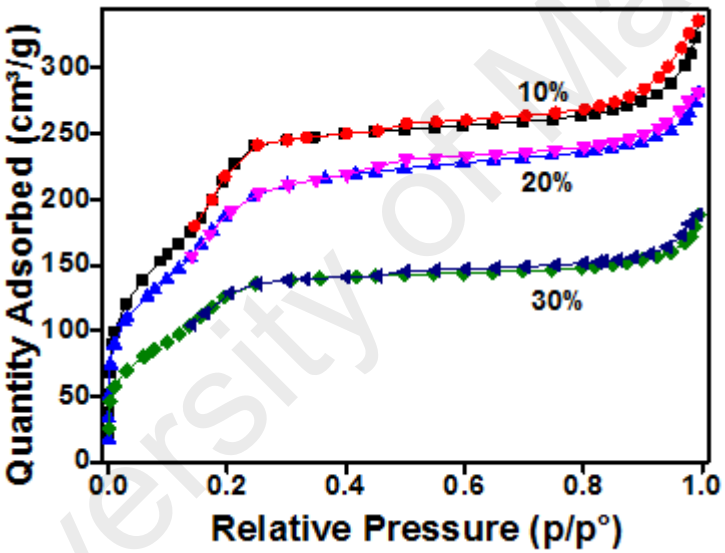

Figure 4.42:The N_2 adsorption-desorption isotherms of y%Ti-MCM-41support (y = 10, 20 and 30 wt.%)

Table 4.9: **Textural and acidic properties of y%Ti-MCM-41support (y = 10, 20 and 30 wt.%).**

Supports	BET Surface area ($m^2 g^{-1}$)	Pore volume ($cm^3 g^{-1}$)	Pore size (nm)	NH_3-TPD Peaks (^oC)		Acids Conc. (µmol/g)
				Medium	Strong	
Ti-MCM-41 (10%)	833	0.5	2.6	394	555	1465.41
Ti-MCM-41 (20%)	731	0.4	2.7	444	661	5173.55
Ti-MCM-41 (30%)	496	0.3	3.0	373	664	1663.35

4.6.2.5 Ammonia temperature programmed desorption (NH_3-TPD)

In order to estimate the concentration of acid sites in the Ti-MCM-41 samples, ammonia temperature programmed desorption (NH_3-TPD) was carried out and the results are presented in Figure 4.44 and Table 4.9. As can be noted from Figure 4.44, the peak noticed at low temperature, aroused due to desorption of NH_3 from the weak acid sites (Sudarsanam et al., 2014, Rao et al., 2015, Mallesham et al., 2016) is shifted to the left side with the increase of Ti loading. On the contrary, the high temperature peak (desorption of NH_3 from strong acidic sites) is shifted to the right side with the increase of Ti loading up to 20 wt.%. However, above 20wt.% Ti loading, the peaks were shifted to the left side of the curved as observed with 30 wt.% Ti loading. These observations indicate that the strength of the strong acidic sites increases as the titanium loading increases from 10 to 20wt.% and subsequently decreased toward 30wt.%. The data presented in Table 4.11 reveal that the 20 wt.% Ti loaded MCM-41 samples has high concentration of acidic sites, which could play a favourable role in HDO of guaiacol as discussed in the later paragraphs.

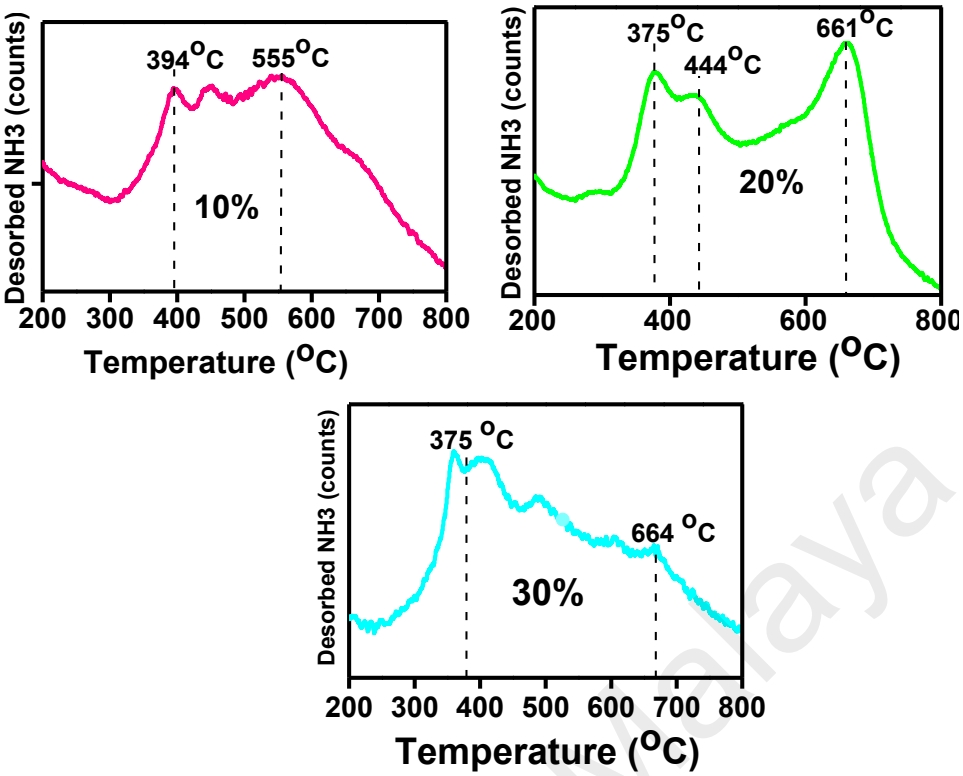

Figure 4.43: TPD profile of y%Ti-MCM-41support (y = 10, 20 and 30 wt.%).

4.5.2. Characterization of Ti-MCM-41 Supported Cu-Ni Catalysts (Ti loading 10-30%)

4.6.2.6 Temperature programmed oxidation (TPO) analysis

The TPO profiles of Cu-Ni catalysts supported on various Ti loaded MCM-41 samples are shown in Figure 4.45. To clearly describe the oxidative thermal decomposition behaviour of Cu-Ni catalysts, both impregnation and drying chemistry needs to be considered. (Sietsma et al., 2008) reveal that, upon impregnation and drying of nickel and copper nitrates, the coordinated complexes of $[Ni(H_2O)_6]^{+2}$ $2NO_3^-$ and $[Cu(H_2O)_6]^{+2}$ $2NO_3^-$ can be formed. Ti-MCM-41 support possess hydrophilic sites from tetrahedral O^{2-} and Ti^{+4} centres which will have some interactions with these Ni and Cu complexes. The obtained results show that, nickel and copper precursors over 10, 20 and 30 wt.% Ti

loaded supports were decomposed at the almost close temperature of 288ºC, 288ºC and 285ºC. This explains that, there were nearly similar interactions between $[Ni\ (H_2O)_6]^{+2}$ $2NO_3^-$ and $[Cu(H_2O)_6]^{+2}$ $2NO_3^-$ with the surfaces of those Ti loaded MCM-41 supports. A shoulder peak at ~420ºC can be observed for all the catalysts, which could be attributed to decomposition of the nitrates within the cylindrical mesopores of the supports that was possibly more adsorbed on the hydrophilic sites or due to poor heat distribution of the silica network (Miranda et al., 2015).

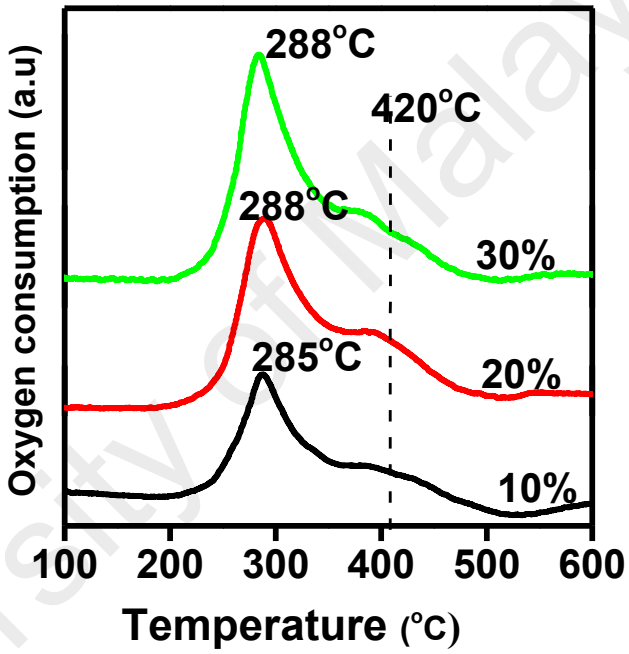

Figure 4.44: TPO profiles of 2.5%Cu and 7.5%Ni precursor supported on y%Ti-MCM-41 catalysts (y = 10, 20 and 30 wt.%).

4.6.2.7 Raman spectroscopy analysis

Two major Raman bands are noticed for 10 and 20wt.% Ti loaded samples Figure 4.46. The first peak located at 580 cm^{-1} is assigned to Ni-O symmetric stretching vibration while the second peak at 1077 cm^{-1} indicates the asymmetric stretching vibration mode of Ni-O (Luo et al., 2014a, Taghvaei et al., 2017). No Raman peaks of CuO were found for 10 and 20 wt.% Ti loaded samples, which could be attributed to low Cu loading. The noticed peaks at ~576 and 1060 cm^{-1} for 30 wt.% Ti loaded catalyst is ascribed to

symmetric and asymmetric stretching modes of Ni-O, respectively (Zhou et al., 2014). The peak at ~690 cm^{-1} is assigned to vibrational mode of Cu-O. A red shifting from 580 and 1077 cm^{-1} to 576 and 1060 cm^{-1} is noticed for 30 wt.% Ti loaded sample. This could be related to high degree of interaction between Ni-O and the support, in line with H_2-TPR results Figure 4.46.

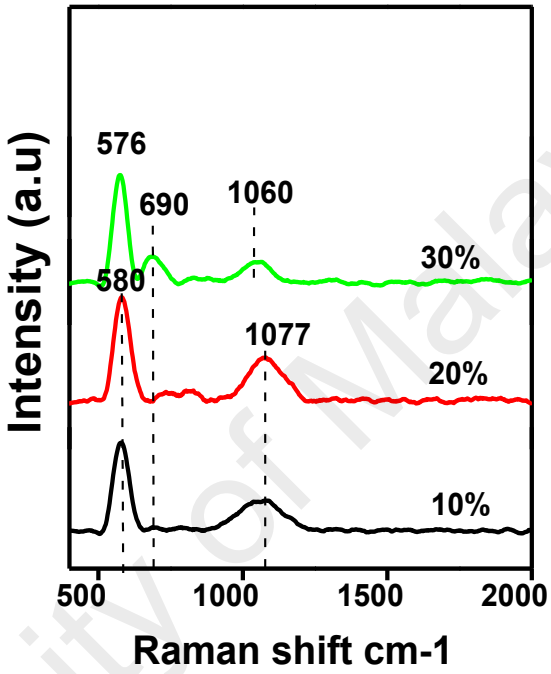

Figure 4.45: Raman spectra of 2.5%CuO-7.5%NiO /y%Ti-MCM-41catalysts (y = 10, 20 and 30 wt.%)

4.6.2.8 High angle X-Ray Diffraction (XRD)

The XRD patterns (Figure 4.47) of Ni-Cu/Ti-MCM-41 samples show various peaks at ~38°, 43° and 63°, corresponding to (111), (200) and (220) planes of cubic phase Ni-O, (Fonseca et al., 2014, Reddy et al., 2009). The 30 wt.% Ti loaded Cu-Ni/Ti-MCM-41 catalyst shows two peaks at ~36 and ~39°, corresponding to (002) and (111) planes of Cu-O, (Sudarsanam et al., 2016). But, only (002) plane of Cu-O was noticed for 20 wt.% Ti containing Cu-Ni/Ti-MCM-41, while no Cu-O XRD peaks were observed for 10 wt.% Ti

containing Cu-Ni/Ti-MCM-41. The noticed broad peak at ~24° is a manifestation of amorphous structures in the synthesized materials (Ryoo and Jun, 1997).

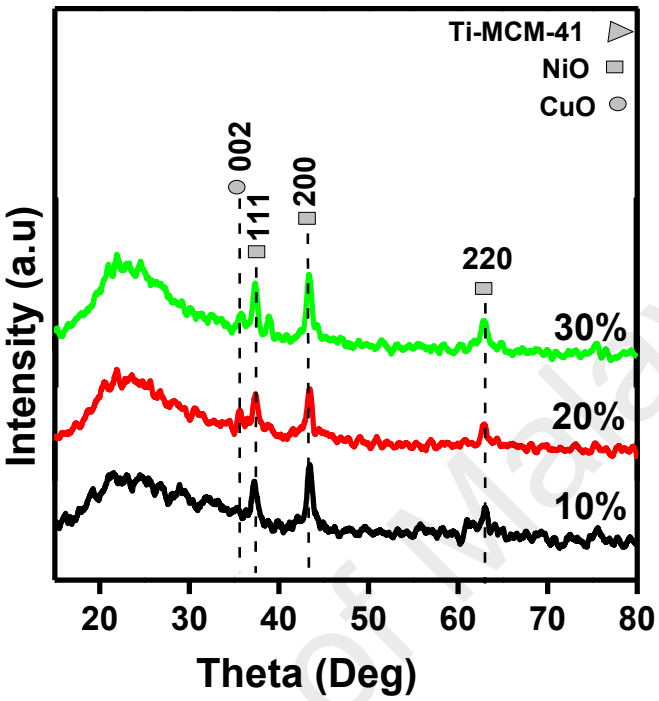

Figure 4.46: Powder XRD spectra of 2.5%CuO-7.5%NiO /y%Ti-MCM-41 catalysts (y = 10, 20 & 30 wt.%).

4.5.2.5 Inductively couple plasma-mass spectrometry (ICP-MS) analysis

The amount of Ti contents in variously loaded supports (from 10-30wt.%) were investigated by ICP-MS analysis. The compared theoretical amount showed little variation of Titanium contents. According to results from Table 4.10, the experimentally observed results (9.09%) in 10 wt.%Ti-MCM-41 supports was less than theoretically calculated amount with 0.10 wt.%. However as the Ti loading increased to 20% Ti loading, there was less loading of 1.94% of Ti content (18.06%) observed experimentally than theoretically calculated amount and then observed to be reduced to 27.74 wt.% in 30 wt.% Ti loading. Also, in the case of Ni and Cu loading over these supports, there were

less experimentally observed amount than theoretical values. As indicated in Table 4.10 as well, the theoretically calculated amount of 7.50wt.% Ni loading over these supports were observed to decreased to 7.01, 7.21 and 7.13% over 10, 20 and 30wt% metal loading. In the case of 2.5% Cu loading over these supports, its founds to decreased to 2.47, 2.42 and 2.35%. This suggest that, the synthesis methods for both supports and supported catalysts could enable small loss of metal contents hence confirming their suitability and appropiation.

Table 4.10: Weight percent of metal in supports and supported catalysts

Catalysts	Metal Loading (wt.%)					
	Ti		Ni		Cu	
	Theo	Expr	Theo	Expr	Theo	Expr
Cu-Ni/Ti-MCM-41 (10%)	10.00	9.09	7.50	7.01	2.5	2.47
Cu-Ni/Ti-MCM-41 (20%)	20.00	18.06	7.50	7.21	2.5	2.42
Cu-Ni/Ti-MCM-41 (10%)	30.00	27.74	7.50	7.13	2.5	2.35

Theo = Theoretical, Expr = Experimental

4.6.2.9 Surface area and porosity analysis

All the Cu-Ni/Ti-MCM-41 catalysts exhibit type IV isotherm with H_3 hysteresis loop (Figure 4.48). The BET surface area of Ti-MCM-41 samples were found to decrease from ~833, ~731, and ~497 m^2/g to ~512, ~497, and ~205 m^2/g after the addition of Cu and Ni to 10, 20 and 30 wt.% Ti-MCM-41 samples, (Table 4.11). Also, the pore volume and average pore size were found to decrease to ~0.3 - ~0.19 cm^3/g and ~2.5 - ~2.3 nm after the addition of Cu and Ni to Ti-MCM-41 samples. The decreased textural properties in supported catalysts could be due to the occupation of dispersed Cu-O and Ni-O species within the internal and external surface of Ti-MCM-41 supports.

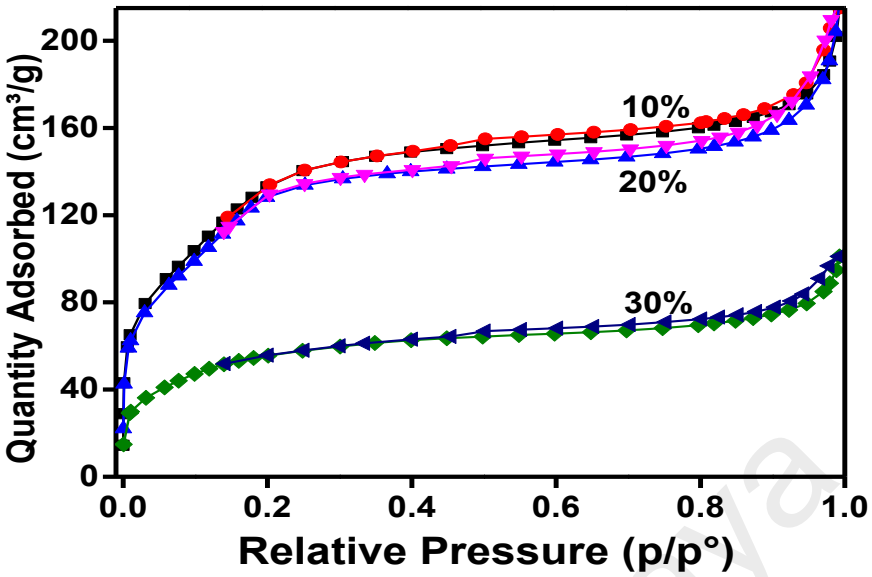

Figure 4.47: The N_2 adsorption-desorption isotherms of 2.5%CuO-7.5%NiO/y%Ti-MCM-41 catalysts (y = 10, 20 and 30 wt.%)

Table 4.11: Textural properties of 2.5%CuO-7.5%NiO/y%Ti-MCM-41 catalysts (y = 10, 20 and 30%).

Catalysts	BET Surface area (m^2/g)	Pore volume (cm^3/g)	Average pore size (nm)
Cu-Ni/Ti-MCM-41 (10%)	~512	~0.33	~2.5
Cu-Ni/Ti-MCM-41 (20%)	~497	~0.33	~2.4
Cu-Ni/Ti-MCM-41 (30%)	~205	~0.19	~2.3

4.6.2.10 Temperature programmed reduction (H_2-TPR) analysis

The H_2-TPR profiles of Cu-Ni/Ti-MCM-41 samples are shown in Figure 4.49. The position of reduction peaks of both copper and nickel oxides is shifted to higher temperatures with the increase of Ti loading. This indicates an enhancement in the interactions of copper and nickel oxides with Ti-MCM-41 as Ti loading increases. The observed peaks at 240 and 280°C for 10 and 20 wt.% Ti loaded samples, could be assigned to reduction of CuO to Cu, while the peaks noticed at 330 and 353°C are associated with

the reduction of NiO to Ni (Ambursa et al., 2016a, Amin et al., 2015). The 30 wt.% Ti loaded sample shows various peaks; the initial tail at 250°C represents the reduction of highly exposed and less interacted CuO to Cu metal. The bands at 310 and 390°C could be attributed to the reduction of bulk CuO to Cu and NiO to Ni, (Marrero-Jerez et al., 2014a).

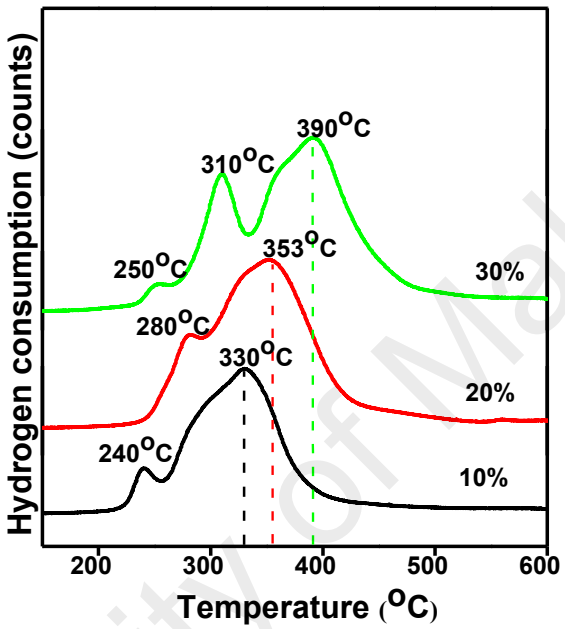

Figure 4.48: H_2-TPR profiles of 2.5%CuO-7.5%NiO /y%Ti-MCM-41 catalysts (y = 10, 20 and 30 wt.%).

4.6.3 Hydrodeoxygenation of guaiacol over 2.5%Cu-7.5%Ni/y%Ti-MCM-41 (y = 10, 20 and 30%) catalysts.

4.6.3.1 Guaiacol conversion and cyclohexane selectivity

The obtained results in hydrodeoxygenation of guaiacol over 2.5%Cu-7.5%Ni/y%Ti-MCM-41 (y = 10, 20 **and** 30 wt.%) catalysts are shown in Figure 4.50. It was found that, the conversion of guaiacol increases from 51.5 to 74.2%, when the Ti loading increases

from 10 to 20 wt.% and then decreases to 55.9% for 30 wt.% Ti loaded catalyst. The initial increase of Guaiacol conversion when the concentration of the incorporated Ti species elevate from 10% and 20 wt.% could be affiliated to more concentration of acids sites (Table 4.9). Although, surface area decreases, but to a lesser extent it appeared not to hindered better performance of Cu-Ni catalysts over 20 wt.% Ti loaded Ti-MCM-41 supports. Due to increase of acids sites in 20 wt.% Ti loaded Ti-MCM-41 there will be well-balanced acid and redox sites. The number of metal sites is expected to be the same due to similar metal loading of Cu and Ni in both 10 and 20 wt.% Ti loaded Cu-Ni/Ti-MCM-41 catalyst. But, the number of acids sites were varied between the two supported catalysts (Table 4.9). The synergetic role between the two functional sites could be enhance by sites balance and consequently more guaiacol conversion. Acids sites play a major role in the oxygen removal through dehydration, whereas the hydrogenation of guaiacol to yield cyclohexane is promoted by the redox sites (Ryoo and Jun, 1997). On the other hand, when the Ti content increase from 20 to 30 wt.% the guaiacol conversion decrease from 74.2% to 55.9%. In this case, the activity lost could be associated to decrease in concentration of acids sites from 20 wt.% Ti loaded Ti-MCM-41 to 30 wt.% Ti loaded Ti-MCM-41 (Table 4.11). In addition, there was decrease in surface area which could also lead to poor performance of this catalysts.

Figure 4.50 also shows the selectivity of cyclohexane obtained in HDO of guaiacol over Cu-Ni/Ti-MCM-41 catalysts. The selectivity of cyclohexane was found to increase from 37.7 to 48.8% when the Ti loading increases from 10 to 20 wt.% in Cu-Ni/Ti-MCM-41 catalyst. In contrast, the cyclohexane selectivity decreases from 48.8 to 39.0% with the increase of Ti loading from 20 to 30 wt.%, respectively. The observed high yield of cyclohexane in the case of 20 wt.% Ti loaded Cu-Ni/Ti-MCM-41 catalyst could also be related to well-balanced acid and redox sites. The total deoxygenation of guaiacol molecule through hydrogenolysis and dehydration could be promoted by acidic sites and

elimination of aromaticity from aromatic ring and subsequent hydrogenation to cyclohexane could be played by the redox sites.

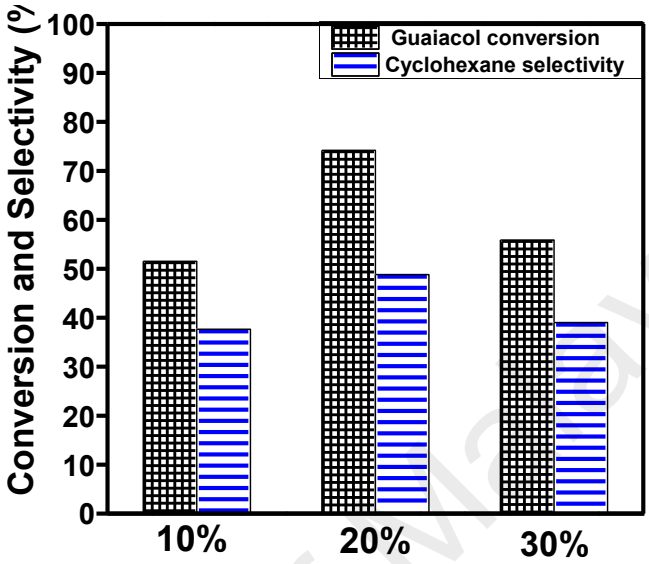

Figure 4.49: Guaiacol conversion and cyclohexane selectivity over 2.5%Cu-7.5%Ni/y%Ti-MCM-41catalysts (y = 10, 20 and 30 wt.%) at 260°C, 10MPa H_2 pressure and 6 hours.

4.6.3.2 Products distribution of Guaiacol HDO.

Figure 4.51 shows the products distribution for HDO of guaiacol over Cu-Ni/Ti-MCM-41 catalysts. In addition to cyclohexane as a major product, eight other different products including cyclohexene, cyclohexanol, cyclohexanone, methyl-cyclohexane, bicyclohexyl, anisole, methoxy-cyclohexane and phenol were found over 2.5%Cu-7.5%Ni/y%Ti-MCM-41 catalysts. Anisole and methoxy-cyclohexane were not observed over 10 wt.% Ti loaded Cu-Ni catalyst (Figure 4.51A). In addition to these two products, phenol was also absent over 20 wt.% Ti loaded Cu-Ni/Ti-MCM-41 catalyst. There are four pure hydrocarbons found including cyclohexane, cyclohexene, methyl-cyclohexane and bicyclohexyl over 10 and 20 wt.% Ti loaded Cu-Ni/Ti-MCM-41 catalysts. On the other hand, methyl-cyclohexane and bicyclohexyl were not found over 30 wt.% Ti loaded

Cu-Ni/Ti-MCM-41 catalysts. This explains that, as Ti loading increases, products selectivity changes toward oxygenated products. The possible reason is that, the number of acid sites generated by coordinated Ti species beyond 20 wt.% Ti loading is decreased and poorly dispersed due to decrease in the surface area of the catalysts. It could be possible that, the decrease in surface area could result to poor distribution of coordinated species leading to loss of acids sites strength to weak ones. This type of behaviour could reduce deoxygenation performance of the catalysts leading to more oxygenated products as observed from 20% to 30 wt.% Ti loaded catalysts. Similar to this observation in which the catalysts with higher acidity and good textural properties show better performance in HDO reactions has been reported by (Lee et al., 2015). According to product distribution, the behaviour of catalytic activity of 2.5%Cu-7.5%Ni/y%Ti-MCM-41 was changing as Ti content varied from 10 to 30 wt.%. Over the 10 and 20 wt.% Ti loaded supported catalysts (Figure 4.51A and 4.51B) there are some products such as methyl-cyclohexane and bicyclohexane which signified occurrence of methyl transfer and ring coupling reaction during HDO reaction. The promoter to this reaction could be affiliated to high strength of acid sites in this catalysts Figure 4.44. However, as the Ti concentration increase to 30 wt.% ring coupling products could be observed and possibly due to low strength of acid sites in this catalyst.

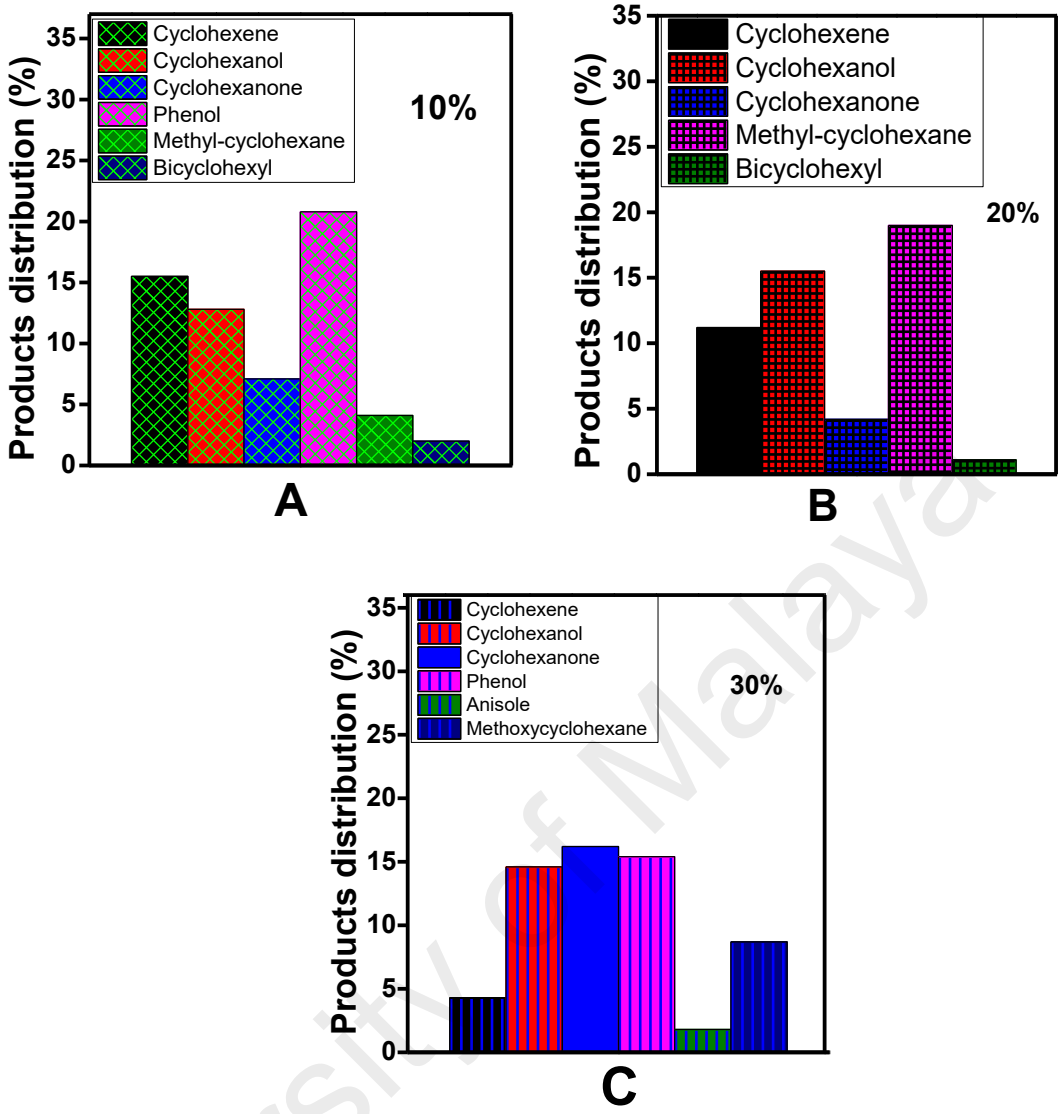

Figure 4.50: Products distribution of Guaiacol HDO over 2.5%Cu7.5%Ni /y%Ti-MCM-41catalysts (y = 10, 20 and 30 wt.%) at 260°C, 10MPa H_2 pressure and 6 hours

4.6.4 Hydrodeoxygenation of dibenzofuran (DBF) over 2.5%Cu-7.5%Ni/y%Ti-MCM-41 (y = 10, 20 and 30 wt.%) catalysts.

4.6.4.1 DBF Conversion and bicyclohexane Selectivity

The influence of Ti incorporation in 2.5%Cu-7.5%Ni/y%Ti-MCM-41 (y = 10, 20 **and** 30 wt.%) catalysts for hydrodeoxygenation of dibenzofuran was investigated under the following experimental condition; 100mg, 260°C, 10MPa and 6-hours reaction time. Like

in guaiacol conversion, Figure 4.52 show that, the conversion of dibenzofuran increased from 10 to 20 wt.% and decreased from 20% to 30 wt.% Ti loading in 2.5%Cu-7.5%Ni/y%Ti-MCM-41. 52.59% DBF conversion was obtained over 10% Ti loaded catalysts (2.5%Cu-7.5%Ni/10%Ti-MCM-41) but, when the Ti loading was increased to 20 wt.% (2.5%Cu-7.5%Ni/20%Ti-MCM-41) the conversion was elevated to 79.22%. Further addition of Ti concertation to 30% resulted to activity decreased to 60.51%. These results show that 20 wt.% Ti loaded catalysts showed relatively better catalytic activity toward DBF conversion under this experimental condition. The maximum activity of this catalysts could be related to its high concentration of acids sites and surface area (Table 4.9). Due to high surface area, there could be better dispersion of supported bimetallic Cu-Ni catalysts leading to balance of redox and acids sites hence more DBF conversion.

The bicyclohexane selectivity as a function of Ti content of 2.5%Cu-7.5%Ni/y%Ti-MCM-41 (y = 10, 20 and 30 wt.%) catalysts were also obtained and presented in Figure 4.52. The selectivity of bicyclohexane also behaves in a similar manner to DBF conversion; it's increase and decrease with increase of Ti loading from 10 to 30 wt.%. Over 10 wt.% Ti loaded catalysts, there was bicyclohexane selectivity of 42.07% which increased to 52.93% over 20 wt.% Ti loaded catalysts due to 10 wt.% increase of Ti loading. However, as the ratio of Ti increase with respect to Si in 30 wt.% Ti loaded catalysts, the bicyclohexane selectivity dropped to 40.94%. The high bicyclohexane selectivity over 20 wt.% Ti loaded catalysts, could be affiliated to balance between redox and acids sites. The balance could also enable appearance of redox and acids sites in a close proximity and hence promoted more hydrogenation of deoxygenated products into saturated hydrocarbons and bicyclohexane in particular, over these catalysts. On the other hand, the low bicyclohexane selectivity observed over 30 wt.% Ti loaded catalysts, could also be associated to its relatively low concentration of acids sites and low surface area.

It could be possible due to low surface area there would be poor dispersion of redox sites and hence low hydrogenation potential in these catalysts.

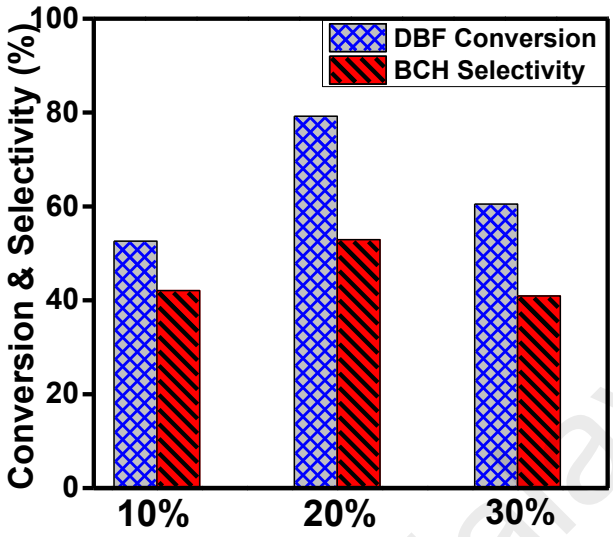

Figure 4.51: DBF conversion and bicyclohexane Selectivity over 2.5%Cu-7.5%Ni/y%Ti-MCM-41 (y = Ti = 10, 20 and 30 wt.%) at 260°C, 10MPa H_2 pressure and hours.

4.6.4.2 Products distributions from hydrodeoxygenation of dibenzofuran

Figure 4.53 show the various products obtained from hydrodeoxygenation of dibenzofuran over bimetallic nickel-copper supported on Ti-MCM-41 with various titanium content (Ti = 10, 20 **and** 30wt.%). The majority of the distributed products over 10, 20 **and** 30 wt.% were observed to be similar with few exceptional products. The resemble products over these catalysts comprises cyclohexyl-benzene, tetrahydrodibenzofuran, 3-methoxy-2-Naphthalenol, 1-cyclohexyl-cyclohexene, 2-cyclohexyl-phenol and phenyl-cyclohexanol. However, the concentration of these products differed between 10, 20 and 30wt.% Ti loaded supported catalysts. The amount of the initial products such as cyclohexyl-benzene, tetrahydrodibenzofuran were observed to be 25.87% and 28.7% over 10 wt.% (Figure 4.53A) and 30 wt.% (Figure 4.53C) Ti loaded supported catalysts which is high than 20 wt.% (Figure 4.53B) Ti loaded supported catalysts. Such disparity could be attributed to rapid deoxygenation and hydrogenation

due more concentration of acids sites in 20 wt.% Ti-MCM-41 than the other two. The concentration of the intermediate products such as 3-methoxy-2-Naphthalenol, 1-cyclohexyl-cyclohexene and 2-cyclohexyl-phenol were also obtained to be 7.51%, 4.24% and 7.54% over 10 wt.% Ti loaded supported catalysts (Figure 4.53A). The same intermediate products were found to be 10.61%, 4.21% and 2.36% over 20 wt.% Ti loaded supported catalysts (Figure 4.53B) which were slightly different from 11.83%, 2.79% and 4.47% as obtained over 30 wt.% Ti loaded supported catalysts (Figure 4.53C). Furthermore, other products such as 2-phenyl-cyclohexanol with little percentage of 5.2% and 3.6% over 10 and 30 wt.% Ti loaded supported catalysts and in addition to that, ample amount of 1,1-Bicyclohexyl-2-one (1.36%) appeared over 10 wt.% Ti loaded supported catalysts which appeared to be absence over 20 wt.% Ti loaded supported catalysts. Possible reasons for disappearance of these products could be related to relatively high hydrodeoxygenation potential of this catalysts. On the contrary, open ring compound such as pentyl-cyclohexane was presence over 20 wt.% Ti loaded supported catalysts which could be affiliated to high strength of oxygen content.

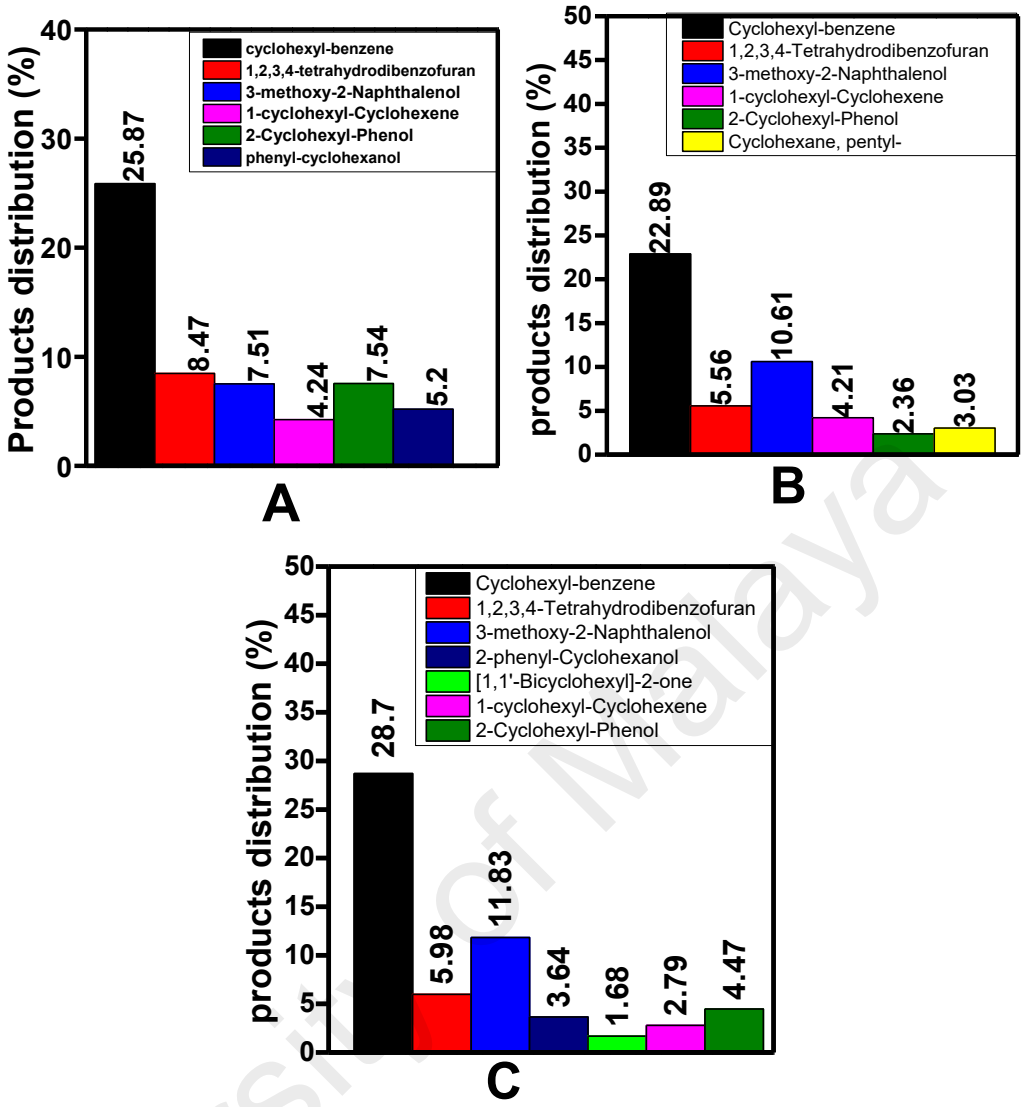

Figure 4.52: Products distribution of hydrodeoxygenation of Dibenzofuran over 2.5%Cu-7.5%Ni/y%Ti-MCM-41 (y = Ti = 10, 20 and 30 wt.%) (100mg, 260°C, 10MPa and 6 hour's reaction time)

4.6.5 Narrow Ti optimization for more enhancement of Acidity of Ti-MCM-41 support (Ti loading: 18 to 25%)

4.6.5.1 Introduction

It was noticed that, the catalytic activity of the 2.5%Cu-7.5%Ni/y%Ti-MCM-41 (y = Ti = 10, 20 and 30 wt.%) catalysts correlate better with acidity of Ti-MCM-41 support (from 10 to 30 wt.% Ti contents). This is confirming that, acidity is the major key player in this reaction. Therefore, there is need to enhance acidity for high catalytic activity. In

order to enhance the acidic content of Ti-MCM-41 support narrow optimization was also carried out around 18 to 25wt.% Ti content with respect to silica content and the characterization results were given below.

4.6.5.2 Physico-chemical characterizations of Ti-MCM-41 (Ti loading: 18 to 25 wt.%)

(a) ***X-Ray diffraction (XRD) analysis***

Figure 4.54 display the XRD patterns for Ti-MCM-41 supports narrowly optimized with different Ti content between 18 to 25 wt.% loading. All the investigated supports within this ranges showed retention of hexagonal mesoporous properties due to manifestation of X-ray reflection (Peaks) at 2.8, 2.7 and 2.7θ position for 18, 22 and 25 wt.% Ti loaded Ti-MCM-41. Even though the three reflections were all indexed at 100 reflection planes and slightly shifted to low angle with increase of Ti content but, structurally these supports appear to be nearly similar with appearance of the intense peaks for all the three. The obtained d-spacing (d_{100}) for these supports further signified little variation with corresponding value of 32.90, 33.22 and 33.82 for 18, 22 and 25 wt.% Ti loaded Ti-MCM-41.

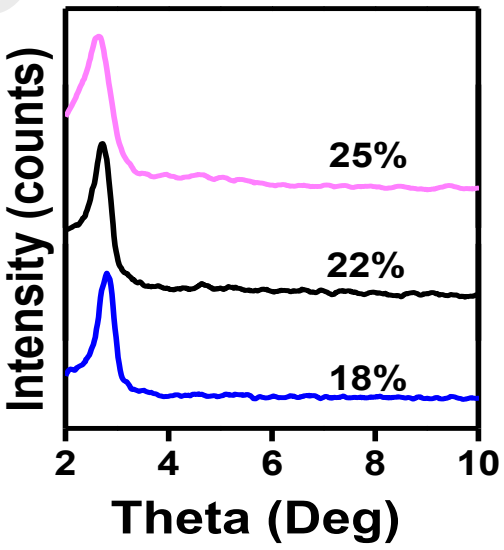

Figure 4.53: Low angle XRD of zTi-MCM-41 supports (z = 18, 22 and 25 wt.%)

(b) ***FTIR Spectroscopy analysis***

Figure 4.55 present the FT-IR spectra of different Ti loaded in Ti-MCM-41 supports. All the synthesized Ti-MCM-41 supports show indefinable peaks for Ti-MCM-41 within the fingerprint region of the FTIR spectra. Within this region, there exist highly intense peaks at ~1086, 1085 and 1085cm^{-1} together with another peak at 960.0, 959 and 959cm^{-1} which confirm the present of Si-O-Si and Ti-O-Si linkages in the mesoporous MCM-41 structures (Anunziata et al., 2008b). Other peaks account for the present of Si-OH, at different vibrational mode are also presents. The appearance of absorption band for Ti-O-Si signified an insight into the formation of acidic site into mesoporous structures. However, the concentration of acidic sites may possibly be differed due to slight red shift in Ti-O-Si peak from 18 to 25 wt.% Ti loaded in Ti-MCM-41. The detailed of acids sites concentration could be obtained in our later study of NH_3-TPD.

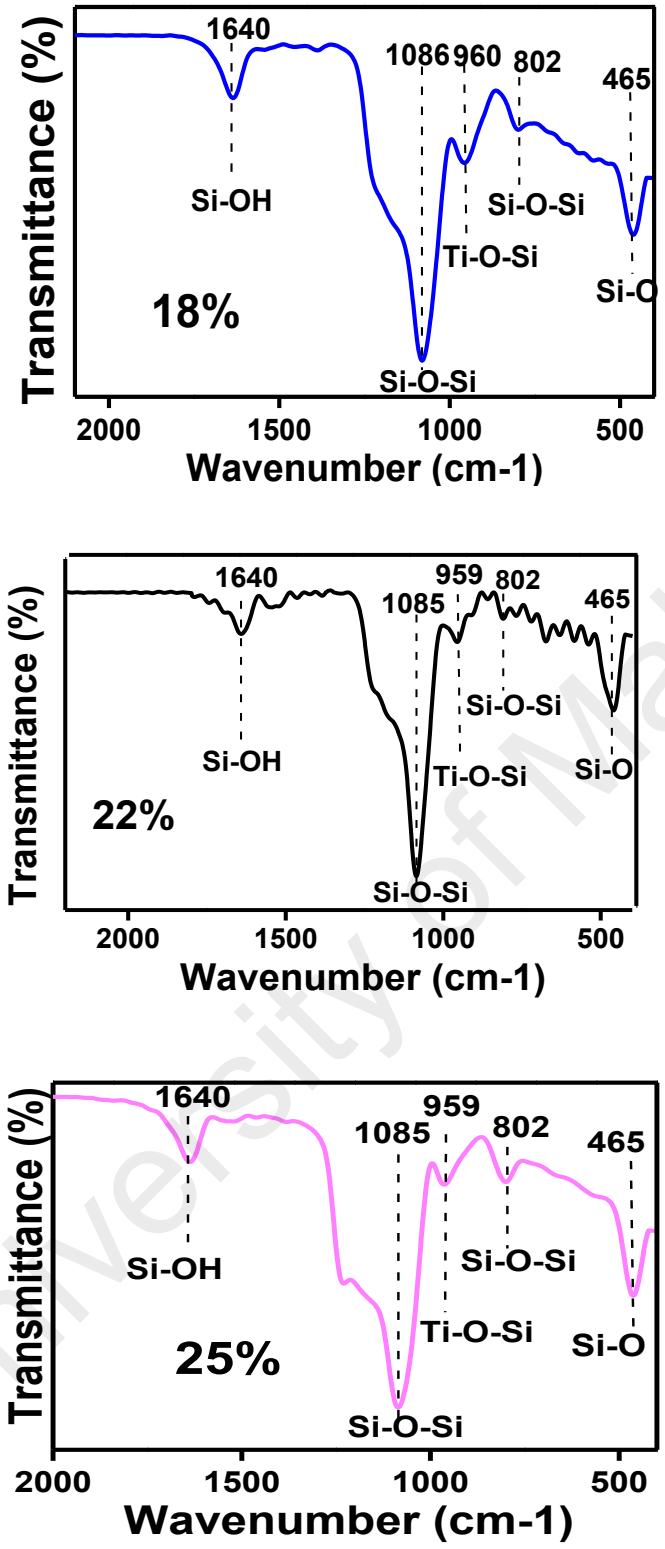

Figure 4.54 : FTIR spectra of zTi-MCM-41 support (z = 18, 22 and 25 wt.%)

(c) ***Inductively couple plasma-mass spectrometry (ICP-MS) analysis***

In order to determine the amount of Ti loading the ICP-MS analysis was conducted. The results from Table 4.12 indicate that, there were not much variation between the experimental and theoretical values. When the calculated theoretical Ti loading was 18, 22 and 25 wt.%the experimentally observed values were found to be 16.65, 19.34 and 22.44% respectively.

Table 4.12: Ti loading and concentration of acids sites for z%Ti-MCM-41 supports

Supports	Ti loading (wt.%)		Conc. of Acids sites (µmol/g)
	Theo	Expr	
Ti-MCM-41 (18%)	18.00	16.65	5573.40
Ti-MCM-41 (22%)	22.00	19.34	4580.11
Ti-MCM-41 (25%)	25.00	22.44	4463.24

Theo = Theoretical, Expr = Experimental

(d) ***Ammonia temperature programmed desorption (NH_3-TPD) analysis***

The concentration of acids sites in the variously Ti loaded Ti-MCM-41 supports were determined using ammonia temperature programmed desorption (NH_3-TPD). The presented NH_3-TPD results in Figure 4.56 indicates that, the strength of acidity is decreasing with increasing Ti loading from 18% to 25 wt.%. There are two dominant of acids strength over each support. Strong acids sites are the dominant sites for 18 wt.% Ti loaded Ti-MCM-41 supports as represented by the most intense peaks at 737^{o}C. However, there could be ample amount of weak of acids sites in this support due to small peak appeared at 172^{o}C. In a slight contrary to that, medium and strong acids sites as represented by the desorption peaks at 388^{o}C and 569^{o}C were found over 22 wt.% Ti loaded Ti-MCM-41 supports. However, as the amount of Ti content increase to 25 wt.% the representative peaks for strong acids sites was shifted to a weak side of the curve. This result discloses that, as the Ti content increase from 18 to 25 wt.% the strength of strong acids sites continuously decreasing toward formation of the medium site. According to

the data presented in Figure 4.56 and Table 4.11 that, 18 wt.% Ti loaded in Ti-MCM-41 display high strength and high concentrations of acids sites (5573.40µmol/g) than 22 wt.% Ti-MCM-41 and 25 wt.%Ti-MCM-41 with (4580.11µmol/g) and (4463.24µmol/g). Hence 18 wt.% Ti-MCM-41 is the optimum support which could play a high performance in HDO of dibenzofuran and guaiacol (Sudarsanam et al., 2014, Rao et al., 2015, Mallesham et al., 2016) as discussed in the later chapter of this thesis.

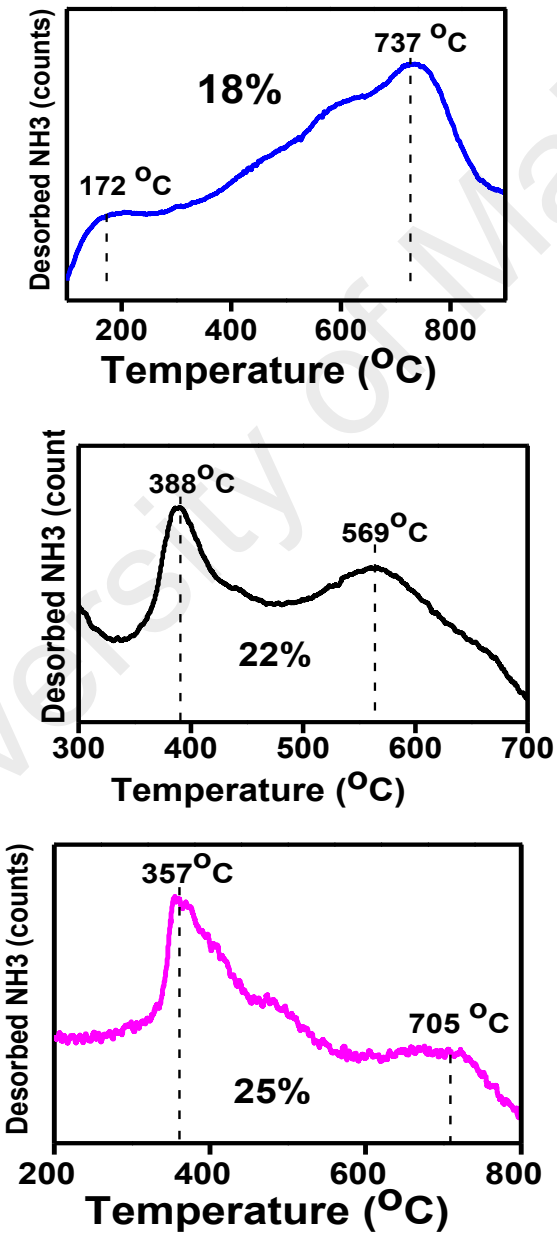

Figure 4.55 : TPD profile of zTi-MCM-41 support (z = 18, 22 and 25%)

(e) ***Transmission electron microscope (TEM) Image analysis***

To investigate the internal microscopic structures of 18 wt.%Ti-MCM-41, transmission electron microscope analysis was conducted. Figure 4.57 displays various internal structures resulted from parallel and perpendicular penetration of electron beam in the hexagonally arrange channels of mesoporous silicate structures of Ti-MCM-41 (Moritz and Geszke-Moritz, 2015). For clear visibility of regular channels, some parts were enlarged as shown in Figure 4.57. Figure 4.57 $_{(1)}$ insert, clearly shows parallel arrangement of mesoporous channels of 18 wt.%Ti-MCM-41. Figure 4.57 $_{(2)}$ insert discloses regular hexagonal channel array with honeycomb-like structures, which are perpendicular to penetrated electron beam in mesoporous silicate structures. These observations further confirm by XRD (Figure 4.54) and FTIR (Figure 4.55) studies. There were no visible TiO_2 deposits in TEM images of Ti-MCM-41, indicating well dispersion of titanium species within the framework of Ti-MCM-41 structures.

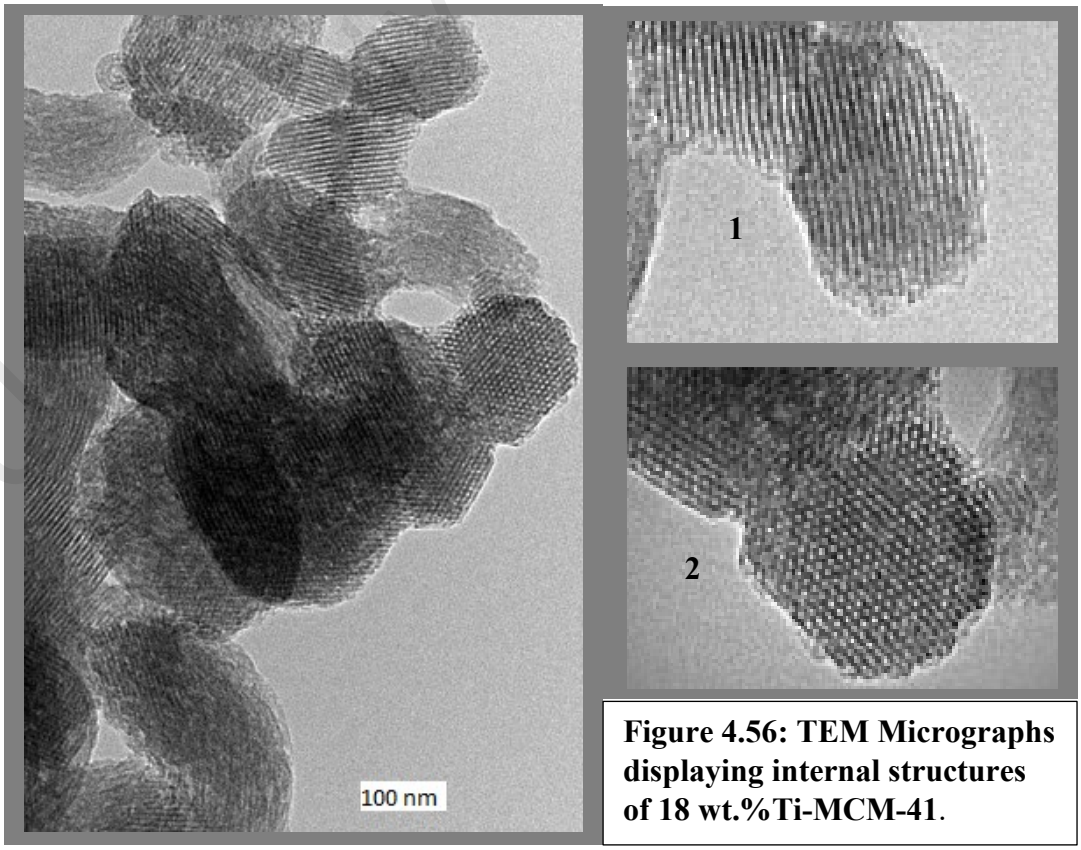

Figure 4.56: TEM Micrographs displaying internal structures of 18 wt.%Ti-MCM-41.

(f) ***X-ray photoelectron spectroscopic (XPS) analysis***

In order to get an overview on the oxidation state of the surface elements as well as the types of linkages available in 18 wt.%Ti-MCM-41 structures, XPS analysis has been undertaken and the results are shown in Figure 4.58. The basic O1s, Ti 2p and Si 2p XP spectra can be noted in Figure 4.58A. Then, Figure.4.58B confirms the existence of Si^{4+} in the 18 wt.%Ti-MCM-41 frame work due to occurrence of Si $2p_{1/2}$ at around 103.3 eV. While Figure. 58C presents spin orbital doublet intense peaks at ~459.3 and 465 eV, corresponding to Ti $2p_{3/2}$ and Ti $2p_{1/2}$ which confirm the existence of Ti^{4+} ions in the hexagonal structures of Ti-MCM-41 (González et al., 2016, Chen et al., 2016). The deconvoluted O1s spectrum (Figure 4.58D) shows three internal peaks at ~531, 532.6 and 534 eV, which can be assigned to Si-O-Ti, Si–O–Si and Si-OH linkages, respectively (Chen et al., 2016). The presence of Si-O-Ti reveals the substitution of Si^{4+} with Ti^{4+} in the hexagonal mesoporous silica structures of Ti-MCM-41.

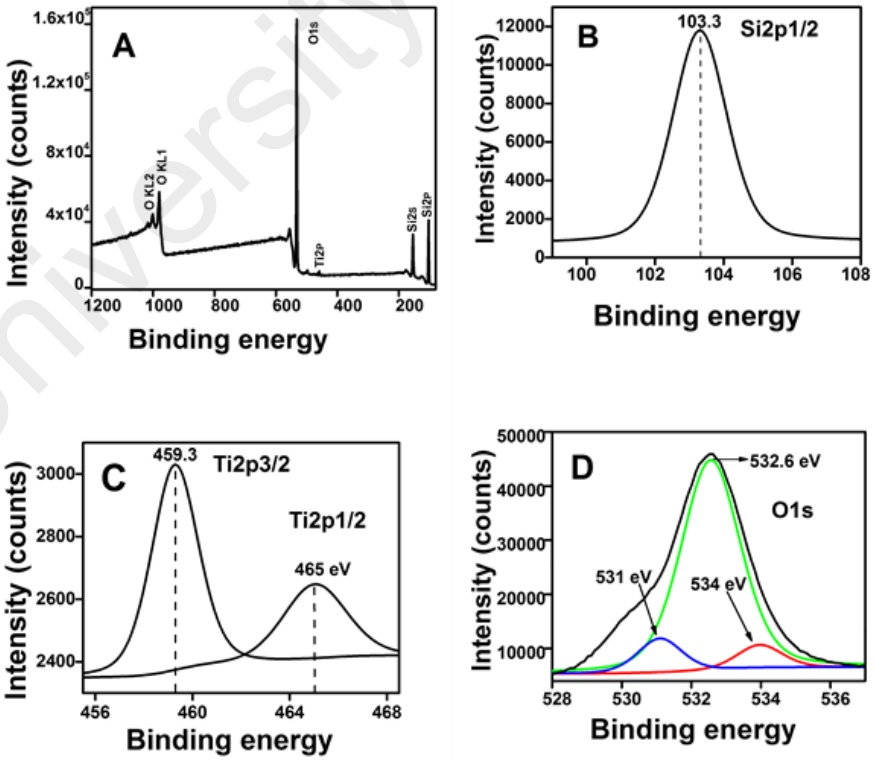

Figure 4.57: XPS spectra of 18%Ti-MCM-41support

4.7 Comparative studies of Cu-Ni supported on mesoporous Ti-MCM-41 with MCM-41 and TiO_2 supports.

In the previous section Cu-Ni/Ti-MCM-41 catalysts appeared to displayed good hydrodeoxygenations potential for hydrodeoxygenation of both Guaiacol and Dibenzofuran. On the other hand, the characterization of regular MCM-41 supports conducted earlier, showed it possessed certain hydrodeoxygenation potential. Then in our preliminary studies, Cu-Ni/TiO_2 catalysts showed high Guaiacol and dibenzofuran conversion as well as hydrocarbon selectivity than Cu-Ni/CeO_2 and Cu-Ni/ZrO_2 catalysts. Therefore, there is need to compared hydrodeoxygenation potential of Cu-Ni/Ti-MCM-41 and Cu-Ni/TiO_2 catalysts under identical reaction conditions. In order to achieve this, Cu-Ni/(18wt.%)Ti-MCM-41, Cu-Ni/TiO_2 and Cu-Ni/MCM-41 were studied for hydrodeoxygenation of Guaiacol and dibenzofuran at 260^{o}C, 10MPa and 6 hours reaction time). In this section, the results for comparative activities, reusability and proposed reaction mechanisms of Guaiacol and DBF over Cu-Ni/(18wt.%)Ti-MCM-41 were presented and discussed. It should be noted that, the characterizations for Cu-Ni/TiO_2 were given in section 2 of this chapter.

4.7.1 Physico-chemical properties of Cu-Ni/Ti-MCM-41 and Cu-Ni/MCM-41

4.7.1.1 Raman spectroscopy analysis

The Raman spectra of Cu-Ni/MCM-41 and Cu-Ni/Ti-MCM-41 catalysts are shown in Figure 4.59. The Cu-Ni/MCM-41 catalyst shows two broad bands at ~578 and 1087 cm^{-1} with an additional small band at 733 cm^{-1}. All these bands were attributed to Ni-O vibrational mode (Sudarsanam et al., 2016). The similar types of peaks were also observed in Cu-Ni/Ti-MCM-41 catalyst. However, the peaks are shifted to higher frequencies ~590, 740 and 1094 cm^{-1}, compared to Cu-Ni/MCM-41 catalyst. The

incorporation of titanium within the structural frame work of MCM-41 led to the generation of strong acid sites as evidenced by NH_3-TPD analysis (Figure 4.56)(Wang et al., 2014b), which can strongly interact with Ni-O resulting in higher adsorption of vibrational energy by the Ni-O species (Reddy et al., 2009). In order to confirm the structure of Ti-MCM-41 support in the supported catalysts as well as existence of Ti species in the amorphous wall of mesoporous MCM-41, the Raman spectra of CuO-NiO/Ti-MCM-41 was deconvoluted. The presence of Ti species in the form of Ti-O-Si with tetrahedral coordination environment was observed at Raman shift of 1125 cm^{-1}. Also, other peaks due to existence of Si-O-Si symmetric and asymmetric vibration was observed at Raman Shift of 820 and 1113 cm^{-1} respectively. In addition to that, besides the observed there was observed peaks at 631 cm^{-1} in the Raman shift accounting for the presence of CuO species in this supported catalyst (Li, 2007, Kornatowski et al., 1996, Yang et al., 2000). In the case of MCM-41 supported catalysts, there is no observed peak due to Ti species after deconvolation of the Raman Shift. Deconvolation of the initial peak revealed the presence of NiO and CuO at ~**578 and 625.8** cm-1 (Reddy et al., 2009, Sudarsanam et al., 2016). Then, Deconvolution of the larger peak described the existance of NiO and Si species in the form of Si-O-Si at the Raman Shift of 1087 and 1111cm^{-1}. This further confirmed the presence of coordinated Ti species within the silica matrix of Ti-MCM-41 support (Li, 2007, Kornatowski et al., 1996, Yang et al., 2000).

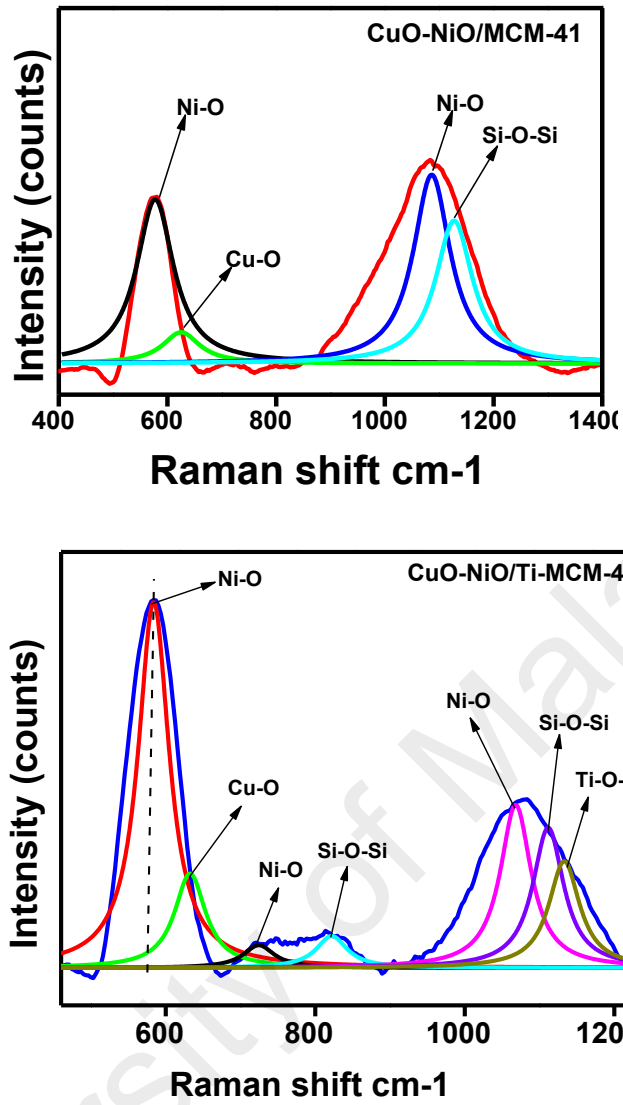

Figure 4.58: The Raman shift of CuO-NiO bimetallic catalyst supported on MCM-41 and (18%)Ti-MCM-41.

4.7.1.2 The X-ray diffraction (XRD) analysis

XRD patterns of supported Cu-Ni catalysts are shown in Figure 4.60. The noticed broad peak at around 24.5° indicates the amorphous nature of silica. The Cu-Ni/MCM-41 catalyst shows various XRD peaks at 37.34, 43.40 and 62.98°, which can be attributed to the reflection planes of (111), (200) and (220), respectively, confirming the cubic phase of NiO (PDF = 96-101-0382). Similar types of peaks at 37.34, 43.4 and 62.98° on the reflection planes of (111), (200) and (220), can be also noticed for the Cu-Ni/Ti-MCM-41 catalyst (PDF= 96-101-0094) (Fonseca et al., 2014, Reddy et al., 2009, Ambursa et al., 2016a). In contrast, the diffraction peaks pertaining to CuO species could not be

observed due to small particle size resulted from its better dispersion within the cylindrical channel mesoporous supports and/or due to low Cu loading, in line with Raman studies (Figure 4.59).

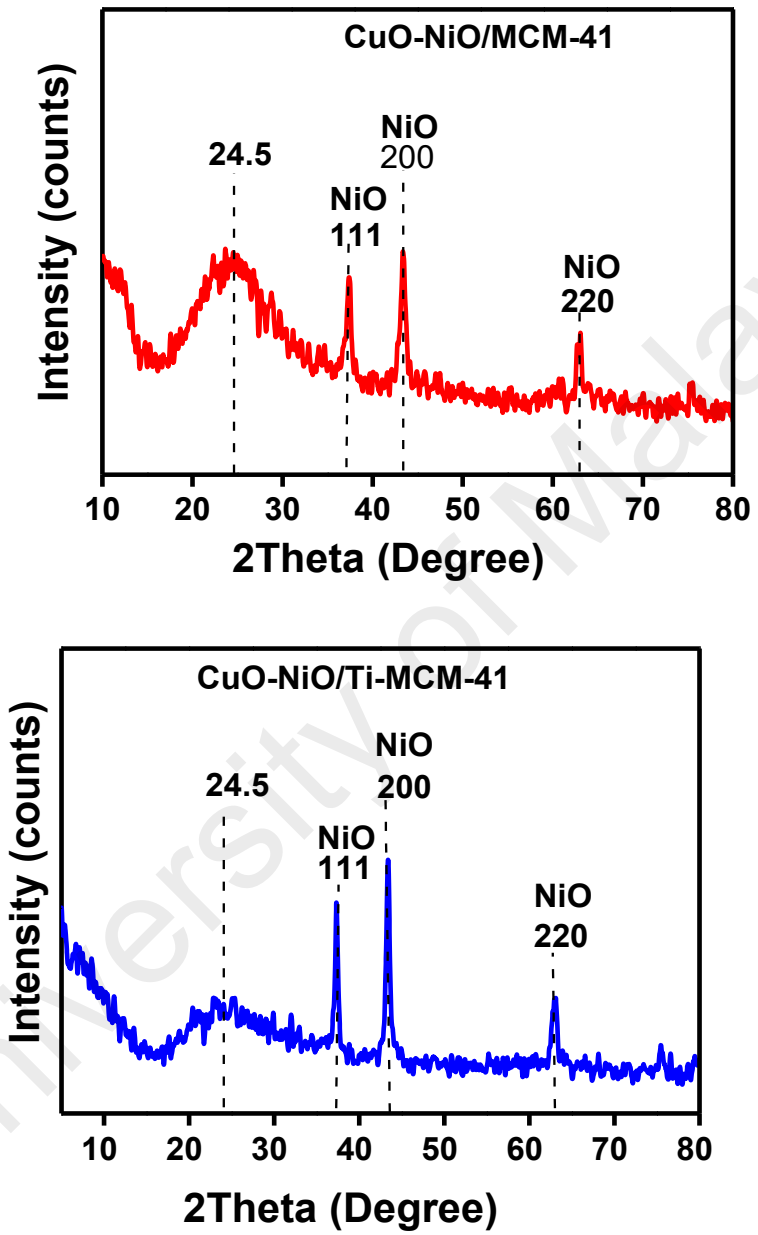

Figure 4.59: The XRD patterns of CuO-NiO bimetallic catalyst supported on MCM-41 and (18%)Ti-MCM-41.

4.7.1.3 Field Emission Scanning Electron Microscopy (FESEM) analysis

In order to have an insight on the morphological dispersion of Cu-O and Ni-O oxides over Ti-MCM-41 and MCM-41, the FESEM analysis has been carried out. As shown in

Figure 4.61, Ni-O species were observed as white dispersed spots over the surface of rope-like mesoporous supports. Although good dispersion of Ni-O can be observed on both supports, dispersion of Ni-O on Ti-MCM-41 is relatively better than on MCM-41 support. The relatively low dispersion of Ni-O on MCM-41 support was due to the weak interaction between the oxides species and weakly attracted surface of MCM-41, which could be resulted to poor distribution of Ni-O during calcination process, thus forming agglomerated particles on the silica surface. It should be noted that, Cu-O species are difficult to observe due to small particle size and high dispersion at lower loading (Sudarsanam et al., 2016). This was in agreement with Raman (Figure 4.59) and XRD (Figure 4.60) results. The better dispersion of active component over Ti-MCM-41 support could be affiliated to its strong acid sites which interact and prevent agglomeration of these active components (Wang et al., 2014b, Selvaraj et al., 2014, Nava et al., 2009).

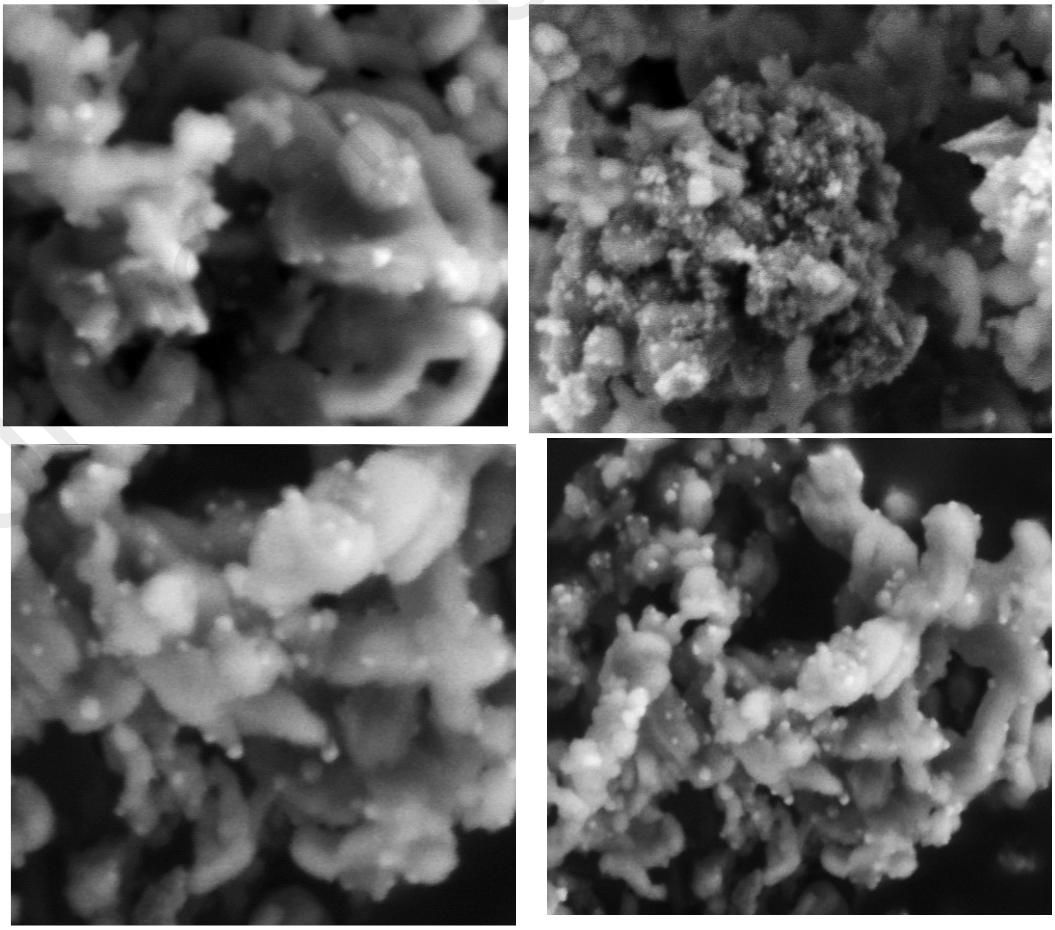

Figure 4.60: The FESEM images of CuO-NiO catalyst supported on (a and b) MCM-41 and (c and d) 18%Ti-MCM-41

4.7.1.4 Hydrogen temperature programmed reduction (H_2-TPR) analysis

The reducibility of Cu-Ni/MCM-41 and Cu-Ni/Ti-MCM-41 catalysts were studied using H_2-TPR technique. As observed from Figure 4.62, the first peak with small hydrogen consumption at ~239.5°C for MCM-41 supported Cu-Ni catalyst can be attributed to the reduction of CuO to Cu (Lin et al., 2008). The noticed second peak at ~321.8°C was assigned to the reduction of bulk CuO-NiO (bi-metallic oxides) to Cu-Ni (bi-metallic catalysts). On the other hand, Ti-MCM-41-supported Cu-Ni catalyst shows a peak with small hydrogen consumption at 165°C, which can be attributed to reduction of highly dispersed Cu-O to Cu (Mallesham et al., 2016). The second peak noticed at 231.4°C can be attributed to the reduction of bulk CuO-NiO (bimetallic oxides) to Cu-Ni (bimetallic state). The presence of interaction between Cu-O and Ni-O led to shifting of both peaks to low temperatures in Cu-Ni/Ti-MCM-41 catalyst compared to Cu-Ni/MCM-41 catalyst (Miranda et al., 2015, Jha et al., 2015, Guo et al., 2015b, Liu et al., 2014). The broad peak observed at 300-500°C region can be assigned to the reduction of Ni-O species to Ni (Amin et al., 2015, Amin et al., 2012). This could be due to (Khromova et al., 2014) the variation of the interaction between Ni-O and Ti-MCM-41 over the adsorption sites located in the mesopores structures (Marrero-Jerez et al., 2014b, Bykova et al., 2012b, Miranda et al., 2015).

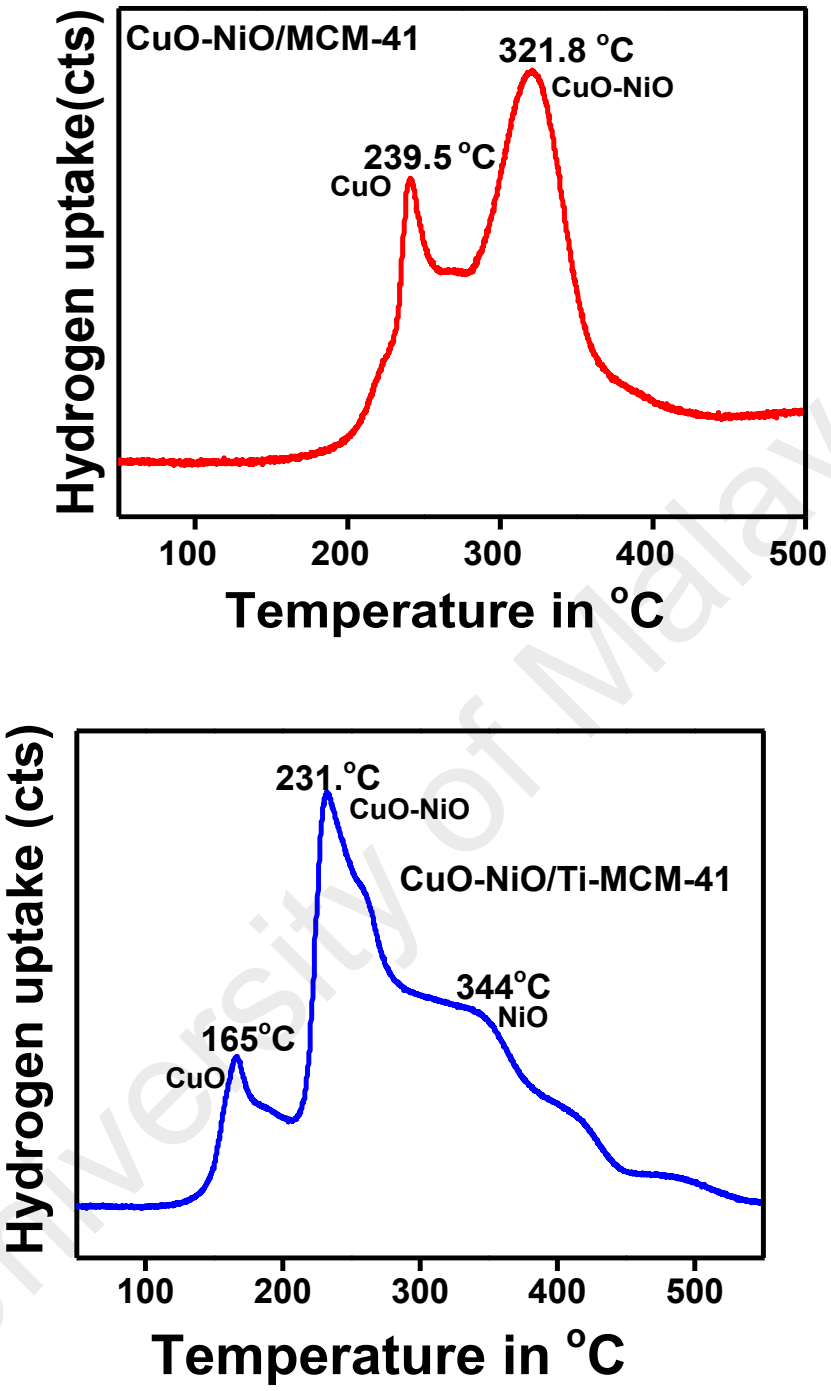

Figure 4.61: The H_2-TPR CuO-NiO bimetallic catalyst supported on MCM-41 and (18%)Ti-MCM-41.

4.7.2 Hydrodeoxygenation of Guaiacol over Cu-Ni catalysts supported on MCM-41, (18%)Ti-MCM-41 and TiO_2

4.7.2.1 Guaiacol conversion and cyclohexane selectivity

The catalytic activity of Cu-Ni catalysts supported on Ti-MCM-41, MCM-41 and TiO_2 were investigated for hydrodeoxygenation of guaiacol under optimized experimental conditions at 260ºC, 10MPa and 6 hours of reaction time (Figure 4.64). The Ti-MCM-41 supported Cu-Ni catalyst showed a higher guaiacol conversion of 91.49% as compared to MCM-41 and TiO_2 supported catalyst with 37.03% and 72.83%, respectively. Also, the calculated selectivity was found to be 50.09% for Cu-Ni/Ti-MCM-41 which is also higher than 10.57% and 34.23% for Cu-Ni/MCM-41 and Cu-Ni/TiO_2 catalysts, respectively. The higher performance of the Cu-Ni/Ti-MCM-41 catalyst could be affiliated to high surface area and strong acidic sites of Ti-MCM-41 support (Figure 4.49) as well as better dispersion supported Cu-Ni catalysts (figure 4.62). Due to high surface area, the synergy between acids and redox sites could be easily achieved hence high catalytic activity of this catalysts. Although, there are high concentration of acids sites and moderate dispersion of supported metals species in Cu-Ni/TiO_2 (Table 4.1 and Figure 4.6) than Cu-Ni/Ti-MCM-41 catalyst but, its performance was limited by the nature of acids site and smaller surface area of TiO_2 support (Figures 4.5 and 4.6). In the case Cu-Ni/MCM-41 catalysts also, there were high surface area and good dispersion of active metal species, but the weak nature and low concentration of acids sites of MCM-41 support denied it relatively high catalytic activity. This suggest that, high surface area and porous support with strong acids sites influence high catalytic performance of Cu-Ni catalysts in hydrodeoxygenation of Guaiacol and dibenzofuran as observed with Cu-Ni/Ti-MCM-41 catalyst. The role of strong acids sites is to promotes deoxygenation either through hydrogenolysis of C-O bonds or dehydration of functional groups and that of redox sites

promote rapid hydrogenation of aromatic ring and other unsaturation within the hydrocarbons molecule to yield saturated hydrocarbons. Other findings with similar observation have been reported earlier (Zhu et al., 2011, Nava et al., 2009, Olcese et al., 2012b, Selvaraj et al., 2014). In general, the catalytic activity of Cu-Ni/Ti-MCM-41 catalysts both in terms of Guaiacol conversion and cyclohexane selectivity, is greater than Cu-Ni/TiO_2 catalysts followed by Cu-Ni/Ti- MCM-41 catalysts respectively.

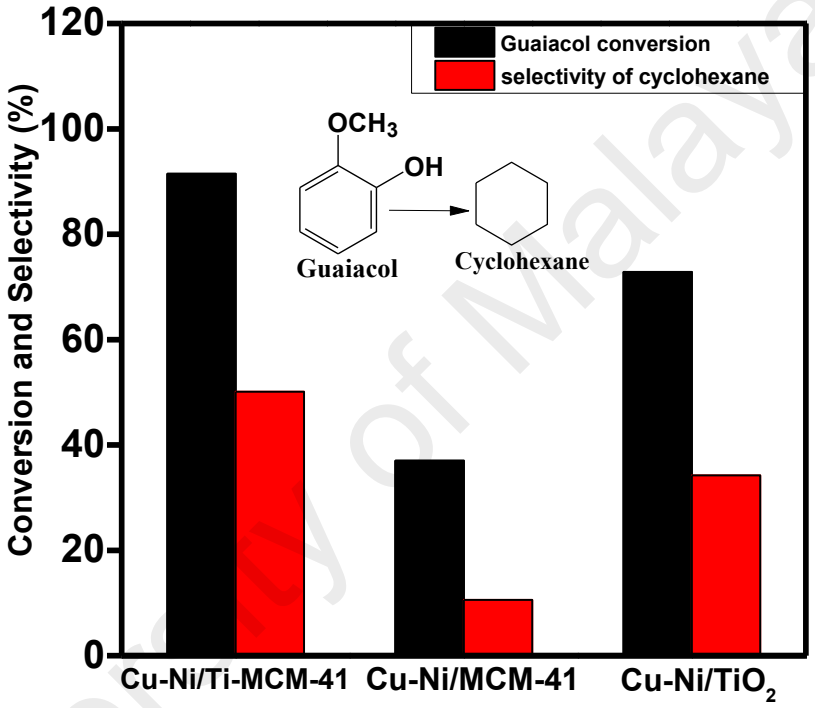

Figure 4.62: Guaiacol conversion and selectivity at 260^{O}C, 10MPa, and 6 hours' reaction time over Cu-Ni/Ti-MCM-41, Cu-Ni/MCM-41 and Cu-Ni/TiO_2.

4.7.2.2 Product distribution

The product distributions from hydrodeoxygenation of guaiacol over Cu-Ni catalysts supported on Ti-MCM-41, MCM-41 and TiO_2 were presented in Figure 4.65. The nature and distribution of products form slightly differed from one catalysts to another. There were four (4) products (cyclohexene (7.07%), cyclohexanone (16.12%), cyclohexanol (17%) and phenol (6.02%)) observed over Cu-Ni/Ti-MCM-41 catalysts. However, different products distribution together with few others which includes (cyclohexene

(11.22%), cyclohexanol (23.14%), phenol (16.13%), methyl-pentane (10.55%), benzene (5.37%) and toluene (20.20%)) were obtained over Cu-Ni/MCM-41 catalysts. On the contrary that, there are more number of distribution of products ((anisole (3.72%), benzene (6.31%), methoxy-cyclohexane (6.57%), phenol (16.11%), cyclohexanone (5.53%), cyclohexanol (10.91%), cyclohexene (9.11%), 1,1-bicyclohexane (4.54%) and others (5.23%)) over Cu-Ni/TiO_2 catalysts. These suggest that, the nature of support influence products distributions in hydrodeoxygenation reactions. The number of products distributions is an indicator to various routes through which hydrodeoxygenation of Guaiacol proceed over these catalysts. The observed products over Cu-Ni/Ti-MCM-41 suggest that, Guaiacol HDO proceed through demethoxylation pathway followed by hydrogenation and dehydration-hydrogenation to cyclohexane. But, in the case of Cu-Ni/MCM-41 guaiacol HDO initially proceed through demethoxylation route to phenol, and thereafter split into two pathways; dihydroxylation through hydrogenolysis to benzene and hydrogenation of aromatic ring to cyclohexanol and each of these routes lead to the formation of cyclohexane. However, the distributed products over Cu-Ni/TiO_2 indicate that, Guaiacol HDO proceed by two possible pathways; 1. Demethoxylation leading to phenol and subsequently to cyclohexane. 2. Dihydroxylation route to anisole which transformed to cyclohexane through few steps.

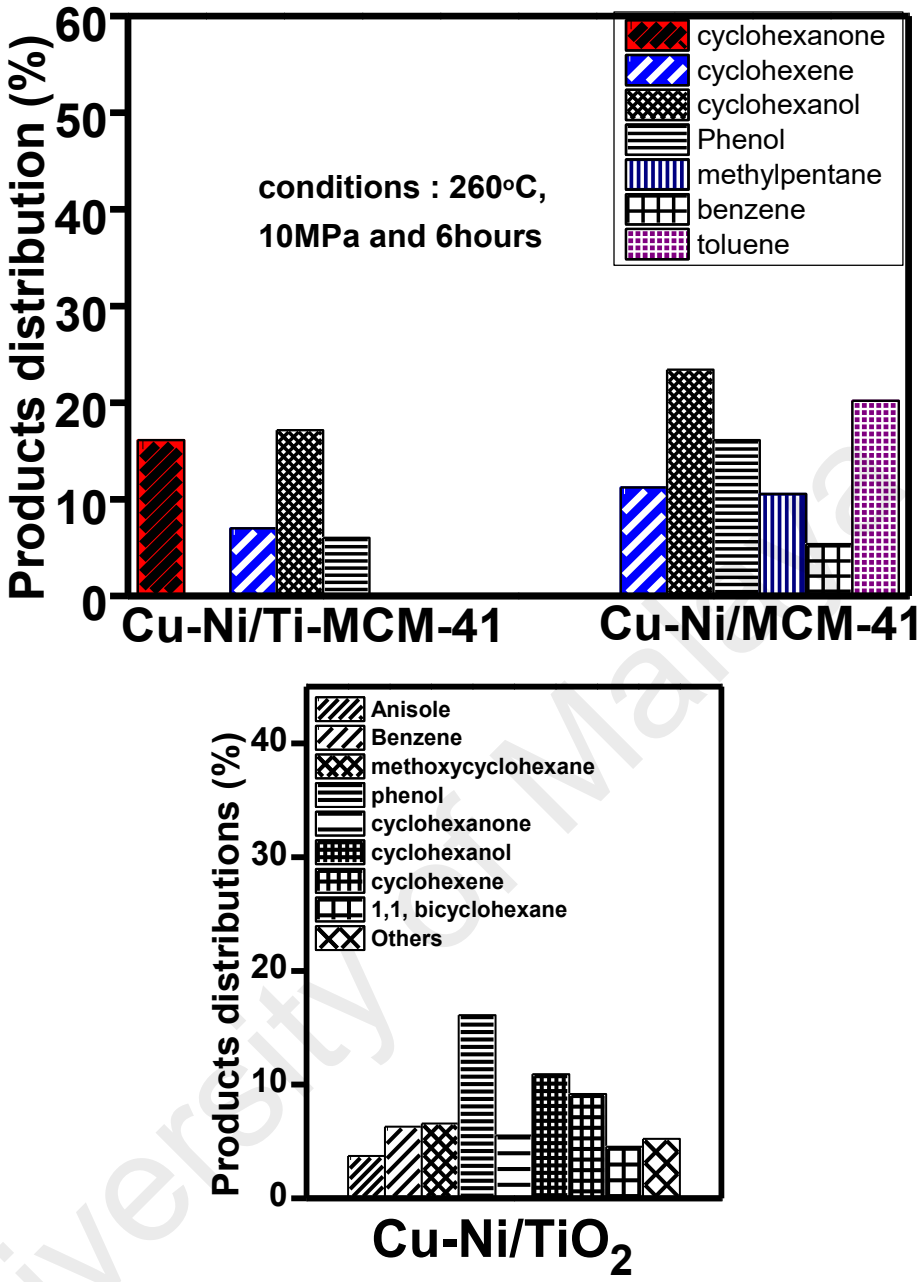

Figure 4.63: Products distributions of Guaiacol HDO over Cu-Ni/Ti-MCM-41, Cu-Ni/MCM-41 and Cu-Ni/TiO_2

4.7.3 Hydrodeoxygenation of dibenzofuran over 2.5%Cu-7.5%Ni catalysts supported on MCM-41, (18%)Ti-MCM-41 and TiO_2

4.7.3.1 Dibenzofuran conversion and Bicyclohexane selectivity

The hydrodeoxygenation of dibenzofuran have been conducted over Cu-Ni/Ti-MCM-41, Cu-Ni/MCM-41and Cu-Ni/TiO_2 catalysts at 260^oC, 10MPa and 6 hrs of reaction time. The dibenzofuran conversion and bicyclohexane selectivity have been shown in Figure 4.65. The results indicate that, there were 96.94%, 41.09% and 75.79% dibenzofuran conversion as well as 65.07%, 11.35% and 41.65% selectivity over Cu-Ni/Ti-MCM-41, Cu-Ni/MCM-41 and Cu-Ni/TiO_2 catalysts. At both conversion and selectivity Cu-Ni/Ti-MCM-41 highly performed than Cu-Ni/MCM-41 and Cu-Ni/TiO_2. The higher catalytic activity of Cu-Ni/Ti-MCM-41 catalyst could be affiliated to strong acid sites of Ti-MCM-41 support as observed from NH_3-TPD analysis (Figure. 4.49) and high surface area (Table 4.9) that were generated by tetrahedral coordinated titanium species within the silica matrix (Wang et al., 2014b, Selvaraj et al., 2014, Nava et al., 2009). The presence of coordinated titanium species could also enhance better dispersion of the active phases within the mesoporous channels of Ti-MCM-41 leading to more reducible number of redox sites over Cu-Ni catalyst (Figure 4.50, Table 4.15), resulting to high conversion and hydrocarbon selectivity over Cu-Ni/Ti-MCM-41 catalyst. On the other hand, the low performance of Cu-Ni/MCM-41 could be affiliated to weak nature and small number sites and that, Cu-Ni/TiO_2 could be associated to small surface area. It's obvious that, Cu-Ni/Ti-MCM-41 catalysts showed better performance than Cu-Ni/MCM-41 but, it should be notice that, the conversion of dibenzofuran over Cu-Ni/MCM-41 and Cu-Ni/TiO_2 were also considerable. The observed conversion and products selectivity over Cu-Ni/TiO_2 could be linked to high concentrations of its medium acids sites of TiO_2 supports as well as moderate dispersion of active components. The performance of Cu-Ni/Ti-MCM-41

could be related to synergetic role between the available weak acids sites of MCM-41 support and dispersed redox sites over high surface area of these catalysts. The deoxygenation through oxygen bearing functional group was promoted by its week acid sites and hydrogenation of the aryl ring is promoted by redox sites. This suggest that, even the week acids sites play key role in HDO reactions. This was coincided with other finding on HDO of model compounds reported in the literature (Zhu et al., 2011, Nava et al., 2009, Olcese et al., 2012b, Selvaraj et al., 2014). The catalytic performance of these catalysts in terms of dibenzofuran conversion and bicyclohexane selectivity followed the following order Cu-Ni/Ti-MCM-41 > Cu-Ni/TiO_2 > Cu-Ni/Ti-MCM-41 respectively.

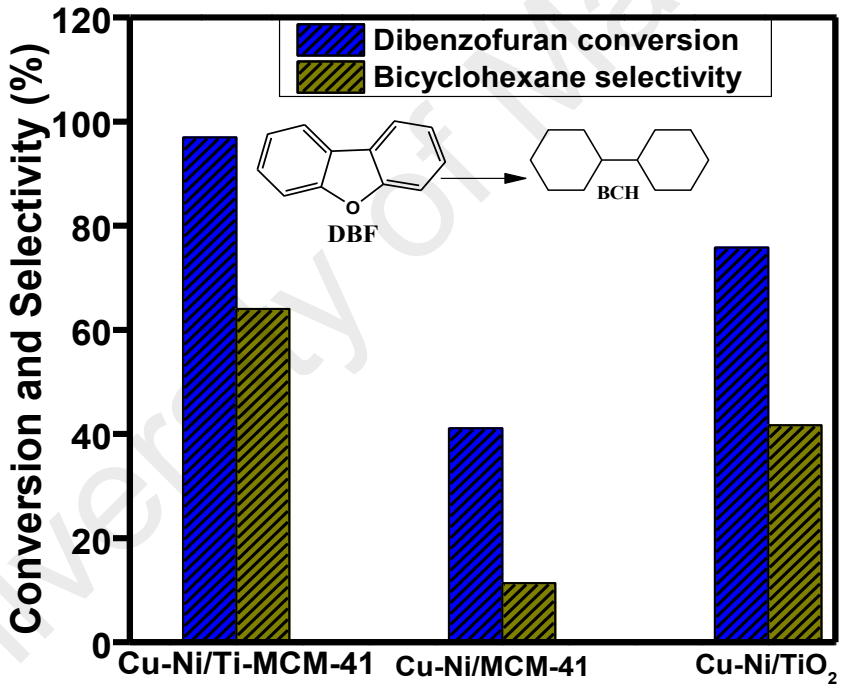

Figure 4.64: Dibenzofuran conversion and bicyclohexane selectivity at 260°C, 10MPa, and 6 hours' reaction time over Cu-Ni/Ti-MCM-41, Cu-Ni/MCM-41 and Cu-Ni/TiO_2

4.7.3.2 Product distributions

The disributed products from hydrodeoxygenation of dibenzofuran over Cu-Ni/Ti-MCM-41, Cu-Ni/MCM-41 and Cu-Ni/TiO_2 are displayed in Figure 4.66. Like in

Guaiacol hydrodeoxygenation, the obtained products distribution over Cu-Ni/Ti-MCM 41 slightly varies in types and percentages with those obtained over Cu-Ni/MCM-41 and Cu-Ni/TiO_2. Basides bicyclohexane, six other products were observed over Cu-Ni/Ti-MCM-41catalysts and percentage amount of these products are cyclohexyl-benzene (4.84%), 2-cyclohexyl-cyclohexanol (5.51%), 1-cyclohexyl-cyclohexene (7.24%), 2-Cyclohexyl-Phenol (7.54%), phenyl-cyclohexanol (5.2%), and [1,1'-Bicyclohexyl]-2-one (7.52%) (5.65%). In addition to these six, another product; 1,2,3,4-Tetrahydrodibenzofuran (22.37%) were also found over MCM-41 supported catalysts. The percentage of those six products (cyclohexyl-benzene (12.05%), 2-cyclohexyl-cyclohexanol (9.76%), 1-cyclohexyl-Cyclohexene (6.55%), 2-Cyclohexyl-Phenol (11.16%), phenyl-cyclohexanol (8.78%), and [1,1'-Bicyclohexyl]-2-one (7.52%) (10.46%) over MCM-41 supported catalysts were observed to be greater than those realized over Ti-MCM-41 supported catalysts.This explained that, the presence of strong acids sites in Ti-MCM-41 supported catalysts (Figure 4.49) enhance rapid transfomation of reaction products/intermidiate toward the oxygen free compounds through hydrogenolysis reactions. The hydrogenation of these compouds into partially or fully saturated compounds was promoted by well dispersed redox sites (Figure 4.61). This suggest that, strong acids sites influence high rate of HDO reactions. On the other hand, due to weak acidic nature of MCM-41 supported catalysts there was slow conversion of the intermidate products leading to more number and concentration of these products over MCM-41 supported catalysts as compared to Ti-MCM-41 supported catalysts. In the case of Cu-Ni/TiO_2 much different products distributions were obtained than those from Ti-MCM-41 and MCM-41 supported catalysts. The products include Decahydro-dibenzofuran (10.09%), 1,2,3,4-Tetrahydro-dibenzofuran (12.55%), bicyclohexylidene (6.78%), 1-cyclohexenyl-cyclohexanol (7.68%), bicyclohexyl-2-one (6.49%), bicyclohexyl-2-ol (9.03%) and bicyclohexyl-1-ene (8.34%). This further suggest that,

products distribution changes with strength of acids sites and serve as indicator to occurance of different reaction routes over different supports.

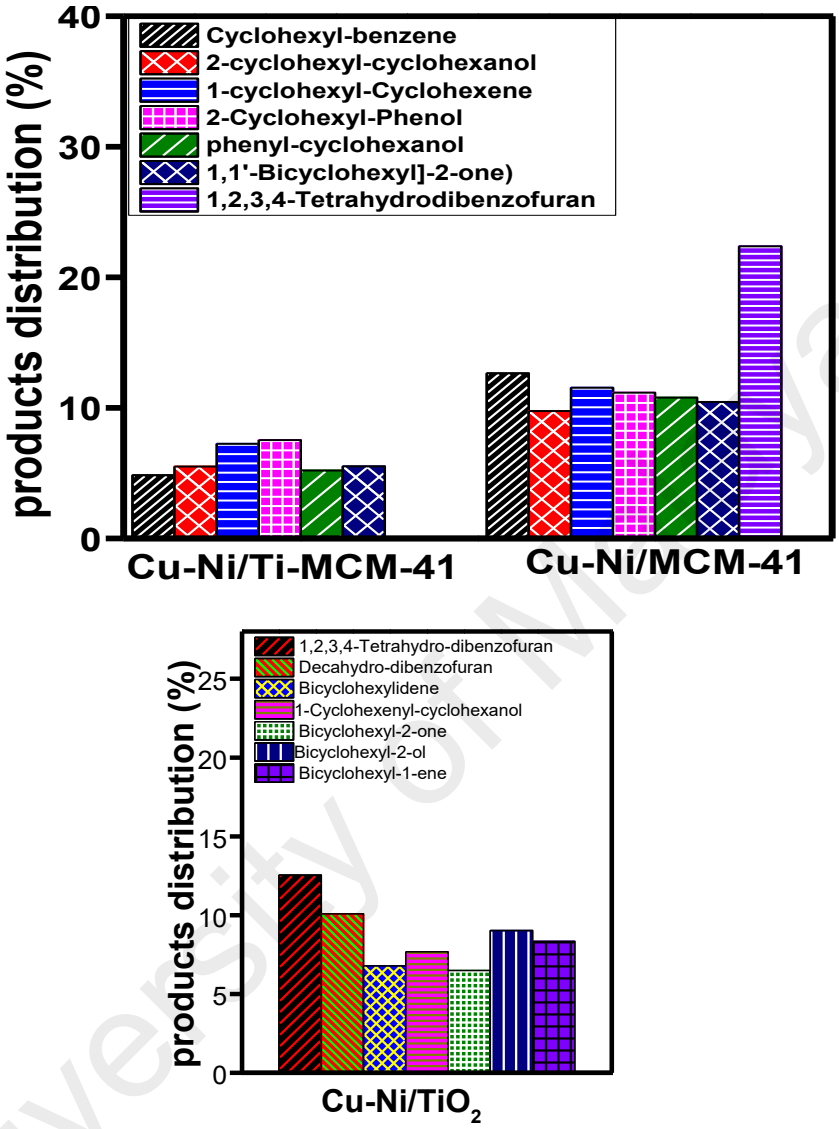

Figure 4.65: Products distributions from HDO of dibenzofuran over Cu-Ni/Ti-MCM-41, Cu-Ni/MCM-41 and Cu-Ni/TiO_2

4.7.4 Proposed reaction pathway for Guaiacol conversion to cyclohexane over 2.5%Cu-7.5%Ni/(18%)Ti-MCM-41 catalysts.

To have an insight into catalytic reaction pathway for Guaiacol conversion to cyclohexane even low reaction time, hydrodeoxygenation was carried out under

experimental conditions of 260ºC, 10MPa with various reaction time from to 6 hours. The obtained products are shown in Figure 4.67 and the results showed six (6) major products with traces of some minor products groups as others. The obtained major oxygenated products include phenol, cyclohexanone and cyclohexanol, the high amount of phenol (35.5%) was observed after one (1) hour of reaction time which continuously decrease as the reaction time proceed to attained the final concentration of 12.04% after six (6) hours. The cyclohexanone and cyclohexanol were realized to have their maximum amount of 19.87 and 23.12% after 2 and 3 hours of reaction time which beyond this time decrease to final amount of 7.12 and 14.15% after six (6) hours of reactions. Pertaining to totally deoxygenated products there are two major products; cyclohexene and cyclohexane which possess the maximum amount of 20 and 53.5% after 5 and 6 hours respectively. The general observation is that, at lower reaction time the concentration of phenol, cyclohexanone and cyclohexanol are higher than cyclohexane and cyclohexane but as the reaction proceed to high reaction time the concentration of these species decreases drastically and those of cyclohexane and cyclohexane increases tremendously. This suggest that, the former ones (phenol, cyclohexanone and cyclohexanol) were the reaction intermediates for the formation of the later ones (cyclohexane and cyclohexane).

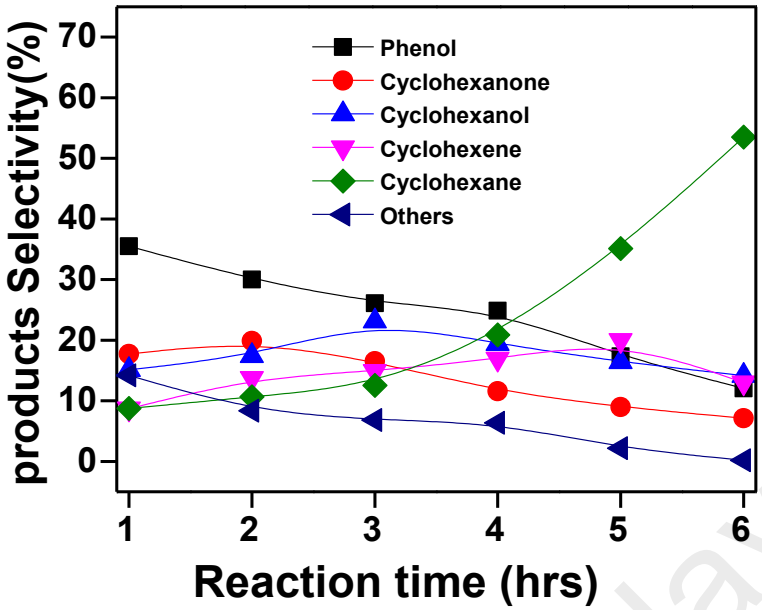

Figure 4.66: Products distributions from Guaiacol HDO over Cu-Ni/Ti-MCM-41 at 260°C, 10MPa and 6 hours of reaction time.

According to observed reactions intermediates, the reaction mechanisms was proposed; Scheme 1 and as shown in the mechnisms that, the reactions is suggested to proceed by hydrogenolysis of C-OCH_3 bond favouring demethoxylation pathway. In this regards, Guaiacol molecules interact with Lewis acids sites of Cu-Ni/Ti-MCM-41 catalysts via lone paired of electron leading to weakening of C-OCH_3 bonds and resulted to elimination of OCH_3 group thereby formation of phenol as the first intermediate compound obtained. The hydrogenation of the phenolic ring by the redox sites was resulted to the formation of cyclohexanol via cyclohexanone. Dehydration of cyclohexanol was promoted by acids sites leading to production of cyclohexene which underwent hydrogenations over redox sites to yield cyclohexane.

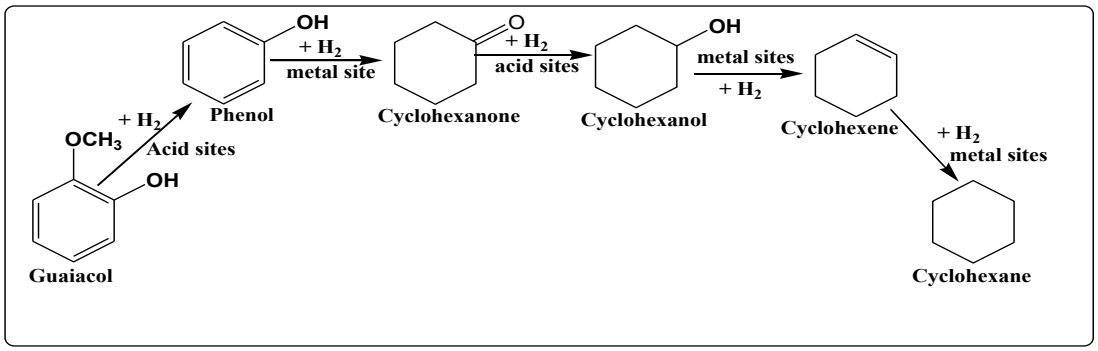

Figure 4.67: Proposed reaction pathway for Guaiacol conversion to cyclohexane over 2.5%Cu-7.5%Ni/ (18%)Ti-MCM-41 catalysts

4.7.5 Reaction pathway for dibenzofuran conversion to bicyclohexane HDO over 2.5%Cu-7.5%Ni/(18%)Ti-MCM-41 catalysts.

In order to proposed catalytic reactions pathways for hydrodeoxygenation of dibenzofuran to bicyclohexane over Cu-Ni/Ti-MCM-41, product formation across the range of reaction time from 1 to 6 hours were studied at our experimental reaction conditions. The obtained products were displayed in Figure 4.69. the number of minor products from 2 to 6 hours of reaction time does not exceed 6.98%. However, the number of major products show periodic trend as the reaction time proceed. It's obvious that, at shorter reaction time, the number of oxygenated products such as tetrahydrodibenzofuran, 2-cyclohexyl-phenol, cyclohexyl-cyclohexanol and cyclohexyl-cyclohexanone were observed to be higher content as compared to totally deoxygenated products. However, as the time proceed to longer reaction time, their concentration was continuously decreasing. It was observed after 2 hours of reactions time that, the amount of tetrahydrodibenzofuran and cyclohexyl-phenol reached maximum concentration of 40.44% and 20.44% respectively. Beyond this point, they continue to decreased to their final concentrations of 3.92% and 0.54% respectively. The amount of saturated oxygenated products such as cyclohexyl-cyclohexanol and cyclohexyl-cyclohexanone reached 6.44% after 5 hours and continuously decrease to final amount of 6.98% after 6 hours of reaction time respectively. Also, the concentration of other intermediates such

as cyclohexyl-benzene, cyclohexyl-cyclohexene attained high amount of 20.11% and 19.21% after 3 and 4 hours of reaction time. On the contrary, the lower amount of totally deoxygenated and saturated products such as bicyclohexane and cyclopentylmethyl-cyclohexane were obtained after 2 and 3 hours of reaction time respectively. These compounds show increasing trend with reaction time with minimum and maximum selectivity of bicyclohexane being 11.31% and 65.56% after 2 to 6 hours of reaction time and that of cyclopentylmethyl-cyclohexane were obtained as 4.12% and 10.38% after 3 and 6 hours of reaction time respectively. As the concentration of bicyclohexane and cyclopentylmethyl-cyclohexane begin to increase substantially, certain quantity of these products underwent partial cracking to yield pentyl-cyclohexane but, it observed concentration is small around 0.52% which was only observed after 5 hours of reaction time. The major observation is that, there were more concentration of oxygenated products at lower reaction time but at higher reaction time the number of deoxygenated compounds outweighed oxygenated products. This means that, the earlier observed oxygenates are the reaction intermediates for the formation of the formation of cyclohexane and it associated saturated hydrocarbons over Cu-Ni/Ti-MCM-41 catalysts.

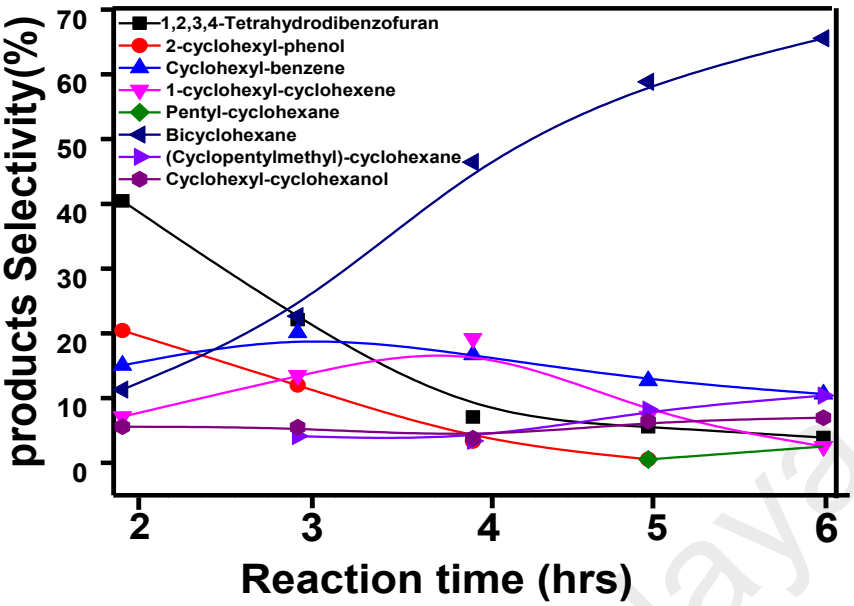

Figure 4.68: Products distributions from HDO of dibenzofuran over Cu-Ni/Ti-MCM-41.

Considering the types of intermediate products observed as the reaction proceed with time, HDO reaction pathway for conversion of dibenzofuran to saturated hydrocarbon molecules have been proposed. As shown in the proposed pathway, the reaction proceeds by hydrogenation of DBF aromatic ring followed by deoxygenation through hydrogenolysis or dehydration and in the final stage total hydrogenation to produced saturated hydrocarbon compounds. The formation of these products over Cu-Ni/Ti-MCM-41 catalysts was briefly described. The 1,2,3,4-Tetrahydrodibenzofuran (TH-DBF) was obtained from partial hydrogenation of dibenzofuran due to consumption of two hydrogen molecule ($2H_2$) over redox sites of Ti-MCM-41 supported catalysts. The hydrogenolysis and hydrogenation of TH-DBF was promoted by acids sites and redox sites within the vicinity to yields 2-cyclohexyl-phenol (CH-POH) which went further hydrolysis to produced cyclohexyl-benzene over acids sites. However, due to heterogenous dispersion of redox sites over the catalysts surface, there could be more number of redox sites in other part of this surface, dominated acids sites functionality hence, transformed CH-POH to cyclohexyl-cyclohexanol (CH-CHOH)/cyclohexyl-

cyclohexanone (CH-CHO)/ through hydrogenation. The CH-CHOH was directly dehydrated or CH-CHO got hydrogenated and further dehydrated to yield 1-cyclohexyl-cyclohexene which reduced to bicyclohexane or isomerized to cyclopentylmethyl-cyclohexane. The presence of pentyl-cyclohexane affiliated to cracking of cyclopentylmethyl-cyclohexane during HDO reaction over Cu-Ni/Ti-MCM-41 catalysts.

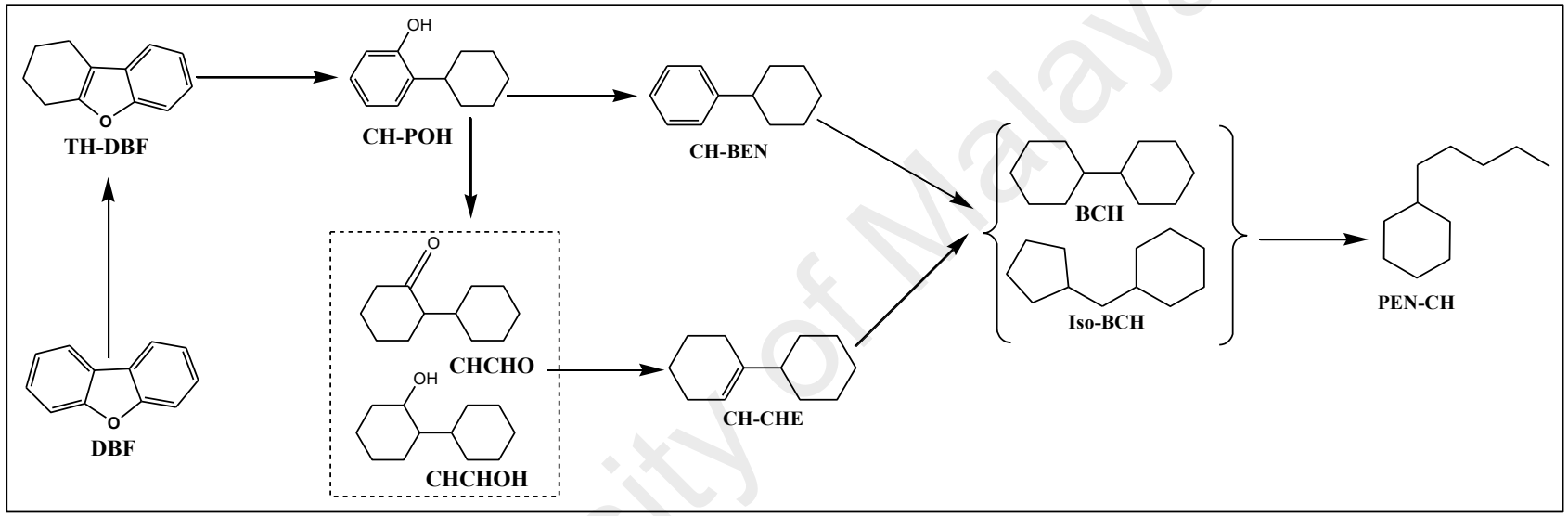

Figure 4.694.69 :Proposed reaction pathways for DBF conversion to bicyclohexane over 2.5%Cu-7.5%Ni/ (18%)Ti-MCM-41 catalysts

4.7.6 Reusability studies

To have an insight into stability of 2.5%Cu-7.5%Ni/(18%)Ti-MCM-41catalysts, hydrodeoxygenaton of dibenzofuran was assessed for upto 4 cycle under experimental conditions of 260ºC, 10MPa and 6 hours of reaction time with 100mg of catalysts and 1000rpm stirring speed for upto 4 run . The experimental results obtained for dibenzofuran conversion and bicyclohexane selectivity were displayed in figure 4.70. According to obtained results, the conversion of dibenzofuran were 95.93%, 95.47%, 94.77% and 90.35% for 1st, 2nd, 3rd, and 4th run. Also the selectivity of bicyclohexane were observed to be 65.11%, 64.65%, 64.45% and 64.01%, respectivily. There was no significance differences in conversion of dibenzofuran for upto 3rd run but, some activity lost of 5.58% were observed after the 4th run. However, the selectivity of bicyclohexane was slightly affected upto the 4th run with lost of 1.1%. in the Ccase of guiacol HDO,high conversions and appreciable selectivity were observed upto 4th run. The observed guaiacol conversions were 91.91%, 89.35%, 88.29% and 87.33% in dicating decresed of 4.98% of guaiacol conversions for upto four cycles. The observed cyclohexane selectivity for upto four cycles were 50.01%, 49.96%, 49.45% and 48.85% which account for the selectivity loss of 2.32%. this suggest that, 2.5%Cu-7.5%Ni/(18%)Ti-MCM-41catalysts has certain degree of stability. The maintainance of surface chemical structures of 2.5%Cu-7.5%Ni/(18%)Ti-MCM-41catalysts during these four (4) runs, could be affiliated to strong acidity, generated by incorporated Ti species in the mesoporous Ti-MCM-41 support.

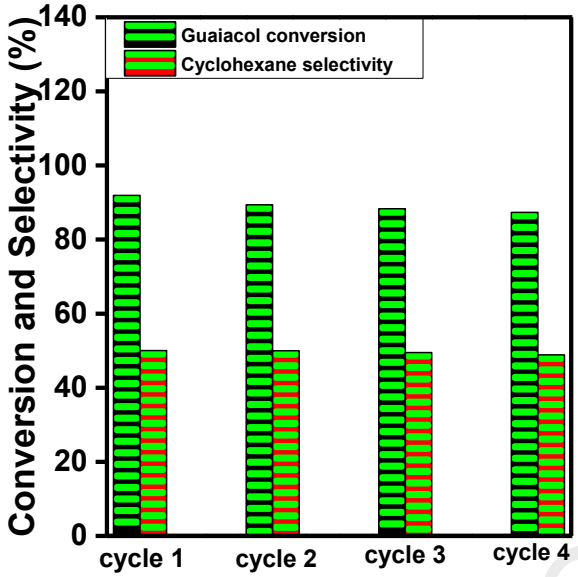

Figure 4.70: Guaiacol conversion and Cyclohexane selectivity for reusability studies at 10MPa, 260°C and 6 hours' reaction time over NiCu/Ti-MCM-41

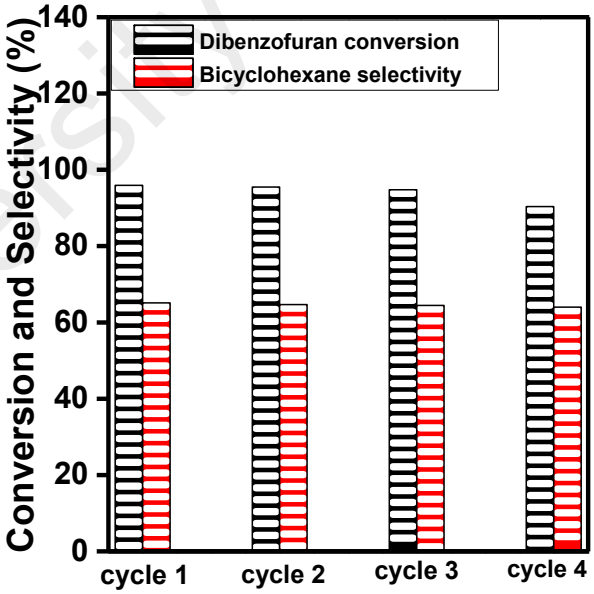

Figure 4.71 : Reusability studies over 2.5%Cu-7.5%Ni/ (18%)Ti-MCM-41 catalysts; DBF conversion and bicyclohexane selectivity at 260°C, 10MPa and 6 hours.

CHAPTER 5: CONCLUSION AND RECOMMENDATION

5.1 CONCLUSION

There are several pulp and paper industry in Asia and Malaysia in particular. Large amount of lignin biomass is extracted by these pulp and paper industry through Kraft process and the potential to convert lignin biomass into bio oil have been explored and revealed to be promising in the sense that, it's renewable, sustainable, and environmentally friendly. The potential of lignin derived bio oil toward transportation fuels has been considered to be enormous. However, it transformation to suitable fuel is mainly depend on the applied catalysts and conversion technology. In order to understand the performance and effective of the new catalysts system for upgrading of lignin derived bio oil, model compounds are usually considered due to it associated complexes compounds. Several catalysts systems have been studies using different model compounds, however, up to now, effective, efficient and promising catalysts remain a big challenge that required continuous focus. The work conducted in this thesis was developing inexpensive non-noble metals supported catalysts for HDO of lignin derived oil model compounds (Guaiacol and Dibenzofuran).

To investigate the potential of metal oxides for hydrodeoxygenations reactions under mild conditions, Cu-Ni/CeO_2, Cu-Ni/ZeO_2 and Cu-Ni/TiO_2 were synthesized via impregnation method and physico-chemical properties of catalysts was further investigated. The catalytic activity of these catalysts was compared for hydrodeoxygenation of Guaiacol and Dibenzofuran under the experimental condition of 250^{o}C, 5MPa and 4 hours reaction time. The results showed that, Cu-Ni/TiO_2 catalysts possessed higher catalytic performance than Cu-Ni/CeO_2 and Cu-Ni/ZeO_2. Hence, Cu-Ni/TiO_2 catalysts was selected for further studies for better improvement in catalyst's properties and catalytic activity.

In order to enhance metal dispersion and catalytic activity of Cu-Ni/TiO_2, Ni loading (5-12.5wt.%) was further optimized. In this regard, each Ni loading was prepared using wet impregnation method, and compared for hydrodeoxygenation of Guaiacol and dibenzofuran at 250^oC, 5MPa and 4 hours of reaction time. The results indicate highest conversion and selectivity for 10% Ni loading in (Cu-Ni/TiO_2) catalyst with 61.00% and 31.66%, for guaiacol and 63% and 41% for dibenzofuran respectively. Hence, this catalyst was selected for further comparative study with mesoporous based catalysts.

To enhance catalytic conversion and hydrocarbon selectivity in HDO of Guaiacol and dibenzofuran, mesoporous materials and metal-doped mesoporous catalysts were incorporated as catalysts support for synthesis of Cu-Ni active bimetallic-based. To achieve this, mesoporous MCM-41 and Ti-MCM-41 (Si/Ti =15%) were synthesized via hydrothermal method and physico-chemically characterized. The results showed that, both MCM-41 and Ti-MCM-41 possess high surface area and moderate pore sizes. Ti-MCM-41 has higher number of acids sites with strong acidic strength as compared to MCM-41. Hence, Ti-MCM-41 support was selected for further optimization in different Ni loading in Cu-Ni/Ti-MCM-41 catalyst.

To optimize Ni loading for mesoporous supported catalysts, Cu-Ni/Ti-MCM-41were prepared using wet impregnation method with various weight percent (from 5 to 12.5wt.%) of Ni by maintained Cu loading unchanged (2.5 wt.%). The catalysts were tested for HDO of Guaiacol and dibenzofuran under optimized reaction condition at 260^oC, 10MPa and 6 hours of reaction time. Results showed that 10wt.% of Ni (7.5wt.%) and Cu (2.5wt.%) loading was much high in conversion and hydrocarbon selectivity than another Ni loading. To also investigate catalysts structure-activity correlation four different Ni loading with high performance were selected and physico-chemically

characterized. The correlation studies showed there was better correlation between activity and metal dispersion.

To further enhance catalytic activity of Cu-Ni/Ti-MCM-41 catalysts by investigating the optimum of Ti content, Ti-MCM-41 support with various Ti loading (10-30wt.%) was prepared by hydrothermal method. The prepared supports were characterized, then impregnated with 10wt.% Ni and Cu loading (3:1), further characterized and tested for HDO of Guaiacol and dibenzofuran at 260^{o}C, 10MPa and 6 hours of reaction time. The results showed that, 2.5wt.%Cu-7.5wt.%Ni/20wt.%Ti-MCM-41 catalysts was much high in Guaiacol and dibenzofuran conversion and hydrocarbon selectivity than other Ti loaded supports. Also, the physico-chemical characterization of three different supports and supported catalysts was conducted and correlated with activity of the catalysts. The structure-activity correlations showed that, catalytic activity correlated strongly with acidity of these catalysts.

Enhancement acidity of Ti-MCM-41 support and catalytic activity of Cu-Ni/Ti-MCM-41 was further narrow down by optimized the Ti content (12, 16 & 18%) with respect to Si content. These supports were also synthesized hydrothermally and characterized. The results showed that, Ti-MCM-41 with 18% Ti content has highest acidity compared to other support with different Ti content. The summary of the hydrodeoxygenation activity of 2.5wt.%Cu-7.5wt.%Ni/18%wt.%Ti-MCM-41 catalysts was highlight herein:The comparative studies of Cu-Ni/(18%)Ti-MCM-41with Cu-Ni/TiO_2 and Cu-Ni/MCM-41 was conducted for hydrodeoxygenation of Guaiacol and dibenzofuran at 260^{o}C, 10MPa and 6 hours of reaction time. The result show that, the catalytic activity of Cu-Ni/Ti-MCM-41 is much higher than other two supported catalysts. The Cu-Ni/Ti-MCM-41 catalysts possess high Guaiacol and dibenzofuran conversion (91.49% and 96.94%) and hydrocarbons selectivity (Cyclohexane. 50.09% and Bicyclohexane. 65.07%,) followed

by Cu-Ni/TiO_2 (Guaiacol = 61.29% and dibenzofuran = 65.24%, Cyclohexane =39.76% and Bicyclohexane = 43.45%) then Cu-Ni/MCM-41(Guaiacol = 37.29% and dibenzofuran = 41.09%, Cyclohexane =10.57% and Bicyclohexane = 11.35%). The evaluation of catalysts structure-activity relationship showed that, there were good correlation between catalysts structures and its activity. The reusability studies showed that, the catalysts were stable for up to 4 cycles.

Finally, the following conclusion were drawn from the entire studies of this thesis:

- The pefomance of metal oxides supported catalysts for HDO of Guaiacol and dibenzofuran under mild temperature conditions were found to decreased in the following order; Cu-Ni/TiO_2 > Cu-Ni/CeO_2 > Cu-Ni/ZeO_2.
- The incorporation of Ti species within the matrix of MCM-41 generate strong acids sites.
- The optimization of Ni loading greatly influence better dispersion of Cu-Ni/Ti-MCM-41 catalysts, hence high catalytic activity of this catalysts for hydrodeoxygenation of Guaiacol and dibenzofuran.
- The optimization of Ti content of Ti-MCM-41 supports strongly enhance it strong acids sites and hence high catalytic activity of Cu-Ni/Ti-MCM-41 catalysts for hydrodeoxygenation of Guaiacol and Dibenzofuran.
- The Catalytic performance of Cu-Ni/Ti-MCM-41 catalysts was much high than Cu-Ni/TiO_2 followed by Cu-Ni/MCM-41 for hydrodeoxygenation of Guaiacol and dibenzofuran.
- The reusability study shows that, Cu-Ni/Ti-MCM-41 catalysts retained it surface chemical stability for upto 4 run (with final dibenzofuran conversion of 90.35% and

bicyclohexane selectivity of 64.01% as well as final Guaiacol conversion of 85.33% and cyclohexane selectivity of 48.74%). Signifying it high thermal stability.

- Finally mesoporous Cu-Ni/Ti-MCM-41 catalysts is an effective supported catalysts for hydrodeoxygenation of lignin derived model compounds (Guaiacol and dibenzofuran) to fuel graded molecules.

5.2 Recommendation for future studies

The finding in this thesis showed that, the prospect and suitability for the application of Ti-MCM-41 as an effective catalysts support for Cu-Ni bimetallic catalysts in hydrodeoxygenation of lignin-derived oil model compounds. However, some recommendation followed before further application for bio-refinary upgrading processes.

- It was also recommended for characterization of re-used catalysts for comparism with un used catalysts.
- There is the need to studies catalytic reaction kinetic modelling for further reactor design.
- There is also need for direct application of Cu-Ni/Ti-MCM-41 catalysts into real lignin derived bio oil and not only model compounds.

References

Adams, K. M., Cavataio, J. V., Sale, T., Rimkus, W. A., & Hammerle, R. H. (1996). *Laboratory screening of diesel oxidation catalysts and validation with vehicle testing: The importance of hydrocarbon storage* (0148-7191). Retrieved from

Akhtar, J., & Amin, N. A. S. (2011). A review on process conditions for optimum bio-oil yield in hydrothermal liquefaction of biomass. *Renewable and Sustainable Energy Reviews, 15*(3), 1615-1624.

Al-Obaidi, H. N. (2015). Beam analysis of scanning electron microscope according to the mirror effect phenomenon. *Journal of Electrostatics, 74*, 102-107.

ALOthman, Z. A. (2012). A review: fundamental aspects of silicate mesoporous materials. *Materials, 5*(12), 2874-2902.

Ambursa, M. M., Ali, T. H., Lee, H. V., Sudarsanam, P., Bhargava, S. K., & Hamid, S. B. A. (2016b). Hydrodeoxygenation of dibenzofuran to bicyclic hydrocarbons using bimetallic Cu–Ni catalysts supported on metal oxides. *Fuel, 180*, 767-776.

Ambursa, M. M., Sudarsanam, P., Voon, L. H., Hamid, S. B. A., & Bhargava, S. K. (2017). Bimetallic Cu-Ni catalysts supported on MCM-41 and Ti-MCM-41 porous materials for hydrodeoxygenation of lignin model compound into transportation fuels. *Fuel Processing Technology, 162*, 87-97.

Amen-Chen, C., Pakdel, H., & Roy, C. (2001). Production of monomeric phenols by thermochemical conversion of biomass: a review. *Bioresource technology, 79*(3), 277-299.

Amin, M. H., Mantri, K., Newnham, J., Tardio, J., & Bhargava, S. K. (2012). Highly stable ytterbium promoted Ni/γ-Al 2 O 3 catalysts for carbon dioxide reforming of methane. *Applied Catalysis B: Environmental, 119*, 217-226.

Amin, M. H., Putla, S., Hamid, S. B. A., & Bhargava, S. K. (2015). Understanding the role of lanthanide promoters on the structure–activity of nanosized Ni/γ-Al 2 O 3 catalysts in carbon dioxide reforming of methane. *Applied Catalysis A: General, 492*, 160-168.

Aneggi, E., de Leitenburg, C., Dolcetti, G., & Trovarelli, A. (2006). Promotional effect of rare earths and transition metals in the combustion of diesel soot over CeO 2 and CeO 2–ZrO 2. *Catalysis Today, 114*(1), 40-47.

Anunziata, O. A., Beltramone, A. R., & Cussa, J. (2008). Synthesis at atmospheric pressure and characterization of highly ordered Al, V, and Ti-MCM-41 mesostructured catalysts. *Catalysis Today, 133–135*, 891-896.

Anunziata, O. A., Beltramone, A. R., & Cussa, J. (2008). Synthesis at atmospheric pressure and characterization of highly ordered Al, V, and Ti-MCM-41 mesostructured catalysts. *Catalysis Today, 133*, 891-896.

Appaturi, J. N., Adam, F., & Khanam, Z. (2012). A comparative study of the regioselective ring opening of styrene oxide with aniline over several types of

mesoporous silica materials. *Microporous and Mesoporous Materials, 156*, 16-21.

Ardiyanti, A., Gutierrez, A., Honkela, M., Krause, A., & Heeres, H. (2011). Hydrotreatment of wood-based pyrolysis oil using zirconia-supported mono-and bimetallic (Pt, Pd, Rh) catalysts. *Applied Catalysis A: General, 407*(1), 56-66.

Argyle, M. D., & Bartholomew, C. H. (2015). Heterogeneous catalyst deactivation and regeneration: a review. *Catalysts, 5*(1), 145-269.

Atribak, I., Bueno-Lopez, A. n., & García-García, A. (2008). Thermally stable ceria–zirconia catalysts for soot oxidation by O 2. *Catalysis Communications, 9*(2), 250-255.

Atribak, I., López-Suárez, F. E., Bueno-López, A., & García-García, A. (2011). New insights into the performance of ceria–zirconia mixed oxides as soot combustion catalysts. Identification of the role of "active oxygen" production. *Catalysis today, 176*(1), 404-408.

Azadi, P., Inderwildi, O. R., Farnood, R., & King, D. A. (2013). Liquid fuels, hydrogen and chemicals from lignin: A critical review. *Renewable and Sustainable Energy Reviews, 21*, 506-523.

Babu, B. (2008). Biomass pyrolysis: a state-of-the-art review. *Biofuels, Bioproducts and Biorefining, 2*(5), 393-414.

Badawi, M., Paul, J.-F., Payen, E., Romero, Y., Richard, F., Brunet, S., . . . Mariey, L. (2013). Hydrodeoxygenation of Phenolic Compounds by Sulfided (Co) Mo/Al2O3 Catalysts, a Combined Experimental and Theoretical Study. *Oil & Gas Science and Technology–Revue d'IFP Energies nouvelles, 68*(5), 829-840.

Badin, J., & Kirschner, J. (1998). Biomass greens US power production. *Renewable Energy World, 1*(3), 40-42, 44.

Badoga, S., Sharma, R. V., Dalai, A. K., & Adjaye, J. (2014). Hydrotreating of Heavy Gas Oil on Mesoporous Mixed Metal Oxides (M–Al2O3, M= TiO2, ZrO2, SnO2) Supported NiMo Catalysts: Influence of Surface Acidity. *Industrial & Engineering Chemistry Research, 53*(49), 18729-18739.

Banoub, J., Delmas, G. H., Joly, N., Mackenzie, G., Cachet, N., Benjelloun-Mlayah, B., & Delmas, M. (2015). A critique on the structural analysis of lignins and application of novel tandem mass spectrometric strategies to determine lignin sequencing. *Journal of Mass Spectrometry, 50*(1), 5-48.

Banoub, J. H., & Delmas, M. (2003). Structural elucidation of the wheat straw lignin polymer by atmospheric pressure chemical ionization tandem mass spectrometry and matrix-assisted laser desorption/ionization time-of-flight mass spectrometry. *Journal of Mass Spectrometry, 38*(8), 900-903.

Barbier, J., Charon, N., Dupassieux, N., Loppinet-Serani, A., Mahé, L., Ponthus, J., . . . Cansell, F. (2012). Hydrothermal conversion of lignin compounds. A detailed

study of fragmentation and condensation reaction pathways. *biomass and bioenergy, 46*, 479-491.

Ben, H., Mu, W., Deng, Y., & Ragauskas, A. J. (2013). Production of renewable gasoline from aqueous phase hydrogenation of lignin pyrolysis oil. *Fuel, 103*, 1148-1153.

Bendahou, K., Cherif, L., Siffert, S., Tidahy, H., Benaissa, H., & Aboukais, A. (2008). The effect of the use of lanthanum-doped mesoporous SBA-15 on the performance of Pt/SBA-15 and Pd/SBA-15 catalysts for total oxidation of toluene. *Applied Catalysis A: General, 351*(1), 82-87.

Berenguer, A., Sankaranarayanan, T., Gómez, G., Moreno, I., Coronado, J., Pizarro, P., & Serrano, D. (2016). Evaluation of transition metal phosphides supported on ordered mesoporous materials as catalysts for phenol hydrodeoxygenation. *Green Chemistry, 18*(7), 1938-1951.

Bianchi, A., Campanati, M., Maireles-Torres, P., Castellon, E. R., López, A. J., & Vaccari, A. (2001). Si/Zr mesoporous catalysts for the vapour phase synthesis of alkylindoles. *Applied Catalysis A: General, 220*(1), 105-112.

Bing, J., Li, L., Lan, B., Liao, G., Zeng, J., Zhang, Q., & Li, X. (2012). Synthesis of cerium-doped MCM-41 for ozonation of p-chlorobenzoic acid in aqueous solution. *Applied Catalysis B: Environmental, 115-116*, 16-24.

Bobleter, O. (1994). Hydrothermal degradation of polymers derived from plants. *Progress in polymer science, 19*(5), 797-841.

Bore, M. T., Marzke, R. F., Ward, T. L., & Datye, A. K. (2005). Aerosol synthesized mesoporous silica containing high loading of alumina and zirconia. *Journal of Materials Chemistry, 15*(47), 5022-5028.

Boukoussa, B., Zeghada, S., Ababsa, G. B., Hamacha, R., Derdour, A., Bengueddach, A., & Mongin, F. (2015). Catalytic behavior of surfactant-containing-MCM-41 mesoporous materials for cycloaddition of 4-nitrophenyl azide. *Applied Catalysis A: General, 489*, 131-139.

Bozzola, J. J., & Russell, L. D. (1999). *Electron microscopy: principles and techniques for biologists*: Jones & Bartlett Learning.

Breysse, M., Portefaix, J., & Vrinat, M. (1991). Support effects on hydrotreating catalysts. *Catalysis today, 10*(4), 489-505.

Bridgwater, A., & Peacocke, G. (2000). Fast pyrolysis processes for biomass. *Renewable and sustainable energy reviews, 4*(1), 1-73.

Bridgwater, A. V. (2012). Review of fast pyrolysis of biomass and product upgrading. *Biomass and Bioenergy, 38*, 68-94.

Bu, Q., Lei, H., Zacher, A. H., Wang, L., Ren, S., Liang, J., . . . Zhang, Q. (2012). A review of catalytic hydrodeoxygenation of lignin-derived phenols from biomass pyrolysis. *Bioresource technology, 124*, 470-477.

Bueno-López, A., Krishna, K., Makkee, M., & Moulijn, J. A. (2005). Active oxygen from CeO2 and its role in catalysed soot oxidation. *Catalysis Letters, 99*(3-4), 203-205.

Bui, V. N., Laurenti, D., Afanasiev, P., & Geantet, C. (2011). Hydrodeoxygenation of guaiacol with CoMo catalysts. Part I: Promoting effect of cobalt on HDO selectivity and activity. *Applied Catalysis B: Environmental, 101*(3), 239-245.

Bui, V. N., Laurenti, D., Delichère, P., & Geantet, C. (2011a). Hydrodeoxygenation of guaiacol. *Applied Catalysis B: Environmental, 101*(3-4), 246-255.

Bui, V. N., Laurenti, D., Delichère, P., & Geantet, C. (2011b). Hydrodeoxygenation of guaiacol: Part II: Support effect for CoMoS catalysts on HDO activity and selectivity. *Applied Catalysis B: Environmental, 101*(3), 246-255.

Bui, V. N., Toussaint, G., Laurenti, D., Mirodatos, C., & Geantet, C. (2009). Co-processing of pyrolisis bio oils and gas oil for new generation of bio-fuels: Hydrodeoxygenation of guaïacol and SRGO mixed feed. *Catalysis Today, 143*(1), 172-178.

Bykova, M., Bulavchenko, O., Ermakov, D. Y., Lebedev, M. Y., Yakovlev, V., & Parmon, V. (2011). Guaiacol hydrodeoxygenation in the presence of Ni-containing catalysts. *Catalysis in Industry, 3*(1), 15-22.

Bykova, M., Ermakov, D. Y., Kaichev, V., Bulavchenko, O., Saraev, A., Lebedev, M. Y., & Yakovlev, V. (2012). Ni-based sol–gel catalysts as promising systems for crude bio-oil upgrading: Guaiacol hydrodeoxygenation study. *Applied Catalysis B: Environmental, 113*, 296-307.

Bykova, M., Ermakov, D. Y., Khromova, S., Smirnov, A., Lebedev, M. Y., & Yakovlev, V. (2014). Stabilized Ni-based catalysts for bio-oil hydrotreatment: Reactivity studies using guaiacol. *Catalysis Today, 220*, 21-31.

Bykova, M., Zavarukhin, S., Trusov, L., & Yakovlev, V. (2013). Guaiacol hydrodeoxygenation kinetics with catalyst deactivation taken into consideration. *Kinetics and Catalysis, 54*(1), 40-48.

Bykova, M. V., Ermakov, D. Y., Kaichev, V. V., Bulavchenko, O. A., Saraev, A. A., Lebedev, M. Y., & Yakovlev, V. A. (2012a). Ni-based sol–gel catalysts as promising systems for crude bio-oil upgrading: Guaiacol hydrodeoxygenation study. *Applied Catalysis B: Environmental, 113-114*, 296-307.

Bykova, M. V., Ermakov, D. Y., Kaichev, V. V., Bulavchenko, O. A., Saraev, A. A., Lebedev, M. Y., & Yakovlev, V. A. (2012b). Ni-based sol–gel catalysts as promising systems for crude bio-oil upgrading: Guaiacol hydrodeoxygenation study. *Applied Catalysis B: Environmental, 113–114*, 296-307.

Carraro, P. M., Blanco, A. A. G., Soria, F. A., Lener, G., Sapag, K., Eimer, G. A., & Oliva, M. I. (2016). Understanding the role of nickel on the hydrogen storage capacity of Ni/MCM-41 materials. *Microporous and Mesoporous Materials, 231*, 31-39.

Centeno, A., Laurent, E., & Delmon, B. (1995). Influence of the support of CoMo sulfide catalysts and of the addition of potassium and platinum on the catalytic

performances for the hydrodeoxygenation of carbonyl, carboxyl, and guaiacol-type molecules. *Journal of Catalysis, 154*(2), 288-298.

Chen, H., Peng, Y.-P., Chen, K.-F., Lai, C.-H., & Lin, Y.-C. (2016). Rapid synthesis of Ti-MCM-41 by microwave-assisted hydrothermal method towards photocatalytic degradation of oxytetracycline. *Journal of Environmental Sciences, 44*, 76-87.

Cherubini, F., & Strømman, A. H. (2011). Chemicals from lignocellulosic biomass: opportunities, perspectives, and potential of biorefinery systems. *Biofuels, Bioproducts and Biorefining, 5*(5), 548-561.

Chiranjeevi, T., Kumaran, G. M., & Dhar, G. M. (2008). Synthesis, characterization, and evaluation of mesoporous MCM-41-supported molybdenum hydrotreating catalysts. *Petroleum Science and Technology, 26*(6), 690-703.

Cimi Daniel, A. (2014). Synthesis characterization and catalytic activity of nanocrystalline ceria modified with zirconia.

Connors, W., Johanson, L., Sarkanen, K., & Winslow, P. (1980). Thermal degradation of kraft lignin in tetralin. *Holzforschung-International Journal of the Biology, Chemistry, Physics and Technology of Wood, 34*(1), 29-37.

Corma, A. (1997). From microporous to mesoporous molecular sieve materials and their use in catalysis. *Chemical reviews, 97*(6), 2373-2420.

Corma, A., Chane-Ching, J., Airiau, M., & Martínez, C. (2004). Synthesis and catalytic properties of thermally and hydrothermally stable, high-surface-area SiO 2–CeO 2 mesostructured composite materials and their application for the removal of sulfur compounds from gasoline. *Journal of Catalysis, 224*(2), 441-448.

Danilatos, G., Kollia, M., & Dracopoulos, V. (2015). Transmission environmental scanning electron microscope with scintillation gaseous detection device. *Ultramicroscopy, 150*, 44-53.

de Souza, P. M., Rabelo-Neto, R. C., Borges, L. E. P., Jacobs, G., Davis, B. H., Sooknoi, T., . . . Noronha, F. B. (2015). Role of Keto Intermediates in the Hydrodeoxygenation of Phenol over Pd on Oxophilic Supports. *ACS Catalysis, 5*(2), 1318-1329.

De Wild, P., Van der Laan, R., Kloekhorst, A., & Heeres, E. (2009). Lignin valorisation for chemicals and (transportation) fuels via (catalytic) pyrolysis and hydrodeoxygenation. *Environmental progress & sustainable energy, 28*(3), 461-469.

Demirbas, A. (2009). Biorefineries: current activities and future developments. *Energy Conversion and Management, 50*(11), 2782-2801.

Dickinson, J. G., & Savage, P. E. (2014). Development of NiCu catalysts for aqueous-phase hydrodeoxygenation. *ACS Catalysis, 4*(8), 2605-2615.

Do, Y.-J., Kim, J.-H., Park, J.-H., Park, S.-S., Hong, S.-S., Suh, C.-S., & Lee, G.-D. (2005). Photocatalytic decomposition of 4-nitrophenol on Ti-containing MCM-41. *Catalysis today, 101*(3), 299-305.

Dongil, A., Bachiller-Baeza, B., Rodriguez-Ramos, I., Fierro, J., & Escalona, N. (2016). The effect of Cu loading on Ni/carbon nanotubes catalysts for hydrodeoxygenation of guaiacol. *RSC Advances, 6*(32), 26658-26667.

Dongil, A. B., Pastor-Pérez, L., Sepúlveda-Escribano, A., García, R., & Escalona, N. (2016). Hydrodeoxygenation of guaiacol: Tuning the selectivity to cyclohexene by introducing Ni nanoparticles inside carbon nanotubes. *Fuel, 172*, 65-69.

Dorrestijn, E., Laarhoven, L. J., Arends, I. W., & Mulder, P. (2000). The occurrence and reactivity of phenoxyl linkages in lignin and low rank coal. *Journal of Analytical and Applied Pyrolysis, 54*(1), 153-192.

Duan, J., Han, J., Sun, H., Chen, P., Lou, H., & Zheng, X. (2012). Diesel-like hydrocarbons obtained by direct hydrodeoxygenation of sunflower oil over Pd/Al-SBA-15 catalysts. *Catalysis Communications, 17*, 76-80.

Dutrow, B. L., & Clark, C. M. (2012). X-ray powder diffraction (XRD). *Geochemical Instrumentation and Analysis*.

Echeandia, S., Arias, P., Barrio, V., Pawelec, B., & Fierro, J. (2010). Synergy effect in the HDO of phenol over Ni–W catalysts supported on active carbon: Effect of tungsten precursors. *Applied Catalysis B: Environmental, 101*(1), 1-12.

Eimer, G. A., Casuscelli, S. G., Chanquia, C. M., Elías, V., Crivello, M. E., & Herrero, E. R. (2008). The influence of Ti-loading on the acid behavior and on the catalytic efficiency of mesoporous Ti-MCM-41 molecular sieves. *Catalysis Today, 133*, 639-646.

Eliche-Quesada, D., Mérida-Robles, J., Maireles-Torres, P., Rodríguez-Castellón, E., & Jiménez-López, A. (2003). Hydrogenation and ring opening of tetralin on supported nickel zirconium-doped mesoporous silica catalysts. Influence of the nickel precursor. *Langmuir, 19*(12), 4985-4991.

Elliott, D. C., Hart, T. R., Neuenschwander, G. G., Rotness, L. J., & Zacher, A. H. (2009). Catalytic hydroprocessing of biomass fast pyrolysis bio-oil to produce hydrocarbon products. *Environmental Progress & Sustainable Energy, 28*(3), 441-449.

Ertl, G., Knözinger, H., Schüth, F., & Weitkamp, J. (2008). *Handbook of heterogeneous catalysis: 8 volumes*: wiley-vch.

Fadley, C., Baird, R., Siekhaus, W., Novakov, T., & Bergström, S. (1974). Surface analysis and angular distributions in x-ray photoelectron spectroscopy. *Journal of Electron Spectroscopy and Related Phenomena, 4*(2), 93-137.

Fang, H., Zheng, J., Luo, X., Du, J., Roldan, A., Leoni, S., & Yuan, Y. (2017). Product tunable behavior of carbon nanotubes-supported Ni–Fe catalysts for guaiacol hydrodeoxygenation. *Applied Catalysis A: General, 529*, 20-31.

Fatih Demirbas, M. (2009). Biorefineries for biofuel upgrading: A critical review. *Applied Energy, 86*, S151-S161.

Ferrari, M., Delmon, B., & Grange, P. (2002). Influence of the impregnation order of molybdenum and cobalt in carbon-supported catalysts for hydrodeoxygenation reactions. *Carbon, 40*(4), 497-511.

Fonseca, R. O. d., Silva, A. A. A. d., Signorelli, M. R. M., Rabelo-Neto, R. C., Noronha, F. B., Simões, R. C. C., & Mattos, L. V. (2014). Nickel / Doped Ceria Solid Oxide Fuel Cell Anodes for Dry Reforming of Methane. *Journal of the Brazilian Chemical Society*.

Furimsky, E. (2000). Catalytic hydrodeoxygenation. *Applied Catalysis A: General, 199*(2), 147-190.

Furimsky, E., Mikhlin, J., Jones, D., Adley, T., & Baikowitz, H. (1986). On the mechanism of hydrodeoxygenation of ortho substituted phenols. *The Canadian Journal of Chemical Engineering, 64*(6), 982-985.

Gajardo, P., Mathieux, A., Grange, P., & Delmon, B. (1982). Structure and catalytic activity of CoMo/γ-Al 2 O 3 and CoMo/Sio 2 hydrodesulphurization catalysts: an xps and esr characterization of sulfided used catalysts. *Applied Catalysis, 3*(4), 347-376.

Gao, D., Xiao, Y., & Varma, A. (2015). Guaiacol Hydrodeoxygenation over Platinum Catalyst: Reaction Pathways and Kinetics. *Industrial & Engineering Chemistry Research, 54*(43), 10638-10644.

Gbadamasi, S., Ali, T. H., Voon, L. H., Atta, A. Y., Sudarsanam, P., Bhargava, S. K., & Hamid, S. B. A. (2016). Promising Ni/Al-SBA-15 catalysts for hydrodeoxygenation of dibenzofuran into fuel grade hydrocarbons: synergetic effect of Ni and Al-SBA-15 support. *RSC Advances, 6*(31), 25992-26002.

Gervasini, A. (2013). Temperature Programmed Reduction/Oxidation (TPR/TPO) Methods *Calorimetry and Thermal Methods in Catalysis* (pp. 175-195): Springer.

Ghampson, I. T., Sepúlveda, C., Garcia, R., Radovic, L. R., Fierro, J. G., DeSisto, W. J., & Escalona, N. (2012). Hydrodeoxygenation of guaiacol over carbon-supported molybdenum nitride catalysts: Effects of nitriding methods and support properties. *Applied Catalysis A: General, 439*, 111-124.

Ghampson, I. T., Sepúlveda, C., Garcia, R., Radovic, L. R., Fierro, J. L. G., DeSisto, W. J., & Escalona, N. (2012). Hydrodeoxygenation of guaiacol over carbon-supported molybdenum nitride catalysts: Effects of nitriding methods and support properties. *Applied Catalysis A: General, 439–440*, 111-124.

Gianotti, E., Dellarocca, V., Marchese, L., Martra, G., Coluccia, S., & Maschmeyer, T. (2002a). NH3adsorption on MCM-41 and Ti-grafted MCM-41. FTIR, DR UV–Vis–NIR and photoluminescence studies. *Phys. Chem. Chem. Phys., 4*(24), 6109-6115.

Gianotti, E., Dellarocca, V., Marchese, L., Martra, G., Coluccia, S., & Maschmeyer, T. (2002b). NH 3 adsorption on MCM-41 and Ti-grafted MCM-41. FTIR, DR UV–Vis–NIR and photoluminescence studies. *Physical Chemistry Chemical Physics, 4*(24), 6109-6115.

Girgis, M. J., & Gates, B. C. (1991). Reactivities, reaction networks, and kinetics in high-pressure catalytic hydroprocessing. *Industrial & Engineering Chemistry Research, 30*(9), 2021-2058.

González-Borja, M. Á., & Resasco, D. E. (2011). Anisole and guaiacol hydrodeoxygenation over monolithic Pt–Sn catalysts. *Energy & Fuels, 25*(9), 4155-4162.

González-Borja, M. A. n., & Resasco, D. E. (2011). Anisole and Guaiacol Hydrodeoxygenation over Monolithic Pt–Sn Catalysts. *Energy & Fuels, 25*(9), 4155-4162.

González, J., Chen, L., Wang, J., Manríquez, M., Limas, R., Schachat, P., . . . Contreras, J. (2016). Surface chemistry and catalytic properties of VO X/Ti-MCM-41 catalysts for dibenzothiophene oxidation in a biphasic system. *Applied Surface Science, 379*, 367-376.

Guidotti, M., Ravasio, N., Psaro, R., Ferraris, G., & Moretti, G. (2003). Epoxidation on titanium-containing silicates: do structural features really affect the catalytic performance? *Journal of Catalysis, 214*(2), 242-250.

Guo, Q., Wu, M., Wang, K., Zhang, L., & Xu, X. (2015a). Catalytic hydrodeoxygenation of algae bio-oil over bimetallic Ni–Cu/ZrO2 catalysts. *Industrial & Engineering Chemistry Research, 54*(3), 890-899.

Guo, Q., Wu, M., Wang, K., Zhang, L., & Xu, X. (2015b). Catalytic Hydrodeoxygenation of Algae Bio-oil over Bimetallic Ni–Cu/ZrO2Catalysts. *Industrial & Engineering Chemistry Research, 54*(3), 890-899.

Gutierrez, A., Kaila, R., Honkela, M., Slioor, R., & Krause, A. (2009). Hydrodeoxygenation of guaiacol on noble metal catalysts. *Catalysis Today, 147*(3), 239-246.

Gutierrez, A., Kaila, R. K., Honkela, M. L., Slioor, R., & Krause, A. O. I. (2009). Hydrodeoxygenation of guaiacol on noble metal catalysts. *Catalysis Today, 147*(3–4), 239-246.

Gutierrez, A., Turpeinen, E.-M., Viljava, T.-R., & Krause, O. (2017). Hydrodeoxygenation of model compounds on sulfided CoMo/γ-Al 2 O 3 and NiMo/γ-Al 2 O 3 catalysts; Role of sulfur-containing groups in reaction networks. *Catalysis Today, 285*, 125-134.

Halilu, A., Ali, T. H., Atta, A. Y., Sudarsanam, P., Bhargava, S. K., & Abd Hamid, S. B. (2016). Highly selective hydrogenation of biomass-derived furfural into furfuryl alcohol using a novel magnetic nanoparticles catalyst. *Energy & Fuels, 30*(3), 2216-2226.

Hamid, S. A., Ambursa, M. M., Sudarsanam, P., Voon, L. H., & Bhargava, S. K. (2017). Effect of Ti loading on structure-activity properties of Cu-Ni/Ti-MCM-41 catalysts in hydrodeoxygenation of guaiacol. *Catalysis Communications, 94*, 18-22.

Hanlon, E., Manoharan, R., Koo, T. W., Shafer, K., Motz, J., Fitzmaurice, M., . . . Feld, M. (2000). Prospects for in vivo Raman spectroscopy. *Physics in medicine and biology, 45*(2), R1.

He, Z., & Wang, X. (2012). Hydrodeoxygenation of model compounds and catalytic systems for pyrolysis bio-oils upgrading. *Catalysis for sustainable energy, 1*, 28-52.

Hinot, K. (2006). *Catalytic soot oxidation by platinum on sintered metal filters.* Dissertation, ISBN: 978-3-86644-103-3.

Hirai, T., Okubo, H., & Komasawa, I. (1999). Size-selective incorporation of CdS nanoparticles into mesoporous silica. *The Journal of Physical Chemistry B, 103*(21), 4228-4230.

Hong, Y.-K., Lee, D.-W., Eom, H.-J., & Lee, K.-Y. (2014a). The catalytic activity of Pd/WO x/γ-Al 2 O 3 for hydrodeoxygenation of guaiacol. *Applied Catalysis B: Environmental, 150*, 438-445.

Hong, Y.-K., Lee, D.-W., Eom, H.-J., & Lee, K.-Y. (2014b). The catalytic activity of Pd/WOx/γ-Al2O3 for hydrodeoxygenation of guaiacol. *Applied Catalysis B: Environmental, 150-151*, 438-445.

Hong, Y.-K., Lee, D.-W., Eom, H.-J., & Lee, K.-Y. (2014c). The catalytic activity of Sulfided Ni/W/TiO 2 (anatase) for the hydrodeoxygenation of Guaiacol. *Journal of Molecular Catalysis A: Chemical, 392*, 241-246.

Honkela, M. L., Viljava, T.-R., Gutierrez, A., & Krause, A. O. I. (2010). Hydrotreating for bio-oil upgrading *Thermochemical Conversion of Biomass to Liquid Fuels and Chemicals* (pp. 288-306).

Huelsman, C. M., & Savage, P. E. (2012). Intermediates and kinetics for phenol gasification in supercritical water. *Physical Chemistry Chemical Physics, 14*(8), 2900-2910.

Izadi, N., Rashidi, A. M., Zeraatkar, A., Varmazyar, H., & Rashtchi, M. (2014). Preparation of highly stable bimetallic ni–cu catalyst for simultaneous production of hydrogen and fish-bone carbon nanofibers: Optimization, effect of catalyst preparation methods and deactivation. *International Journal of Hydrogen Energy, 39*(15), 7765-7779.

Jasik, A., Wojcieszak, R., Monteverdi, S., Ziolek, M., & Bettahar, M. (2005). Study of nickel catalysts supported on Al 2 O 3, SiO 2 or Nb 2 O 5 oxides. *Journal of Molecular Catalysis A: Chemical, 242*(1), 81-90.

Jegers, H. E., & Klein, M. T. (1985). Primary and secondary lignin pyrolysis reaction pathways. *Industrial & Engineering Chemistry Process Design and Development, 24*(1), 173-183.

Jha, A., Jeong, D.-W., Jang, W.-J., Rode, C. V., & Roh, H.-S. (2015). Mesoporous NiCu–CeO2oxide catalysts for high-temperature water–gas shift reaction. *RSC Adv., 5*(2), 1430-1437.

Jian, L., Zhen, Z., Chunming, X., Aijun, D., & Jiang, G. (2010). CeO 2-supported vanadium oxide catalysts for soot oxidation: the roles of molecular structure and nanometer effect. *Journal of Rare Earths, 28*(2), 198-204.

Jiménez-López, A., Rodrıguez-Castellón, E., Maireles-Torres, P., Dıaz, L., & Mérida-Robles, J. (2001). Chromium oxide supported on zirconium-and lanthanum-doped mesoporous silica for oxidative dehydrogenation of propane. *Applied Catalysis A: General, 218*(1), 295-306.

Jin, C., Li, G., Wang, X., Zhao, L., Liu, L., Liu, H., . . . Bao, X. (2007). Synthesis, characterization and catalytic performance of Ti-containing mesoporous molecular sieves assembled from titanosilicate precursors. *Chemistry of Materials, 19*(7), 1664-1670.

Joffres, B., Laurenti, D., Charon, N., Daudin, A., Quignard, A., & Geantet, C. (2013). Thermochemical conversion of lignin for fuels and chemicals: A review. *Oil & Gas Science and Technology–Revue d'IFP Energies nouvelles, 68*(4), 753-763.

Joffres, B., Laurenti, D., Charon, N., Daudin, A., Quignard, A., & Geantet, C. (2013). Thermochemical Conversion of Lignin for Fuels and Chemicals: A Review. *Oil & Gas Science and Technology – Revue d'IFP Energies nouvelles, 68*(4), 753-763.

Jongerius, A. L., Bruijnincx, P. C. A., & Weckhuysen, B. M. (2013). Liquid-phase reforming and hydrodeoxygenation as a two-step route to aromatics from lignin. *Green Chemistry, 15*(11), 3049.

Jongerius, A. L., Gosselink, R. W., Dijkstra, J., Bitter, J. H., Bruijnincx, P. C., & Weckhuysen, B. M. (2013). Carbon Nanofiber Supported Transition-Metal Carbide Catalysts for the Hydrodeoxygenation of Guaiacol. *ChemCatChem, 5*(10), 2964-2972.

Kaminsky, W., & Schwesinger, H. (1980). Properties and Decomposition of Lignins Isolated by Means of an Alcoholic-Water-Mixture. Part 3: Decomposition by Pyrolysis in a Fluid-Bed. *Holzforschung-International Journal of the Biology, Chemistry, Physics and Technology of Wood, 34*(3), 73-75.

Karagöz, S., Bhaskar, T., Muto, A., & Sakata, Y. (2005). Comparative studies of oil compositions produced from sawdust, rice husk, lignin and cellulose by hydrothermal treatment. *Fuel, 84*(7), 875-884.

Katta, L., Sudarsanam, P., Thrimurthulu, G., & Reddy, B. M. (2010). Doped nanosized ceria solid solutions for low temperature soot oxidation: Zirconium versus lanthanum promoters. *Applied Catalysis B: Environmental, 101*(1), 101-108.

Khalil, K. M. (2007). Cerium modified MCM-41 nanocomposite materials via a nonhydrothermal direct method at room temperature. *J Colloid Interface Sci, 315*(2), 562-568.

Khromova, S. A., Smirnov, A. A., Bulavchenko, O. A., Saraev, A. A., Kaichev, V. V., Reshetnikov, S. I., & Yakovlev, V. A. (2014). Anisole hydrodeoxygenation over Ni–Cu bimetallic catalysts: The effect of Ni/Cu ratio on selectivity. *Applied Catalysis A: General, 470*, 261-270.

Kim, K. H., Lee, D. J., Cho, K. M., Kim, S. J., Park, J. K., & Jung, H. T. (2015). Complete magnesiothermic reduction reaction of vertically aligned mesoporous silica channels to form pure silicon nanoparticles. *Sci Rep, 5*, 9014.

Krár, M., Kasza, T., Kovács, S., Kalló, D., & Hancsók, J. (2011). Bio gas oils with improved low temperature properties. *Fuel Processing Technology, 92*(5), 886-892.

Lange, J. P. (2007). Lignocellulose conversion: an introduction to chemistry, process and economics. *Biofuels, bioproducts and biorefining, 1*(1), 39-48.

Laurent, E., & Delmon, B. (1994). Influence of water in the deactivation of a sulfided NiMoγ-Al2O3 catalyst during hydrodeoxygenation. *Journal of Catalysis, 146*(1), 281-291.

Lee, C. R., Yoon, J. S., Suh, Y.-W., Choi, J.-W., Ha, J.-M., Suh, D. J., & Park, Y.-K. (2012). Catalytic roles of metals and supports on hydrodeoxygenation of lignin monomer guaiacol. *Catalysis Communications, 17*, 54-58.

Lee, H. W., Jun, B. R., Kim, H., Kim, D. H., Jeon, J.-K., Park, S. H., . . . Park, Y.-K. (2015). Catalytic hydrodeoxygenation of 2-methoxy phenol and dibenzofuran over Pt/mesoporous zeolites. *Energy, 81*, 33-40.

Leiva, K., Martinez, N., Sepulveda, C., García, R., Jiménez, C. A., Laurenti, D., . . . Escalona, N. (2015). Hydrodeoxygenation of 2-methoxyphenol over different Re active phases supported on SiO2 catalysts. *Applied Catalysis A: General, 490*, 71-79.

Lensveld, D. J., Gerbrand Mesu, J., Jos van Dillen, A., & de Jong, K. P. (2001). Synthesis and characterisation of MCM-41 supported nickel oxide catalysts. *Microporous and Mesoporous Materials, 44–45*, 401-407.

Li, C., Yamahara, H., Lee, Y., Tabata, H., & Delaunay, J. J. (2015). CuO nanowire/microflower/nanowire modified Cu electrode with enhanced electrochemical performance for non-enzymatic glucose sensing. *Nanotechnology, 26*(30), 305503.

Li, K., Wang, R., & Chen, J. (2011). Hydrodeoxygenation of anisole over silica-supported Ni2P, MoP, and NiMoP catalysts. *Energy & Fuels, 25*(3), 854-863.

Li, M., Hu, Y., Liu, C., Huang, J., Liu, Z., Wang, M., & An, Z. (2014). Synthesis of cerium oxide particles via polyelectrolyte controlled nonclassical crystallization for catalytic application. *RSC Adv., 4*(2), 992-995.

Li, X., Chen, G., Liu, C., Ma, W., Yan, B., & Zhang, J. (2016). Hydrodeoxygenation of lignin-derived bio-oil using molecular sieves supported metal catalysts: A critical review. *Renewable and Sustainable Energy Reviews*.

Li, X., Su, L., Wang, Y., Yu, Y., Wang, C., Li, X., & Wang, Z. (2012). Catalytic fast pyrolysis of Kraft lignin with HZSM-5 zeolite for producing aromatic hydrocarbons. *Frontiers of Environmental Science & Engineering, 6*(3), 295-303.

Liguori, L., & Barth, T. (2011). Palladium-Nafion SAC-13 catalysed depolymerisation of lignin to phenols in formic acid and water. *Journal of Analytical and Applied Pyrolysis, 92*(2), 477-484.

Lin, K., Pescarmona, P. P., Vandepitte, H., Liang, D., Van Tendeloo, G., & Jacobs, P. A. (2008). Synthesis and catalytic activity of Ti-MCM-41 nanoparticles with highly active titanium sites. *Journal of Catalysis, 254*(1), 64-70.

Lin, Y.-C., Li, C.-L., Wan, H.-P., Lee, H.-T., & Liu, C.-F. (2011). Catalytic hydrodeoxygenation of guaiacol on Rh-based and sulfided CoMo and NiMo catalysts. *Energy & Fuels, 25*(3), 890-896.

Liu, H., Yin, C., Li, H., Liu, B., Li, X., Chai, Y., . . . Liu, C. (2014). Synthesis, characterization and hydrodesulfurization properties of nickel–copper–molybdenum catalysts for the production of ultra-low sulfur diesel. *Fuel, 129*, 138-146.

Luo, C., Li, D., Wu, W., Zhang, Y., & Pan, C. (2014a). Preparation of porous micro–nano-structure NiO/ZnO heterojunction and its photocatalytic property. *RSC Adv., 4*(6), 3090-3095.

Luo, C., Li, D., Wu, W., Zhang, Y., & Pan, C. (2014b). Preparation of porous micro–nano-structure NiO/ZnO heterojunction and its photocatalytic property *RSC Adv.* (Vol. 4, pp. 3090-3095).

Lup, A. N. K., Abnisa, F., Daud, W. M. A. W., & Aroua, M. K. (2017). A review on reactivity and stability of heterogeneous metal catalysts for deoxygenation of bio-oil model compounds. *Journal of Industrial and Engineering Chemistry*.

Majid Saidi, F. S., Dornaz Karimipourfard, Tarit Nimmanwudipong, Bruce C. Gates and Mohammad Reza Rahimpour. (2014). Upgrading of lignin-derived bio-oils by catalytic hydrodeoxygenation. *Energy & Environmental Science, 7*, 103–129.

Małecka, B., Łącz, A., Drożdż, E., & Małecki, A. (2014). Thermal decomposition of d-metal nitrates supported on alumina. *Journal of Thermal Analysis and Calorimetry, 119*(2), 1053-1061.

Mallesham, B., Sudarsanam, P., Raju, G., & Reddy, B. M. (2013). Design of highly efficient Mo and W-promoted SnO 2 solid acids for heterogeneous catalysis: acetalization of bio-glycerol. *Green Chemistry, 15*(2), 478-489.

Mallesham, B., Sudarsanam, P., Reddy, B. V. S., & Reddy, B. M. (2016). Development of cerium promoted copper–magnesium catalysts for biomass valorization: Selective hydrogenolysis of bioglycerol. *Applied Catalysis B: Environmental, 181*, 47-57.

Marler, B., Oberhagemann, U., Vortmann, S., & Gies, H. (1996). Influence of the sorbate type on the XRD peak intensities of loaded MCM-41. *Microporous Materials, 6*(5), 375-383.

Marrero-Jerez, J., Murugan, A., Metcalfe, I., & Núñez, P. (2014). TPR–TPD–TPO studies on CGO/NiO and CGO/CuO ceramics obtained from freeze-dried precursors. *Ceramics International, 40*(9), 15175-15182.

Marrero-Jerez, J., Murugan, A., Metcalfe, I. S., & Núñez, P. (2014). TPR–TPD–TPO studies on CGO/NiO and CGO/CuO ceramics obtained from freeze-dried precursors. *Ceramics International, 40*(9), 15175-15182.

Massoth, F., Politzer, P., Concha, M., Murray, J., Jakowski, J., & Simons, J. (2006). Catalytic hydrodeoxygenation of methyl-substituted phenols: Correlations of kinetic parameters with molecular properties. *The Journal of Physical Chemistry B, 110*(29), 14283-14291.

Masui, T., Hirai, H., Hamada, R., Imanaka, N., Adachi, G.-y., Sakata, T., & Mori, H. (2003). Synthesis and characterization of cerium oxide nanoparticles coated with turbostratic boron nitride. *Journal of Materials Chemistry, 13*(3), 622-627.

Meier, D., Ante, R., & Faix, O. (1992). Catalytic hydropyrolysis of lignin: influence of reaction conditions on the formation and composition of liquid products. *Bioresource Technology, 40*(2), 171-177.

Mekhilef, S., Saidur, R., Safari, A., & Mustaffa, W. (2011). Biomass energy in Malaysia: current state and prospects. *Renewable and Sustainable Energy Reviews, 15*(7), 3360-3370.

Meléndez-Ortiz, H. I., Mercado-Silva, A., García-Cerda, L. A., Castruita, G., & Perera-Mercado, Y. A. (2013). Hydrothermal synthesis of mesoporous silica MCM-41 using commercial sodium silicate. *Journal of the Mexican Chemical Society, 57*(2), 73-79.

Mendes, M., Santos, O., Jordão, E., & Silva, A. (2001). Hydrogenation of oleic acid over ruthenium catalysts. *Applied Catalysis A: General, 217*(1), 253-262.

Miranda, B. C., Chimentão, R. J., Szanyi, J., Braga, A. H., Santos, J. B. O., Gispert-Guirado, F., . . . Medina, F. (2015). Influence of copper on nickel-based catalysts in the conversion of glycerol. *Applied Catalysis B: Environmental, 166-167*, 166-180.

Moore, D. M., & Reynolds, R. C. (1989). *X-ray Diffraction and the Identification and Analysis of Clay Minerals* (Vol. 378): Oxford university press Oxford.

Moreno-Tost, R., Santamaría-González, J., Maireles-Torres, P., Rodríguez-Castellón, E., & Jiménez-López, A. (2002). Nickel oxide supported on zirconium-doped mesoporous silica for selective catalytic reduction of NO with NH 3. *Journal of Materials Chemistry, 12*(11), 3331-3336.

Moritz, M., & Geszke-Moritz, M. (2015). Mesoporous silica materials with different structures as the carriers for antimicrobial agent. Modeling of chlorhexidine adsorption and release. *Applied Surface Science, 356*, 1327-1340.

Mortensen, P. M., Gardini, D., Damsgaard, C. D., Grunwaldt, J.-D., Jensen, P. A., Wagner, J. B., & Jensen, A. D. (2016). Deactivation of Ni-MoS 2 by bio-oil impurities during hydrodeoxygenation of phenol and octanol. *Applied Catalysis A: General, 523*, 159-170.

Mortensen, P. M., Grunwaldt, J.-D., Jensen, P. A., & Jensen, A. D. (2013). Screening of catalysts for hydrodeoxygenation of phenol as a model compound for bio-oil. *Acs Catalysis, 3*(8), 1774-1785.

Mullen, C. A., & Boateng, A. A. (2010). Catalytic pyrolysis-GC/MS of lignin from several sources. *Fuel Processing Technology, 91*(11), 1446-1458.

Nava, R., Pawelec, B., Castaño, P., Álvarez-Galván, M. C., Loricera, C. V., & Fierro, J. L. G. (2009). Upgrading of bio-liquids on different mesoporous silica-supported CoMo catalysts. *Applied Catalysis B: Environmental, 92*(1-2), 154-167.

Neale, N. R., & Frank, A. J. (2007). Size and shape control of nanocrystallites in mesoporous TiO2 films. *Journal of Materials Chemistry, 17*(30), 3216.

Nguyen, T. L., Ung, T. D. T., & Nguyen, Q. L. (2014). Non-chapped, vertically well aligned titanium dioxide nanotubes fabricated by electrochemical etching. *Advances in Natural Sciences: Nanoscience and Nanotechnology, 5*(2), 025016.

Nimmanwudipong, T., Runnebaum, R. C., Block, D. E., & Gates, B. C. (2011a). Catalytic Conversion of Guaiacol Catalyzed by Platinum Supported on Alumina: Reaction Network Including Hydrodeoxygenation Reactions. *Energy & Fuels, 25*(8), 3417-3427.

Nimmanwudipong, T., Runnebaum, R. C., Block, D. E., & Gates, B. C. (2011b). Catalytic reactions of guaiacol: reaction network and evidence of oxygen removal in reactions with hydrogen. *Catalysis letters, 141*(6), 779-783.

Oasmaa, A., & Johansson, A. (1993). Catalytic hydrotreating of lignin with water-soluble molybdenum catalyst. *Energy & fuels, 7*(3), 426-429.

Olcese, R., Bettahar, M., Petitjean, D., Malaman, B., Giovanella, F., & Dufour, A. (2012). Gas-phase hydrodeoxygenation of guaiacol over Fe/SiO 2 catalyst. *Applied Catalysis B: Environmental, 115*, 63-73.

Olcese, R. N., Bettahar, M., Petitjean, D., Malaman, B., Giovanella, F., & Dufour, A. (2012). Gas-phase hydrodeoxygenation of guaiacol over Fe/SiO2 catalyst. *Applied Catalysis B: Environmental, 115-116*, 63-73.

Park, B. H., Kim, Y.-I., & Kim, K. H. (1999). Effect of silicon addition on microstructure and mechanical property of titanium nitride film prepared by plasma-assisted chemical vapor deposition. *Thin Solid Films, 348*(1), 210-214.

Parlett, C. M. A., Bruce, D. W., Hondow, N. S., Lee, A. F., & Wilson, K. (2011). Support-Enhanced Selective Aerobic Alcohol Oxidation over Pd/Mesoporous Silicas. *ACS Catalysis, 1*(6), 636-640.

Pejova, B. (2013). Phonon Confinement and Related Effects in Three-Dimensional Assemblies of Cubic Cadmium Selenide Quantum Dots Synthesized by Conventional Chemical and Sonochemical Routes. *The Journal of Physical Chemistry C*, 130918102741006.

Pérez-Hernández, R., Gutiérrez-Martínez, A., Espinosa-Pesqueira, M. E., Estanislao, M. L., & Palacios, J. (2015). Effect of the bimetallic Ni/Cu loading on the ZrO2 support for H2 production in the autothermal steam reforming of methanol. *Catalysis Today, 250*, 166-172.

Pińkowska, H., Wolak, P., & Złocińska, A. (2012). Hydrothermal decomposition of alkali lignin in sub-and supercritical water. *Chemical engineering journal, 187*, 410-414.

Popov, A., Kondratieva, E., Goupil, J. M., Mariey, L., Bazin, P., Gilson, J.-P., . . . Maugé, F. (2010). Bio-oils hydrodeoxygenation: adsorption of phenolic molecules on oxidic catalyst supports. *The Journal of Physical Chemistry C, 114*(37), 15661-15670.

Popova, M., Szegedi, Á., Németh, P., Kostova, N., & Tsoncheva, T. (2008). Titanium modified MCM-41 as a catalyst for toluene oxidation. *Catalysis Communications, 10*(3), 304-308.

Procházková, D., Zámostný, P., Bejblová, M., Červený, L., & Čejka, J. (2007). Hydrodeoxygenation of aldehydes catalyzed by supported palladium catalysts. *Applied Catalysis A: General, 332*(1), 56-64.

Rahemi, N., Haghighi, M., Babaluo, A. A., Allahyari, S., & Jafari, M. F. (2014). Syngas production from reforming of greenhouse gases CH4/CO2 over Ni–Cu/Al2O3 nanocatalyst: Impregnated vs. plasma-treated catalyst. *Energy Conversion and Management, 84*, 50-59.

Rajakovic, V., Mintova, S., Senker, J., & Bein, T. (2003). Synthesis and characterization of V-and Ti-substituted mesoporous materials. *Materials Science and Engineering: C, 23*(6), 817-821.

Ramsurn, H., & Gupta, R. B. (2012). Production of biocrude from biomass by acidic subcritical water followed by alkaline supercritical water two-step liquefaction. *Energy & Fuels, 26*(4), 2365-2375.

Rao, B. G., Sudarsanam, P., Rangaswamy, A., & Reddy, B. M. (2015). Highly Efficient CeO2–MoO3/SiO2 Catalyst for Solvent-Free Oxidative Coupling of Benzylamines into N-Benzylbenzaldimines with O2 as the Oxidant. *Catalysis Letters, 145*(7), 1436-1445.

Reddy, B. M., Rao, K. N., & Bharali, P. (2009). Copper Promoted Cobalt and Nickel Catalysts Supported on Ceria−Alumina Mixed Oxide: Structural Characterization and CO Oxidation Activity. *Industrial & Engineering Chemistry Research, 48*(18), 8478-8486.

Reddy Kannapu, H. P., Mullen, C. A., Elkasabi, Y., & Boateng, A. A. (2015). Catalytic transfer hydrogenation for stabilization of bio-oil oxygenates: Reduction of p-cresol and furfural over bimetallic Ni–Cu catalysts using isopropanol. *Fuel Processing Technology, 137*, 220-228.

Reddy, P. S., Sudarsanam, P., Raju, G., & Reddy, B. M. (2012). Selective acetylation of glycerol over CeO 2–M and SO 4 2−/CeO 2–M (M= ZrO 2 and Al 2 O 3) catalysts for synthesis of bioadditives. *Journal of Industrial and Engineering Chemistry, 18*(2), 648-654.

Reed, S. J. B., & Reed, S. J. B. (1975). *Electron microprobe analysis* (Vol. 2): Cambridge University Press Cambridge.

Reiche, M., Maciejewski, M., & Baiker, A. (2000). Characterization by temperature programmed reduction. *Catalysis today, 56*(4), 347-355.

Reimer, L. (2013). *Transmission electron microscopy: physics of image formation and microanalysis* (Vol. 36): Springer.

Ritchie, N. W. (2013). Is Scanning Electron Microscopy/Energy Dispersive X-ray Spectrometry (SEM/EDS) Quantitative? *Scanning, 35*(3), 141-168.

Roberts, V., Stein, V., Reiner, T., Lemonidou, A., Li, X., & Lercher, J. A. (2011). Towards quantitative catalytic lignin depolymerization. *Chemistry–A European Journal, 17*(21), 5939-5948.

Romero, Y., Richard, F., & Brunet, S. (2010). Hydrodeoxygenation of 2-ethylphenol as a model compound of bio-crude over sulfided Mo-based catalysts: promoting effect and reaction mechanism. *Applied Catalysis B: Environmental, 98*(3), 213-223.

Rouquerol, J., Rouquerol, F., Llewellyn, P., Maurin, G., & Sing, K. S. (2013). *Adsorption by powders and porous solids: principles, methodology and applications*: Academic press.

Ruddy, D. A., Schaidle, J. A., Ferrell III, J. R., Wang, J., Moens, L., & Hensley, J. E. (2014). Recent advances in heterogeneous catalysts for bio-oil upgrading via “ex situ catalytic fast pyrolysis”: catalyst development through the study of model compounds. *Green Chemistry, 16*(2), 454-490.

Runnebaum, R. C., Nimmanwudipong, T., Block, D. E., & Gates, B. C. (2012). Catalytic conversion of compounds representative of lignin-derived bio-oils: a reaction network for guaiacol, anisole, 4-methylanisole, and cyclohexanone conversion catalysed by Pt/γ-Al2O3. *Catalysis Science & Technology, 2*(1), 113.

Rutkowski, P. (2012). Chemical composition of bio-oil produced by co-pyrolysis of biopolymer/polypropylene mixtures with K2CO3 and ZnCl2 addition. *Journal of Analytical and Applied Pyrolysis, 95*, 38-47.

Ryoo, R., & Jun, S. (1997). Improvement of hydrothermal stability of MCM-41 using salt effects during the crystallization process. *The Journal of Physical Chemistry B, 101*(3), 317-320.

Saha, B. C. (2004). Lignocellulose Biodegradation and Applications in Biotechnology. *889*, 2-34.

Saidi, M., Samimi, F., Karimipourfard, D., Nimmanwudipong, T., Gates, B. C., & Rahimpour, M. R. (2014). Upgrading of lignin-derived bio-oils by catalytic hydrodeoxygenation. *Energy & Environmental Science, 7*(1), 103-129.

Sankaranarayanan, S., Shankar, V. H., Jayalakshmi, S., Bau, N. Q., & Gupta, M. (2015). Development of high performance magnesium composites using Ni 50 Ti 50 metallic glass reinforcement and microwave sintering approach. *Journal of Alloys and Compounds, 627*, 192-199.

Santillan-Jimenez, E., Perdu, M., Pace, R., Morgan, T., & Crocker, M. (2015). Activated carbon, carbon nanofiber and carbon nanotube supported molybdenum carbide catalysts for the hydrodeoxygenation of guaiacol. *Catalysts, 5*(1), 424-441.

Sasaki, M., & Goto, M. (2008). Recovery of phenolic compounds through the decomposition of lignin in near and supercritical water. *Chemical Engineering and Processing: Process Intensification, 47*(9), 1609-1619.

Schimming, S. M., LaMont, O. D., König, M., Rogers, A. K., D'Amico, A. D., Yung, M. M., & Sievers, C. (2015). Hydrodeoxygenation of Guaiacol over Ceria–Zirconia Catalysts. *ChemSusChem, 8*(12), 2073-2083.

Schumacher, B., Plzak, V., Kinne, M., & Behm, R. (2003). Highly active Au/TiO 2 catalysts for low-temperature CO oxidation: preparation, conditioning and stability. *Catalysis letters, 89*(1), 109-114.

Selvaraj, M., Shanthi, K., Maheswari, R., & Ramanathan, A. (2014). Hydrodeoxygenation of Guaiacol over MoO3-NiO/mesoporous silicates: effect of incorporated heteroatom. *Energy & Fuels, 28*(4), 2598-2607.

Şenol, O., Ryymin, E.-M., Viljava, T.-R., & Krause, A. (2007). Effect of hydrogen sulphide on the hydrodeoxygenation of aromatic and aliphatic oxygenates on sulphided catalysts. *Journal of Molecular Catalysis A: Chemical, 277*(1), 107-112.

Şenol, O. İ., Ryymin, E. M., Viljava, T. R., & Krause, A. O. I. (2007). Effect of hydrogen sulphide on the hydrodeoxygenation of aromatic and aliphatic oxygenates on sulphided catalysts. *Journal of Molecular Catalysis A: Chemical, 277*(1–2), 107-112.

Sepúlveda, C., Escalona, N., García, R., Laurenti, D., & Vrinat, M. (2012). Hydrodeoxygenation and hydrodesulfurization co-processing over ReS2 supported catalysts. *Catalysis Today, 195*(1), 101-105.

Sietsma, J. R., Meeldijk, J. D., Versluijs-Helder, M., Broersma, A., Dillen, A. J. v., de Jongh, P. E., & de Jong, K. P. (2008). Ordered mesoporous silica to study the preparation of Ni/SiO2 ex nitrate catalysts: Impregnation, drying, and thermal treatments. *Chemistry of materials, 20*(9), 2921-2931.

Sing, K. (2001). The use of nitrogen adsorption for the characterisation of porous materials. *Colloids and Surfaces A: Physicochemical and Engineering Aspects, 187*, 3-9.

Sjöström, E. (1993). *Wood chemistry: fundamentals and applications*: Gulf Professional Publishing.

Skoog, D. A., & West, D. M. (1980). *Principles of instrumental analysis* (Vol. 158): Saunders College Philadelphia.

Song, H., Wang, J., Wang, Z., Song, H., Li, F., & Jin, Z. (2014). Effect of titanium content on dibenzothiophene HDS performance over Ni2P/Ti-MCM-41 catalyst. *Journal of Catalysis, 311*, 257-265.

Song, W., Liu, Y., Baráth, E., Zhao, C., & Lercher, J. A. (2015). Synergistic effects of Ni and acid sites for hydrogenation and C–O bond cleavage of substituted phenols. *Green Chemistry, 17*(2), 1204-1218.

Spanier, J. E., Robinson, R. D., Zhang, F., Chan, S.-W., & Herman, I. P. (2001). Size-dependent properties ofCeO2−ynanoparticles as studied by Raman scattering. *Physical Review B, 64*(24).

Stakheev, A. Y., & Kustov, L. (1999). Effects of the support on the morphology and electronic properties of supported metal clusters: modern concepts and progress in 1990s. *Applied Catalysis A: General, 188*(1), 3-35.

Sudarsanam, P., Hillary, B., Mallesham, B., Rao, B. G., Amin, M. H., Nafady, A., . . . Bhargava, S. K. (2016). Designing CuO x Nanoparticle-Decorated CeO2 Nanocubes for Catalytic Soot Oxidation: Role of the Nanointerface in the Catalytic Performance of Heterostructured Nanomaterials. *Langmuir, 32*(9), 2208-2215.

Sudarsanam, P., Rangaswamy, A., & Reddy, B. M. (2014). An efficient noble metal-free Ce–Sm/SiO 2 nano-oxide catalyst for oxidation of benzylamines under ecofriendly conditions. *RSC Advances, 4*(86), 46378-46382.

Suga, M., Asahina, S., Sakuda, Y., Kazumori, H., Nishiyama, H., Nokuo, T., . . . Cho, H. S. (2014). Recent progress in scanning electron microscopy for the characterization of fine structural details of nano materials. *Progress in Solid State Chemistry, 42*(1), 1-21.

Sun, D., Kiyobayashi, T., Takeshita, H. T., Kuriyama, N., & Jensen, C. M. (2002). X-ray diffraction studies of titanium and zirconium doped NaAlH 4: elucidation of

doping induced structural changes and their relationship to enhanced hydrogen storage properties. *Journal of alloys and compounds, 337*(1), L8-L11.

Sun, J., Karim, A. M., Zhang, H., Kovarik, L., Li, X. S., Hensley, A. J., . . . Wang, Y. (2013). Carbon-supported bimetallic Pd–Fe catalysts for vapor-phase hydrodeoxygenation of guaiacol. *Journal of Catalysis, 306*, 47-57.

Szegedi, Á., Popova, M., Dimitrova, A., Cherkezova-Zheleva, Z., & Mitov, I. (2010). Effect of the pretreatment conditions on the physico-chemical and catalytic properties of cobalt- and iron-containing Ti-MCM-41 materials. *Microporous and Mesoporous Materials, 136*(1-3), 106-114.

Taghvaei, H., Rahimpour, M. R., & Bruggeman, P. (2017). Catalytic hydrodeoxygenation of anisole over nickel supported on plasma treated alumina–silica mixed oxides. *RSC Advances, 7*(49), 30990-30998.

Tao, F. F. (2012). Synthesis, catalysis, surface chemistry and structure of bimetallic nanocatalysts. *Chem Soc Rev, 41*(24), 7977-7979.

Telysheva, G., Dobele, G., Meier, D., Dizhbite, T., Rossinska, G., & Jurkjane, V. (2007). Characterization of the transformations of lignocellulosic structures upon degradation in planted soil. *Journal of Analytical and Applied Pyrolysis, 79*(1–2), 52-60.

Toba, M., Abe, Y., Kuramochi, H., Osako, M., Mochizuki, T., & Yoshimura, Y. (2011). Hydrodeoxygenation of waste vegetable oil over sulfide catalysts. *Catalysis Today, 164*(1), 533-537.

Toor, S. S., Rosendahl, L., & Rudolf, A. (2011). Hydrothermal liquefaction of biomass: a review of subcritical water technologies. *Energy, 36*(5), 2328-2342.

Tran, N. T., Uemura, Y., & Ramli, A. (2016). Hydrodeoxygenation of guaiacol over Al-MCM-41 supported metal catalysts: A comparative study of Co and Ni. *Procedia Engineering, 148*, 1252-1258.

Tran, N. T. T., Uemura, Y., Chowdhury, S., & Ramli, A. (2016). Vapor-phase hydrodeoxygenation of guaiacol on Al-MCM-41 supported Ni and Co catalysts. *Applied Catalysis A: General, 512*, 93-100.

Tropsoe, H., Clausen, B., & Massoth, F. (1996). Hydro treating catalysis: Science and Technology: Berlin.

Tyrone Ghampson, I., Sepúlveda, C., Garcia, R., García Fierro, J. L., Escalona, N., & DeSisto, W. J. (2012). Comparison of alumina- and SBA-15-supported molybdenum nitride catalysts for hydrodeoxygenation of guaiacol. *Applied Catalysis A: General, 435-436*, 51-60.

van de Wiel, H. J. (2003). Determination of elements by ICP-AES and ICP-MS. *National Institute of Public Health and the Environment (RIVM). Bilthoven, The Netherlands*, 1-19.

Viljava, T.-R., Komulainen, R., & Krause, A. (2000). Effect of H 2 S on the stability of CoMo/Al 2 O 3 catalysts during hydrodeoxygenation. *Catalysis Today, 60*(1), 83-92.

Vo-Dinh, T. (1998). Surface-enhanced Raman spectroscopy using metallic nanostructures. *TrAC Trends in Analytical Chemistry, 17*(8), 557-582.

Vuori, A. (1986). Pyrolysis studies of some simple coal related aromatic methyl ethers. *Fuel, 65*(11), 1575-1583.

Vuori, A. (1988). Liquefaction of Kraft Lignin: 1. Primary Reactions under Mild Thermolysis Conditions. *Holzforschung-International Journal of the Biology, Chemistry, Physics and Technology of Wood, 42*(3), 155-161.

Wang, H., Ruan, H., Pei, H., Wang, H., Chen, X., Tucker, M. P., . . . Yang, B. (2015). Biomass-derived lignin to jet fuel range hydrocarbons via aqueous phase hydrodeoxygenation. *Green Chem., 17*(12), 5131-5135.

Wang, H. Y., & Lua, A. C. (2015). Methane decomposition using Ni–Cu alloy nano-particle catalysts and catalyst deactivation studies. *Chemical Engineering Journal, 262*, 1077-1089.

Wang, J. (2005). Carbon-nanotube based electrochemical biosensors: A review. *Electroanalysis, 17*(1), 7-14.

Wang, L., Li, C., Jin, S., Li, W., & Liang, C. (2014). Hydrodeoxygenation of dibenzofuran over SBA-15 supported Pt, Pd, and Ru catalysts. *Catalysis letters, 144*(5), 809-816.

Wang, L., Wan, H., Jin, S., Chen, X., Li, C., & Liang, C. (2015). Hydrodeoxygenation of dibenzofuran over SiO 2, Al 2 O 3/SiO 2 and ZrO 2/SiO 2 supported Pt catalysts. *Catalysis Science & Technology, 5*(1), 465-474.

Wang, L., Zhang, M., Zhang, M., Sha, G., & Liang, C. (2013). Hydrodeoxygenation of dibenzofuran over mesoporous silica COK-12 supported palladium catalysts. *Energy & Fuels, 27*(4), 2209-2217.

Wang, Q., Park, S. Y., Duan, L., & Chung, J. S. (2008). Activity, stability and characterization of NO oxidation catalyst Co/K x Ti 2 O 5. *Applied Catalysis B: Environmental, 85*(1), 10-16.

Wang, S., Ma, C., Shi, Y., & Ma, X. (2014). Ti incorporation in MCM-41 mesoporous molecular sieves using hydrothermal synthesis. *Frontiers of Chemical Science and Engineering, 8*(1), 95-103.

Wang, Y., Fang, Y., He, T., Hu, H., & Wu, J. (2011). Hydrodeoxygenation of dibenzofuran over noble metal supported on mesoporous zeolite. *Catalysis Communications, 12*(13), 1201-1205.

Weckhuysen, B. M., Ramachandra Rao, R., Bodart, P., Debras, G., Collart, O., Voort, P., . . . Vansant, E. (2000). Synthesis, spectroscopy and catalysis of [Cr (acac) 3] complexes grafted onto MCM-41 materials: Formation of polyethylene

nanofibres within mesoporous crystalline aluminosilicates. *Chemistry: a European journal, 6*(16), 2960-2970.

Wei, H., Xie, K., Zhang, J., Zhang, Y., Wang, Y., Qin, Y., . . . Wu, Y. (2014). In situ growth of Ni(x)Cu(1-x) alloy nanocatalysts on redox-reversible rutile (Nb,Ti)O(4) towards high-temperature carbon dioxide electrolysis. *Sci Rep, 4*, 5156.

Whiffen, V. M., & Smith, K. J. (2010). Hydrodeoxygenation of 4-Methylphenol over Unsupported MoP, MoS2, and MoO x Catalysts†. *Energy & Fuels, 24*(9), 4728-4737.

Wildschut, J., Mahfud, F. H., Venderbosch, R. H., & Heeres, H. J. (2009). Hydrotreatment of fast pyrolysis oil using heterogeneous noble-metal catalysts. *Industrial & Engineering Chemistry Research, 48*(23), 10324-10334.

Wolf, R. E. (2005). What is ICP-MS? and more importantly, what can it do. *US Geological Survey, 7*.

Wolfbeisser, A., Klotzer, B., Mayr, L., Rameshan, R., Zemlyanov, D., Bernardi, J., . . . Rupprechter, G. (2015). Surface modification processes during methane decomposition on Cu-promoted Ni-ZrO catalysts. *Catal Sci Technol, 5*(2), 967-978.

Wu, C., Wang, L., Williams, P. T., Shi, J., & Huang, J. (2011). Hydrogen production from biomass gasification with Ni/MCM-41 catalysts: Influence of Ni content. *Applied Catalysis B: Environmental, 108–109*, 6-13.

Wu, P., Tatsumi, T., Komatsu, T., & Yashima, T. (2002). Postsynthesis, characterization, and catalytic properties in alkene epoxidation of hydrothermally stable mesoporous Ti-SBA-15. *Chemistry of materials, 14*(4), 1657-1664.

Xiang, L., & Zhong, L. (2008). Adsorption kinetics of dibenzofuran in activated carbon packed bed. *Chinese Journal of Chemical Engineering, 16*(2), 203-208.

Xiu, S., & Shahbazi, A. (2012). Bio-oil production and upgrading research: A review. *Renewable and Sustainable Energy Reviews, 16*(7), 4406-4414.

Xu, C., Arancon, R. A., Labidi, J., & Luque, R. (2014). Lignin depolymerisation strategies: towards valuable chemicals and fuels. *Chem Soc Rev, 43*(22), 7485-7500.

Xu, H., Dong, P., Liu, L., Wang, J.-G., Deng, F., & Dong, J.-X. (2007). Synthesis and characterization of zeolite mazzite analogue in Na2O–Al2O3–SiO2–Piperazine–H2O. *Journal of Porous Materials, 14*(1), 97-101.

Yakovlev, V., Khromova, S., Sherstyuk, O., Dundich, V., Ermakov, D. Y., Novopashina, V., . . . Parmon, V. (2009). Development of new catalytic systems for upgraded bio-fuels production from bio-crude-oil and biodiesel. *Catalysis Today, 144*(3), 362-366.

Yan, N., Yuan, Y., Dykeman, R., Kou, Y., & Dyson, P. J. (2010). Hydrodeoxygenation of Lignin-Derived Phenols into Alkanes by Using Nanoparticle Catalysts Combined with Brønsted Acidic Ionic Liquids. *Angewandte Chemie International Edition, 49*(32), 5549-5553.

Yan, N., Zhao, C., Dyson, P. J., Wang, C., Liu, L. t., & Kou, Y. (2008). Selective Degradation of Wood Lignin over Noble-Metal Catalysts in a Two-Step Process. *ChemSusChem, 1*(7), 626-629.

Yang, Y.-n., Zhang, H.-k., En-jing, L., Zhang, C.-h., & Ren, J. (2011). Effect of Fe, Mo promoters on acetic acid hydrodeoxygenation performance of nickel-based catalyst. *Journal of Molecular Catalysis (China), 25*, 30-36.

Yang, Y., Gilbert, A., & Xu, C. (2009). Hydrodeoxygenation of bio-crude in supercritical hexane with sulfided CoMo and CoMoP catalysts supported on MgO: A model compound study using phenol. *Applied Catalysis A: General, 360*(2), 242-249.

Yang, Y., Ochoa-Hernández, C., Víctor, A., Pizarro, P., Coronado, J. M., & Serrano, D. P. (2014). Effect of metal–support interaction on the selective hydrodeoxygenation of anisole to aromatics over Ni-based catalysts. *Applied Catalysis B: Environmental, 145*, 91-100.

Yu, J., Xiang, Q., & Zhou, M. (2009). Preparation, characterization and visible-light-driven photocatalytic activity of Fe-doped titania nanorods and first-principles study for electronic structures. *Applied Catalysis B: Environmental, 90*(3), 595-602.

Zakzeski, J., Bruijnincx, P. C., Jongerius, A. L., & Weckhuysen, B. M. (2010). The catalytic valorization of lignin for the production of renewable chemicals. *Chemical reviews, 110*(6), 3552-3599.

Zanuttini, M., Peralta, M., & Querini, C. (2015). Deoxygenation of m-Cresol: Deactivation and Regeneration of Pt/γ-Al2O3 Catalysts. *Industrial & Engineering Chemistry Research, 54*(18), 4929-4939.

Zhang, W., Chen, J., Liu, R., Wang, S., Chen, L., & Li, K. (2014). Hydrodeoxygenation of lignin-derived phenolic monomers and dimers to alkane fuels over bifunctional zeolite-supported metal catalysts. *ACS Sustainable Chemistry & Engineering, 2*(4), 683-691.

Zhang, W., Tiejun, Ma, L., Yu, Y., & Chen, L. (2013). Hydrodeoxygenation of lignin-derived phenolic compounds to hydrocarbons over Ni/SiO2–ZrO2 catalysts. *Bioresource Technology, 134*, 73-80.

Zhang, X., Wang, T., Ma, L., Zhang, Q., Yu, Y., & Liu, Q. (2013). Characterization and catalytic properties of Ni and NiCu catalysts supported on ZrO2–SiO2 for guaiacol hydrodeoxygenation. *Catalysis Communications, 33*, 15-19.

Zhang, X., Zhang, Q., Wang, T., Ma, L., Yu, Y., & Chen, L. (2013). Hydrodeoxygenation of lignin-derived phenolic compounds to hydrocarbons over Ni/SiO2-ZrO2 catalysts. *Bioresour Technol, 134*, 73-80.

Zhang, X., Zhang, Q., Wang, T., Ma, L., Yu, Y., & Chen, L. (2013). Hydrodeoxygenation of lignin-derived phenolic compounds to hydrocarbons over Ni/SiO 2–ZrO 2 catalysts. *Bioresource technology, 134*, 73-80.

Zhang, Z., Ji, Y., Li, J., Zhong, Z., & Su, F. (2015). Synergistic effect in bimetallic copper–silver (CuxAg) nanoparticles enhances silicon conversion in Rochow reaction. *RSC Adv., 5*(67), 54364-54371.

Zhao, C., He, J., Lemonidou, A. A., Li, X., & Lercher, J. A. (2011). Aqueous-phase hydrodeoxygenation of bio-derived phenols to cycloalkanes. *Journal of Catalysis, 280*(1), 8-16.

Zhao, C., & Lercher, J. A. (2012). Selective Hydrodeoxygenation of Lignin-Derived Phenolic Monomers and Dimers to Cycloalkanes on Pd/C and HZSM-5 Catalysts. *ChemCatChem, 4*(1), 64-68.

Zhao, X., Lu, G., Whittaker, A., Millar, G., & Zhu, H. (1997). Comprehensive study of surface chemistry of MCM-41 using 29Si CP/MAS NMR, FTIR, pyridine-TPD, and TGA. *The Journal of Physical Chemistry B, 101*(33), 6525-6531.

Zhou, M., Chai, H., Jia, D., & Zhou, W. (2014). The glucose-assisted synthesis of a graphene nanosheet–NiO composite for high-performance supercapacitors. *New Journal of Chemistry, 38*(6), 2320-2326.

Zhou, X.-F. (2014). Conversion of kraft lignin under hydrothermal conditions. *Bioresource technology, 170*, 583-586.

Zhu, W., Sugano, N., & Pezzotti, G. (2013). Nondestructive inspection of phase transformation in zirconia-containing hip joints by confocal Raman spectroscopy. *J Biomed Opt, 18*(12), 127002.

Zhu, X., Lobban, L. L., Mallinson, R. G., & Resasco, D. E. (2011). Bifunctional transalkylation and hydrodeoxygenation of anisole over a Pt/HBeta catalyst. *Journal of Catalysis, 281*(1), 21-29.

LIST OF PUBLICATIONS AND PAPER PRESENTED

Publications

Ambursa, M. M., Ali, T. H., Lee, H. V., Sudarsanam, P., Bhargava, S. K., & Hamid, S. B. A. (2016a). Hydrodeoxygenation of dibenzofuran to bicyclic hydrocarbons using bimetallic Cu–Ni catalysts supported on metal oxides. *Fuel, 180*, 767-776.

Ambursa, M. M., Sudarsanam, P., Voon, L. H., Hamid, S. B. A., & Bhargava, S. K. (2017). Bimetallic Cu-Ni catalysts supported on MCM-41 and Ti-MCM-41 porous materials for hydrodeoxygenation of lignin model compound into transportation fuels. *Fuel Processing Technology, 162*, 87-97.

Hamid, S. A., Ambursa, M.M., Sudarsanam, P., Voon, L. H., & Bhargava, S. K. (2017). Effect of Ti loading on structure-activity properties of Cu-Ni/Ti-MCM-41 catalysts in hydrodeoxygenation of guaiacol. *Catalysis communication, 94, 18-22*

Influence of metal loading on Ti-MCM-41 supported bimetallic catalysts for hydrodeoxygenation of Dibenzofuran. **Submitted**

Reactivity studies of Cu-Ni/Ti-MCM-41 catalysts for hydrodeoxygenations of dibenzofuran: Hydrocarbons Selectivity and Reactions Pathways. **Under preparations.**

Conferences

Transition metal containing mesoporous silica as effective catalysts support for hydrodeoxygenation of Dibenzofuran to fuels graded molecules. ***(98th International Conference on Science, Technology and Management (ICSTM) Kuala Lumpur, Malaysia 5th-6th November, 2016)***